The Development of Fibre-Reinforced Ceramic Matrix Composites of Oxide Ceramic Electrolyte

Cassian Middleton Marriner-Edwards

Hertford College

Department of Materials

University of Oxford

A thesis submitted for the degree of Doctor of Philosophy (DPhil)

Trinity 2016

To My Love and Family

"Our Knowledge Has Made Us Cynical.

Our Cleverness, Hard and Unkind.

We Think Too Much and Feel Too Little.

More Than Machinery We Need Humanity.

More Than Cleverness We Need Kindness and Gentleness."

Charlie Chaplin

Declaration of Originality

I, Cassian M. Marriner-Edwards, hereby declare that all work presented in this doctoral thesis, which is approximately 39,000 words in length, is original and where the work of others has been included it has been clearly referenced and acknowledged. This thesis is an account of work carried out at the School of Chemistry, University of St Andrews between September 2012 and November 2014 and the Department of Materials, University of Oxford between November 2014 and October 2016, under the supervision of Prof. Peter G. Bruce. No part of this thesis has been submitted towards another degree at the University of Oxford or elsewhere.

Acknowledgements

I would first like to thank my supervisor Prof. Peter G. Bruce for giving me the fantastic opportunity to work in his research group, for always encouraging brighter ideas and providing the resources to enact them. I am also very thankful for the generous funding provided by the School of Chemistry, University of St Andrews and the Department of Materials, University of Oxford. Thanks also to Hertford College and MPLS for administrative support during my time at Oxford.

A special thanks goes to all the members of the Bruce group, both past and present. Particularly, I would like to thank Dr Yuri Andreev, Dr Ola Hekselman, Dr Felix Richter, Dr Jitti Kasemchainan and Stefanie Zekoll, for their advice, help and direction on this project. A further thanks to Dr Matthew Roberts and Dr Lee Johnson for steadying the ship. Additionally, I would like to thank my collaborators Dr Job Thijssen (University of Edinburgh) for his guidance on bijels and providing micro-computed tomography data and Dr Robert Wallace (University of Edinburgh) for his help with micro-computed tomography. I would also like to acknowledge Dr Kalin Dragnevski and Dr Marzena Tkaczyk at the Laboratory for in-situ Microscopy and Analysis, Department of Engineering Science, University of Oxford, for their assistance with Brazilian disk testing.

Finally, thank you to my parents for their love and support and for always providing a space of sanctuary and calm for me to grow. Also to my sisters who have always been inspiring examples of successful, fun and caring people and to their families who fill me

with warmth, even in cold times. To my love, Jacqueline, who has always stood by me with an open heart and radiating energy. You are truly an amazing woman and I will always be in awe of your hunger for life and care for others. To Alex, Calum and Emma whose friendship I cherish and who keep me young with their laughter and encouragement. And to Sam, the diamond in the rough whose love of coffee breaks and Freddos always brought a smile to my face.

Abstract

Flammable solvents contained in liquid electrolytes pose a serious safety risk when used in lithium batteries. Oxide ceramic electrolytes are a safer alternative, but suffer from inadequate mechanical properties and ionic conductivity. Thin electrolyte layers resolve the issue of conductance, but accentuate the detrimental mechanical properties of oxide ceramics. The presented work has investigated oxide ceramic electrolyte reinforcement in composite electrolytes for all-solid-state batteries.

Fabricating oxide ceramic electrolytes with engineered microstructure enabled development of a reinforced composite. This approach is based on the formation of 3D-porous ceramics via stereolithography printing of polymer templates from designed cubic, gyroid, diamond and bijel architectures. The microstructural parameters of templates were analysed and modified using computational techniques. Infiltration of the prepared 3D-porous electrolyte with polymeric-fibre reinforcement created the reinforced composite electrolyte. The prepared ceramic composite showed excellent reproduction of the template microstructure, good retention of ionic conductivity and enhanced mechanical properties.

The final composite was composed of NASICON-type $Li_{1.6}Al_{0.6}Ge_{1.4}(PO_4)_3$ oxide ceramic electrolyte and epoxy and aramid fibre reinforcement. The gyroid architecture was computationally determined as having the optimal stress transfer efficiency between two phases. The printed gyroid polymer template gave excellent pore microstructure reproduction in ceramic that had 3D-interconnected porosity, high relative density and the most uniform thickness distribution. The ceramic matrix porosity allowed for complete infiltration of reinforcement by aramid and epoxy forming the fibre-reinforced ceramic matrix composite. The interpenetrating composite microstructure with ceramic and epoxy gave a flexural strength increase of 45.65 MPa compared to the ceramic. Unfortunately, the infiltration procedure of aramid-epoxy reinforcement did not realise the full tensile strength potential of aramid fibres.

Abbreviations

μCT	- Micro-computed Tomography
AC EIS	- Alternating Current Electrochemical Impedance Spectroscopy
CAD	- Computer-Aided Design
CMC	- Ceramic Matrix Composite
CPE	- Constant Phase Element
CSD	- Channel Size Distribution
DMSO	- Dimethyl Sulfoxide
EDS	- Energy Dispersive X-ray Spectroscopy
ESEM	- Environmental Scanning Electron Microscopy
FR	- Fibre-Reinforced
FRP	- Fibre-Reinforced Polymer
IPC	- Interpenetrating Composite
LAGP	- $Li_{1.6}Al_{0.6}Ge_{1.4}(PO_4)_3$
LATP	- $Li_{1.3}Al_{0.3}Ti_{1.7}(PO_4)_3$
LGPS	- $Li_{10}GeP_2S_{12}$
LIBs	- Lithium-Ion Batteries
LLTO	- $Li_5La_3Ta_2O_{12}$
LLZO	- $Li_7La_3Zr_2O_{12}$
LPS	- Li_3PS_4
NASICON	- Sodium Super Ion Conductor
NW	- Non-Woven
PECS	- Precision Etching Coating System
PPTA	- Poly(Paraphenylene Terephthalamide)
PXRD	- Powder X-ray Diffraction
SAVR	- Surface-Area-to-Volume Ratio
SEM	- Scanning Electron Microscopy
STD	- Sample Thickness Distribution
SVF	- Solid Volume Fraction
TGA	- Thermogravimetric Analysis

Table of Contents

Declaration of Originality ..... **ii**

Acknowledgements ..... **iii**

Abstract ..... **v**

Abbreviations ..... **vi**

Table of Contents ..... **vii**

Chapter 1: Introduction **1**

1.1 Battery Requirements 1

1.2 Lithium-ion Battery Technology 3

1.3. Solid Electrolytes 5

1.4. Ceramic Electrolytes 7

1.5. Physical Properties of Ceramics 9

1.6. Mechanical Properties 10

1.7. Solid-Solid Interface 16

1.7.1. High Interfacial Resistivity 16

1.7.2. Lithium Dendrite Formation 18

1.8. Fibre-Reinforced Ceramic Matrix Composite (FR-CMC) 19

1.9. Interpenetrating Composite (IPC) 24

1.10. Additive Manufacturing 28

1.11. Aim 29

1.12. References 30

Chapter 2: Experimental Techniques **34**

2.1. Powder X-ray Diffraction (PXRD) 34
2.2. Scanning Electron Microscopy (SEM) and Energy Dispersive Spectroscopy (EDS) 35
2.3. Alternating Current Electrochemical Impedance Spectroscopy (AC EIS) 36
2.4. Brazilian Disk Testing 40
2.5. Thermogravimetric Analysis (TGA) 41
2.6. Micro-computed Tomography (μCT) 41
2.7. Four-Point Bending Analysis 42
2.8. References 45
Chapter 3: Structural Composite Reinforcement of Oxide Ceramic Electrolyte 46
3.1. Aim 46
3.2. Introduction 46
3.3. Experimental Methods 47
3.3.1. Synthesis of $Li_{1.6}Al_{0.6}Ge_{1.4}(PO_4)_3$ (LAGP) 47
3.3.2. Synthesis of Fibre-Reinforced Polymer 48
3.3.3. Synthesis of Structural Fibre-Reinforced Ceramic Matrix Composite 48
3.4. Characterisation 48
3.5. Result and Discussion 50
3.5.1. LAGP Oxide Ceramic Electrolyte Synthesis 50
3.5.2. Fibre-Reinforced Polymer Fabrication 59
3.5.3. Structural Fibre-Reinforced Ceramic Matrix Composite 61
3.5.4. Mechanical Analysis of Structural Fibre-Reinforced Composite 63
3.6. Conclusion 68

3.7. References 70

Chapter 4: Composite Fabrication from Developed Bijel Templates 72

4.1. Aim 72

4.2. Introduction 72

4.3. Experimental Methods 74

4.3.1. Solidification of Liquid Bijel Synthesis 74

4.3.2. Etching of Solidified Bijel 75

4.3.3. $Li_{1.6}Al_{0.6}Ge_{1.4}(PO_4)_3$ (LAGP) Adapted Sacrificial Templating 75

4.3.4. Polypropylene Impregnation of LAGP Preform 76

4.4. Characterisation 76

4.5. Results & Discussion 78

4.5.1. Bijel Polymer Template Fabrication 78

4.5.2. Microstructural Parameter Analysis 84

4.5.3. Bijel Gyroidal Architecture 91

4.5.4. Preform Formation via Sacrificial Templating with Bijel Template 94

4.6. Conclusion 100

4.7. References 101

Chapter 5: Computer-Aided Design & Template Fabrication 102

5.1. Aim 102

5.2. Introduction 102

5.3. Experimental Methods 104

5.3.1. Architecture Generation 104

5.3.2. Bijel Architecture Modification 104

5.3.3. Synthesis of 2-Photon Stereolithography 105

5.3.4. Architectural Print Extension Generation 105
5.4. Characterisation 105
5.5. Results & Discussion 107
5.5.1. 3D-Interconnected Sacrificial Templates 107
5.5.1.1. Computational 3D Architecture Generation: Gyroid, Diamond and Cubic Lattice 107
5.5.1.2. Computational 3D-Analysis and Design 111
5.5.1.3. Computational 3D-Modification 115
5.5.1.4. 2-Photon Stereolithography Synthesis 121
5.5.2. Hierarchical Template Microstructure for Replication 127
5.5.3. Print Optimisation 134
5.6. Conclusion 141
5.7. References 142
Chapter 6: 3D-Porous Oxide Ceramic Electrolyte Preform Formation 144
6.1. Aim 144
6.2. Introduction 144
6.3. Experimental Methods 149
6.3.1. $Li_{1.6}Al_{0.6}Ge_{1.4}(PO_4)_3$ (LAGP) Adapted Replication Procedure 149
6.3.2. LAGP Adapted Sacrificial Templating 150
6.3.3. Polypropylene Impregnation of LAGP Preform 151
6.4. Characterisation 151
6.5. Results & Discussion 153
6.5.1. Replication 153
6.5.1.1. Sol-Gel Synthesis 153

6.5.1.2. Printed Template Replication 156
6.5.1.3. Hierarchical Template Replication 159
6.5.2. Sacrificial Templating 169
6.5.2.1. Sacrificial Particles 169
6.5.2.2. Printed Templates with Sacrificial Templating Sedimentation 170
6.5.2.3. Adapted Sacrificial Templating Procedure 171
6.5.2.4. Ceramic Preform Analysis 177
6.5.2.5. Ionic Conductivity of Preform via Sacrificial Templating.. 185
6.6. Conclusion 190
6.7. References 191
Chapter 7: Fibre-Reinforced Ceramic Matrix Composite Fabrication 192
7.1 Aim 192
7.2. Introduction 192
7.3. Experimental Techniques 193
7.3.1. Preparation of Aramid Dispersion 193
7.3.2. Infiltration of Ceramic Preform with Aramid 194
7.3.3. Epoxy Infiltration of Aramid-LAGP Preform 194
7.4. Characterisation 194
7.5. Results & Discussion 195
7.5.1. Aramid Preparation 195
7.5.2. LAGP Preform Infiltration and Deposition with Aramid 198
7.5.3. FR-CMC Preparation by Epoxy Infiltration of Aramid-LAGP Preform 200

7.5.4. FR-CMC Mechanical Analysis..... 202

7.6. Conclusion..... 209

7.7 References..... 210

Chapter 8: Conclusion & Outlook 211

Appendices 216

Chapter 1: Introduction

1.1 Battery Requirements

The ability to generate and store electric energy on demand has shaped our lives in the modern era. Energy can be stored, transported and generated without having to rely on stationary sources or fuel combustion. The storage of chemical energy in battery technology has enabled such freedom. Portable electronic devices, transportation systems and power grids have all benefitted from battery storage.

Meeting the demands of modern society requires ever improving battery technologies. Rechargeable lithium-ion batteries (LIBs) have demonstrated great versatility with superior energy densities (100-265 W h kg^{-1}) and high cell voltages (3.2-3.8 V).[1, 2] *Figure 1.1* shows different battery types and their varied gravimetric and volumetric energy densities.[3] Higher densities result in lighter and smaller LIBs, more suitable for applications such as portable electronic devices.

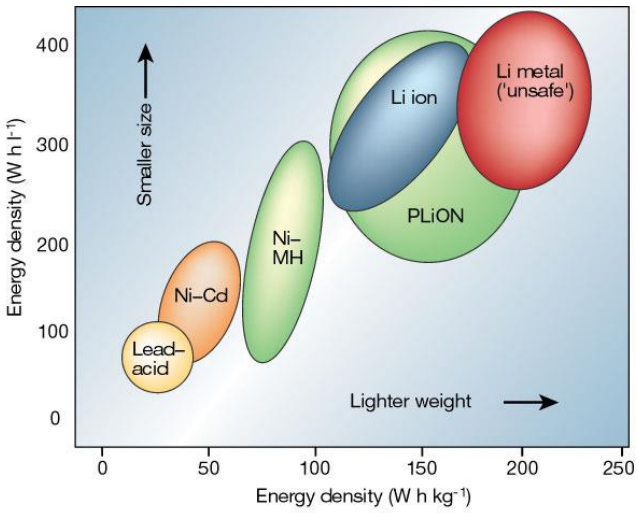

Figure 1.1 Graph of gravimetric and volumetric energy densities of different battery systems.[3]

Lithium ions are superb charge carriers for high energy density electrochemical cells, as the lightest metal ion. However, the full potential of LIBs has not yet been realised.[4] Increasing demand and reliance on LIBs is fuelling the need for further improvement to achieve their full potential. For example, since Sony sold the first commercial LIBs in 1991, innovation in cell design and engineering has more than doubled the energy storage of modern LIBs.[4] Currently, the Joint Center for Energy Storage Research at the Argonne National Laboratory in Illinois is aiming to achieve 400 W h kg^{-1} by 2017.[4]

Despite advances in cell design, some inherent safety issues remain and the pursuit of higher power batteries intensifies this issue due to increasing voltage and reactivity.[3] Under certain circumstances, the materials used in conventional LIBs can pose a serious safety risk. Improper methods of or error in assembly can result in short-circuits. The heat generated from short-circuiting is dangerous when in the presence of flammable solvents used in liquid electrolytes for conventional LIBs. Damage to the cell may also result in leakage of flammable solvents. Safer cell design and packaging has been a focus of industry, but often leads to a decrease in energy density.[5] As of September 2016, the Federal Aviation Administration (FAA) has recorded 129 incidents involving batteries since March 1991.[6] More recently, Samsung has announced a global recall of its Galaxy Note 7 mobile phones over reports of exploding LIBs due to manufacturing errors.[7] Many industries, where safety is paramount, demand safer electrochemical devices.

1.2 Lithium-ion Battery Technology

The reversible electrochemical redox reactions that store chemical potential energy and generate electrical energy define a secondary (rechargeable) battery. Depending on the cell's electrochemistry, charge carrier species ensure charge balance and may gain or lose electrons allowing for such reactions. The basic LIB cell consists of two electrodes that intercalate the lithium-ion charge carrier species, separated by an ionically conducting liquid electrolyte. *Figure 1.2* illustrates the 'rocking-chair' battery model describing the flow of lithium ions cycling back and forth from one electrode to the other and the corresponding flow of electrical current.

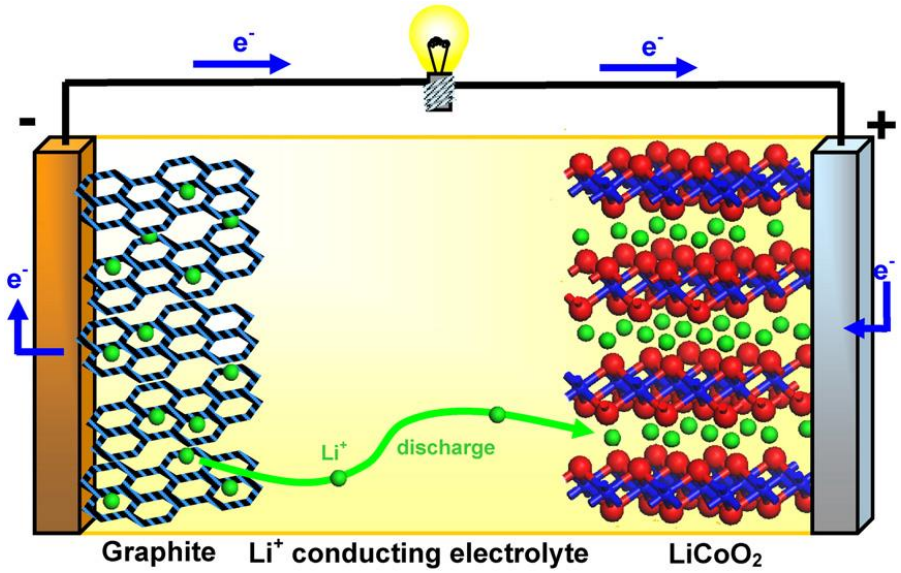

Figure 1.2 Schematic representation of a rocking chair battery model with conventional graphite anode and lithium cobalt oxide cathode.[5]

Transportation of lithium ions between the electrodes occurs through the electrolyte.[5] Firstly, the electrolyte must be non-electronically conductive to ensure electric current flow to the external circuit. Secondly, the electrolyte must be ionically conductive to transport ions and maintain charge balance during cycling. Conventional

LIBs use liquid electrolytes of lithium hexafluorophosphate ($LiPF_6$) dissolved in a mixture of ethylene carbonate and diethyl carbonate to transport lithium ions and maintain charge balance.

Electrodes are distinct regions where electric current enters or leaves the cell. They are typically composites composed of binders, electronically conductive additives and electrochemically active materials, making them both ion- and electron-conducting.[5] Active materials are compounds that intercalate or chemically bond with charge-carrier species and the site of electrochemical redox reactions. The electrochemical oxidation of the negative electrode (anode) during the discharge process releases electrons to the external electronic circuit through the supporting current collector. The positive electrode (cathode) accepts electrons from the external electronic circuit and undergoes electrochemical reduction after lithium ion insertion. The electrodes thereby undergo electrochemical redox reactions on (de)lithiation during the charge and discharge processes. Connecting to an external circuit the LIB cell spontaneously discharges. Applying an external potential, to induce current flow in the opposite direction of the discharge current, charges the cell. The most common active materials in LIBs are lithium cobalt oxide ($LiCO_2$) in the cathode and graphite in the anode.

Silicon anodes in lithium batteries have the greatest theoretical charge capacity of 4200 mA h g^{-1}. Unfortunately, silicon undergoes large volume changes (400 %) on lithium insertion and extraction, resulting in anode pulverisation and capacity fading.[8] On the other hand, metallic lithium anodes offer high theoretical charge capacity of 3860 mA h g^{-1} and low negative electrochemical potential (-3.04 V vs SHE).[9] This is due to the metal being the elemental form of the lithium ion charge carriers and having

high concentration of lithium per volume and weight. *Figure 1.3* compares the capacity and electrochemical potential of common electrode materials. However, lithium dendrites and low coulombic efficiency prevent the full implementation of metallic lithium. Unregulated lithium deposition can occur during charging, especially at high currents, leading to dendrite formation and short-circuiting.[9] In the presence of flammable solvents, the result is the same as with poorly manufactured LIBs mentioned above. Furthermore, low coulombic efficiency is the result of lithium being strongly reducing. Chemical reduction can occur when other substances are in contact with lithium, forming unwanted, possibly non-conductive, by-products. An excess of metallic lithium for the anode can compensate for the loss of efficiency, but has the effect of decreasing energy density.[9]

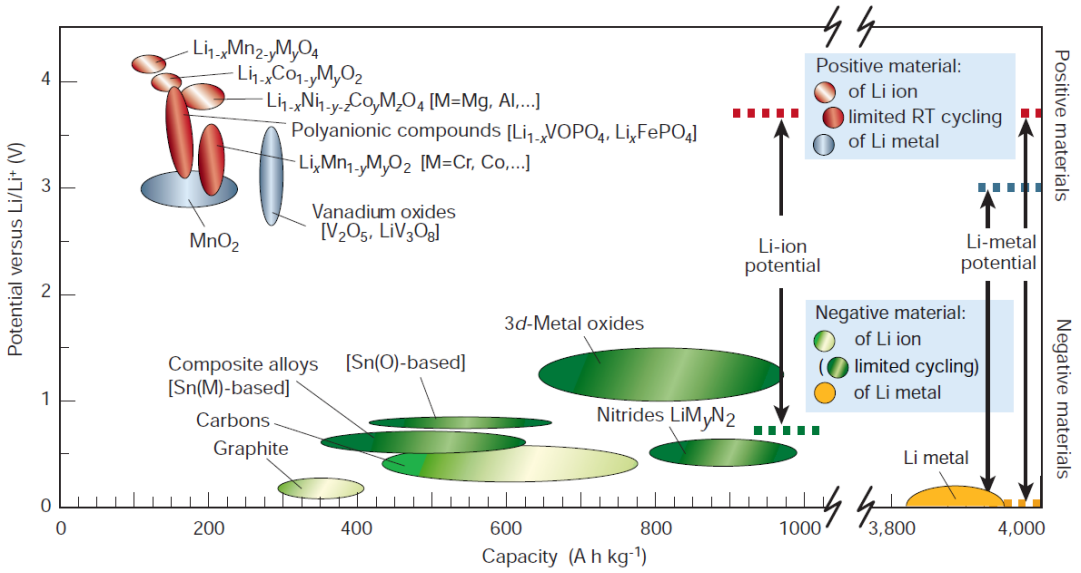

Figure 1.3 Graph of specific capacity against potential for common cathode and anode battery materials.[3]

1.3. Solid Electrolytes

With liquid electrolytes containing flammable components, conventional LIBs (manufacturing) and lithium-metal batteries (dendrites) remain safety hazards. Solid

electrolytes can replace liquid electrolytes, making for safer battery designs. Solid electrolytes are non-flammable, present a physical barrier to lithium dendrites and increase the energy density for all-solid-state batteries. Cells designed with solid electrolytes are simpler, acting as both an electrolyte and separator with no need for added leak-proof packaging. They also allow for a wider variety of cell types including the all-solid-state lithium-ion and lithium-metal batteries and solid separators for lithium-air batteries.[10] However, poor contact between solid components, poor mechanical properties and lower conductivity of solid electrolytes decreases the performance of cells. For instance, ionic conduction in solids is typically less than in liquids due to ion migration through bottleneck points rather than free exchange of solvated ions in liquid.[11] The realisation of an ideal solid replacement to liquid electrolytes is a substantial challenge.

The ideal electrolyte for an all-solid-state lithium-metal battery has to meet the following requirements:[12]

- High ionic conductivity (at least 10^{-2} S cm^{-1} at room temperature) with transference number of cationic species close to 1
- Negligible electronic conductivity ($<10^{-10}$ S cm^{-1})
- Wide electrochemical stability window (0-5 V vs. Li^{+}/Li^{0})
- Chemical and thermal stability
- Mechanical robustness
- Interfacial compatibility with electrodes (accommodating electrode volume changes)
- Low toxicity and flammability
- Low cost

With all these criteria met, the all-solid-state lithium-metal battery would be a strong candidate to replace conventional LIBs. The all-solid-state lithium-metal battery would be safer than conventional LIBs and using like-for-like chemistries would outperform them with higher energy densities.

Two main classes divide solid electrolytes: inorganic (ceramic) electrolytes and organic (polymer) electrolytes.[13] The disadvantages of current solid electrolytes are the formation of inadequate solid-solid interfaces with the electrodes, low ionic conductivity at room temperature and poor mechanical properties. For instance, the low room temperature lithium-ion conductivity ($<10^{-5}$ S cm^{-1}), poor thermal stability and low rigidity of polymer electrolytes have limited their application.[13]

1.4. Ceramic Electrolytes

Ceramic materials demonstrate many advantageous properties over polymers; chemical inertness, shock and wear resistance, strength-to-weight ratio and thermal stability at elevated temperatures make them potential candidates for superior all-solid-state cells.[12-15] Ceramic electrolytes can also have good electronic insulating and ionic conducting properties. However, the adoption of ceramic electrolytes in all-solid-state batteries has been limited due to the formation of poor solid-solid interfaces with electrodes (**Section 1.7**), susceptibility to mechanical failure due to brittleness (**Section 1.6**) and toxicity of some materials. [13, 15]

The chemical bonding, atomic arrangement and lattice structure of a ceramic electrolyte defines key material properties.[16] Mechanical properties depend largely on the ability of chemical bonds to strain under stress, whereas ionic conduction depends on the size and percolation of conduction pathways and electromagnetic interactions

between the mobile ions and sub-lattice.[13, 15, 16] The bond energy between atoms defines the strength of chemical bonds and compounds. The ionic radius and polarisability of sulfur is ideal to form ion pathways and support lattice interactions facilitating excellent ionic conduction.[15]

Two main categories divide ceramic electrolytes possessing favourable properties: sulfides and oxides. Sulfide ceramic electrolytes achieve higher ionic conductivity than oxides and are more ductile. On the other hand, oxide ceramic electrolytes are more moisture and atmosphere stable, stiffer and more rigid.[17, 18] The ionic radius of sulfur is much larger than oxygen and therefore the electrostatic attraction or bond strength of oxides are typically much stronger than sulfides.

Research has focused on overcoming the current disadvantages of both types of ceramic electrolytes. Developing new materials and fabrication techniques aims to improve all-solid-state batteries. Decreasing the thickness of the electrolyte layer overcomes the typically low ionic conductivity of solids by reducing the conductance length. Sulfide ceramic electrolytes are best suited for thin-film application being more ductile than oxides, but are chemically reactive with metallic lithium and difficult to handle being hygroscopic and potentially forming toxic hydrogen sulfide gas.[19] More atmospherically stable oxide ceramic electrolytes are typically very brittle and thin layers increase their susceptibility to mechanical failure.[17] Due to the inherent safety risk of sulfide ceramic electrolytes, the focus of this work is on improving the mechanical properties of oxide ceramic electrolytes. Enhancing the mechanical properties of oxide ceramic electrolytes requires an understanding of the physical and mechanical properties.

1.5. Physical Properties of Ceramics

Ceramic materials can be characterised by their atomic arrangement (crystallinity). Crystallinity has a large effect on the physical properties of a solid and the solid-solid interface formed with other materials, as discussed in **Section 1.7**. Crystallinity can be characterised as being: crystalline, semi-crystalline or non-crystalline amorphous.[19] Crystalline materials can also exist as monocrystalline (single crystal) or polycrystalline (numerous crystallites), though the former is grown only under highly controlled conditions. The sintering process of stiff material powders typically forms well defined polycrystalline materials.[18, 20] The garnet-type polycrystalline ceramic electrolyte lithium lanthanum zirconium oxide (LLZO), $Li_7La_3Zr_2O_{12}$, sinters at 1100 °C with an elastic modulus of 140 GPa[17], compared to softer less defined Li_2S-P_2S_5, cold pressed with an elastic modulus of 20 GPa.[21]

Many polycrystalline ceramic electrolytes are excellent lithium-ion conductors in the bulk phase (~10^{-3} S cm^{-1}) and yet have low total ionic conductivity. The presence of crystallites (grains) introduces crystallite-crystallite interfaces, known as grain boundaries. Impeding ion flow across the grain boundaries, by grain-boundary resistance, decreases the total ionic conductivity in polycrystalline materials. *Figure 1.4* shows a scanning electron microscope (SEM) image of the grains of polycrystalline LLZO.[20]

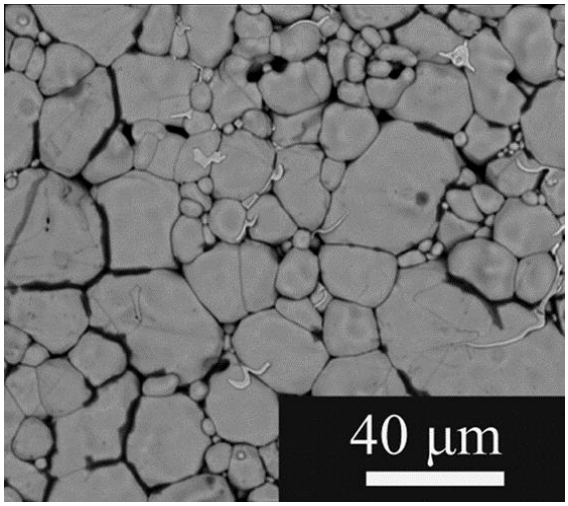

Figure 1.4 SEM image of sintered polycrystalline LLZO.[20]

1.6. Mechanical Properties

Materials can be classified by their mechanical properties - how they deform (strain) under an applied force (stress). The strength of chemical bonds and their ability to stretch (deform) and break (dislocate) are the primary mechanical defining properties of material strain.[16] The type of strain and magnitude of stress required for mechanical failure can also differ depending on the direction and type of applied force, defining different mechanical properties such as elasticity, rigidity, strength, hardness and toughness.[16]

The orientation of applied force defines the analytical technique used to determine a mechanical property. The key defining mechanical properties of ceramics are elasticity, rigidity, brittleness and toughness. The ratio of uniaxial (u) or shear (s) stress (σ) and strain (ε), quantifies the elasticity and rigidity of a material, respectively, known as the elastic modulus, E, and shear modulus, G:

$$E = \sigma_u / \varepsilon_u \tag{1.1}$$

$$G = \sigma_s / \varepsilon_s \tag{1.2}$$

When the ratio of stress to strain is constant during the loading and unloading process (fully recovers), the material behaves elastically. This is due to the chemical bonds' ability to stretch and recover causing the stress-strain curve in *Figure 1.5* region (a) to show linear elastic behaviour. When a material requires more stress to strain, the elastic modulus and shear modulus increases. Therefore, the 'elasticity' or 'stiffness' refers to the resistance of a material to elastic (reversible) deformation by uniaxial force, describing the elastic modulus. Similarly, the 'rigidity' refers to the resistance of a material to elastic deformation by opposing forces parallel to one of the surfaces (shear), describing the shear modulus. Due to strong chemical bonding, ceramics typically have high elastic modulus under compressive uniaxial force and high shear modulus under shear forces. Therefore, ceramics typically have high compressive strength. The elastic modulus of LLZO is approximately 140 GPa[17] compared to known polymer electrolyte membranes of 1 GPa.[22]

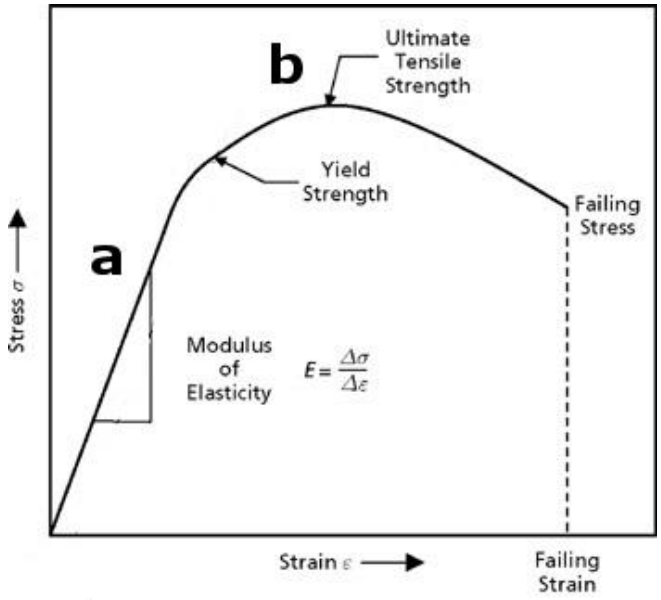

Figure 1.5 Graph of a typical stress-strain curve showing elastic and plastic behaviour.[23]

Materials can also demonstrate non-linear behaviour on loading known as plastic deformation. Plastic deformation, shown in *Figure 1.5* region (b), is the permanent (irreversible) yielding of material in response to stress without fracture. In order for plastic deformation to occur, the chemical bonding of the material must allow for dislocations involving bond breaking and reforming. The type and strength of chemical bond determines the likelihood of plastic deformation. Therefore, ionic and covalent bonds with high bond strength do not reform after bond breaking and hence do not demonstrate plastic deformation. Brittleness describes the non-plasticity of a material and therefore susceptibility to brittle fracture. Oxide ceramic materials are brittle due to their mixture of strong covalent and ionic bonding. Ceramics typically have low elastic moduli under tensile uniaxial force, due to the orientation of force against chemical bonds (pulling apart). Therefore, ceramics typically have low tensile strength.[16]

The strain response of a material after yielding (*Figure 1.5* yield strength) and before fracture characterises another key mechanical property: toughness. The ability of a material to absorb further energy after yielding, either by plastic deformation or by reinforcement, defines toughness. The amount of energy absorbed prior to fracture quantifies the toughness of a material (area under *Figure 1.5* region (b)). Brittle ceramic materials fracture immediately after yielding and therefore have low toughness.[16]

Microstructural features of crystallinity, (micro-) cracks, chemically distinct phases or defects can alter the mechanical properties.[17] The concentration of microstructural features increases or decreases depending on the material, fabrication technique and environmental stresses. Microstructural features act as stress concentrators increasing local stress in materials under load.[16, 17] Non-uniform stress distributions, shown in *Figure 1.6*, have a large effect on the mechanical properties due to local yielding at the crack tip. The most common crack propagation mode, along atomic slip planes within a lattice structure, is by tensile force. Plastic deformation can absorb the energy of propagating cracks, preventing fracture and increasing toughness.[16] Other features caused by damage or scratching, can affect the mechanical properties of a material in a similar way.

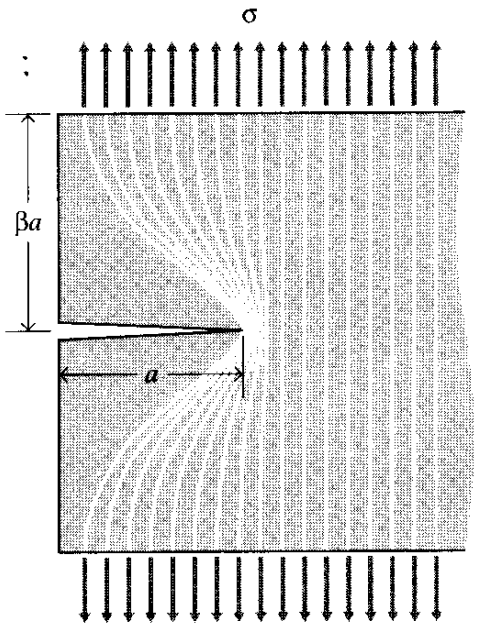

Figure 1.6 Schematic representation of stress concentration at a crack tip.[16]

In brittle materials, microstructural features can have a large weakening effect.[16, 17, 24] The concentration and geometry of microstructural features defines the number and magnitude of local stress concentrations and therefore the amount of formed (micro-) cracks on loading. Increasing (micro-) crack number increases the likelihood of a crack propagating the length of the part by local stresses and therefore the probability of brittle fracture.[24]

Poor mechanical properties in conventional LIB cells can affect performance.[25, 26] Sakuda *et al*. have briefly discussed mechanical failure in all-solid-state lithium cells based on sulfides, but current literature does not report a full investigation.[21] Regardless, poor mechanical properties increase the susceptibility of mechanical failure and issues at the solid-solid interface with electrodes, as discussed in **Section 1.7**. Therefore, one assumes mechanical failure of the solid electrolyte could cause high resistivity, loss of ionic conduction, short-circuiting and further mechanical failure in the cell. The typical environmental operating stresses of a cell include vibrations, impact

shocks, thermal expansion, stress-inducing fabrication processes, electrode volume changes and/or lithium deposition.

The low tensile strength and toughness of oxide ceramic electrolytes increases susceptibility to mechanical failure. As a result, increasing the conductance by decreasing the thickness of electrolyte layer poses a risk. *Figure 1.7* demonstrates the relationship between thickness and toughness.[16] Decreasing thickness decreases the crack-propagation or damage-penetration distance required to cause fracture.[16, 27] Apart from investigations of the fracture toughness and elastic properties of LLZO by Wolfenstine *et al*.[28] and Yu *et al*.,[17] respectively, there has been little investigation into the specific fracture mechanics of solid electrolytes. Therefore, enhancing and sustaining the mechanical properties of thin oxide ceramic electrolytes is a challenge for materials research. **Section 1.7** discusses the advantage of solid-solid interfaces also requiring tough and thin oxide ceramic electrolytes.

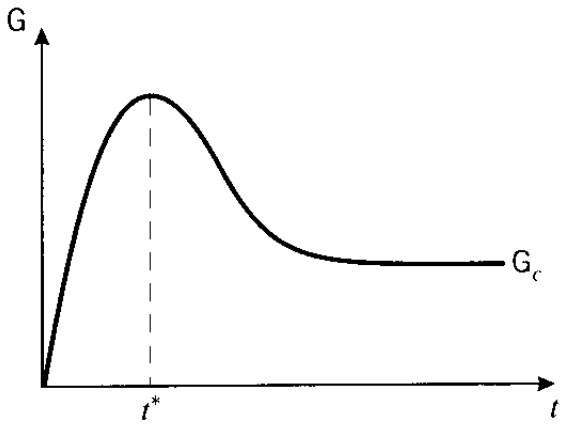

Figure 1.7 Graph showing toughness, G, against thickness, t, where t and G_c are the critical thickness and the critical strain energy release rate, respectively.*[16]

1.7. Solid-Solid Interface

1.7.1. High Interfacial Resistivity

Good interfacial properties between the different components of a battery are essential for cell performance.[19] The two types of solid-solid interfaces in all-solid-state lithium cells are those between solid electrolytes and either an intercalation electrode or a metallic lithium or lithium-alloy anode. Lithium-ion flow across the interfaces between electrodes and electrolyte must occur in order to maintain charge balance and for the cell to charge and discharge. Good interfacial contact at the interfaces ensures unimpeded ion flow maintaining charge balance and cycle efficiency. Liquid electrolytes typically form excellent interfacial contact with electrodes due to their wetting of active material, whereas a solid-solid interface is typically very poor.[29] High interfacial resistances and short-circuiting by lithium dendrite growth can form due to incompatible solid electrolytes, electrodes, and the degradation of their interfaces.

High interfacial resistances between metallic lithium anodes and solid electrolytes result when poor contact, electrochemical and chemical reactivity and/or electrochemical effects between the solid surfaces occur.[30] Cheng *et al*. demonstrated the poor solid-solid interfacial contact formed between metallic lithium anodes and solid electrolytes due to the deterioration of the electrolyte surface microstructure after sintering.[20] The work reports lithium-ion flow concentration along grain boundaries during charge and discharge. High interfacial resistivity occurs when large grains are present at the interface causing an un-even distribution of lithium ion flow to the electrode. Where smaller grains populate the interface, a more even distribution of lithium ion flow occurs resulting in lower interfacial resistivity. Polycrystalline oxide

electrolytes requiring high sintering temperatures for formation typically have poor contact.[17]

Different fabrication techniques for ceramic electrolytes can be utilised to avoid the deterioration of surface microstructures and prevent high interfacial resistances.[21] Conventional high temperature sintering techniques limit microstructural features, but deteriorate surface microstructure due to grain growth.[20] Cheng *et al*. showed that surface microstructure modification of ceramic electrolytes sintered at high temperatures prevents substantial grain growth.[20] By mixing small powder particles with larger ones, grain growth during sintering is limited resulting in a more beneficial surface microstructure and lower interfacial resistance. However, the nonconformity of particle size results in additional microstructural features forming as pores, shown in *Figure 1.8*. Fabricating a thin oxide ceramic electrolyte with beneficial surface microstructure requires a means of toughening and eradicating microstructural features.

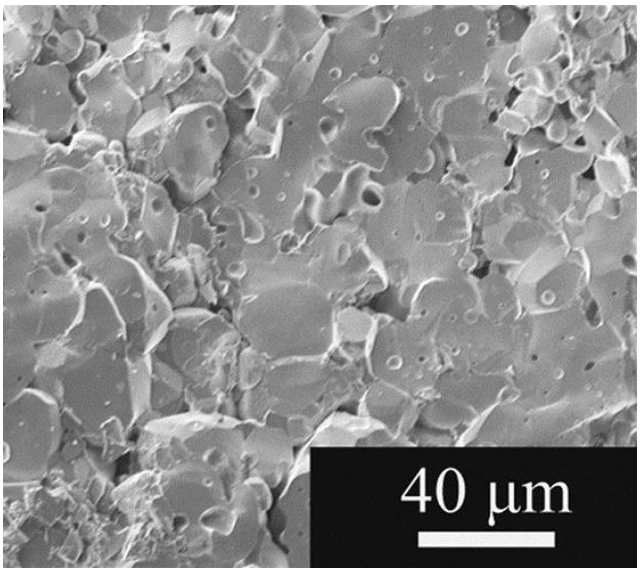

Figure 1.8 Cross-sectional SEM image of sintered LLZO made with 1 µm and 10 µm particles at a 90:10 weight ratio.[20]

Microstructural features (porosity) can act as stress concentrators, discussed in the previous section (**Section 1.6**), and pathways for lithium dendrite growth. Ren *et al*. demonstrated the formation of lithium dendrites and short-circuiting through low-density garnet-type oxide ceramic electrolytes with added microstructural features, shown in *Figure 1.9*.[31] However, microstructural features are not the only mode of lithium dendrite formation through solid electrolytes.

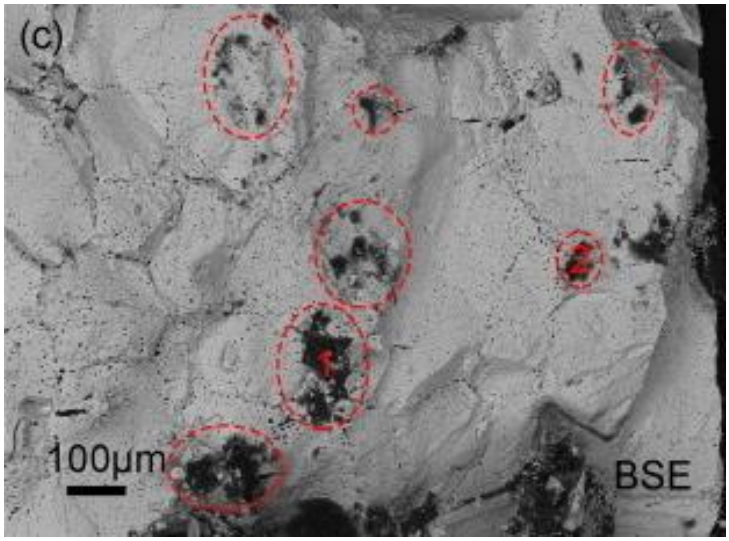

Figure 1.9 Cross-sectional SEM image of sintered LLZO after short-circuiting.[31]

1.7.2. Lithium Dendrite Formation

Mechanical incompatibility between solid electrolytes and electrode materials can result in lithium dendrite formation and eventually short-circuiting. In 2005, Monroe and Newman demonstrated how uneven re-distribution of metallic lithium on charging (plating) leads to lithium dendrites.[32] Furthermore, the uneven re-distribution of metallic lithium was dependent on the stability of the solid-solid interface. The work showed that an electrolyte with a higher rigidity could stabilise the interface, even the distribution of lithium plating and prevent lithium dendrite growth and short-

circuiting.[32] The surface tension, deformation and compressive forces correlate to the stability of the interface and the rigidity (shear modulus) of the electrolyte. An increase in the rigidity of the solid electrolyte results in an increase in the stability of the interface. According to the work, solid electrolytes with twice the shear modulus of lithium suppress surface roughening and dendrite formation.

Oxide ceramic electrolytes have a significantly higher shear modulus than both sulfide and polymer electrolytes and are therefore of great interest to stabilise interfaces with metallic lithium and prevent lithium dendrite growth.[17, 21] Thin oxide ceramic electrolyte must be rigid and tough in order to increase ionic conductivity and prevent lithium dendrites. Thin oxide ceramic electrolytes with enhanced mechanical and interfacial properties seek to benefit all-solid-state metallic lithium anode batteries.

1.8. Fibre-Reinforced Ceramic Matrix Composite (FR-CMC)

Two or more distinct constituent materials that combine to modify their properties define a composite. The two types of constituent materials are the matrix and the reinforcement. The reinforcement imparts specific mechanical, physical or chemical properties that enhance those of the matrix. The designed composite affords a wider range of desired properties due to the synergy of its constituent materials. In the case of a mechanically reinforced composite under a given load, the force will transfer from the matrix to the reinforcement by stress transfer. The effect is a toughening of the matrix material.

Previous work has investigated composites of solid electrolytes.[18, 33-37] The three general types of mechanically reinforced composites, shown in *Figure 1.10*, are *(a)* fibre-reinforced, *(b)* particle-reinforced and *(c)* structural. A dispersion of particles

of varying size and property in a matrix material define particle-reinforced composites. The varying or continuous length of fibres and fibre alignment, having ordered or random orientation, define the fibre-reinforced composites. Layered matrix and reinforcement phases that laminate together define structural composites.

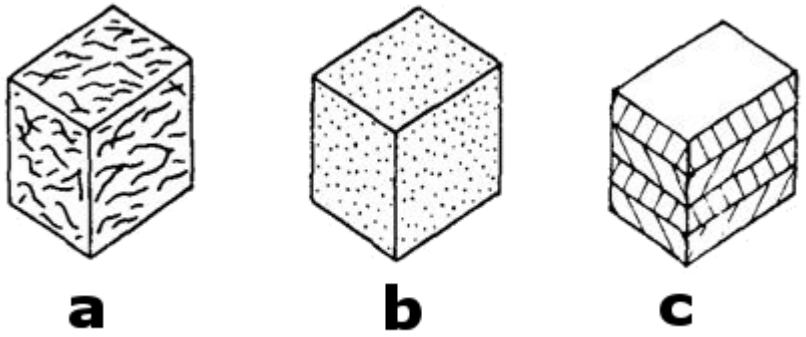

Figure 1.10 Schematic representations of the general types of (a) fibre-, (b) particle- and (c) structural reinforced composites.

The main mechanisms for reinforcement against brittle fracture are crack bridging, matrix grain bridging, process zone shielding and crack deflection.[38] Crack bridging is the process by which reinforcement traverses the opening of a crack, shown in *Figure 1.11*, and is thought to be the most effective method for toughening brittle ceramics.[38] The reinforcement can reduce the effective stress intensity at the tip of the crack by plastically deforming, in the case of ductile materials, and/or adding tensile strength.[38] The FR-CMC reinforces brittle ceramics by crack bridging.

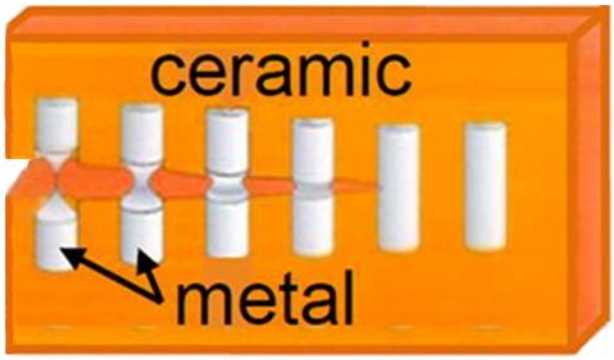

Figure 1.11 Schematic representation of ceramic crack bridging by metal. [38]

The type of fibre-reinforcement and microstructure characterise the FR-CMC. The three distinct microstructures of fibre-reinforcement are isolated bars, continuous phases and interpenetrating phases.[38] Metals or polymeric fibres encased in either polymer (fibre-reinforced polymer (FRP)) or the ceramic matrix composes fibre-reinforcement. The most common form of FR-CMC is that of reinforced concrete, where a continuous phase of stainless steel reinforces the low tensile strength of concrete.[39]

A FR-CMC where ceramic electrolyte composes the ceramic matrix poses a substantial fabrication challenge. The general constituent requirements for optimal fabrication of a suitably reinforced composite are as follows:[38]

- Chemical and physical compatibility
- Good bonding (including during stress loading)
- Thermal compatibility (similar thermal expansion)
- Non-detrimental synthesis
- Minimum required amount of reinforcement

The fibre-reinforcement of ceramic electrolytes must also consider suitability within an electrochemical cell. This includes the required properties of different ceramic electrolytes, the synthesis limitations of different materials, maintenance of ionic conductivity in the cell and chemical stability with metallic lithium.

Depending on the mechanical properties, a given ceramic electrolyte may require different types of fibre-reinforcements to introduce specific properties. Electronically conductive reinforcements, such as metals, are inappropriate in an electrochemical cell due to the potential risk of short-circuiting. On the other hand, the low thermal stability of non-conductive polymeric-fibre reinforcements creates a synthetic challenge for those electrolytes requiring high temperature sintering, such as oxide ceramic electrolytes. The fabrication process would need to have a limited effect on the ionic conductivity and electrode contact of the electrolyte. Nam *et al*. reported a FR-CMC of thin-film sulfide electrolyte.[18] Cold pressed Li_3PS_4 (LPS) or $Li_{10}GeP_2S_{12}$ (LGPS) encase polymeric fibres of non-woven (NW) poly(paraphenylene terephthalamide) (PPTA), also known as Kevlar® or aramid. The NW-PPTA reinforcement adds flexibility and toughness to the already ductile sulfide electrolytes, resulting in the bendable thin-film composite cell, demonstrated in *Figure 1.12*.

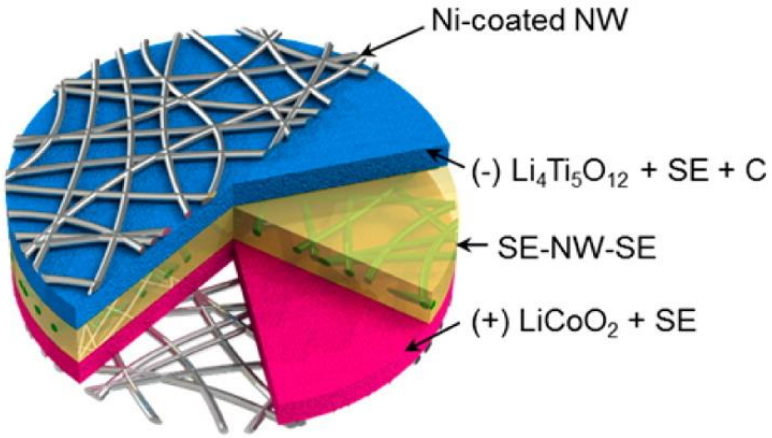

Figure 1.12 Schematic representation of a cell with a fibre-reinforced sulfide electrolyte composite.[18]

Increasing the toughness of stiff and brittle oxide ceramic electrolytes using FR-CMC is a novel approach. However, toughening non-ionically conductive oxide ceramics with ductile metals using FR-CMC is common.[38] The release rate of elastic strain energy (stress transfer efficiency), ΔG_{el}, relating to crack bridging of reinforcement follows the equation:

$$\Delta G_{el} = f \int_0^u \sigma(u) \mathrm{d}u \tag{1.3}$$

Where f is the area fraction of reinforcement intercepted by the crack, σ is the stress and u is the opening of the crack. Increasing the interception area fraction of reinforcement increases the stress transfer efficiency between the ceramic matrix and the fibre reinforcement, therefore increasing the toughness of the FR-CMC. FR-CMC with an interpenetrating-phase microstructure, known as an interpenetrating composite,

is likely to maximise the reinforcement-interception area fraction of a random oriented crack that propagates through the interpenetrating phases of the composite.[38]

1.9. Interpenetrating Composite (IPC)

Previous work reported the fabrication of IPC microstructure for metal-ceramic composites.[38, 40] An IPC is composed of two bicontinuous 3D-interpenetrating phases, as shown in *Figure 1.13*. The typical method for forming an IPC is to fabricate a porous ceramic and then infiltrate with a metal. The architecture of the ceramic defines the architecture of the interpenetrating phases and can influence the overall properties of the IPC (*Equation 1.3*). A functional and optimised FR-CMC of oxide ceramic electrolyte requires an IPC microstructure for conduction between two electrodes and optimised crack bridging, respectively.

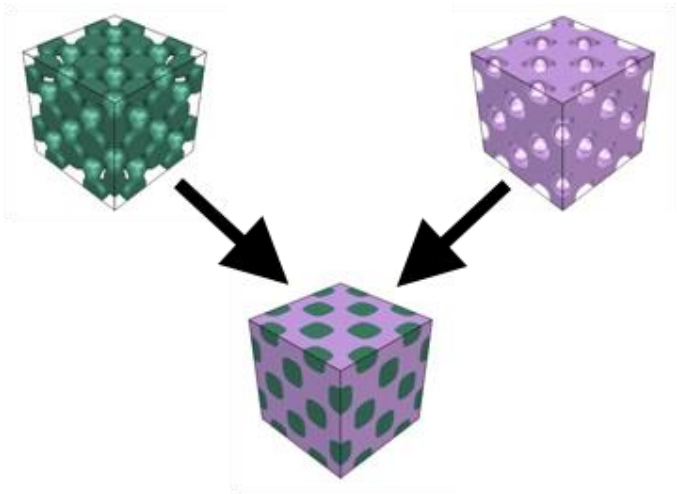

Figure 1.13 Schematic representation of a generic interpenetrating composite microstructure.[41]

The fabrication of porous ceramics with interconnected pores is essential for infiltration of the reinforcement. The resultant porous ceramic is known as a ‘preform’.

There are many ways to fabricate a porous ceramic preform; *Figure 1.14* shows the conventional techniques of replication, sacrificial templating and direct foaming.[40, 42] Air is incorporated into a suspension or liquid that is then set to produce a porous material by direct foaming. The amount of incorporated gas can control the porosity, but 3D-interconnected pores are not typical. The replication technique uses a template to infiltrate a ceramic precursor or suspension. The infiltration, drying and sintering procedure of ceramic precursor, replicates the porous ceramic preform from the template architecture. Preforms fabricated via replication are also known as 'replicas'. On the other hand, sacrificial templating requires the addition of sacrificial material to the ceramic precursor and removal after sintering. For oxide ceramic electrolyte, the major challenge will be to fabricate an adequately sintered porous preform, which maintains ionic conductivity, compressive strength and the 3D-interconected porosity of the interpenetrating microstructure. There is limited work in this area; *Figure 1.15* shows the fabrication of $Li_5La_3Ta_2O_{12}$ (LLTO) via a colloidal crystal sacrificial templating procedure.[43]

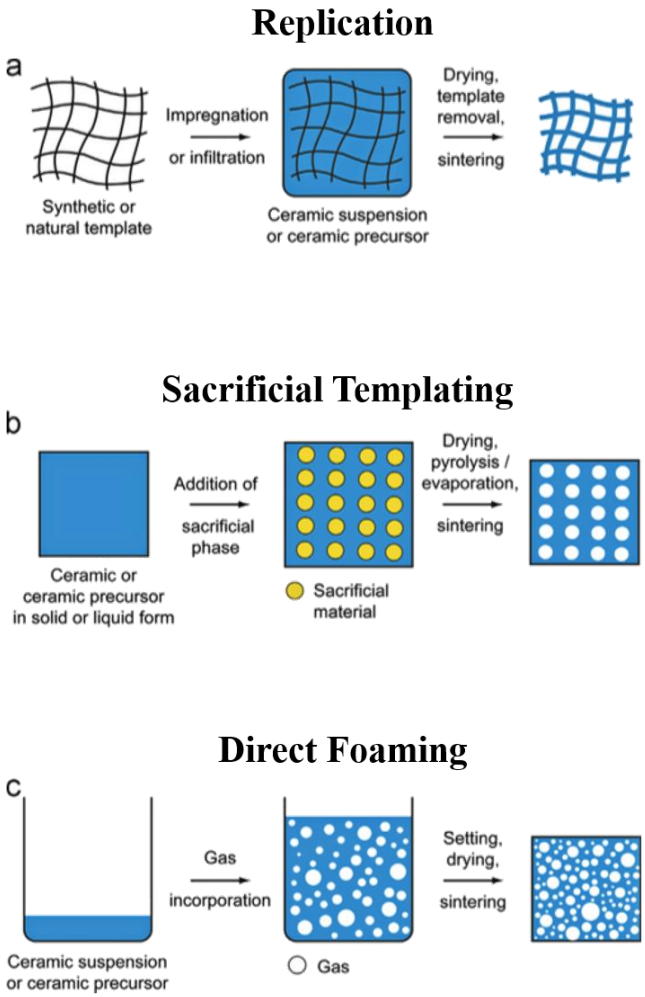

Figure 1.14 Schematic representations of processing routes for porous ceramic preform fabrication via (a) replication, (b) sacrificial templating and (c) direct foaming.[42]

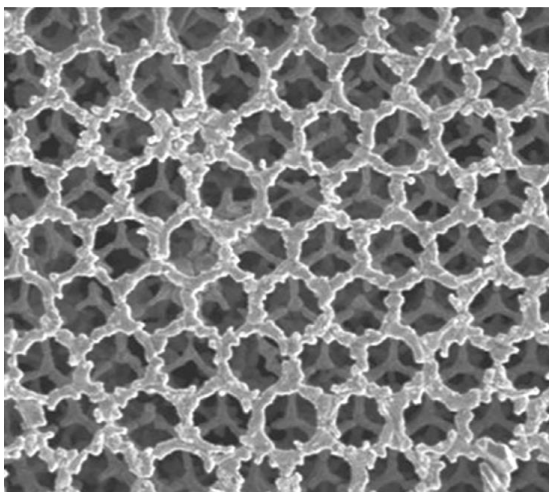

Figure 1.15 SEM image of LLTO preform fabricated from 5 μm mono-dispersed polystyrene sacrificial templates.[43]

The replication procedure (Fi*gure 1.14 (a)*) is advantageous due to architecture control of templates, enabling the bicontinuous 3D-interpenetration required for IPC microstructure. The template architecture defines the architecture of the ceramic and therefore microstructural parameters. The overall mechanical properties of the FR-CMC can be modified and controlled through the design of templates (interpenetrating microstructure), as the crack bridging of reinforcement can improve stress transfer efficiency (*Equation 1.3*).[38] However, maintaining the compressive strength of ceramic requires a high solid volume fraction preform; a potential challenge with the replication procedure.[40, 42] Unless a thick layer of ceramic precursor deposits on the template surface before sintering, the CMC may be too weak for application.

The viability of FR-CMC fabrication via the sacrificial templating procedure (*Figure 1.14 (b)*) depends largely on the size and volume fraction of sacrificial template.[40, 42] Sacrificial particles are typically used as templates to disperse in ceramic precursor or consolidate before precursor addition. Introduced low volume fraction porosity maintains the compressive strength of the ceramic matrix, but with no guarantee of the interconnectivity required for complete reinforcement infiltration. Introduced high volume fraction porosity (*Figure 1.15*) to ensure interconnectivity of the ceramic matrix increases susceptibility to fracture by local stress concentrations and short fracture distances, therefore decreasing the compressive strength, as discussed in **Section 1.6**. However, a low volume fraction ceramic matrix with interconnectivity is only achievable with novel 3D-interconnected sacrificial templates.

To realise a designed FR-CMC with an IPC microstructure of oxide ceramic electrolyte and FRP, the template fabrication, ceramic preform formation and reinforcement infiltration procedures must be reliable and accurate. The initial challenge

is to fabricate complex-designed 3D parts being appropriate templates for ceramic electrolyte preforms. Without successful preform formation, the interconnected pores may hinder infiltration with reinforcement. Any hindrance could lead to unwanted porosity in the final FR-CMC causing detrimental effects to the mechanical properties, due to pores acting as stress concentrators. The most precise and versatile template fabrication technique is additive manufacturing.

1.10. Additive Manufacturing

Additive manufacturing refers to a variety of processes involved in the fabrication of 3D parts. Modelling, printing and finishing are the key processing steps of 3D part fabrication. In modern additive manufacturing, modelling involves designing the desired 3D-architecture that defines the geometry of the part. Designing digital models utilises computer-aided design (CAD) software packages. The printing step refers to a large number of processes that are categorised by their technique and material. The main types of additive manufacture printing techniques are extrusion deposition, granular powder bed binding, lamination, powder fed direct energy deposition, metal wire processes and photo-polymerisation. Finally, the finishing process involves any post-processing preparations to ready the part for use. As an emerging field, Ambrosi and Pumera reported the use of additive manufacturing for electrochemical applications.[44]

Stereolithography is an additive manufacturing process that utilises photo-polymerisation to fabricate precise parts. Typically, a UV laser is focused and ‘writes’ into a bath of photo-polymerisable monomer resin that initiates photo-polymerisation to a solid polymeric part. The CAD model defines the exact writing of the 3D-part,

produced in a layer-by-layer fashion. Stereolithography is most suitable for template fabrication due to a wide range of instrument resolutions, part feature sizes and polymeric materials. Specifically, the elevated sintering temperatures required for ceramic preform formation combusts polymer templates formed by stereolithgraphy, making them removable templates. On this technical basis, this work looks to investigate a designed fibre-reinforced ceramic matrix composite with an interpenetrating microstructure of oxide ceramic electrolyte and fibre-reinforced polymer.

1.11. Aim

A novel route for reinforcing thin oxide ceramic electrolytes can afford the following advantages:

- Reduced susceptibility to brittle fracture
- Increased ionic conductance by thin electrolyte layer
- Maintained high compressive strength preventing lithium dendrites
- Enable enhancement of surface microstructure without degradation of property

By addressing the mechanical and ionic conductivity disadvantages, oxide ceramic electrolytes become a preferable candidate to replace liquid electrolytes, rather than sulfides that pose a safety risk.

The initial aim of this work is to demonstrate the ability of polymeric reinforcement to improve the mechanical properties of an oxide ceramic electrolyte. A ceramic electrolyte must be successfully synthesised and reinforcement materials prepared. The composite will then have to be fabricated and analysed to investigate the compatibility of the components and the mechanical properties.

The next aim is to establish a procedure for the fabrication of suitable templates for use in replication and sacrificial templating procedures. Materials with 3D-interpenetrating microstructure must be prepared with adequate chemical properties to function as templates. Determining the optimal microstructure for a reinforced composite and analysing the microstructure of the prepared templates will be required.

A further aim will be to develop a replication and sacrificial templating procedure for preform formation of oxide ceramic electrolyte. The procedures will need to be optimised and adapted to the prepared templates should preforms with desired properties be fabricated. The properties of the prepared preforms will need to be analysed and the most suitable procedure be chosen for further investigation.

The final aim of this research is to fabricate the first generation of FR-CMC with an IPC microstructure of oxide ceramic electrolyte matrix and FRP reinforcement. The prepared ceramic preforms will require an infiltration procedure to incorporate the reinforcement before analysing the mechanical properties of FR-CMC.

1.12. References

[1] Rechargeable Lithium Ion OEM Batteries - Panasonic. Web.archive.org (2016). at https://web.archive.org/web/20100413182032/http://www.panasonic.com/industrial/batteries-oem/oem/lithium-ion.aspx.

[2] [Press Release] Develop High-Capacity Lithium-Ion Battery. Panasonic Newsroom Japan. News.panasonic.com (2016). at http://news.panasonic.com/jp/press/data/jn091225-1/jn091225-1.html

[3] Tarascon, J. & Armand, M. Issues and challenges facing rechargeable lithium batteries. *Nature* **414**, 359-367 (2001).

[4] Van Noorden, R. The rechargeable revolution: a better battery. *Nature* **507**, 26-28 (2014).

[5] Bruce, P. G. Energy storage beyond the horizon: Rechargeable lithium batteries. *Solid State Ionics* **179**, 752-760 (2008).

[6] *Lithium Batteries & Lithium Battery-Powered Devices*. (FAA Office of Security and Hazardous Materials Safety, 2016). at http://www.faa.gov/about/office_org/headquarters_offices/ash/ash_programs/hazmat/aircarrier_info/media/battery_incident_chart.pdf

[7] [Statement] Samsung Will Replace Current Note7 with New One. News.samsung.com (2016). at https://news.samsung.com/global/statement-on-galaxy-note7

[8] Chan, C. K. *et al*. High-performance lithium battery anodes using silicon nanowires. *Nat. Nanotechnol.* **3**, 31-35 (2008).

[9] Xu, W. *et al*. Lithium metal anodes for rechargeable batteries. *Energy Environ. Sci.* **7**, 513-537 (2014).

[10] Quartarone, E. & Mustarelli, P. Electrolytes for solid-state lithium rechargeable batteries: recent advances and perspectives. *Chem. Soc. Rev.* **40**, 2525-2540 (2011).

[11] Bachman, J. C. *et al*. Inorganic solid-state electrolytes for lithium batteries: mechanisms and properties governing ion conduction. *Chem. Rev.* **116**, 140-162 (2016).

[12] Thangadurai, V., Narayanan, S. & Pinzaru, D. Garnet-type solid-state fast Li ion conductors for Li batteries: critical review. *Chem. Soc. Rev.* **43**, 4714-4727 (2014).

[13] Fergus, J. W. Ceramic and polymeric solid electrolytes for lithium-ion batteries. *J. Power Sources* **195**, 4554-4569 (2010).

[14] Goodenough, J. B. & Singh, P. Review—Solid electrolytes in rechargeable electrochemical cells. *J. Electrochem. Soc.* **162**, A2387-A2392 (2015).

[15] Cao, C., Li, Z., Wang, X., Zhao, X. & Han, W. Recent advances in inorganic solid electrolytes for lithium batteries. *Front. Energy Res.* **2** (2014).

[16] Roylance, D. in *Mechanics of Materials.* 336 (Wiley, 1996).

[17] Yu, S. *et al*. Elastic properties of the solid electrolyte Li7La3Zr2O12 (LLZO). *Chem. Mater.* **28**, 197-206 (2016).

[18] Nam, Y. J. *et al*. Bendable and thin sulfide solid electrolyte film: a new electrolyte opportunity for free-standing and stackable high-energy all-solid-state lithium-ion batteries. *Nano Lett.* **15**, 3317-3323 (2015).

[19] Tatsumisago, M., Nagao, M. & Hayashi, A. Recent development of sulfide solid electrolytes and interfacial modification for all-solid-state rechargeable lithium batteries. *Journal of Asian Ceramic Societies* **1**, 17-25 (2013).

[20] Cheng, L. *et al*. Effect of surface microstructure on electrochemical performance of garnet solid electrolytes. *ACS Appl. Mater. Interfaces* **7**, 2073-2081 (2015).

[21] Sakuda, A., Hayashi, A. & Tatsumisago, M. Sulfide solid electrolyte with favorable mechanical property for all-solid-state lithium battery. *Nature Scientific Reports* **2261**, 1-5 (2013).

[22] Schulze, M. W., McIntosh, L. D., Hillmyer, M. A. & Lodge, T. P. High-modulus, high-conductivity nanostructured polymer electrolyte membranes via polymerization-induced phase separation. *Nano Lett.* **14**, 122-126 (2014).

[23] Campbell, F. C. in *Manufacturing Technology for Aerospace Structural Materials.* 616 (Elsevier Science, 2006).

[24] Case, E. D. & Kim, Y. The effect of surface-limited microcracks on the effective Young's modulus of ceramics. *J. Mater. Sci.* **28**, 1885-1900 (1993).

[25] Santhanagopalan, S. *et al*. in *Design and Analysis of Large Lithium-Ion Battery Systems* 250 (Artech House, 2014).

[26] Daniel, C. & Besenhard, J. O. in *Handbook of Battery Materials, Second Edition.* 1023 (Wiley VCH, 2011).

[27] Dudney, N. J., West, W. C. & Nanda, J. in *Handbook of Solid State Batteries 2nd Edition (Materials and Energy - Volume 6).* 836 (World Scientific Publishing Co, 2015).

[28] Wolfenstine, J. *et al*. A preliminary investigation of fracture toughness of Li7La3Zr2O12 and its comparison to other solid Li-ionconductors. *Material Letters* **96**, 117-120 (2013).

[29] Kalaga, K. *et al*. Quasi-solid electrolytes for high temperature lithium ion batteries. *ACS Appl. Mater. Interfaces* **7**, 25777-25783 (2015).

[30] Zhu, Y., He, X. & Mo, Y. First principles study on electrochemical and chemical stability of solid electrolyte-electrode interfaces in all-solid-state Li-ion batteries. *J. Mater. Chem. A* **4**, 3253-3266 (2016).

[31] Ren, Y., Shen, Y., Lin, Y. & Nan, C. Direct observation of lithium dendrites inside garnet-type lithium-ion solid electrolyte. *Electrochem. Commun.* **57**, 27-30 (2015).

[32] Monroe, C. & Newman, J. The impact of elastic deformation on deposition kinetics at lithium/polymer interfaces. *J. Electrochem. Soc.* **152**, A396-A404 (2005).

[33] Aetukuri, N. B. *et al*. Flexible ion-conducting composite membranes for lithium batteries. *Advanced Energy Materials* **5**, 1500265 (2015).

[34] Jung, Y., Lee, S., Choi, J., Jang, S. S. & Kim, D. All solid-state lithium batteries assembled with hybrid solid electrolytes. *J. Electrochem. Soc.* **162**, A704-A710 (2015).

[35] Lim, Y. J. *et al*. Ceramic-based composite solid electrolyte for lithium-ion batteries. *ChemPlusChem* **80**, 1100-1103 (2015).

[36] Takahashi, K. *et al*. A Water stable high lithium ion conducting Li1.4Ti1.6Al0.4(PO4)3-epoxy resin hybrid sheet. *J. Electrochem. Soc.* **159**, A1065-A1069 (2012).

[37] Manuel Stephan, A. & Nahm, K. S. Review on composite polymer electrolytes for lithium batteries. *Polymer* **47**, 5952-5964 (2006).

[38] Travitzky, N. Processing of ceramic–metal composites. *Advances in Applied Ceramics* **111**, 286-300 (2012).

[39] Zhang, J. & Li, V. C. Simulation of crack propagation in fiber-reinforced concrete by fracture mechanics. *Cem. Concr. Res.* **34**, 333-339 (2004).

[40] Hammel, E. C., Ighodaro, O. L. -R. & Okoli, O. I. Processing and properties of advanced porous ceramics: An application based review. *Ceram. Int.* **40**, 15351-15370 (2014).

[41] Wang, L., Lau, J., Thomas, E. L. & Boyce, M. C. Co-continuous composite materials for stiffness, strength, and energy dissipation. *Adv. Mater. (Weinheim, Ger.)* **23**, 1524-1529 (2011).

[42] Studart, A. R., Gonzenbach, U. T., Tervoort, E. & Gauckler, L. J. Processing routes to macroporous ceramics: a review. *J. Am. Ceram. Soc.* **89**, 1771-1789 (2006).

[43] Kokal, I., van den Ham, E. J., Delsing, A. C. A., Notten, P. H. L. & Hintzen, H. T. Preparation and characterization of three dimensionally ordered macroporous Li5La3Ta2O12 by colloidal crystal templating for all-solid-state lithium-ion batteries. *Ceram. Int.* **41**, 737-741 (2015).

[44] Ambrosi, A. & Pumera, M. 3D-printing technologies for electrochemical applications. *Chem. Soc. Rev.* **45**, 2740-2755 (2016).

Chapter 2: Experimental Techniques

2.1. Powder X-ray Diffraction (PXRD)

PXRD is a technique used for determining the arrangement of atoms in a crystal structure. X-ray radiation is produced when a high-energy electron beam hits a metal target and can then be diffracted (Bragg diffraction) by a solid specimen containing crystalline, ordered domains. Crystal structures with long-range atomic ordering form lattice planes. Diffraction occurs when the spacing between atomic planes is similar to the wavelength of irradiating X-rays. Diffraction of incident radiation follows Bragg's law:

$$2d_{hkl} \sin \theta_{hkl} = \lambda \tag{2.1}$$

Where d_{hkl}, θ, n and λ are the spacing between two parallel scattering planes, the angle between the incident ray and scattering plane, an integer and the wavelength of the incident ray, respectively. Depending on the incident angle, atomic ordering can diffract radiation with either constructive or destructive interference. Constructive interference is caused by the diffraction of waves existing in the same phase. This occurs when the difference in pathway length equals an integer number of the wavelength, causing constructive interference (*Figure 2.1*). The variation in intensity of constructive radiation at a given angle produces a diffraction pattern with intensity peaks.

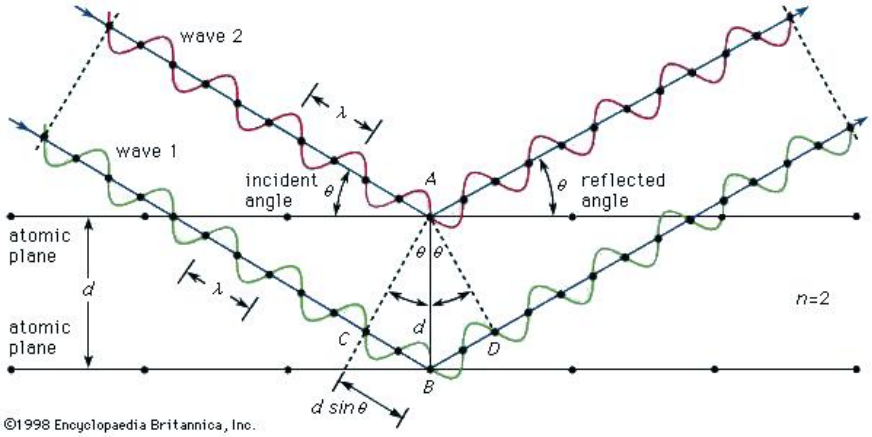

Figure 2.1 Schematic representation of constructive interference by Bragg diffraction.[1]

2.2. Scanning Electron Microscopy (SEM) and Energy Dispersive Spectroscopy (EDS)

SEM is a technique used to image a specimen and gain information about its morphology, texture and topography. Emission of electrons are produced from a field emission gun at a cathode (tungsten or lanthanum hexaboride-tipped filament) with a potential gradient. An electric field then accelerates the electrons toward an anode at a given voltage. Electromagnetic lenses focus and direct the electron beam to the sample surface where interactions result in the production of primary backscattered, secondary and Auger electrons as well as X-rays with specific energies. Detectors of the emitted signals can form an image of the sample surface or an elemental analysis of the material. Secondary electrons give the highest resolution images.

X-ray radiation occurs when first the incident electron beam excites an electron of a sample atom causing it to eject and create an electron hole. An electron can change state from higher-energy to fill the electron hole. The change in states of the electron releases energy in the form of X-ray radiation (*Figure 2.2*). EDS detectors measure the

energy and intensity of emitted X-ray radiation from the sample. Different elements have unique X-ray energy values that enables the elemental analysis of the material.

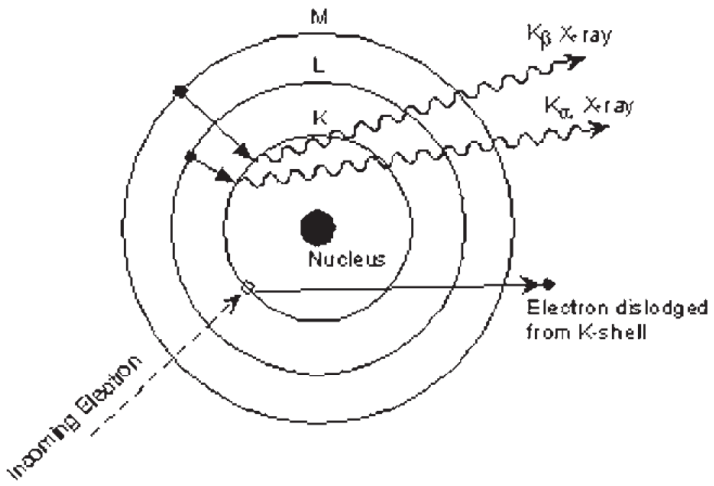

Figure 2.2 Schematic representation of the excitation of an electron and X-ray emission.[2]

2.3. Alternating Current Electrochemical Impedance Spectroscopy (AC EIS)

AC EIS is a potentiostatic technique used to characterise the current response of an ionically conducting material to an applied oscillating potential, with a specific frequency and amplitude, causing an alternating current response in the system. The response to the alternating current distinguishes and quantifies different electrochemical phenomena, such as ionic conductivity and capacitance.

The electrochemical impedance spectrometer applies a sinusoidal excitation potential across a cell and measures the current response. The difference in phase shift and ratio of maxima between the excitation potential and current response gives the

impedance of a cell. The phase shift and ratio of maxima are complex functions of impedance, which can be represented as a complex number, Z.

$$Z = Z' - jZ"$$

(2.2)

Where Z', j and Z" are the real part, complex number operator ($\sqrt{-1}$) and imaginary part, respectively. The frequency dependent impedance can be represented by plotting the imaginary versus the real parts of Z in a Nyquist plot (*Figure 2.3*), where each point gives the impedance at a certain frequency.

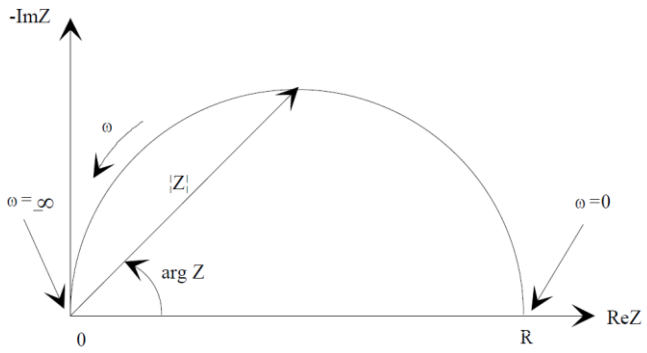

Figure 2.3 Nyquist plot showing the impedance of an electrical circuit as a function of frequency.[3]

An equivalent circuit model of electrical elements can be used to fit electrochemical phenomena observed in the experimental data to individual components. The quantified values of each component determine those of the corresponding phenomena. *Figure 2.4* shows the equivalent circuit for a cell with non-ionically conducting blocking electrodes and a one-type mobile ion species electrolyte.

A capacitor and resistor in parallel and two more capacitors in series compose the equivalent circuit. The resistor, R_b, represents the bulk resistivity of migrating ions across the electrolyte under an applied potential. The capacitor, C_b, represents the bulk capacitance across the electrolyte under an applied potential. The set of parallel components represent what's known as the time constant of the bulk. The two in series capacitors, C_e, represent the electrode capacity.

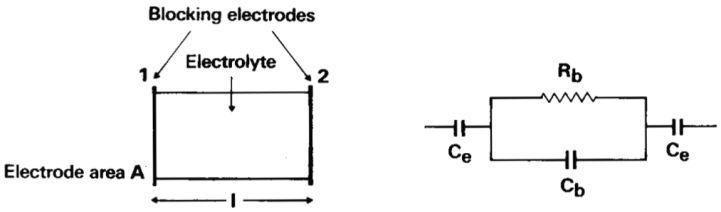

Figure 2.4 Schematic representation of a cell with electrolyte and blocking electrodes with the equivalent electrical circuit.[4]

The magnitude of a resistor and capacitor are given by the following equations, respectively:

$$|Z| = R \tag{2.3}$$

$$|Z| = \frac{-j}{\omega C} \tag{2.4}$$

Where ω is the angular frequency ($2\pi f$). The connectivity of the components in the equivalent circuit gives the total impedance of the cell as follows:

$$Z_{total} = \frac{1}{\left(\frac{1}{R}\right) + j\omega C} = R\left[\frac{1}{1 + (\omega CR)^2}\right] - jR\left[\frac{\omega RC}{1 + (\omega CR)^2}\right]$$

(2.5)

The equation is represented in a Nyquist Plot (*Figure 2.3*) being a complex impedance plane. Polycrystalline (granular) ceramic electrolytes observe an additional electrochemical phenomenon in the form of grain boundaries. Another set of parallel components represent the phenomenon's current response of migration of ions and capacitance across grain boundaries. *Figure 2.5* shows the equivalent circuit of an electrolyte with granular properties and the corresponding Nyquist plot. The two sets of parallel components with subscript b and gb represent the intra-crystallite bulk and grain boundary time constants, respectively.

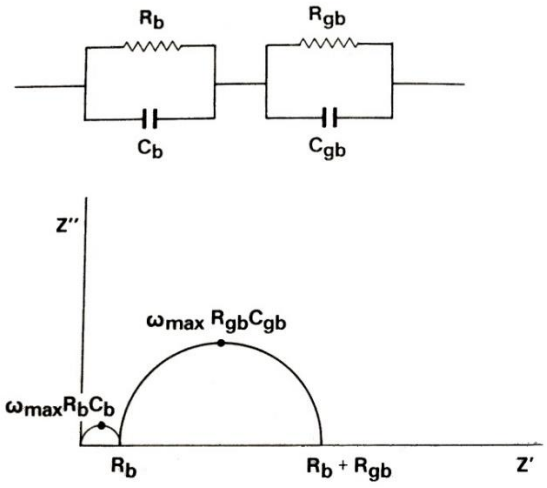

Figure 2.5 An equivalent electrical circuit of a polycrystalline electrolyte with grain boundaries and the corresponding Nyquist plot.[4]

The total resistivity of the granular electrolyte is given by the low frequency intercept of the horizontal axis, being the sum of R_b and R_{gb} (*Figure 2.5*). The specific conductivity, σ, can be calculated from the resistance, R, of the electrolyte as follows:

$$\sigma = \frac{1}{R} \cdot \frac{L}{A} \tag{2.6}$$

Where A and L are the cell constants of contact area of one of the electrodes to the electrolyte and the thickness of the electrolyte, respectively.

2.4. Brazilian Disk Testing

Brazilian disk testing is a technique used to measure the tensile properties of disks by diametral compression. The compression forces applied diametrally across a disk induce tensile stress perpendicular to the line of action of the applied load (*Figure 2.6*). At a given applied load the tensile stress causes crack initiation at the centre of the disk before further load propagates the crack leading to complete failure.

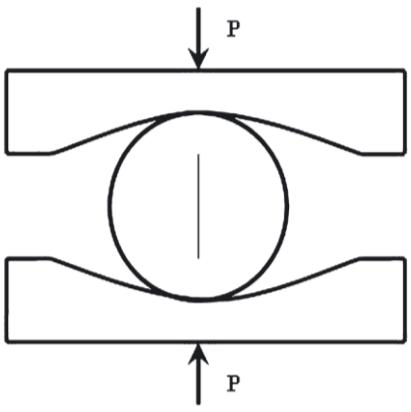

Figure 2.6 Schematic representation of the disk geometry in Brazilian testing.[5]

The following equation gives the maximum tensile stress, σ_{xx}, at the centre of the disk when curved anvils, that reduce end crushing, apply compressive load:

$$\sigma_{xx} = \left[1 - \left(\frac{b}{R}\right)^2\right]\frac{2P}{\pi D t} \tag{2.7}$$

Where b, R, P, D and t are the contact half-width, disk radius, applied load, disk diameter and disk thickness, respectively. The greatest applied load to the disk before fracture gives the tensile yield strength of the material.

2.5. Thermogravimetric Analysis (TGA)

TGA is a technique used to measure the weight change of a material as a function of increasing temperature. A high precision balance supports and weighs a crucible with sample located within a furnace. A constant heating rate applied by the furnace causes weight loss of the sample under a flow of gas (typically inert gas or air). The analysis derives information about the sample's thermal stability and composition.

2.6. Micro-computed Tomography (μCT)

μCT is a non-invasive and non-destructive technique used to image the internal structure of a sample on the micrometer scale. Exposure of the sample to X-ray radiation at numerous rotations (around a single axis) generates a 3D image (*Figure 2.7*). The intensity of detected radiation distinguishes regions of the sample by density and atomic number. Each stepwise rotation provides a new 2D X-ray image of the

sample of which a 3D image can be created by computational reconstruction. The detector resolution and sample detector distance define the spatial resolution of the X-ray image.

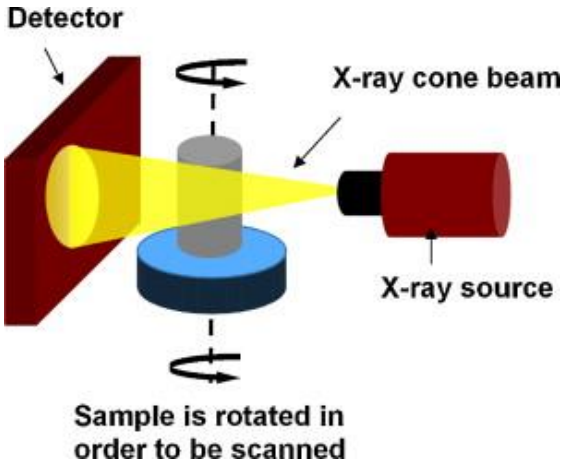

Figure 2.7 Schematic representation of sample rotation in µCT.[6]

2.7. Four-Point Bending Analysis

Four-point bending analysis is a technique used to measure the flexural properties of a material. Two symmetrically placed loads between supports that carry a flat rectangular sample induce four-point bending (*Figure 2.8*). The flexural response of the specimen is recorded by measuring the applied load and the displacement at the centre of the beam.

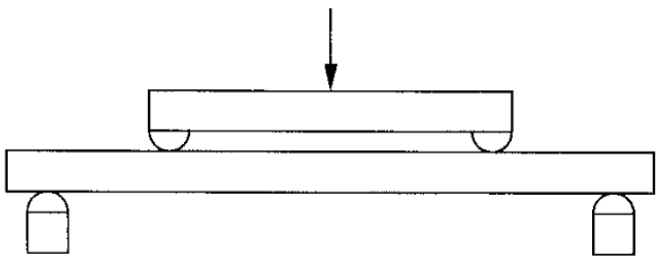

Figure 2.8 Schematic representation of a beam under four-point bending.[7]

The four-point loading generates an increased portion of constant bending moment (material reaction to an applied force) between the inner two loads compared to three-point loading. This is beneficial for analysing brittle materials where the flexural strength is directly related to the number and size of stress concentrators exposed to the maximum stress. For unidirectional or isotropic materials, the normal stress varies linearly from one surface of the specimen to the other, where the surface of loading is under maximum compression and the surface of support is under maximum tension. The maximum normal stress, σ, is given by the following equation:

$$\sigma = \frac{6M}{bh^2} \tag{2.8}$$

Where M, b and h are the bending moment, specimen width and specimen thickness, respectively. Depending on the failure mode (*Figure 2.9*), the flexural strength is defined by the stress experienced at one of the two specimen surfaces at the point of fracture. For brittle materials, the failure mode is expected to be via tensile fracture of the outer surface.

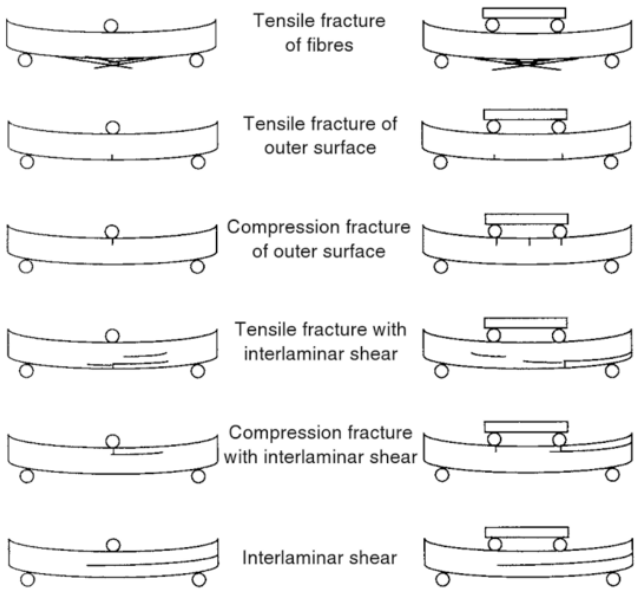

Figure 2.9 The different failure modes of three- and four-point bending.[7]

The flexural strength, σ_f, at the outer surface of the specimen is calculated by *Equation 2.9* and *2.10* for loading span to support span ratios of 1/3 and 1/2, respectively.

$$\sigma_f = \frac{PS}{bh^2} \tag{2.9}$$

$$\sigma_f = \frac{3PS}{4bh^2} \tag{2.10}$$

Where P and S are the applied load at fracture and the support span length, respectively.

2.8. References

[1] Encyclopædia Britannica Online,. Bragg reflection [Illustration]. at https://www.britannica.com/science/Bragg-law/images-videos/Bragg-diffraction/17859

[2] Energy Dispersive Spectroscopy. 10 (Wiley, 2015). at http://www.essentialknowledgebriefings.com/downloads/energy-dispersive-spectroscopy-second-edition/

[3] Basics of Electrochemical Impedance Spectroscopy. 2-3 (Gamry Instruments, 2009). at http://www.gamry.com/assets/Application-Notes/Basics-of-EIS.pdf

[4] Bruce, P. G. in *Polymer Electrolyte Reviews, Volume 1* (eds MacCallum, J. R. & Vincent, C. A.) (Elsevier Applied Science, 1987).

[5] Islam, O., Dragnevski, K. I. & Siviour, C. R. In situ environmental scanning electron microscope observations of colloidal failure mechanisms using the brazilian disk test. *Experimental Techniques.* **39**, 12-18 (2015).

[6] Moreno-Atanasio, R., Williams, R. A. & Jia, X. Combining X-ray microtomography with computer simulation for analysis of granular and porous materials. *Particuology* **8**, 81-99 (2010).

[7] Hodgkinson, J. M. in *Mechanical Testing of Advanced Fibre Composites* (ed Hodgkinson, J. M.) (CRC Press, 2000).

Chapter 3: Structural Composite Reinforcement of Oxide Ceramic Electrolyte

3.1. Aim

The main aim of this chapter is to fabricate a structural oxide ceramic electrolyte composite and demonstrate improved mechanical properties by reinforcement. This first requires a ceramic electrolyte to be successfully synthesised with the expected properties. Furthermore, the reinforcement will need to be prepared before fabricating the composite with ceramic. Improving the mechanical properties of the ceramic using polymeric reinforcements will justify the development of an optimised composite to function in an electrochemical cell.

3.2. Introduction

The fabrication of a fibre-reinforced ceramic matrix composite (FR-CMC) with oxide ceramic electrolyte is a novel challenge. Nam *et al*. reported FR-CMC with polymeric fibre reinforcement encased in sulfide ceramic electrolyte.[1] However, the formation of similar composites with oxide ceramic electrolyte and polymeric fibres is a greater challenge due to sintering requirements. Therefore, a novel FR-CMC of oxide ceramic electrolyte matrix requires an interpenetrating composite (IPC) microstructure for post-sintering infiltration of fibre-reinforced polymer (FRP).

Travitzky and Hammel *et al*. reported FR-CMC with IPC microstructure of non-ionically conducting oxide ceramic matrices with metal.[2, 3] However, the functional

requirements of oxide ceramic electrolytes in an electrochemical cell prevent the use of metals for reinforcement due to their electronic conductivity.

This work makes an initial investigation into increasing the tensile strength of oxide ceramic electrolytes with FRP by preparing a structural FR-CMC of oxide ceramic electrolyte and FRP for mechanical analysis. The following sections discuss appropriate materials for the oxide ceramic electrolyte matrix and reinforcing polymer and respective syntheses before presenting the fabrication of the FR-CMC.

3.3. Experimental Methods

3.3.1. Synthesis of $Li_{1.6}Al_{0.6}Ge_{1.4}(PO_4)_3$ (LAGP)

LAGP was prepared by a Pechini sol-gel synthesis according to literature.[4] Synthetic grade starting materials were purchased from Sigma-Aldrich. 275.8 mg of lithium nitrate (99.99 %), 562.7 mg of aluminium nitrate nonahydrate (99.997 %), 885.5 mg of germanium ethoxide (≥99.95 %) and 880.3 mg of ammonium dihydrogen phosphate (99.999 %) were dissolved in a 0.2 M aqueous solution of 3.8 g of citric acid monohydrate (≥99.0 %) and 90 mL of distilled water. 1.1 g of ethylene glycol (99.8 %) was added and the solution stirred and heated at 80 ˚C for 1 h to form a homogeneous solution. The temperature was increased to 170 ˚C for 24 h to initiate gelation. The gel was heated to 400 ˚C for 4 h in air using a platinum crucible. The obtained product was ground in an agate mortar and pestle before being heated again in air using a platinum crucible at 800 ˚C for 5 h to produce the powder LAGP product. The powder was uniaxially pressed at 500 MPa into a pellet of 13 mm diameter and approximately 1 mm thickness. The pellet was sintered in air using a platinum crucible at 900 ˚C for 5 h.

3.3.2. Synthesis of Fibre-Reinforced Polymer

Fibre-reinforced polymer was prepared by a typical lamination synthesis. Starting materials were purchased from Easy Composites Ltd. Aramid filament yarn (3220 dtex) was cut to length with Kevlar shears and aligned on a substrate. A mixture of 0.77 g of EL2 epoxy laminating resin and 0.23 g of AT30 fast epoxy hardener was prepared, poured onto the aligned aramid fibres and allowed to soak for 1 minute. A glass slide was used to remove excess epoxy. Finally, the composite was left for 3 h to gel and left another 3 h to fully hardened to the substrate.

3.3.3. Synthesis of Structural Fibre-Reinforced Ceramic Matrix Composite

The fibre-reinforced ceramic matrix composite was prepared utilising the materials and techniques reported in the previous experimental methods sections (**Section 3.3.1** and **Section 3.3.2**). Aramid filament yarn of (3220 dtex) was cut with Kevlar shears and aligned on the surface of the sintered LAGP pellet. 0.77 g of EL2 epoxy laminating resin and 0.23 g of AT30 fast epoxy hardener epoxy mixture was then prepared and poured onto the aligned aramid fibres. Excess epoxy was removed with a glass slide and then the composite was left for 6 h to fully harden to the pellet. Finally, the excess aramid and epoxy around the pellet was cut off with Kevlar shears, forming the structural FR-CMC.

3.4. Characterisation

Powder X-ray diffraction (PXRD) data from synthesised LAGP powder was collected using a 3 kW Rigaku SmartLab X-ray diffractometer with Cu $K_{\alpha 1}$ radiation.

The diffraction patterns were collected at room temperature in the 2θ range of 10-50 ˚ at 0.01 ˚ increments. CelRef (V3) was used to refine the unit cell dimensions of the obtained experimental data.

The morphology of materials was investigated using a Carl Zeiss Merlin field emission scanning electron microscope (SEM) with a Gemini II column. Samples were mounted on adhesive copper tape applied to a stub and holder. Measurements were taken at a voltage range of 1-5 kV with a current range between 100-1500 pA. Cross-sections were prepared using a scalpel or an argon ion beam from the Gatan precision etching coating system (PECS). For samples prepared by PECS, an acceleration voltage of 8 keV was aimed with an incident beam angle of 4˚ at a rotation speed of 6 RPM. The chemical characterisation of materials was analysed by energy dispersive X-ray spectroscopy (EDS) using an Oxford Instruments X-Max^N silicon drift detector with 150 mm^2 size detector attached to the Merlin microscope.

Alternating current electrochemical impedance spectroscopy (AC EIS) was used to investigate the electrical behaviour of a pellet of LAGP from uniaxially pressed powder at 500 MPa, sintered in air at 900 ˚C for 5 h to form pellets of 5 mm diameter and approximately 1 mm thickness. The pellet surface was polished using 3M Tri-M-ite Fre-Cut abrasive sheet (P1200) before drying at 70 °C for 20 minutes, sonicating in cyclohexane for 10 minutes and drying again at 70 °C for 20 minutes. Gold blocking electrodes approximately 30 nm thick were sputtered onto opposite sides of the pellet. Conductivity measurements were made using a Solartron Analytical Modulab over 0.1 Hz – 1 MHz frequency range and voltage amplitude of 10 mV. Impedance data were fitted against an equivalent circuit to calculate the total ionic conductivity. All temperature variable measurements were carried out on a Julabo F32-MA cryostat. Low

temperature measurements used liquid nitrogen to reach -30 ˚C. Temperature dependent measurements were carried out in the range of -30 to 75 ˚C in 5 ˚C steps. The data were analysed using ZView (3.4c) and an equivalent circuit generated to the best fit.

The tensile strength of the FR-CMC was measured by Brazilian disk testing with *in-situ* environmental scanning electron microscopy (ESEM). The samples were analysed with ESEM using a Carl Zeiss Evo variable pressure scanning electron microscope. All measurements were collected at the Laboratory for *in-situ* Microscopy and Analysis (LIMA) at the Department of Engineering Science, University of Oxford, with assistance from Dr Kalin Dragnevski and Dr Marzena Tkaczyk. Samples were placed in the loading adaptors of the Brazilian disk testing instrument and inserted into the ESEM. Force-displacement measurements were collected at a rate of 0.2 mm min^{-1} with a maximum force limit of 660 N until fracture. ESEM recorded live video during loading and captured images after fracture.

3.5. Result and Discussion

3.5.1. LAGP Oxide Ceramic Electrolyte Synthesis

NASICON-type lithium oxide ceramic electrolytes adopt structures with general formula $Li_{1+x}Al_xA_{2-x}^{IV}(PO_4)_3$ (where A^{IV} = Ti or Ge). The compound $Li_{1.3}Al_{0.3}Ti_{1.7}(PO_4)_3$ (LATP) shows high room temperature conductivity (3 x 10^{-3} S cm^{-1}) with stability in air and moisture.[5] The major disadvantage of these systems is the tendency of Ti^{4+} to be reduced by metallic lithium.[6, 7] Other analogues of LATP with aliovalent substitution, being $Li_{1+x}Al_xGe_{2-x}(PO_4)_3$, have room temperature ionic conductivities of approximately 1.4-3.5 x 10^{-4} S cm^{-1}.[4, 5, 8, 9] Replacing Ti^{4+} ions can increase the stability of analogues to metallic lithium, but reactivity is still observed.[4]

The NASICON-type oxide ceramic electrolyte $Li_{1.6}Al_{0.6}Ge_{1.4}(PO_4)_3$ (LAGP) was used in this work as a matrix material due to relative ease of preparation and to demonstrate increased tensile strength by reinforcement. The relatively low sintering temperature, reasonable ionic conductivity, air and moisture stability and numerous and varied syntheses of LAGP make it an ideal material for initial composite fabrication experiments.[4, 5, 8, 9] However, NASICON-type electrolytes are typically not stable in contact with metallic lithium.[4, 6, 7] The prevention of solid electrolyte reactivity with metallic lithium is not the aim of this work and so despite its continued reactivity this investigation utilises NASICON-type oxide ceramic electrolytes, as they are reasonably stable in air.

LAGP was prepared from precursor by a Pechini sol-gel method detailed in literature and described in the experimental methods section (**Section 3.3.1**).[4] *Figure 3.1* shows the PXRD diffraction patterns of an LAGP pressed pellet sintered at 900 °C for 5 h and the closely matched pattern of $LiGe_2(PO_4)_3$ (PDF #01-080-1924) obtained from single-crystal diffraction as reference.[10] The LAGP pellet pattern demonstrates the main reflections corresponding to the NASICON-type structure having $R\bar{3}c$ space group. The unit cell dimensions calculated from refinement of the diffraction peaks of the LAGP pellet pattern , as described in the characterisation section (**Section 3.4**), were 8.268 x 8.268 x 20.645 Å, in good agreement with literature.[5]

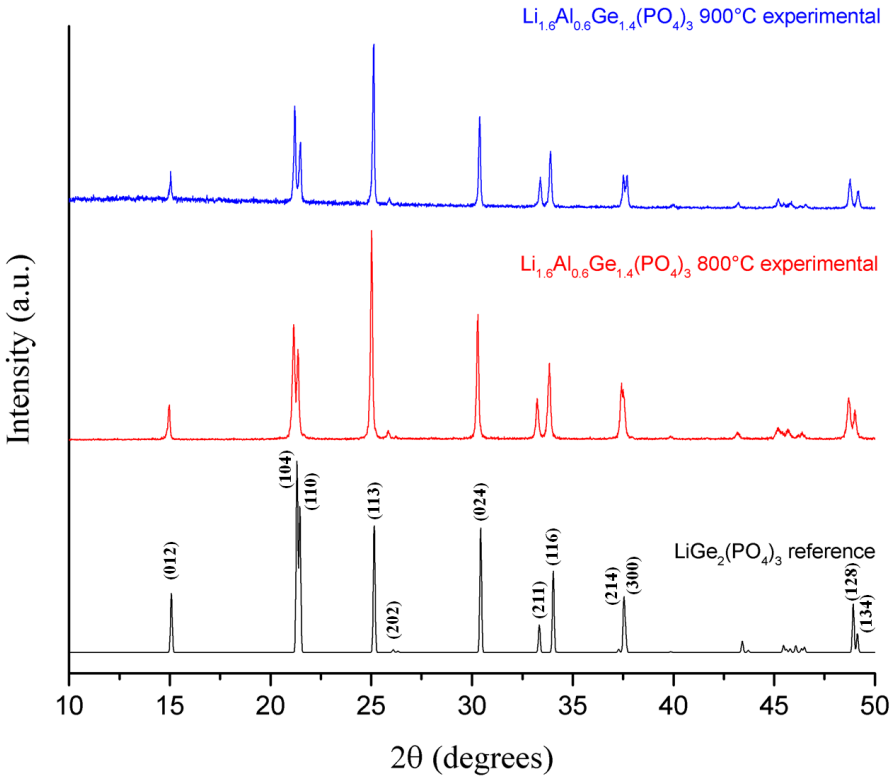

Figure 3.1 Calculated PXRD diffraction pattern of $LiGe_2(PO_4)_3$ and experimental diffraction pattern for LAGP powder at 800 ℃ for 5 h and an LAGP pellet at 900 ℃ for 5 h.

Microstructure analysis was performed using SEM to study the morphology and particle size of the LAGP pellet material. *Figure 3.2 (a)* shows SEM images of the surface of pelletised LAGP sintered at 900 °C for 5 h. Individual crystallites compose a densely packed material characteristic of a polycrystalline ceramic. The crystallite size ranges from 0.1 to 2 μm whilst showing good intergranular contact. The microstructure shows low porosity with few distinguishable pores. From the weight and dimension, the pellet has a density of 3.02 g cm^{-1}. This corresponds to 90 % of the theoretical density of 3.37 g cm^{-1} (calculated from the refined unit cell dimensions), being lower due to pores, impurity phases and glassy phases known to exist in the material.[11] *Figure 3.2 (b)* shows the regions of solid impurity analysed by SEM after cross-section preparation

by argon ion polishing (PECS). The flat darker regions show solid impurity and the darker indented regions show pores, which correlates to the lower density of the LAGP pellet compared to the theoretical density. PXRD is not a suitable technique for the complete identification of impurities due to detection limits and an inability to identify amorphous materials. Therefore, other techniques are employed to identify impurities.

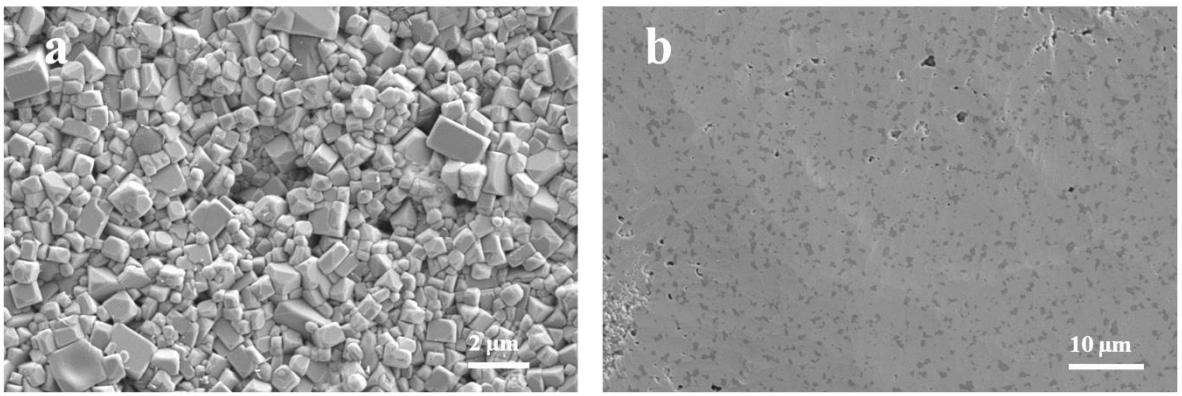

Figure 3.2 SEM images of LAGP after pelletisation and sintering at 900 ℃ for 5 h (a) surface grains and (b) PECS cross-section.

Figure 3.3 shows the SEM image (*Figure 3.3 (a)*), elemental maps and spectra from EDS analysis of an LAGP cross-section prepared by PECS. The theoretical weight percentage was calculated from the molecular weight of LAGP without lithium, which is not detected via EDS. The elemental maps of *Figure 3.3 (b)* and *(c)* show the distributed concentrations of elements, with the increased brightness in different regions corresponds to the increased abundance of aluminium and germanium, respectively. Regions of higher abundance of germanium correspond to regions of lower abundance of aluminium and vice versa. EDS spectra taken of just the high brightness regions (*Figure 3.3 (b)* and *(c)*) confirms the increased abundance of respective elements when compared to that of the overall cross-section (*Figure 3.3 (a)*). The elemental distribution and impurity regions observed in *Figure 3.2 (b)* are chemically distinct regions of

aluminium phosphate and germanium oxide, respectively.[4, 8] These impurities can be limited by controlling specific synthesis parameters and though not observed in PXRD, may still be present in small quantities.

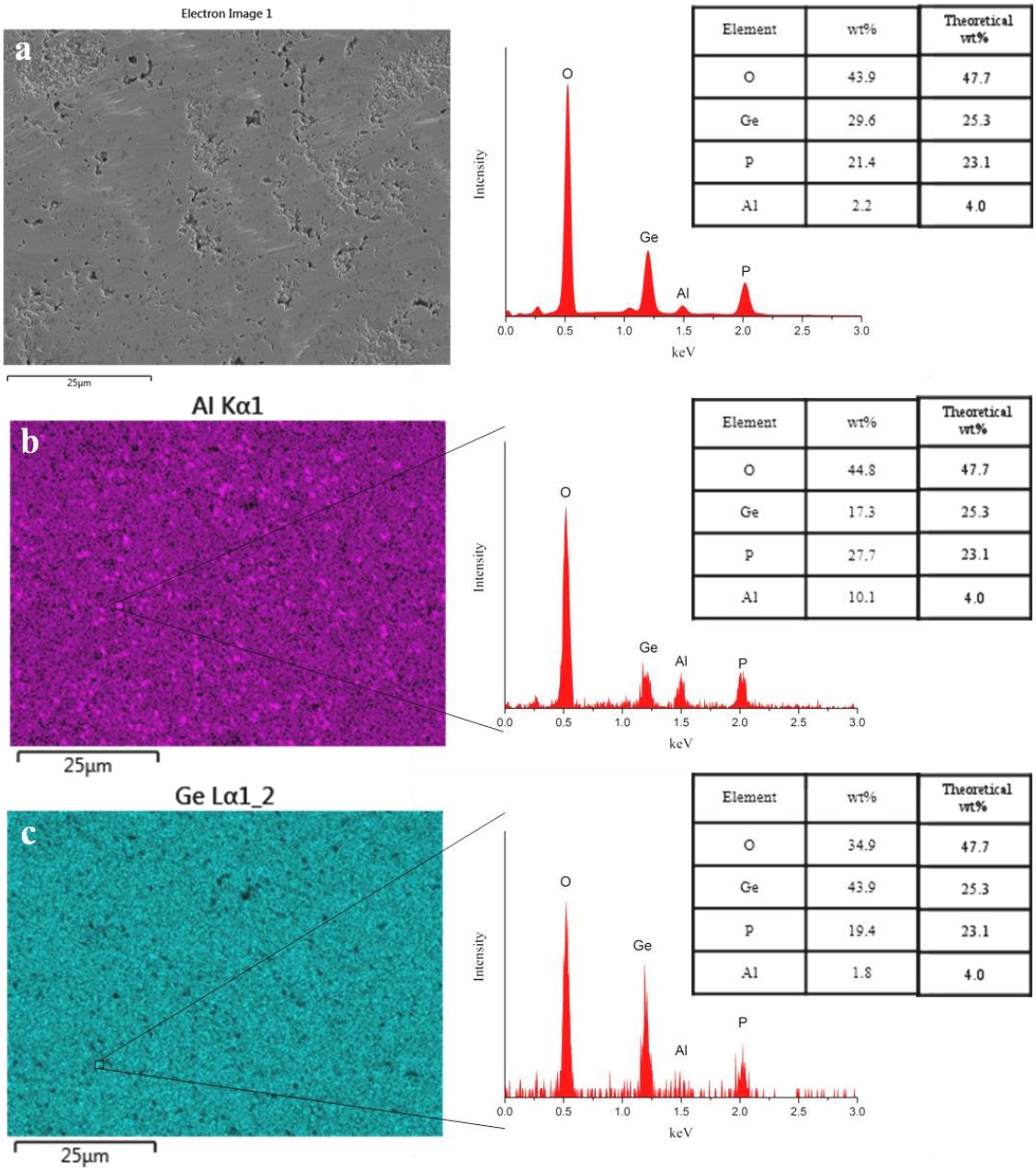

Figure 3.3 EDS elemental mapping and respective spectra of LAGP after pelletisation and sintering at 900 ℃ for 5 h (a) whole PECS cross-section (b) selected aluminium-rich region and (c) selected germanium-rich region.

Figure 3.4 shows a Nyquist plot of LAGP derived from AC EIS and an equivalent circuit that simulates the experimental data to give a best fit (red line), according to the characterisation section (**Section 3.4**). The impedance behaviour of a polycrystalline electrolyte with expected Nyquist plot and equivalent circuit was discussed in **Chapter 2 Section 2.3**. However, the equivalent circuit that best fits the experimental data (*Figure 3.4*) differs from the typical circuit of polycrystalline electrolytes. The full electrical behaviour of the electrolyte is not observed within the frequency window of the experiment at room temperature (*Figure 3.4*). With only a spike and partial semi-circle being observed (*Figure 3.4*), only the intercept of the *Z*' axis is reliable for calculating the total ionic conductivity (**Chapter 2 Section 2.3**). Therefore, an equivalent circuit containing only a single set of parallel components, accounting for the observed experimental data, is used and only the total ionic conductivity reported (*Figure 3.4*). Additionally, one capacitor is replaced with an inductor and the other capacitors are replaced with constant phase elements (CPE). This is due to inductance effects that are best fit by an inductor instead of a capacitor and CPE behaving as an imperfect capacitor, respectively. Inductance effects are observed in experimental measurements at frequencies of 1 MHz or above, caused by cabling or sample holders.[12] Whereas, the capacitance of electrochemical phenomena in electrolytes analysed experimentally are typically non-perfect capacitors.

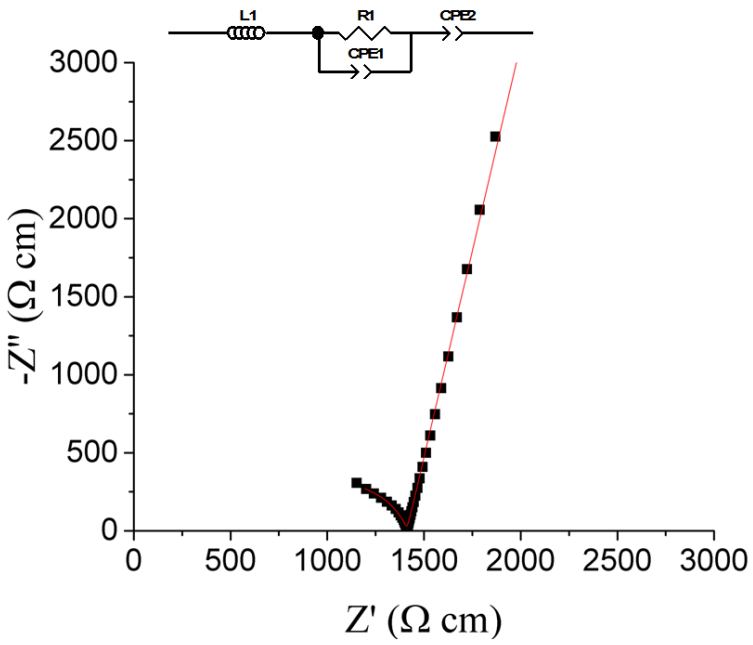

Figure 3.4 Impedance plot of LAGP after pelletisation and sintering at 900 ℃ for 5 h measured at room temperature.

The plot consists of a low frequency (further right) spike and a partial high frequency (further left) semi-circle. The low frequency linear impedance component inclined to the Z' axis is attributed to the typical blocking behaviour of the electrolyte-electrode interface, represented by L1 and CPE2 of the equivalent circuit (*Figure 3.4*). The high frequency semi-circle component relates to the AC impedance response of electrolyte grain boundaries, represented by R1 and CPE1 of the equivalent circuit. The low frequency intercept of the semi-circle to the horizontal axis (*Figure 3.4*) gives the total resistance of bulk and grain boundary responses and therefore the total resistance of the electrolyte (**Chapter 2 Section 2.3**). The total resistance of the synthesised LAGP relates directly to the specific ionic conductivity. The total ionic conductivity of prepared LAGP at room temperature is 2.84 x 10^{-4} S cm^{-1} and in good comparison with literature values.[4, 9] The full component values of the equivalent circuit are reported in **Appendix 1**.

At room temperature, the resistivity of the electrolyte intra-crystallite bulk phase is too low to be measured in the experimental frequency range (0.1 Hz – 1 MHz). Previously reported measurements of the bulk impedance response of LAGP have been acquired at low temperatures (<-10 °C) and/or high frequencies (>1 MHz).[5, 9, 13, 14] *Figure 3.5* shows a low-temperature measurement (-30 °C) demonstrating two semi-circles and the corresponding equivalent circuit (red line). The full component values of the equivalent circuit are reported in **Appendix 2**. The high frequency semi-circle capacitance is 11.0 pF cm^{-1} corresponding to the electrolyte intra-crystallite bulk phase. The low temperature experiment slows ion migration, increasing the resistivity of the system and shifting the frequency window such that the current response of both components is observed as two semi-circles. The lower resistivity of the bulk, compared to the grain boundary, accounts for the different current responses and separation of the observed semi-circles.

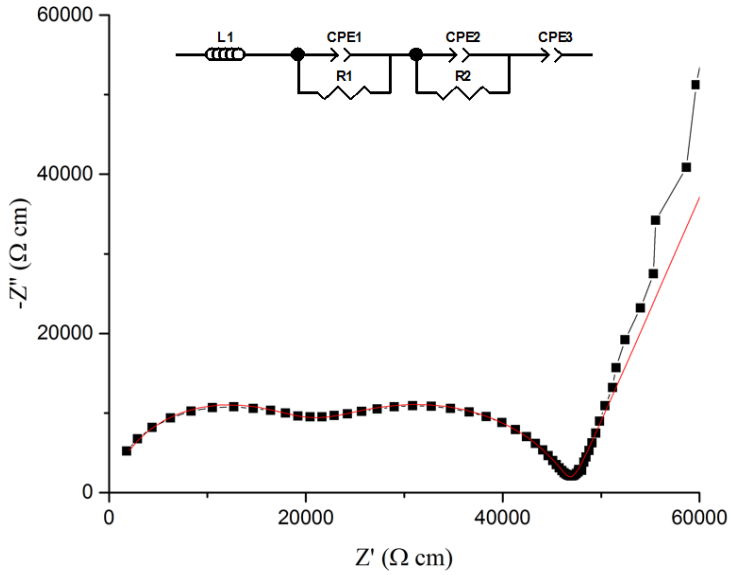

Figure 3.5 Impedance plot of LAGP after pelletisation and sintering at 900 ℃ for 5 h measured at -30 ℃.

The total ionic conductivity at -30 °C is 8.87 x 10^{-6} S cm^{-1}. The ionic conductivity calculations, including for the individual bulk and grain boundary components, are reported in **Appendix 2**. *Figure 3.6* reports the temperature dependent total ionic conductivity. The total ionic conductivity was calculated at each temperature with the appropriate equivalent circuit, as with *Figure 3.4* and *Figure 3.5*. At higher temperatures (*Figure 3.6*) less of a partial semicircle is observed, as with *Figure 3.4*, though the intercept of the Z' axis is still distinguishable in order to calculate the total ionic conductivity. The linear behaviour of conductivity against temperature is characteristic of ionic conductivity in crystalline solids. The Arrhenius equation describes ionic conductivity, σ, in crystalline solids:

$$\sigma = A\ exp\left(\frac{-E_a}{kT}\right) \tag{3.1}$$

Where A is a pre-exponential factor, E_a is the activation energy of conduction, k is the Boltzmann constant and T is the temperature.

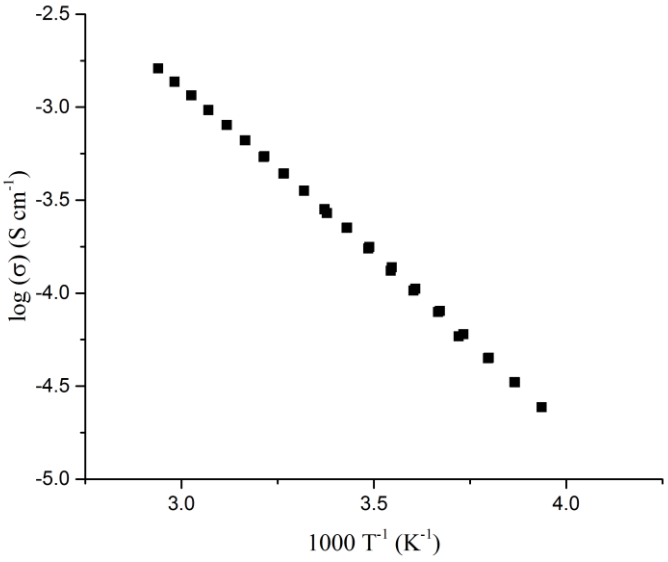

Figure 3.6 Arrhenius plot of total conductivity on heating and cooling of LAGP after pelletisation and sintering at 900 ℃ for 5 h.

The value for activation energy (0.36 eV) and total ionic conductivity at room temperature (2.84 x 10^{-4} S cm^{-1}) is in good agreement with literature.[4, 9] The reported PXRD, SEM and AC EIS analysis characterised the prepared material in good agreement with the reported literature and therefore confirms the successful synthesis of LAGP.

3.5.2. Fibre-Reinforced Polymer Fabrication

The polymeric material with highest tensile yield strength is Kevlar® (aramid) with chemical formula $[\text{-CO-C}_6\text{H}_4\text{-CO-NH-C}_6\text{H}_4\text{-NH-}]_n$. The highly ordered orientation of aromatic polyamide molecular chains along the fibre axis gives the material a tensile yield strength of approximately 3.5 GPa. As such, aerospace, military and body-armour applications have found common use of Kevlar®.[15] This work looks to increase the

oxide ceramic electrolytes tensile yield strength by fabricating a FR-CMC with aramid reinforcement.

Effective polymeric reinforcement of a FR-CMC requires efficient stress transfer between the ceramic and aramid fibres. The polymer matrix encasement of a fibre-reinforced polymer ensures even and efficient stress transfer to the individual fibres, making it ideal for a composite when in contact with ceramic. Fibre encasement typically uses epoxy to set fibres in place with a given orientation. Highly cross-linked polymer epoxy typically forms when low molecular weight pre-polymer resins containing epoxide groups undergo curing (polymerisation) by co-reactants. A ring opening reaction of the epoxide occurs during polymerisation by a species containing a reactive hydrogen atom.

The microstructural and macrostructural arrangement of fibres characterises the material. The most basic form of fibre is yarn - a continuous length of interlocked fibres. Alignment of parallel yarn prepared on the glass slide, according to experimental methods section (**Section 3.3.2**), has anisotropic tensile strength along the fibre axis.

In this work, encasement of fibres in epoxy resin uses the commercial 'EL2 laminating epoxy' with 'AT30 slow' epoxy hardener for curing. *Figure 3.7* shows the final FRP of aramid and epoxy prepared according to **Section 3.3.2**. *Figure 3.8* shows a SEM cross-section image of prepared FRP microstructure. It shows the fibres of aramid encased in epoxy, confirming the successful preparation of the intended FRP. The smoother lighter regions (*Figure 3.8*) are circular in shape being the cross-sections of the aramid fibres. The rougher darker regions are the epoxy polymer that encases the fibres, confirmed by the encompassing of the fibre cross-sections.

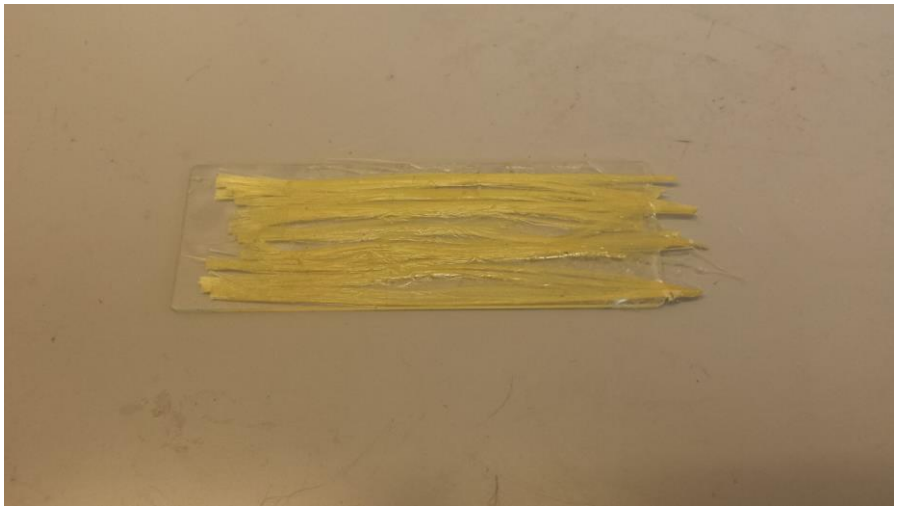

Figure 3.7 Image of aligned aramid and epoxy FRP on a glass substrate.

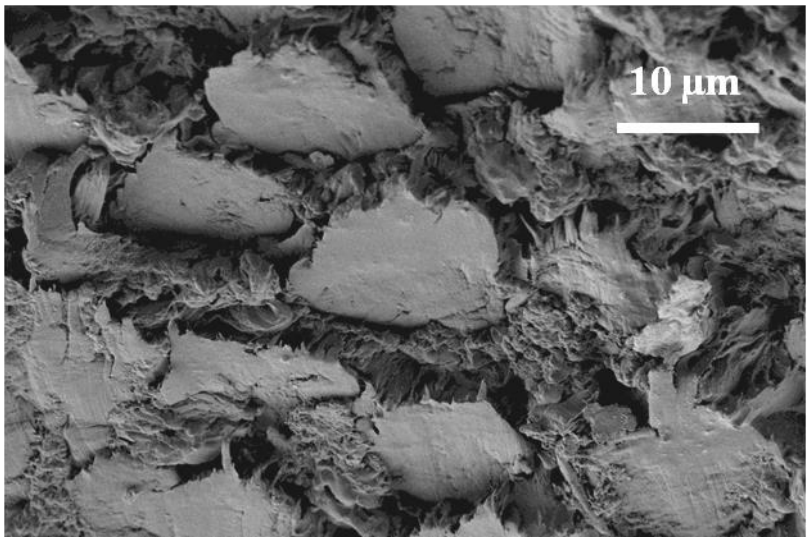

Figure 3.8 SEM cross-section image of aramid fibres (light grey) and epoxy FRP (dark grey).

3.5.3. Structural Fibre-Reinforced Ceramic Matrix Composite

The structural FR-CMC for mechanical analysis in this chapter combines an LAGP pellet with aramid-epoxy, such as those reported in **Section 3.5.1** and the previous section (**Section 3.5.2**), respectively. A structural composite of laminated layers was fabricated to demonstrate the compatibility and mechanical enhancement of oxide ceramic electrolytes with FRP.

A laminated bilayer of LAGP and aramid-epoxy was formed by curing of epoxy pre-polymer and hardener resin directly onto aramid yarn aligned at the surface of the pellet, according to the experimental methods section (**Section 3.3.3**). After curing, the FRP adheres to the surface of the pellet forming the FR-CMC. *Figure 3.9* shows an image of the prepared LAGP pellet covered in a layer of aramid-epoxy along with a schematic of the composite cross-section.

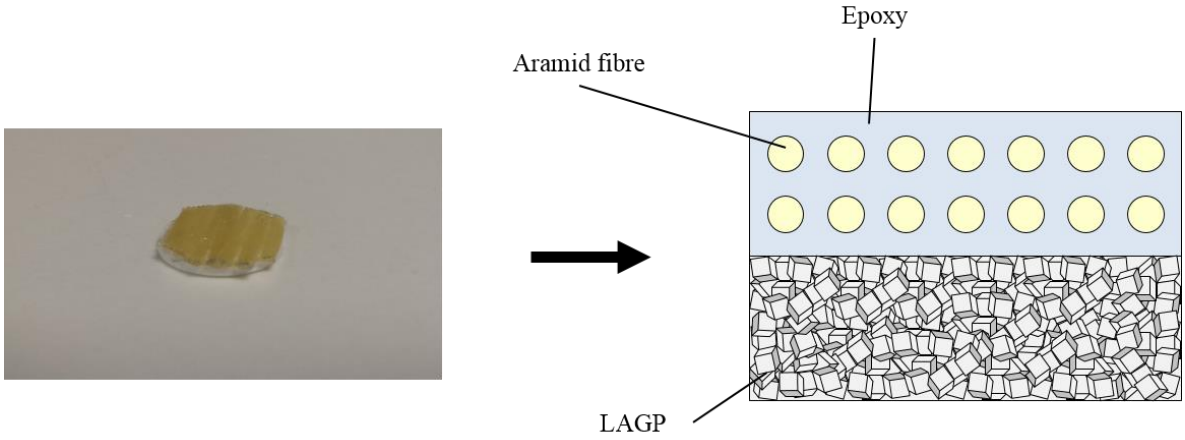

Figure 3.9 Image of the prepared FR-CMC with LAGP, epoxy and aramid and schematic representation of FR-CMC cross-section.

The bilayer formation conceals one surface of the pellet preventing ionic conduction of the electrolyte and rendering the FR-CMC non-functional. The opposite surface is bare for analytical purposes, discussed in the next section. *Figure 3.10* shows SEM images of the polymer-encased fibre microstructure of the aramid-epoxy layer atop the LAGP surface coated with excess epoxy. There appears to be good adhesion between the layers indicating a successful fabrication of FR-CMC. A number of loose fibres are also visible resulting from fibre 'pull out', a common failure mechanism in FRP.[2, 16]

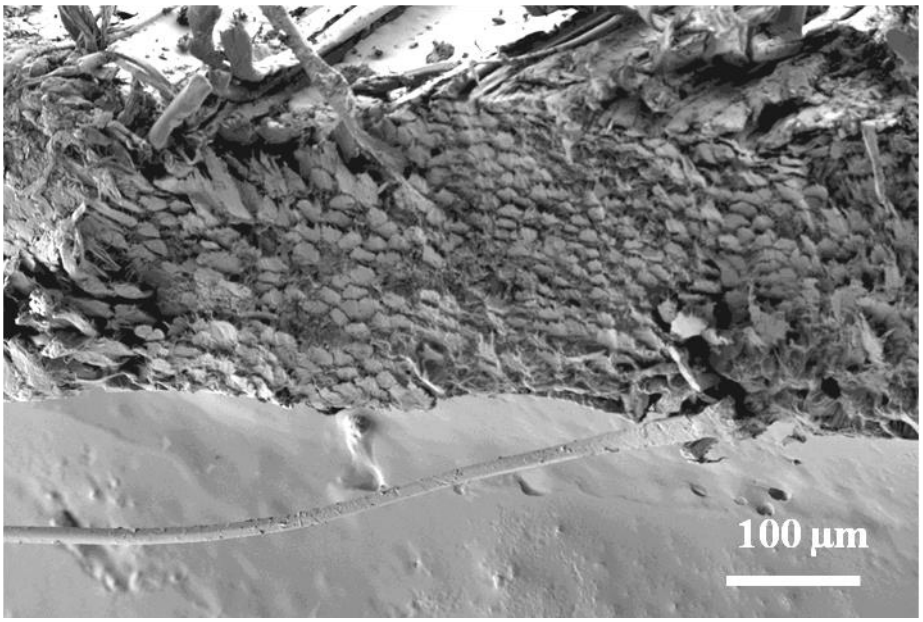

Figure 3.10 SEM cross-section image of aramid and epoxy FRP and side edge of epoxy coated LAGP of the structural FR-CMC.

3.5.4. Mechanical Analysis of Structural Fibre-Reinforced Composite

Brazilian disk testing, described in **Chapter 2 Section 2.4** and characterisation section (**Section 3.4**), is an analytical method that measures the tensile characteristics of pellets. The technique has been developed for concrete and rock-type materials,[17] including steel fibre reinforced concrete.[18] However, there has been no extensive study of ceramic electrolyte either with or without reinforcement. Compressive force applied diametrally to the circular disk induces tensile stress perpendicular to loading. The applied load increases until crack initiation upon which full fracture occurs in the disk.

Brazilian disk testing was used to analyse the tensile characteristics of fabricated FR-CMC reported in the previous section (**Section 3.5.3**). *Figure 3.11* shows an image of the fractured FR-CMC pellet in the Brazilian disk-testing instrument. The fracture runs along the line of applied compressive force and therefore indicates successful inducement of tensile force within the sample. The FRP layer did not fracture during

loading, suggesting the FR-CMC does not utilise the full tensile strength of the aramid, as discussed below.

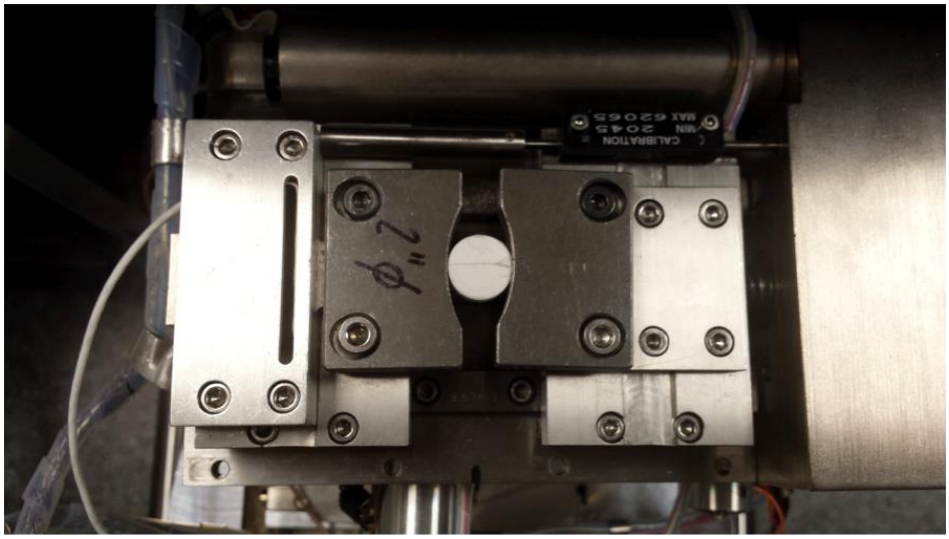

Figure 3.11 Image of LAGP, epoxy and aramid structural FR-CMC held between the curved clamps of Brazilian disk testing loading adaptor.

Figure 3.12 reports the force-displacement curve of the FR-CMC with a reference sample of LAGP and epoxy, prepared similarly to the experimental methods section (**Section 3.3.3**) without fibre reinforcement. The tensile strength of aramid is along the axis of the fibres and therefore the aligned fibres of the FRP are oriented in the direction of tensile stress (*Figure 3.11*).

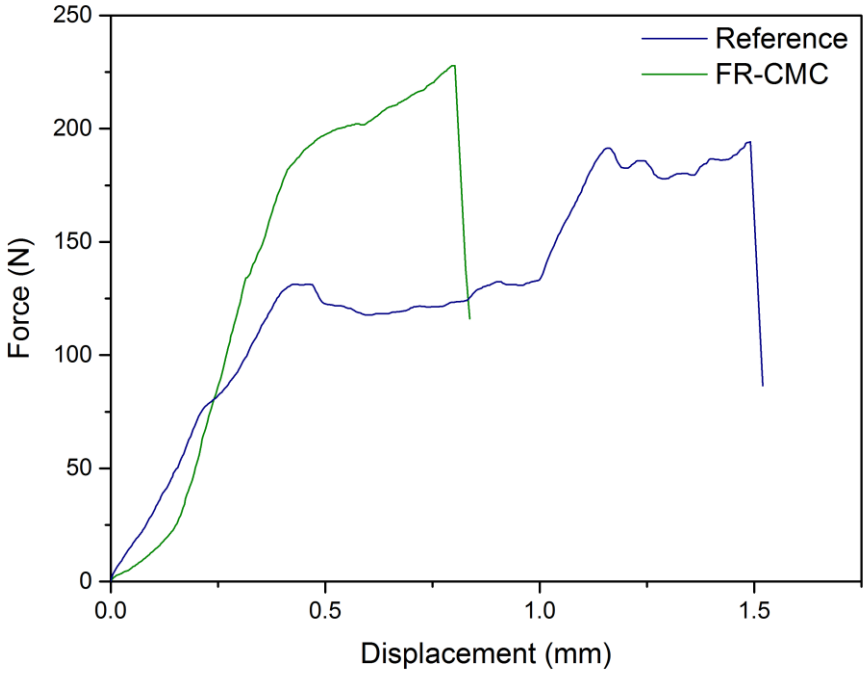

Figure 3.12 Brazilian disk testing force-displacement curves of LAGP and epoxy reference sample and LAGP, aramid and epoxy FR-CMC.

The small peaks and plateaus seen in the reference plot between 0.4-1.0 mm and 1.2-1.4 mm are likely due to end crushing observed in SEM (*Figure 3.13 (b)*) that also accounts for larger final displacement. The initial curve in the FR-CMC plot is likely due to pre-loading of the pellet. The final drop in both plots relates to the fracture of each pellet and the point of maximum tensile strength. The aramid-reinforced pellet (FR-CMC) fractures at a load of 228 N and displacement of 0.802 mm, whereas the LAGP-epoxy reference pellet fractures at 195 N and 1.491 mm. The following equation calculates the maximum tensile strength, σ_{xx}, in a disk:[19]

$$\sigma_{xx} = \left[1 - \left(\frac{b}{R}\right)^2\right]\frac{2P}{\pi D t} \tag{3.2}$$

Where b, R, P, D and t are the contact half-width, disk radius, applied load, disk diameter and disk thickness, respectively. A maximum tensile strength of 11.92 MPa is calculated for aramid-reinforced pellet (FR-CMC) and 10.28 MPa for the reference sample (*Figure 3.12*). Therefore, the aramid increases the maximum tensile strength of an LAGP pellet by 1.64 MPa.

The reference sample (*Figure 3.12*) shows only the linear elastic behaviour of LAGP until fracture. However, the initial straight line of the FR-CMC plot changes at approximately 183 N. The tensile strength at this point is 9.52 MPa, calculated according to *Equation 3.2*. This value refers to the onset of yielding for LAGP and is similar to the maximum tensile strength of the reference sample. Rather than complete fracture, the applied force increases with further displacement and the plot curves to form another straight line between 0.4 mm displacement and final fracture for FR-CMC (*Figure 3.12*). One assumes the second straight line is the contribution of the aramid fibres. The fibres prevent LAGP from fracturing after it starts yielding at 183 N, increasing the maximum tensile yield strength and in effect toughening the ceramic matrix.

In-situ ESEM images were taken during the loading process of the Brazilian disk testing, according to the characterisation section (**Section 3.4**), with the reported composites (*Figure 3.11*). Placing the FR-CMC with LAGP facing the secondary electron detector allows for imaging of the ceramic surface and visualisation of fracture behaviour. *Figure 3.13* shows ESEM images of LAGP after *(a)* fracturing of the FR-CMC and *(b)* reference sample end crushing caused by the clamps. End crushing accounts for the small peaks, plateaus and larger final displacement of the reference sample in the force-displacement curve in *Figure 3.12*. The curved design of clamps for

the Brazilian disk-testing instrument reduces the amount of end crushing, though it may not be avoided entirely.[19]

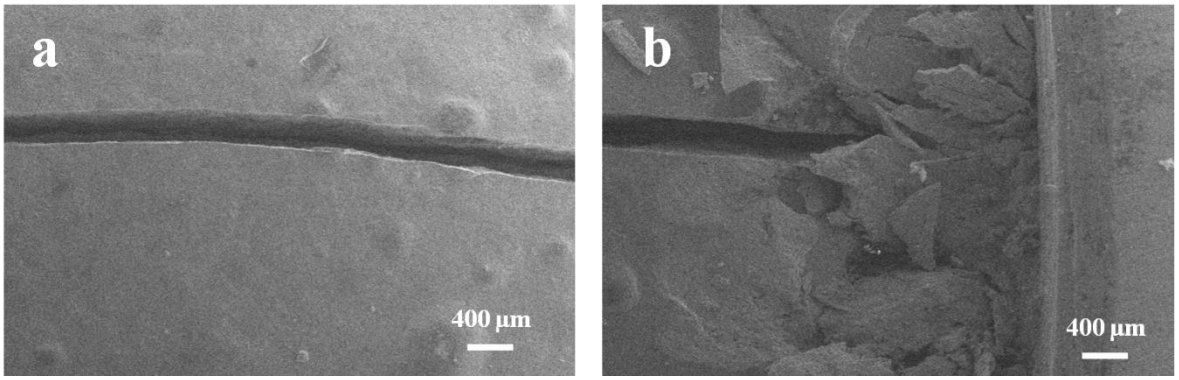

Figure 3.13 In-situ ESEM image of (a) FR-CMC LAGP, epoxy and aramid pellet and (b) end crushing in the LAGP and epoxy reference sample fractured during Brazilian disk testing.

Crack bridging of the aramid-epoxy FRP is limited due to the structural composite. However, this work proves that FRP can in fact reinforce oxide ceramic electrolyte in a FR-CMC. Brazilian disk testing demonstrates the limitations of the FR-CMC by the lone fracture of the LAGP layer and not the FRP or aramid fibres. Minimal stress is transferred to the FRP layer from the LAGP pellet. Therefore, the maximum tensile yield strength of LAGP increases only by 1.64 MPa on reinforcement with FRP (11.92 MPa), far from the known tensile yield strength of aramid (3.5 GPa).

Figure 3.14 shows the stress-strain curve analysed by conventional tensile strength techniques reported from literature that also observed the increased maximum tensile yield strength behaviour in cement reinforced with FRP.[16]

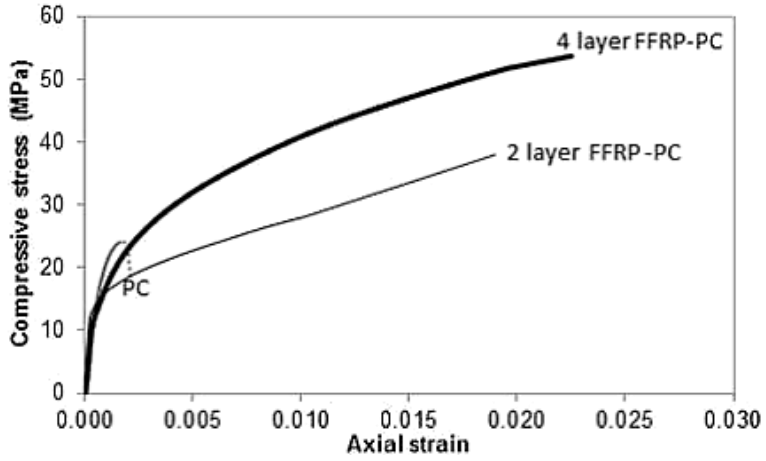

Figure 3.14 Axial compressive stress-strain curves of plain concrete (PC) and flax fibre-reinforced polymer (FFRP) confined PC.[16]

The graph (*Figure 3.14*) shows an increase in tensile yield strength achieved with more iterations of internal crack bridging (layers). Structural composites reported in this chapter lack internal crack bridging, which therefore limits the maximum tensile yield strength and toughening effect of the reinforcement (*Figure 3.12*). A fibre-reinforced ceramic matrix composite, for use in an electrochemical cell with increased crack bridging and maximum tensile yield strength and toughness, requires an interpenetrating microstructure, discussed in **Chapter 4** and **Chapter 5**. An ideal composite featuring interpenetration of reinforcement and ceramic phases at the length scale of initiating cracks is likely to increase the tensile yield strength, beyond that of the structural composites in *Figure 3.14* (approximately 25 MPa) or that observed in *Figure 3.12* (1.64 MPa).

3.6. Conclusion

This work has shown that fabricated LAGP and aramid-epoxy can form ceramic matrix and reinforcement for novel FR-CMC application. LAGP and FRP have formed a FR-CMC through the curing of FRP adhering to the surface of pelletised LAGP.

PXRD analysis has shown the crystalline phase of LAGP with other common impurities reported in literature identified by EDS analysis. Further SEM analysis confirmed the morphology of LAGP with a well-sintered polycrystalline microstructure, the dispersed fibres of aramid in epoxy and the microstructure of prepared FR-CMC. AC EIS of LAGP has confirmed ionic conduction comparable to literature.

The obtained results indicate that an oxide ceramic electrolyte and fibre-reinforced polymer are suitable materials for application as FR-CMC that can increase the tensile yield strength of ceramic. However, the fabricated structural FR-CMC is not functional as a solid electrolyte and prepared only for mechanical analysis. Brazilian disk testing has shown an increase in the maximum tensile strength of the aramid-epoxy-LAGP FR-CMC compared to a non-aramid reinforced reference sample. The analysis confirmed the strengthening of LAGP by FRP.

The FR-CMC utilised the high tensile strength of aramid fibres to reinforce LAGP, proving the novel concept of increasing the tensile strength and toughness of oxide ceramic electrolytes with reinforcement. Therefore, FR-CMC of oxide ceramic electrolyte and FRP is a promising candidate for the development of superior oxide ceramic electrolytes, which combine the ionic conductivity of solid electrolytes and the improved mechanical property of composites, in optimised all-solid-state batteries. However, a FR-CMC electrolyte layer requires an IPC microstructure for electrochemical performance and further increased tensile yield strength through internal crack bridging. The following chapters investigate the implementation of this system for functional FR-CMC with IPC microstructure.

3.7. References

[1] Nam, Y. J. *et al*. Bendable and thin sulfide solid electrolyte film: a new electrolyte opportunity for free-standing and stackable high-energy all-solid-state lithium-ion batteries. *Nano Lett.* **15**, 3317-3323 (2015).

[2] Travitzky, N. Processing of ceramic–metal composites. *Advances in Applied Ceramics* **111**, 286-300 (2012).

[3] Hammel, E. C., Ighodaro, O. L. -R. & Okoli, O. I. Processing and properties of advanced porous ceramics: An application based review. *Ceram. Int.* **40**, 15351-15370 (2014).

[4] Zhang, M. *et al*. Preparation and electrochemical properties of Li1+xAlxGe2-x(PO4)3 synthesized by a sol-gel method. *J. Electrochem. Soc.* **159**, A1114-A1119 (2012).

[5] Cretin, M. & Fabry, P. Comparative study of lithium ion conductors in the system Li1+xAlxA2−xIV (PO4)3 with AIV=Ti or Ge and 0≤x≤0·7 for use as Li+ sensitive membranes. *J. Eur. Ceram. Soc.* **19**, 2931-2940 (1999).

[6] Hasegawa, S. *et al*. Study on lithium/air secondary batteries—Stability of NASICON-type lithium ion conducting glass–ceramics with water. *J. Power Sources* **189**, 371-377 (2009).

[7] Hartmann, P. *et al*. Degradation of NASICON-type materials in contact with lithium metal: formation of mixed conducting interphases (MCI) on solid electrolytes. *J. Phys. Chem. C* **117**, 21064-21074 (2013).

[8] Chowdari, B. V. R., Subba Rao, G. V. & Lee, G. Y. H. XPS and ionic conductivity studies on Li2O–Al2O3–(TiO2 or GeO2)–P2O5 glass–ceramics. *Solid State Ionics* **136–137**, 1067-1075 (2000).

[9] Thokchom, J. S., Gupta, N. & Kumar, B. Superionic conductivity in a lithium aluminum germanium phosphate glass–ceramic. *J. Electrochem. Soc.* **155**, A915-A920 (2008).

[10] Alami, M. *et al*. Structure and thermal expansion of LiGe2(PO4)3. *J. Solid State Chem.* **90**, 185-193 (1991).

[11] Yang, J., Huang, Z., Huang, B., Zhou, J. & Xu, X. Influence of phosphorus sources on lithium ion conducting performance in the system of Li2O–Al2O3–GeO2–P2O5 glass–ceramics. *Solid State Ionics* **270**, 61-65 (2015).

[12] Christensen, B. J. *et al*. Impedance spectroscopy of hydrating cement-based materials: measurement, interpretation, and application. *J. Am. Ceram. Soc.* **77**, 2789-2804 (1994).

[13] Fu, J. Fast Li+ ion conducting glass-ceramics in the system Li2O–Al2O3–GeO2–P2O5. *Solid State Ionics* **104**, 191-194 (1997).

[14] Mariappan, C. R., Yada, C., Rosciano, F. & Roling, B. Correlation between micro-structural properties and ionic conductivity of Li1.5Al0.5Ge1.5(PO4)3 ceramics. *J. Power Sources* **196**, 6456-6464 (2011).

[15] Jassal, M. & Ghosh, S. Aramid fibres-an overview. *Indian J. Fibre Text. Res.* **27**, 290-306 (2002).

[16] Yan, L. & Chouw, N. Dynamic and static properties of flax fibre reinforced polymer tube confined coir fibre reinforced concrete. *Journal of Composite Materials* **48**, 1595-1610 (2014).

[17] Liu, C., Lovato, M. L., Stout, M. G. & Huang, Y. Measurement of the fracture toughness of a fiber-reinforced composite using the Brazilian disk geometry. *Int. J. Fract.* **87**, 241 (1997).

[18] Lameiras, R., Barros, J. A. O. & Azenha, M. Influence of casting condition on the anisotropy of the fracture properties of Steel Fibre Reinforced Self-Compacting Concrete (SFRSCC). *Cement and Concrete Composites* **59**, 60-76 (2015).

[19] Islam, O., Dragnevski, K. I. & Siviour, C. R. In situ environmental scanning electron microscope observations of colloidal failure mechanisms using the brazilian disk test. *Experimental Techniques* **39**, 12-18 (2015).

Chapter 4: Composite Fabrication from Developed Bijel Templates

4.1. Aim

The reinforcement of oxide ceramic electrolyte with polymeric-fibres has been demonstrated, but formed a non-ionically conducting composite with only a moderate increase in tensile strength. The main aim of this chapter is to fabricate an oxide ceramic electrolyte composite with an interpenetrating microstructure. The bicontinuous interfacially jammed emulsion gels (bijel) system has been selected to introduce such microstructure. The first requirement is to prepare a solidified bijel having appropriate chemical and microstructural properties to be a template. A procedure is then required to form the ceramic interpenetrating microstructure from the bijel template. Fabricating an interpenetrating composite would be an excellent demonstration of this novel route for oxide ceramic electrolyte reinforcement.

4.2. Introduction

The previous chapter confirmed the ability of fibre-reinforcement to increase the tensile strength and therefore toughness of a pellet of oxide ceramic electrolyte. The structural composite of laminated fibre-reinforced ceramic is inappropriate for an electrolyte between two electrodes due to the blocking of the surface by reinforcement. To optimise the mechanical enhancement and functionality of a fibre-reinforced (FR) ceramic matrix composite (CMC) of oxide ceramic electrolyte requires a 3D-

interpenetrating composite (IPC) microstructure. The realisation of such a composite requires a precise and versatile procedure.

This chapter considers a composite fabrication procedure based on sacrificial templating of oxide ceramic electrolyte with bijel templates. The interpenetrating microstructure of the bijel makes it appealing for reproduction in oxide ceramic electrolyte. A resultant ceramic preform would possess 3D-interconnected porosity enabling complete infiltration with reinforcement. However, the template microstructure will have an effect on ceramic preform formation, reinforcement infiltration and the properties of the final composite. Therefore, this chapter investigates the microstructural parameters of the bijel and discusses desirable parameters for an ideal FR-CMC and fabrication procedure.

This chapter reports the fabrication of templates from the liquid bijel system with solidification and silica removal procedures. The interpenetrating template requires a suitable sacrificial templating procedure for optimal reproduction of the microstructure in ceramic, also reported. The procedure aims to fabricate a ceramic matrix with adequate lithium-ion conduction, high density for inherent ceramic compressive strength and allow for subsequent infiltration of reinforcement. Further work presents analysis of the template and ceramic preform microstructural parameters along with a discussion of the optimal parameters for reinforcement of a ceramic matrix. Finally, a polymer-ceramic composite with bijel microstructure is reported and analysed.

4.3. Experimental Methods

4.3.1. Solidification of Liquid Bijel Synthesis

Solid bijels were prepared using known literature procedures, as demonstrated by *Figure 4.1*.[1-3] Approximately 60 mg of desiccated silica particles were dried for 3-4 h at 160 ˚C and 20 mbar in a Binder Model VD 23 vacuum oven. 1.03 mL of Mili Q water was added to the silica particles and sonicated at 8 W for 4 minutes with a Sonics Vibra-Cell probe before vortex mixing for 10 seconds. A 1.5 μM solution of nile red dye in 2,6-lutidine (99 %, Sigma-Aldrich) was prepared. 0.3905 g (28 wt%) of the lutidine-dye solution was added to the water-silica mixture and vortex mixed for 10 seconds. 300 μL of the mixture was irradiated in a microwave oven for 10 seconds then immediately left unperturbed for at least 20 minutes in an incubator at 53 ˚C. 60 μL of a preheated (53 ˚C) photoinitiator (2-hydroxy-2-methylpropiophenone) and monomer (1,6-hexanediol diacrylate) mixture at a 1:10 weight ratio was added to the top of the water-lutidine mixture. The mixture was moved to an oven at 55 ˚C and left for 5 h. Photopolymerisation was then carried out using an Omnicure 1000 UV lamp for 10 seconds. The samples were left to dry in ambient conditions overnight.

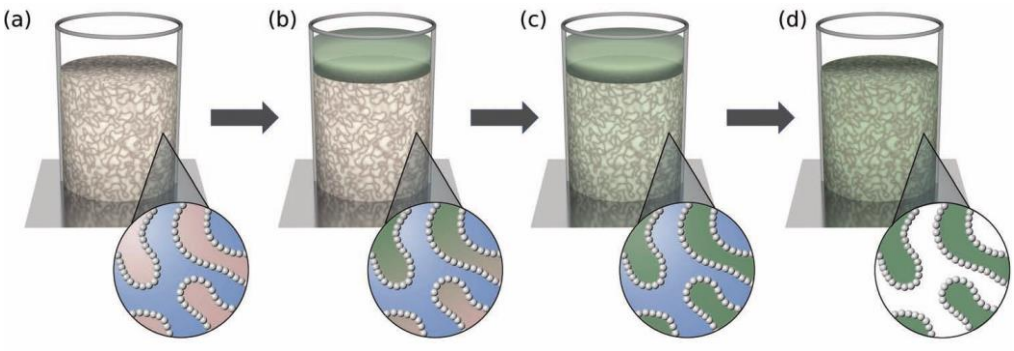

Figure 4.1 Schematic representation of the solidification of a bijel by the (a) formation of a bijel on spinodal decomposition with water (blue), alcohol (pink) and silica (white), (b) addition and selective dissolution of monomer and photo-initiator (green), (c) photopolymerisation of the monomer by exposure to UV to form the solid bijel and (d) draining and drying the remaining liquid.[3]

4.3.2. Etching of Solidified Bijel

The solidified bijels prepared according to the previous section (**Section 4.3.1**) were soaked in an excess 2 M solution of sodium hydroxide (99.3 %, Fisher Scientific) and distilled water for 24 h. The solidified bijels were recovered, rinsed with distilled water and dried at 80 °C for 1 h.

4.3.3. $Li_{1.6}Al_{0.6}Ge_{1.4}(PO_4)_3$ (LAGP) Adapted Sacrificial Templating

LAGP was prepared by a Pechini sol-gel synthesis according to literature.[4] Synthetic grade starting materials were purchased from Sigma-Aldrich, unless otherwise stated. 275.8 mg of lithium nitrate (99.99 %), 562.7 mg of aluminium nitrate nonahydrate (99.997 %), 885.5 mg of germanium ethoxide (≥99.95 %) and 880.3 mg of ammonium dihydrogen phosphate (99.999 %) were dissolved in a 0.2 M aqueous solution of 3.8 g of citric acid monohydrate (≥99.0 %) and 90 mL of distilled water. 1.1 g of ethylene glycol (99.8 %) was added and the solution stirred and heated at 80 ˚C for 1 h to form a homogeneous solution. The temperature was increased to 170 ˚C for 24 h to initiate gelation. The gel was heated to 400 ˚C for 4 h in air using a platinum crucible. The obtained product was ground in an agate mortar and pestle before being heated in air using a platinum crucible at 800 ˚C for 5 h to produce the powder LAGP product that was again ground in an agate mortar and pestle. 0.5 g of LAGP powder in 0.5 mL of ethanol (≥99.8 %) were then ball milled in a Retsch EMAX high energy ball mill with zirconia-lined milling vessel and 21.5 g of zirconia 5 mm balls at 600 rpm for 10 minutes. The resultant LAGP powder was recovered and dried at 80 ˚C overnight. 100 mg of LAGP ball milled powder was then mixed in 0.7 mL of methanol (99.99 %, Fisher Scientific) before immersing a template. The mixture was twice sonicated for 5

minutes and centrifuged at 2000 rpm for 2 minutes giving sediment of the LAGP powder. The supernatant methanol was removed and the sediment was left to dry at room temperature for 2 minutes. The template was recovered from the sediment with excess LAGP rubbed from the surface. The impregnated template was heated to 900 ˚C for 5 h at a rate of 2 ˚C min^{-1} to yield the LAGP preform.

4.3.4. Polypropylene Impregnation of LAGP Preform

An excess of polypropylene (isostatic, average Mw ~12000 Da, Sigma-Aldrich) was melted at 180 ˚C. An LAGP preform was added to the melt and polymer allowed to percolate the porosity under dynamic vacuum for 2 h. The preform was removed from the melt and left to cool to ambient temperature. Excess polymer was removed by placing the polypropylene-filled preforms on aluminium foil covering a hot plate at 100 ˚C.

4.4. Characterisation

The morphology of materials was investigated using a Carl Zeiss Merlin field emission scanning electron microscope (SEM) with a Gemini II column. Samples were mounted on adhesive copper tape applied to a stub and holder. Measurements were taken at a voltage range of 1-3 kV with a current range between 72-100 pA. Cross-sections were prepared using a scalpel. The chemical character of materials was analysed by energy dispersive X-ray spectroscopy (EDS) using an Oxford Instruments X-Max^N silicon drift detector with 150 mm^2 size detector attached to the Merlin microscope.

Thermogravimetric analysis (TGA) was carried out using a Netzsch STA 449 F3. Alumina crucibles under a flow of synthetic air were used during the investigation of thermal effects at room temperature to 1000 °C at 10 °C min^{-1}.

The 3D-interconnectivity of computational 3D-models was investigated in Netfabb Professional (7.4.0). An inverse phase model was generated using a Boolean operation before both the original model and inverse phase were analysed for number of individual (non-connecting) shells.

The microstructural parameters of different architectural models were analysed using a variety of software packages. The solid volume fraction was calculated as an automatic function in Netfabb Professional (7.4.0). The internal surface-area-to-volume ratio used the repair function of Netfabb Professional (7.4.0) to remove external faces of each model to give only the internal surfaces, before automatic calculations of surface area were given. The sample thickness distribution and channel size distribution were analysed using the auto-skeletonisation and distance mapping tools of Avizo (9.1.1).

Micro-computed tomography (μCT) data from the LAGP preform were collected using a Carl Zeiss Xradia 510 Versa X-ray microscope. The source voltage was 80 kV with a current of 87.5 μA.

Alternating current electrochemical impedance spectroscopy (AC EIS) was used to investigate the electrical behaviour of a composite of LAGP and polypropylene, prepared according to the previous section (**Section 4.3.4**). The sample surface was polished using 3M Tri-M-ite Fre-Cut abrasive sheet (P1200) before drying at 70 °C for 20 minutes, sonicating in cyclohexane for 10 minutes and drying again at 70 °C for 20 minutes. Gold blocking electrodes approximately 30 nm thick were sputtered onto opposite sides of the preform. Conductivity measurements were made using a Solartron

Analytical Modulab over 0.1 Hz – 1 MHz frequency range and voltage amplitude of 10 mV. Impedance data were fitted against an equivalent circuit to calculate the total ionic conductivity. All temperature variable measurements were carried out on a Julabo F32-MA cryostat. Low temperature measurements used liquid nitrogen to reach -30 ˚C. Temperature dependent measurements were carried out in the range of -30 to 75 ˚C in 5 ˚C steps. The data were analysed using ZView (3.4c) and an equivalent circuit generated to the best fit.

4.5. Results & Discussion

4.5.1. Bijel Polymer Template Fabrication

Sacrificial templating requires the addition of sacrificial material to the ceramic precursor and removal after sintering, as demonstrated in *Figure 4.2*. The typical procedure uses particles dispersed in ceramic precursor to press as a powder mixture, cast as a wet colloidal suspension or impregnate pre-ceramic polymer or ceramic suspension into the consolidated sacrificial material.[5] The disadvantage of particle dispersions is non-guaranteed 3D-interconnectivity of pores or high porosity that can lead to ceramic weakening. A low solid volume fraction template with 3D-interconnected porosity is required for further processing of the preform by complete infiltration of reinforcement and maintaining inherent ceramic compressive strength, respectively.

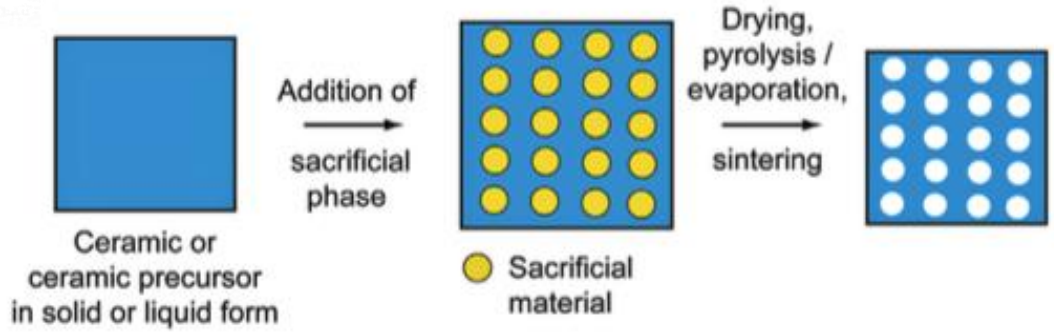

Figure 4.2 Schematic representation of sacrificial templating ceramic preform fabrication.[6]

Bijels are a suitable chemically prepared template for sacrificial templating. The 3D-interconnectivity of the bicontinuous liquid domains is very beneficial for a 3D-interpenetrating composite microstructure of FR-CMC. New liquid bijel systems have been invented for various application and material processing routes that have formed macroporous ceramic, copper and nickel structures.[3] The solidification of the bijel is of particular interest here and has potential scalability. Procedures involving colloidal crystals as sacrificial templates, as shown in **Chapter 1 Section 1.9**, are more suited for highly porous ceramic preforms with limited control of architecture. Bijels, on the other hand, offer a more suitable and modifiable volume fraction range.

Solidified-bijel frameworks of poly(1,6-hexanediol diacrylate) were prepared according to the literature procedure described in the experimental methods section (**Section 4.3.1**). The morphology of obtained samples was investigated by SEM. *Figure 4.3* shows SEM images and EDS data of the solidified bijel and fractured cross-section. The cross-section exposes spherical silica particles of size approximately 1 μm. Silica is lithiated at elevated temperatures making it unsuitable in the presence of solid lithium-ion conductors. Solidified-bijel templates etched to remove silica were prepared according to the procedure described in the experimental methods section (**Section**

4.3.2). *Figure 4.4* shows SEM images and EDS data of the etched solidified bijel and fractured cross-section. No silica particles are visible in the polymer template after etching.

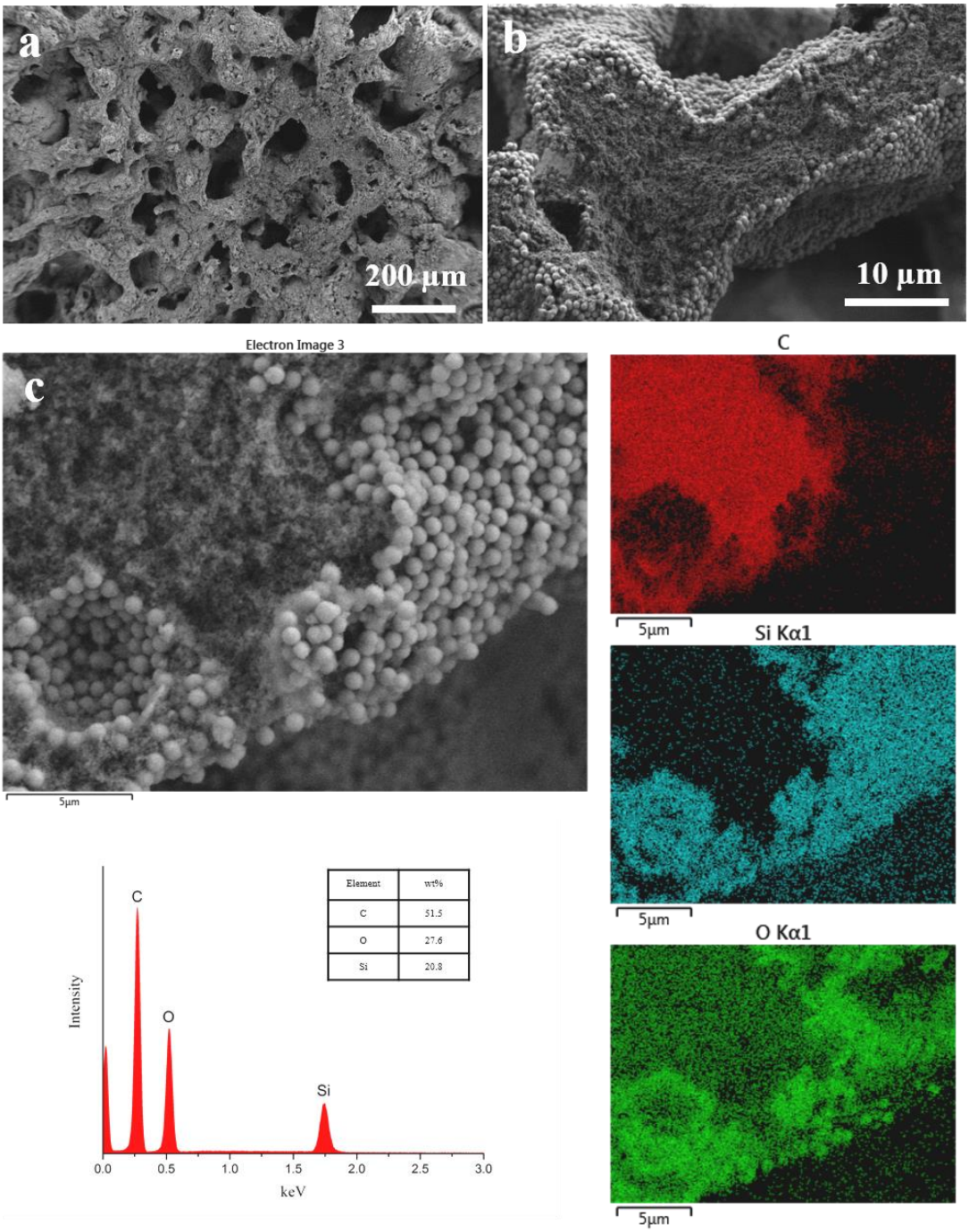

Figure 4.3 SEM images of polymer bijel microstructure at the (a) surface, (b) cross-section and (c) magnified cross-section with respective EDS spectrum and elemental mapping.

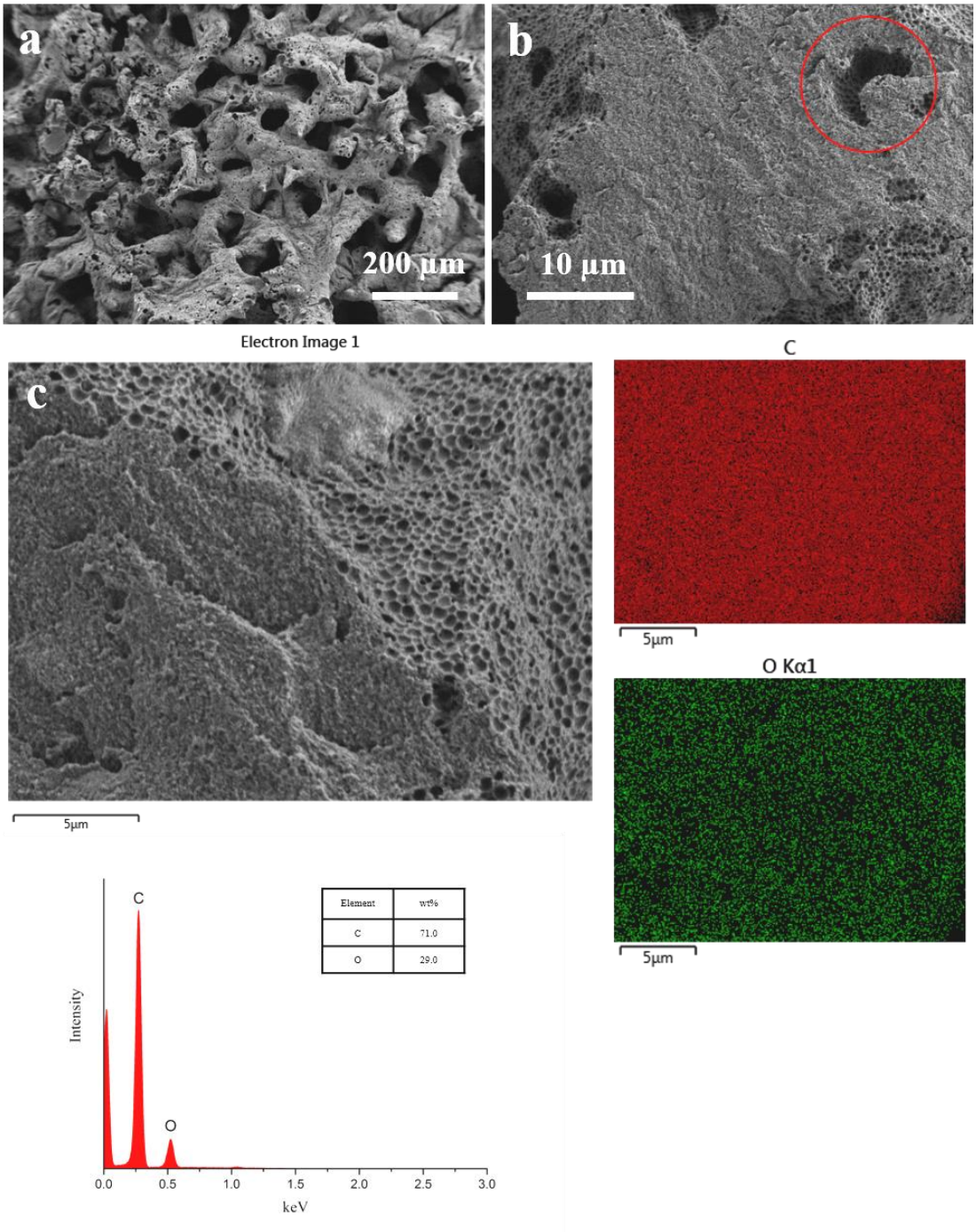

Figure 4.4 SEM images of etched bijel microstructure at the (a) surface, (b) cross-section and (c) magnified cross-section with respective EDS spectrum and elemental mapping.

The etched solidified bijel is now usable as a 'bijel template' due to the removal of silica and presence of original microstructure. *Figure 4.5* shows the TGA data of the bijel template in air before and after etching. Low-temperature weight loss at 250-400

°C is due to loss of moisture and oxidation of organics. The high temperature weight loss at 400-550 °C is due to the oxidation, pyrolysis and combustion of the remaining material.

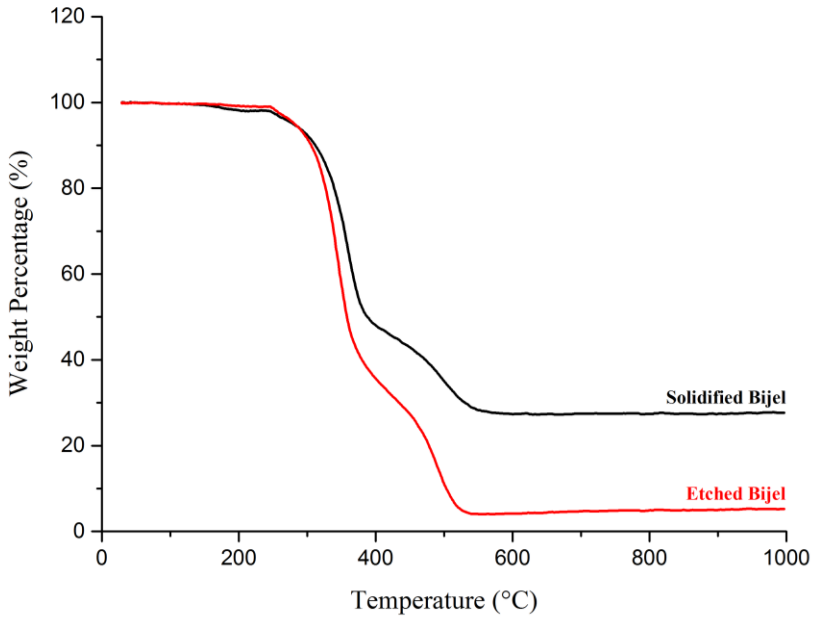

Figure 4.5 TGA curves of a bijel in air before and after etching.

The remaining weight of the etched bijel template on heating from room temperature to 900 °C was 4 wt% compared to 27 wt% of the bijel before etching. The remaining weight corresponds to the silica present in the bijel. This confirms the removal of the majority of silica by etching as only 4 wt% of the etched bijel remains. Trapped regions of silica within the bijel polymer prevent etching by and exposure to sodium hydroxide solution. The red circle in *Figure 4.4 (b)* highlights the remnants of an internal silica pocket within the solid polymer, which is an example of poor spinodal decomposition during the synthesis. However, the removal of surface silica particles should ready the bijel for template use, preventing reactions between silica and ceramic

involving lithium. The TGA data also demonstrates the templates thermal suitability for preform formation. The template remains physically stable until combustion in air at 250 °C before complete removal at 550 °C. The oxide ceramic electrolyte synthesis used for sacrificial templating requires a compatible combustion profile with the template. The TGA data reported in *Figure 4.5* suggests the template will be present during precursor drying and removed before sintering in air at 900 °C. This is appropriate for an impurity free ceramic preform.

μCT data used computational 3D rendering to create a 3D model of the bijel template. *Figure 4.6* shows an image of a computational 3D bijel model taken as a 400 x 400 x 400 μm portion of the total μCT data.

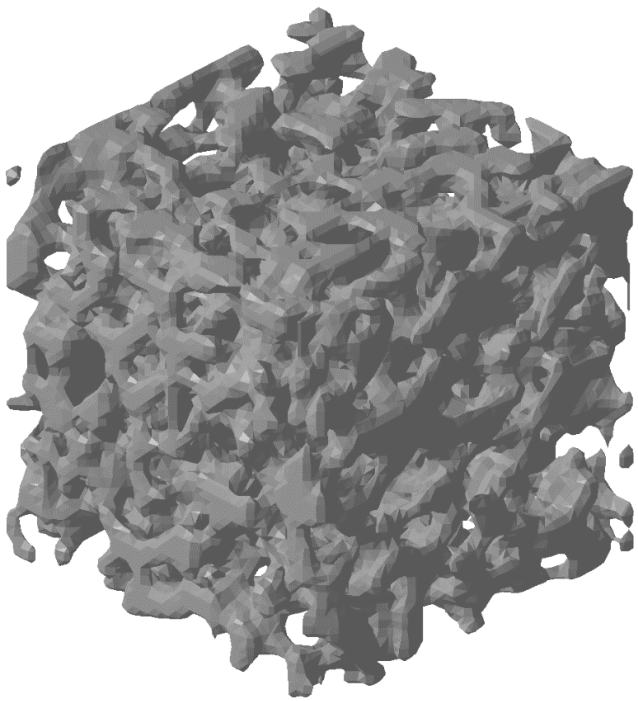

Figure 4.6 3D-rendered computational 400 x 400 x 400 μm model from μCT data of an etched bijel template.[1]

[1] μCT data acquired and provided by Dr Job Thijssen at the School of Physics and Astronomy, The University of Edinburgh

The 3D model proves the continuous 3D-interconnectivity of the bijel template, implying the presence of an interpenetrating microstructure. Boolean transformations, where parts are merged or subtracted, form the inverse phase model of the original structure (*Figure 4.6*), demonstrated in *Figure 4.7*. The method, described in the characterisation section (**Section 4.4**), selects connected surfaces of the models in *Figure 4.7 (a)* and *(c)* that confirm the bicontinuity of the bijel template.

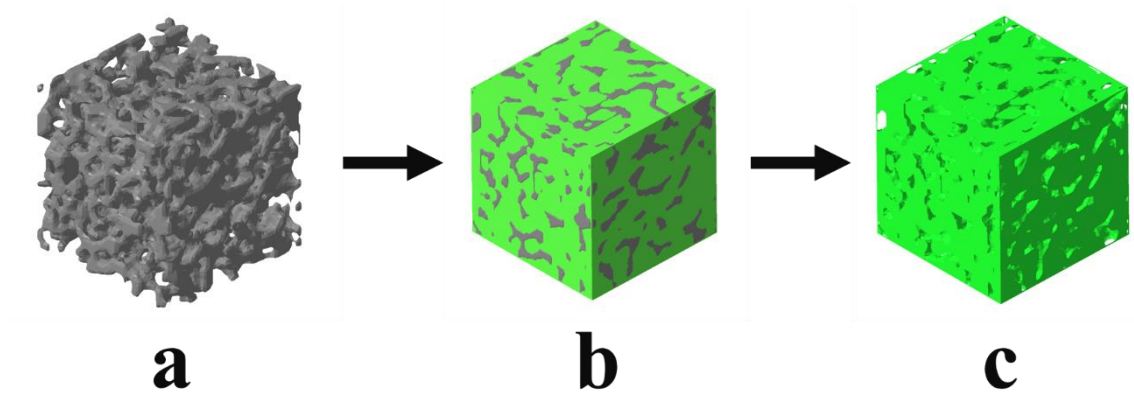

Figure 4.7 3D-models of the (a) etched bijel template, (b) both bijel phase and inverse phase generated by a Boolean operation and (c) inverse bijel phase, used for phase analysis.

The bijel template reported in this section is now ready for use as a template in sacrificial templating. The following sections discuss the characterisation of microstructural parameters that determine the suitability of template architecture for further work.

4.5.2. Microstructural Parameter Analysis

The key microstructural parameters of IPC microstructures are solid volume fraction, surface-area-to-volume ratio, channel size distribution, sample thickness distribution and tortuosity. The solid volume fraction defines the fraction of total

volume occupied by solid. In this work, the surface-area-to-volume ratio considers only the internal surface area within the microstructure that predicts the shared surface area between ceramic and reinforcement. The channel size and sample thickness are local 3D measures of internal empty (pore) and solid volume fractions in porous materials, respectively. The channel size distribution and sample thickness distribution refer to the distributions in local size of the empty and solid volume fractions in a total defined volume, respectively. The tortuosity, defined as the degree of tortuous (twisted) curvature, is a complex parameter the detailed computational analysis of which is beyond the scope of this work. The parameters are discussed in further detail below, but are ideal for a FR-CMC when:

- Solid volume fraction is high (maintains ceramic compressive strength)
- Surface-area-to-volume ratio is high (increases crack bridging through specimen)
- Channel size distribution is uniformly distributed (increases isotropic reinforcement)
- Sample thickness distribution is uniformly distributed (decreases weaker narrow regions of local stress concentration)
- Tortuosity is high (increases crack deflection)

The IPC microstructure enables crack bridging within the ceramic matrix as opposed to the surface of structural composites, as discussed in the previous chapter (**Chapter 3**). Therefore, an IPC microstructure expects to increase the toughness of the ceramic by increasing the release rate of elastic strain energy (stress transfer efficiency), ΔG_{el}, according to reinforcement by crack bridging (**Chapter 1 Section 1.8**):

$$\Delta G_{el} = f \int_0^u \sigma(u)\mathrm{d}u$$

(4.1)

Where f, σ and u are the area fraction of reinforcement intercepted by the crack, stress and opening of the crack, respectively. Microstructural parameters predict the area fraction of reinforcement intercepted by a crack (f). The surface-area-to-volume ratio of reinforcement predicts the number of local reinforcements intercepted when comparing equivalent volume, demonstrated by *Figure 4.8 (a)*. On the other hand, the channel size distribution and sample thickness distribution of reinforcement indicate the distribution of volume affecting the area of local reinforcements intercepted, demonstrated by *Figure 4.8 (b)*. The average sample thickness of reinforcement indicates the area of local reinforcements intercepted. Furthermore, the standard deviation is a useful measure of channel size distribution and sample thickness distribution uniformity as the amount of variation in the distributions. With a large degree of non-uniformity, regions of lower size or thickness may create bottlenecks affecting ceramic preform formation, reinforcement infiltration, ionic conductivity, mechanical properties or the isotropic nature of reinforcement.

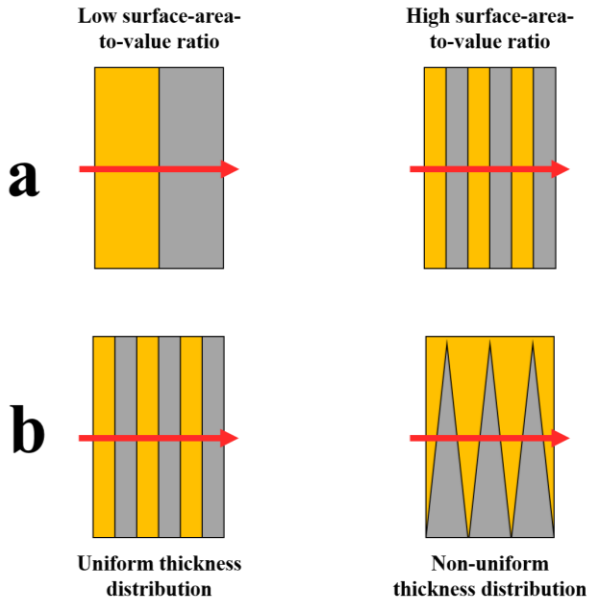

Figure 4.8 Schematic representation of crack propagation (red arrow) through ceramic matrix (yellow) and reinforcement (grey) of different (a) surface-area-to-volume ratios and (b) thickness distribution uniformities.

The above example (*Figure 4.8*) uses structural composites (**Chapter 3**) to demonstrate the effect microstructural parameters have on stress transfer efficiency. However, it is clear from *Figure 4.8* that ionic conduction through structural composites is not possible (along the path of the red arrow). Employing IPC microstructure allows ionic conduction where the effect of microstructural parameters on stress transfer efficiency remains true. Reinforcement with IPC microstructure of high surface-area-to-volume ratio, uniform sample thickness and channel size distribution and high average sample thickness and channel size maximises the area fraction of reinforcement intercepted by the crack (f), for a theoretical crack of random orientation and opening (u) (*Equation 4.1*). Therefore, optimised reinforcements maximise the stress transfer efficiency (ΔG_{el}) and toughness of resultant composites (*Equation 4.1*).

The other microstructural parameter to consider is solid volume fraction. The ceramic matrix requires a high solid volume fraction in order to maintain compressive

strength (**Chapter 1 Section 1.9**).[5, 6] Though superior compared to particles, the bijel synthesis is challenging in its limited range of solid volume fraction and control of sample thickness and channel size distributions.[7] The following paragraphs discuss the methods for analysing template microstructure and its relation to the final composite.

In ceramic preform formation, the template defines the ceramic matrix and reinforcement microstructure. For a sacrificial templating procedure, the solid volume of the template defines the microstructure of the pore volume of the ceramic preform, demonstrated by *Figure 4.9 (a)* and *(b)*, respectively. On reinforcement infiltration, the pore volume defines the microstructure of the reinforcement, demonstrated by *Figure 4.9 (b)* and *(c)*.

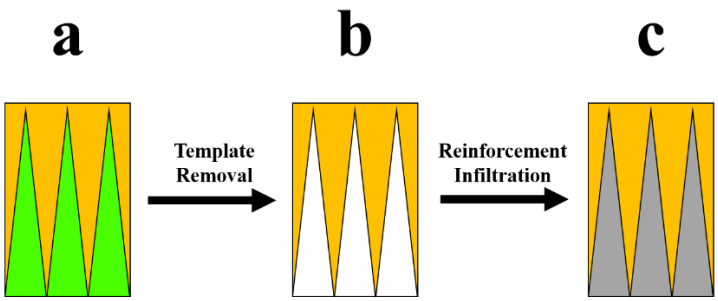

Figure 4.9 Schematic representation of microstructural phase transitions in ceramic matrix (yellow), template (green), porosity (white) and reinforcement (grey).

Analysing the template predicts the microstructural parameters of the final composite and therefore differentiates the optimum template for stress transfer efficiency. Evaluative software can obtain quantitative results for the microstructural parameters of solid volume fraction, surface-area-to-volume ratio, channel size distribution and sample thickness distribution, as described in the characterisation section (**Section 4.4**). These methods analyse the microstructural parameters of the bijel template 3D-model, shown in the previous section (*Figure 4.6*). The solid volume

fraction of the solidified-bijel template is 40.0 %. Considering an ideal preform formation, the solid volume fraction of the ceramic matrix will be 60.0 %. However, to maintain compressive strength and prevent a significant increase in material susceptibility to fracture, the solid volume fraction of the preform will need to be higher.[5]

The bijel internal surface-area-to-volume ratio for a unit of volume is 0.11 μm^{-1}. This will need to be compared with other template architectures to determine the optimal and most efficient use of reinforcement volume for stress transfer efficiency. For an ideal preform formation procedure the surface area of the template and preform should be equal, though changes in volume will affect the value.

Figure 4.10 reports the sample thickness distribution of the bijel template. The average sample thickness has a diameter of 24.0 μm and standard deviation of 7.95 μm. Considering an ideal preform formation and reinforcement infiltration, the reported sample thickness distribution, average sample thickness and standard deviation of the template become those of the preform porosity and then the reinforcement.

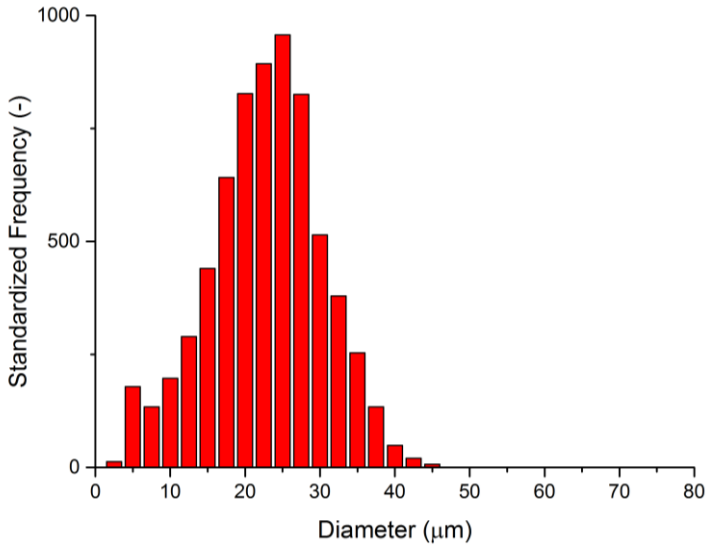

Figure 4.10 Frequency distribution plot of sample thickness for bijel template architecture.

Figure 4.11 reports the channel size distribution of the bijel template. The average channel size has a diameter of 29.6 μm and the standard deviation is 13.64 μm. Considering an ideal preform formation and reinforcement infiltration, the channel size distribution, average channel size and standard deviation of the template become the sample thickness distribution, average sample thickness and standard deviation of the ceramic matrix.

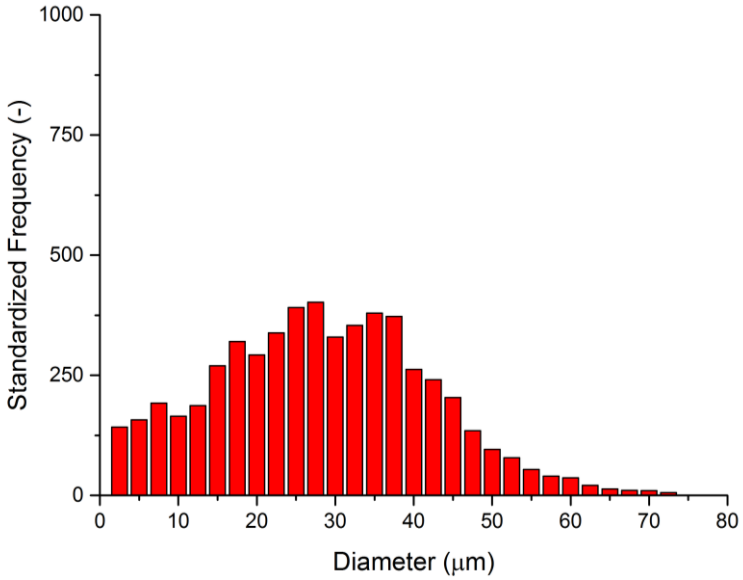

Figure 4.11 Frequency distribution plot of channel size for bijel template architecture.

The bijel template shows acceptable average sample thickness and channel sizes for further processing and crack bridging reinforcement. However, the solid volume fraction of the template is too high, which may result in ceramic preforms with low solid volume fraction and therefore mechanical weakening. Additionally, the standard deviations of sample thickness distribution and channel size distribution result in the presence of bottlenecks that may affect ceramic preform formation, reinforcement infiltration, ionic conductivity, mechanical properties or the isotropic nature of reinforcement. Nevertheless, the bijel template architecture and synthesis method remain of interest for ceramic preform formation and have some scope for improvement.

4.5.3. Bijel Gyroidal Architecture

The distribution of interfacial curvatures is a valuable means of characterising complex 3D architectures such as the bijel. At any point on the surface of a 3D-

architecture, two principal radii of curvature, R_1 & R_2, and two principal curvatures, κ_1 & κ_2 ($\kappa_i = \pm 1/R_i$), can be defined. The mean ($H = 1/2(\kappa_1 + \kappa_2)$) and Gaussian ($K = \kappa_1\kappa_2$) curvatures define the extrinsic and intrinsic measure of the two principal curvatures.

Reeves *et al*. studied the morphological characterisation of the liquid-bijel system.[7] They showed that bijels have a negative average Gaussian curvature ($K < 0$) and a zero average mean curvature ($H = 0$) suggesting their bicontinuous nature in three-dimensions. For the principal curvatures to satisfy both $K < 0$ and $H = 0$, they must be equal in magnitude and opposite in sign. The resultant surfaces have increasingly hyperbolic character with increasing magnitude of Gaussian curvature ($K < 0$), also known as 'saddle surfaces' shown in *Figure 4.12*. Reeves *et al*. demonstrated the correlation between synthesis parameters of the bijel and increasing magnitude of Gaussian curvature.[7]

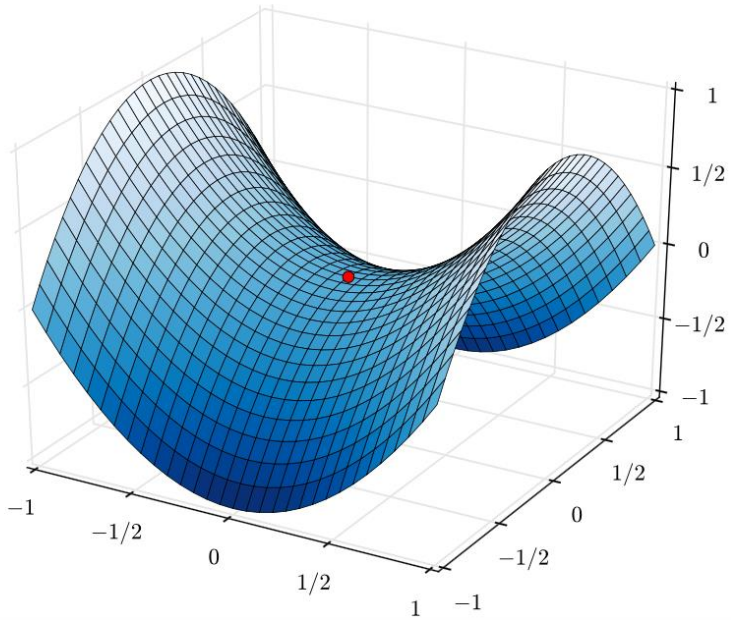

Figure 4.12 Plot demonstrating a saddle point of a saddle surface.[8]

For its similar curvature characteristics, the bijel is closely comparable to the gyroid, shown in *Figure 4.13*. The triply-periodic minimal surfaces of the gyroid are defined as having a mean curvature of zero at every point, unlike the bijel. The result is a regular repeating bicontinuous architecture with uniformly distributed variations of negative Gaussian curvature.[7]

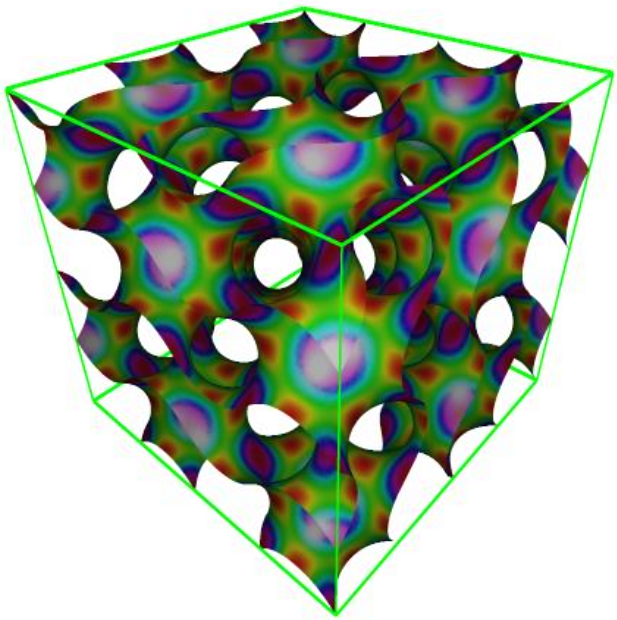

Figure 4.13 Computational image of a generic gyroid surface showing the Gaussian curvature at each point (colour).

The regularity and zero mean curvature of the gyroid makes it an interesting architecture as an IPC microstructure. The regular repeating architecture with zero mean curvature increases the uniformity of the sample thickness distribution and therefore the area of local reinforcements intercepted by a crack. A more uniform sample thickness distribution and channel size distribution also decreases the likelihood of structural bottlenecks (weak points, impeded ionic conductivity, impeded infiltration). The gyroid

structure is therefore an appealing comparative architecture for further work, as discussed in the following chapter (**Chapter 5**).

Adjusting the bijel process can make spinodal decomposition become more gyroidal in nature. Modifying the synthesis is a substantial challenge, though recent work has demonstrated the potential.[7]

4.5.4. Preform Formation via Sacrificial Templating with Bijel Template

The bijel templates prepared in **Section 4.5.1** were used to fabricate ceramic preforms via a sacrificial templating procedure, described in the experimental methods section (**Section 4.3.3**) and discussed in more detail in **Chapter 6**. *Figure 4.14* shows μCT images of the LAGP preform internal microstructure fabricated from the bijel template, according to the above mentioned synthesis.

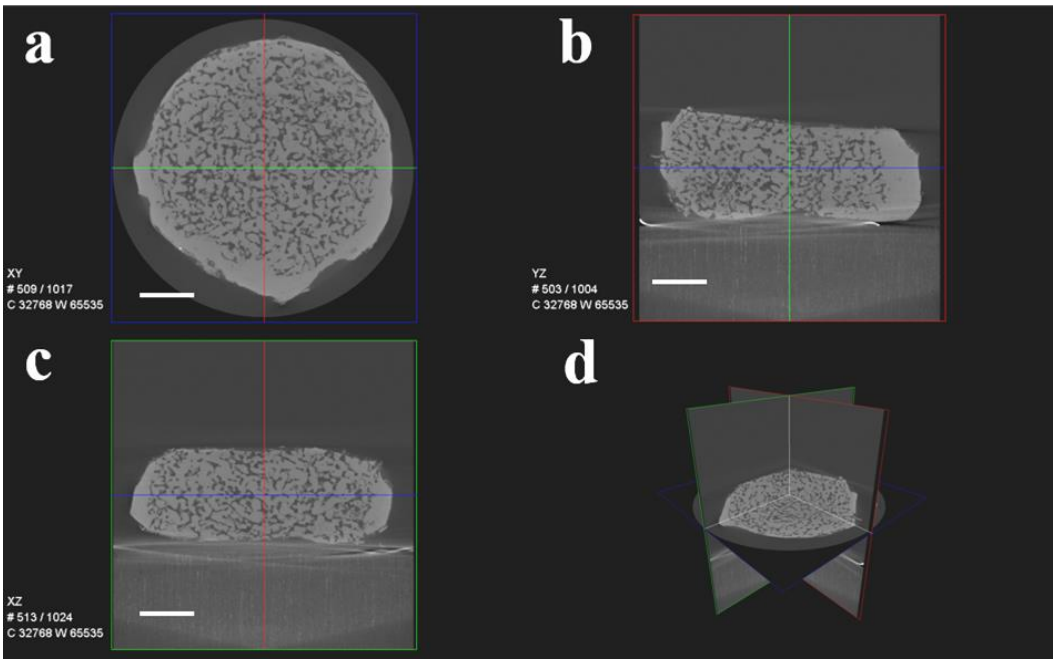

Figure 4.14 μCT images of an LAGP preform via sacrificial templating with a bijel template view from (a) xy, (b) yz, (c) xz and (d) xyz orientations with scale bar of 500 μm.

The microstructure resembles the expected bijel architecture and the LAGP preform appeared to be mechanically stable on handling. However, the microstructure does appear to have shrunk from the template (*Figure 4.6*). *Figure 4.15* shows an image of a computational 3D model of a 2250 x 2250 x 560 µm portion of the bijel preform µCT data (*Figure 4.14*). Though the majority of the preform was found to be bicontinuous, a number of artifacts were discovered in the model suggesting the susceptibility of the microstructure to fracture or a poor preform formation procedure.

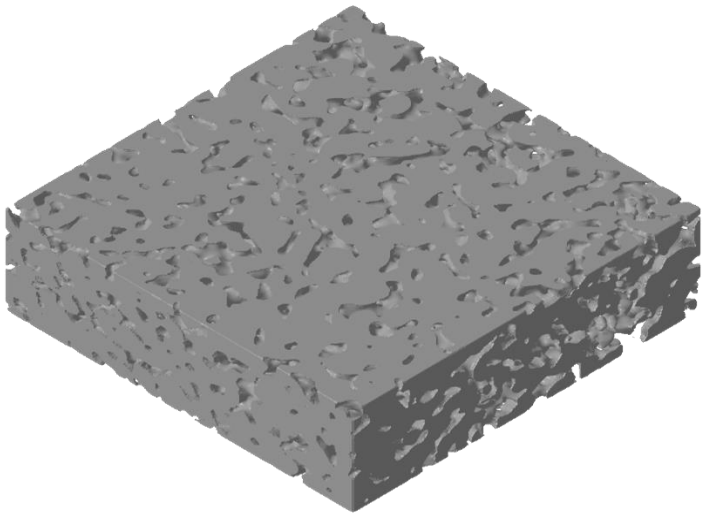

Figure 4.15 3D-rendered computational 2250 x 2250 x 560 µm model from µCT data of bijel LAGP preform via sacrificial templating.

The microstructural parameters of the bijel LAGP preform and bijel template (**Section 4.5.1**) µCT data were analysed according to the characterisation section (**Section 4.4**). In an ideal sacrificial templating procedure, where ceramic particles impregnate the channels of the template, the channel (pore) microstructure of the template should equal the sample (solid) microstructure of the preform and vice versa.

The solid volume fraction gives an indication to the quality of the preform formation procedure. Here, the bijel template and preform are 40.0 % and 72.5 %,

respectively. The preform solid volume fraction is well above the ideal 60.0 % volume fraction expected from the template, suggesting the reported preform (*Figure 4.14*) had either shrunk and/or collapsed. However, a higher solid volume fraction could be beneficial for maintaining compressive strength.

In an ideal procedure the internal surface areas of the template and resultant preform should be equal. The internal surface-area-to-volume ratio changes from 0.11 μm^{-1} for the template to 0.02 μm^{-1} for the preform. The majority of this decrease is accounted for by the increase in solid volume fraction from the template to the preform. However, when the increase in volume fraction is taken into consideration, the surface-area-to-volume ratio is slightly lower than the expected value (0.04 μm^{-1}). This suggests that shrinkage has occurred during the procedure causing the surface area to decrease relative to the volume.

The average sample thickness of the template is 24.0 µm compared to 19.0 µm for the average channel size of the preform, again suggesting shrinkage. However, the average channel size of the template is 29.6 µm compared to 50.5 µm for the average sample thickness of the preform. The large increase in thickness of the preform suggests densification of the ceramic, most likely during sintering. This would indicate previously separate regions of the template channels now collapsing and densifying to thicker regions of the ceramic preform solid. This too would account for shrinkage.

Another indicator of microstructure collapse is the standard deviation of channel size distribution and sample thickness distribution. The sample thickness standard deviation for the template is 7.89 µm and 12.25 µm for the channel size standard deviation of the preform. Such an increase in the channel size standard deviation of the preform paired with the decrease in average channel size (19.0 µm) is likely to create

major bottlenecks in the porosity for latter infiltration of reinforcement. An increase in reinforcement non-uniformity would also be detrimental to the FR-CMC, due to increasing anisotropy of reinforcement and therefore a decrease in intercepted area of local reinforcement by a crack, as discussed in **Section 4.5.2**.

The channel size standard deviation for the template is 13.64 μm and 35.65 μm for the sample thickness standard deviation of the preform. Such a large change suggests a significant collapse of the expected solid microstructure from the template. The resultant non-uniformity of the ceramic thickness will have a large effect on the mechanical and ionic conductivity properties with the presence of bottlenecks. Despite having a high solid volume fraction (72.5 %), thinner bottleneck regions will be more susceptible to fracture than the average thickness. Indeed, signs of preform fracture have already been observed in μCT 3D model by a number of sub-shells (*Figure 4.15*).

Despite clear microstructural issues with the bijel preform, the prepared samples were immersed and impregnated with polypropylene melt, as described in the experimental methods section (**Section 4.3.4**), before cooling and polishing steps. With complete filling of the preform, the polymer takes on the preform channel microstructure with parameters reported above. *Figure 4.16* shows SEM images of the LAGP preform surface after impregnation with polypropylene and surface preparation, as described above and in the characterisation section (**Section 4.4**). Heavy elements scatter electrons more strongly than lighter elements and therefore appear brighter in the SEM images. The bijel microstructure is clearly visible, with the lighter regions of the SEM images being LAGP and the darker regions being polypropylene.

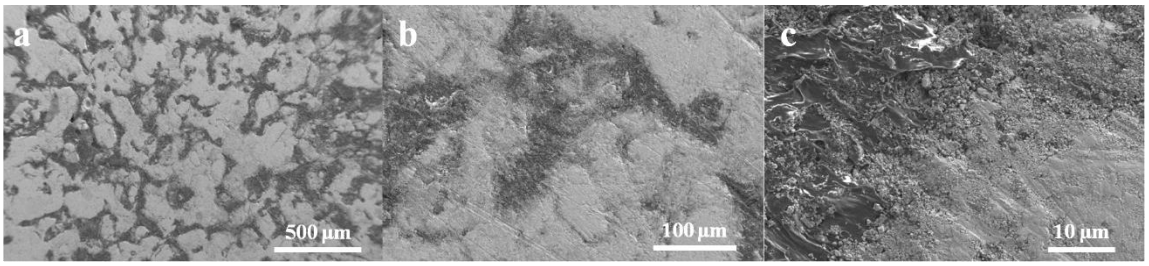

Figure 4.16 SEM surface microstructure images of polypropylene filled and polished LAGP composite via sacrificial templating with a bijel template at magnification (a) x50, (b) x250 and (c) x2000.

Figure 4.17 shows a Nyquist plot of an LAGP pellet and the LAGP bijel composite (*Figure 4.16*) derived from AC EIS, using a gold blocking electrode symmetric cell setup, prepared according to the characterisation section (**Section 4.4**). The bijel perform plot shows a depressed broad semicircle (*Figure 4.17*), which is characteristic of both bulk and grain boundary time constants merging. This often occurs when the time constants become similar and overlap at certain frequencies. To account for this, a typical equivalent circuit with two sets of parallel components (**Chapter 2 Section 2.3**) is used for the bijel composite (*Figure 4.17*), with an inductor and constant phase elements (CPE), according to **Chapter 3 Section 3.5.1**. The full component values are reported in **Appendix 3**.

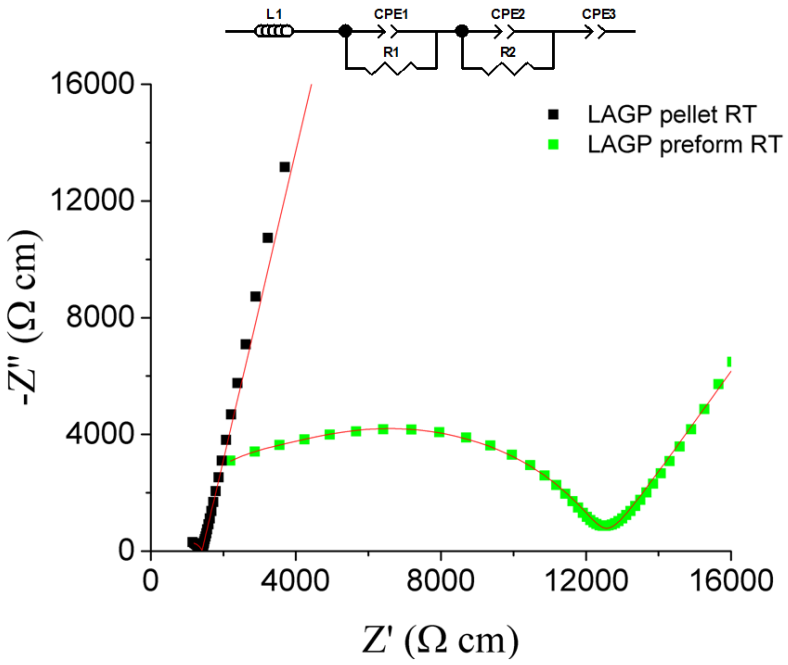

Figure 4.17 Impedance plot of an LAGP pellet and LAGP bijel composite via sacrificial templating measured at room temperature.

The total ionic conductivity of the bijel LAGP-polymer composite at room temperature is 1.56 x 10^{-5} S cm^{-1}, which is significantly lower than the LAGP pellet (2.84 x 10^{-4} S cm^{-1}). The decrease is likely due to increased grain boundary impedance being caused by poor sintering between grains or bottlenecks in the ceramic. Bottlenecks in the bijel microstructure have been indentified by microstructural parameter analysis (*Figure 4.15*). The microstructure may impede impregnation and compaction of LAGP particles into the bijel template, resulting in poorly sintered grains and hence low ionic conductivity. Therefore, an improved polymer template and ceramic preform microstructure is sought to increase the total ionic conductivity. This work does not report further investigation into sacrificial templating by bijel templates. However, the material is an interesting route for further work and has scope for improvement.

4.6. Conclusion

An oxide ceramic electrolyte-polymer composite with interpenetrating microstructure has been prepared. Polymer bijel templates from liquid bijel systems were prepared for sacrificial templating of ceramic. TGA analysis of the templates showed improved chemical compatibility with the ceramic electrolyte and appropriate combustion at elevated temperatures for removal as template. Microstructural parameters have been discussed with desirable parameters identified. The bijel templates were then analysed with μCT and a computational technique developed to analyse the microstructural parameters. The template was found to be non-ideal with high solid volume fraction and non-uniform thickness distributions. Nevertheless, ceramic preform formation via sacrificial templating from the bijel template was carried out.

An adapted sacrificial templating procedure has been developed to produce ceramic electrolyte preforms with reproduction of the original template microstructure. The microstructural parameters of the preform were analysed and found to be non-ideal with high non-uniform thickness distributions showing significant signs of microstructure collapse and shrinkage. A preliminary ceramic-polymer composite was prepared and ionic conductivity analysis carried out, but showed to be significantly lower than an equivalent pellet due to increased grain boundary contributions.

The reported composite with bijel microstructure has demonstrated the ability to fabricate ceramic matrix composites with interpenetrating microstructure. However, the prepared composite was shown to have non-desirable properties. Therefore, another route for fabricating a fibre-reinforced ceramic matrix composite is required. An improved composite should possess optimised stress transfer efficiency and tensile

strength with excellent retention of the inherent ionic conductivity and compressive strength of the ceramic electrolyte.

4.7. References

[1] Herzig, E. M., White, K. A., Schofield, A. B., Poon, W. C. K. & Clegg, P. S. Bicontinuous emulsions stabilized solely by colloidal particles. *Nat. Mater.* **6**, 966-971 (2007).

[2] Lee, M. N. & Mohraz, A. Bicontinuous macroporous materials from bijel templates. *Adv. Mater. (Weinheim, Ger.)* **22**, 4836-4841 (2010).

[3] Lee, M. N., Thijssen, J. H. J., Witt, J. A., Clegg, P. S. & Mohraz, A. Making a robust interfacial scaffold: bijel rheology and its link to processability. *Adv. Funct. Mater.* **23**, 417-423 (2013).

[4] Zhang, M. *et al*. Preparation and electrochemical properties of Li1+xAlxGe2-x(PO4)3 synthesized by a sol-gel method. *J. Electrochem. Soc.* **159**, A1114-A1119 (2012).

[5] Studart, A. R., Gonzenbach, U. T., Tervoort, E. & Gauckler, L. J. Processing routes to macroporous ceramics: a review. *J. Am. Ceram. Soc.* **89**, 1771-1789 (2006).

[6] Hammel, E. C., Ighodaro, O. L. -R. & Okoli, O. I. Processing and properties of advanced porous ceramics: An application based review. *Ceram. Int.* **40**, 15351-15370 (2014).

[7] Reeves, M., Stratford, K. & Thijssen, J. H. J. Quantitative morphological characterization of bicontinuous pickering emulsions via interfacial curvatures. *Soft Matter* **12**, 4082-4092 (2016).

[8] "A saddle point on the graph of z=x2-y2 (in red)" by Nicoguaro is licensed under CC BY 3.0 and no changes were made. at https://en.wikipedia.org/wiki/Saddle_point#/media/File:Saddle_point.svg.

Chapter 5: Computer-Aided Design & Template Fabrication

5.1. Aim

The introduction of an interpenetrating microstructure to oxide ceramic electrolyte has been demonstrated, but the resultant bijel microstructure and composite were shown to have inadequate properties. The main aim of this chapter is to fabricate templates with specific architectures and microstructural parameters. Sacrificial templating and replication procedures have been selected as routes for preform formation from templates. Improving on the bijel synthesis and microstructure requires the ability to design and fabricate templates with exact microstructures. Furthermore, specific properties of the templates must be considered to meet the requirements of the selected preform formation procedures.

5.2. Introduction

The previous chapter confirmed the ability of fabricating templates with interpenetrating microstructure (porosity) and therefore the ability to introduce the microstructure in oxide ceramic electrolyte. The composite with bijel microstructure is inadequate for maintaining the ionic conductivity, due to non-uniform thickness distributions. To maintain the properties of the ceramic electrolyte and optimise the mechanical enhancement of a fibre-reinforced (FR) ceramic matrix composite (CMC) requires a designed 3D-interpenetrating composite (IPC) microstructure. The realisation of such a composite requires a precise and versatile procedure.

This chapter considers templates for ceramic preform fabrication procedures based on replication and sacrificial templating. Both procedures aim to introduce porosity into an oxide ceramic electrolyte matrix for reinforcement. Engineering the porosity and therefore architecture of the ceramic preform and eventual FR-CMC, requires a 3D-template design and fabrication procedure. Maintaining the inherent compressive strength of oxide ceramic electrolyte requires a high solid volume fraction of ceramic with minimal amount of reinforcement. Therefore, optimising the effectiveness of minimal reinforcement requires control of the ceramic microstructure and should maximise the release rate of elastic strain energy (stress transfer efficiency), ΔG_{el}, as described in **Chapter 1 Section 1.8**.

This chapter reports template fabrication by stereolithography. The designed template architectures and microstructures, presented in this chapter, depend on the intended preform formation procedure. The precise preparation of different template architectures by stereolithography employs a variety of computer-aided design (CAD) methods, to demonstrate the versatility of the technique. The following discusses the ability to control microstructural parameters of the template, such as solid volume fraction, surface-area-to-volume ratio and average thickness, and a method for analysing the CAD architectures. Controlling the properties of designed templates enables the fabrication of a series of architectures with normalised parameters to compare properties and the investigation of an optimised FR-CMC. Finally, this chapter reports an optimised procedure for increasing the speed of printing. The increased throughput of templates is essential to obtain a high number of samples with which to experiment.

5.3. Experimental Methods

5.3.1. Architecture Generation

The gyroid architecture was first prepared using Matlab R2014b (8.4.0.150421) to generate the gyroid surface with the input parameters reported in **Appendix 4**. The surface was then exported as a .obj file that was imported into Netfabb Professional (7.4.0). Using the repair function, triangle faces were added to the open faces of the surface model creating a water-tight solid model, defining the printable volume. The diamond architecture was prepared using OpenSCAD (2015.03-1) to generate the structure with a shape radius of 0.33. The cubic architecture was prepared using Netfabb Professional (7.4.0) to generate and arrange beams with the desired properties. Further adjustments and repairs to the architectures were carried out in Netfabb Professional (7.4.0).

5.3.2. Bijel Architecture Modification

The original bijel 3D-rendered model was first computationally sliced into a stack of 2D image files that represent the 3D-microstructure, using Netfabb Professional (7.4.0). The image stacks were then imported to Avizo (9.1.1) and arranged as a 3D model. The auto-skeletonisation operation generated the medial axis of the model. The thickness of the line representing the medial axis was adjusted to the required solid volume fraction. The medial axis model was then converted to an .stl file. Trimming of the model was performed in Netfabb Professional (7.4.0).

5.3.3. Synthesis of 2-Photon Stereolithography

DeScribe (2.3.4) was used to convert .stl files of different print block architecture 3D-models to a print ready .gwl file format. The .gwl files were then imported to Nanowrite (1.8.3) and printed using a Nanoscribe Photonics Professional GT and a drop of IP-S or IP-Dip resin (Nanoscribe GmbH) placed on an indium tin oxide coated glass slide substrate (Nanoscribe GmbH). The templates were washed with propylene glycol monomethyl ether acetate (>99.5 %, Sigma-Aldrich) then isopropanol (99.5 %, Sigma-Aldrich).

5.3.4. Architectural Print Extension Generation

Netfabb Professional (7.4.0) was used to first import a prepared print block. A second print block was duplicated and aligned adjacent to the original in order to maintain repeating architectural continuity between the two. A cutting operation was then used on the second print block 10 µm from the surface of the adjacent block. The bulk of the cut block was then removed leaving behind the print extension. This process was repeated for each side of the original print block before the separate shells were merged together to generate the print block with print extensions.

5.4. Characterisation

The 3D-interconnectivity of computational 3D-models was investigated in Netfabb Professional (7.4.0). An inverse phase model was generated using a Boolean operation before both the original model and inverse phase were analysed for number of individual (non-connecting) shells.

The microstructural parameters of different architectural models were analysed using a variety of software packages. The solid volume fraction was calculated as an automatic function in Netfabb Professional (7.4.0). The internal surface-area-to-volume ratio used the repair function of Netfabb Professional (7.4.0) to remove external faces of each model to give only the internal surfaces, before automatic calculations of surface area were given. The sample thickness distribution and channel size distribution were analysed using the auto-skeletonisation and distance mapping tools of Avizo (9.1.1).

The morphology of materials was investigated using a Carl Zeiss Merlin field emission scanning electron microscope (SEM) with a Gemini II column. Samples were mounted on adhesive copper tape applied to a stub and holder. Measurements were taken at a voltage range of 1-3 kV with a current range between 72-100 pA. Cross-sections were prepared using a scalpel. The chemical characterisation of materials was analysed by energy dispersive X-ray spectroscopy (EDS) using an Oxford Instruments X-Max^{N} silicon drift detector with 150 mm^{2} size detector attached to the Merlin microscope.

Thermogravimetric analysis (TGA) was carried out using a Netzsch STA 449 F3. Alumina crucibles under a flow of synthetic air were used during the investigation of thermal effects at room temperature to 1000 °C at 10 °C min^{-1}.

5.5. Results & Discussion

5.5.1. 3D-Interconnected Sacrificial Templates

5.5.1.1. Computational 3D Architecture Generation: Gyroid, Diamond and Cubic Lattice

The major advantage of computational architecture generation is the ability to define microstructural parameters. Computer-aided design (CAD) techniques allow for the creation of complex architectures and control of parameters. A variety of complex architectures were generated to demonstrate the capability of this approach and architecture analysis was carried out to establish the optimal architecture for a reinforced composite.

Complex architectures, such as the gyroid discovered by Schoen in 1970, are composed of surfaces defined by trigonometric implicit functions. The architecture is infinitely connected and a triply periodic minimal surface similar to those of the Schwarz P and D surfaces.[1, 2] The function below approximates the general surface of the gyroid:

$$\cos(x) \cdot \sin(y) + \cos(y) \cdot \sin(z) + \cos(z) \cdot \sin(x) = 0 \tag{5.1}$$

Figure 5.1 shows a computational model with gyroid architecture generated according to the experimental methods section (**Section 5.3.1**) that utilises *Equation 5.1* to define the surface. When solidified the surface model can be further processed and readied for printing. *Figure 5.2* shows a computational model of the reduced gyroid unit

having been solidified according to the procedure described in the experimental methods section (**Section 5.3.1**).

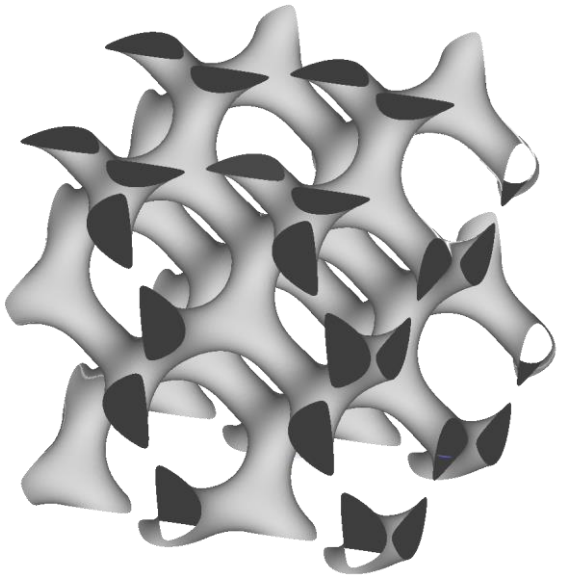

Figure 5.1 Computational image of a generated gyroid architecture.

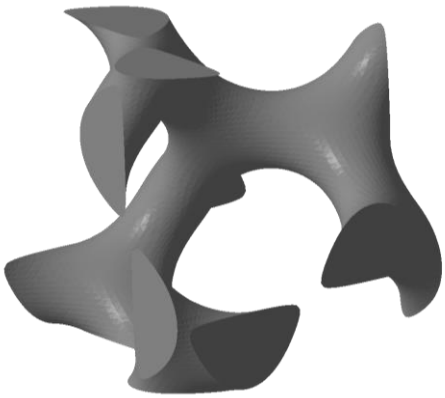

Figure 5.2 Computational image of a solidified gyroid 3D-model architecture.

Crystal structures, such as diamond cubic, are repeating arrangements of atoms that form lattice structures. The tetrahedral bonding of atoms in the diamond cubic form face-centered cubic Bravais lattice with a $Fd\bar{3}m$ space group. The bonding of the

diamond cubic crystal structure yields compressive strength and hardness to compounds. The experimental methods section (**Section 5.3.1**) describes the generation of the ball-and-stick 3D-model of the diamond cubic architecture, shown in *Figure 5.3*.

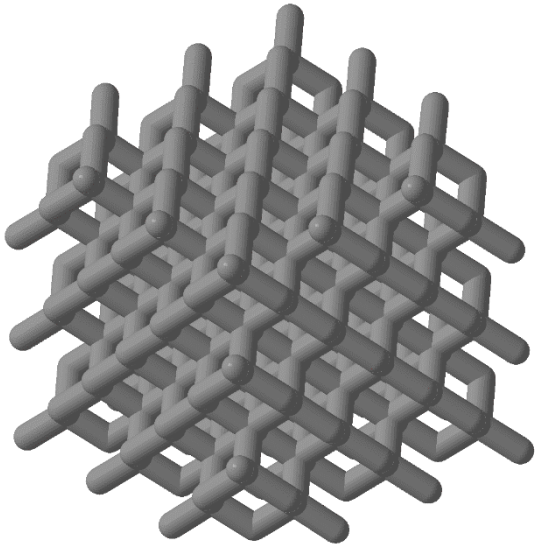

Figure 5.3 Computational image of a generated solid diamond 3D-model architecture.[3]

Complex trigonometric and crystal structure architectures require an advanced fabrication method as templates, as discussed in the experimental methods section (**Section 5.5.1.4**). Many additive manufacturing techniques (**Chapter 1 Section 1.10**) are restricted to simpler architectures, such as a cubic anisotropic lattice-like architecture. The experimental methods section (**Section 5.3.1**) describes the generation of the cubic architecture with final 3D-model shown in *Figure 5.4*.

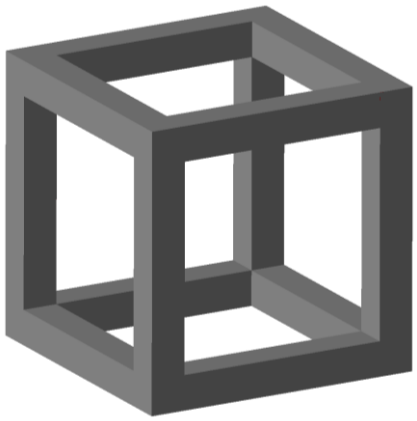

Figure 5.4 Computational image of a generated solid cubic 3D-model architecture.

Changing parameters in CAD architecture generation modifies the microstructural parameters of architectures to give the desired specifications. The solid volume fraction of the gyroid, diamond and cubic architectures are adjusted computationally by defining offset values in *Equation 5.1*, radii size of ball-and-stick models and the size of struts, respectively. These parameters are adjusted in the software packages described in the experimental methods section (**Section 5.3.1**). For instance, *Figure 5.5* demonstrates the change in volume fractions of the gyroid architecture with change of offset values during the CAD generation.

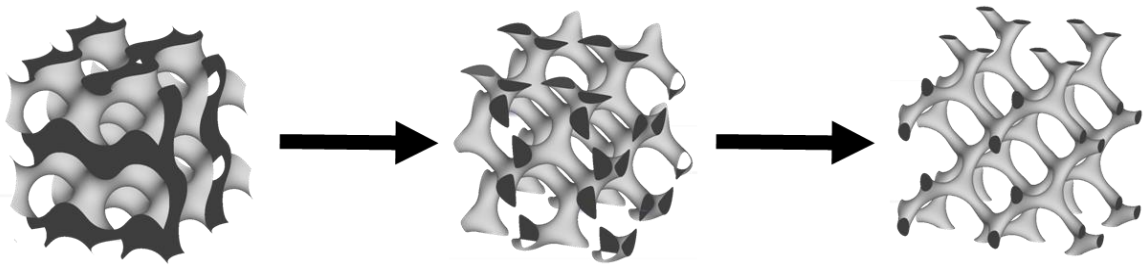

Figure 5.5 Computational images showing the solid volume fraction modification of gyroid architecture during CAD generation by changing offset values.

The sample thickness distribution and channel size distribution are also modifiable in a similar way, once the models have been solidified. Specific dimensions given to the gyroid, diamond and cubic architectures change the size and thickness, as demonstrated in *Figure 5.6*. As the unit cell size changes the sample thickness distribution and channel size distribution changes as well.

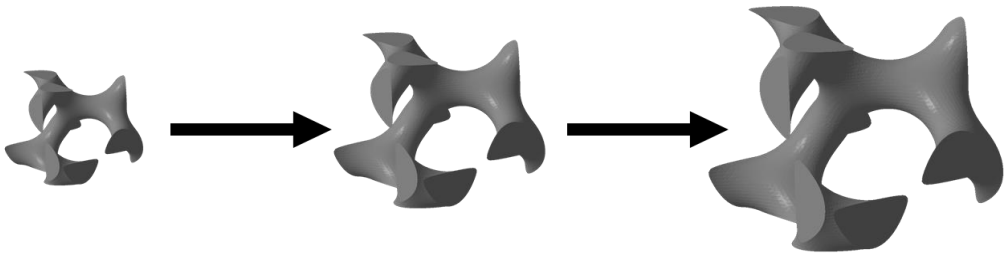

Figure 5.6 Computational images showing the size modification of gyroid architecture.

5.5.1.2. Computational 3D-Analysis and Design

To compare the mechanical properties of FR-CMC with different IPC microstructures, the microstructural parameters require normalisation. Microstructural parameter analysis, as discussed in the previous chapter (**Chapter 4 Section 4.5.2**), determines the microstructural parameters of modified templates. The CMC requires a high solid volume fraction in order to maintain the inherent compressive strength of the ceramic. For a sacrificial templating procedure, a template with low solid volume fraction is required.

The nominally low solid volume fraction of approximately 15% for architecture models and therefore templates corresponds to an 85% solid volume fraction ceramic preform matrix; however, modification and investigation of these parameters is possible for future work. *Figure 5.7* reports architectures normalised for solid volume fraction. These parameters should maintain the compressive strength of ceramic preforms.

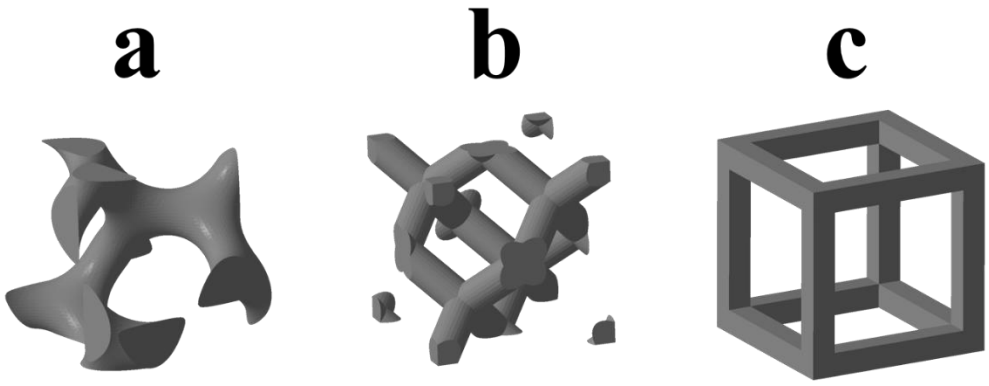

Figure 5.7 Computational images of the (a) gyroid, (b) diamond and (c) cubic unit cell 3D-models.

Table 5.1 reports the internal surface-area-to-volume ratio of the designed architectures (*Figure 5.7*) and the chemically prepared bijel template reported in the previous chapter (**Chapter 4 Section 4.5.2**). Considering an ideal preform formation and reinforcement infiltration, the internal surface-area-to-volume ratio of the template will become that of the FR-CMC reinforcement, for respective architectures. The designed architectures increase the surface-area-to-volume ratio of the expected FR-CMC reinforcement with the cubic architecture having the highest value.

Prior to size modification (*Figure 5.6*) the architectures are without defined dimension. The standard deviations of channel size and sample thickness distributions are directly proportional to the dimension of the unit. *Table 5.1* also reports the respective standard deviations including the previously reported chemically prepared bijel template (**Chapter 4 Section 4.5.2**).

Table 5.1 Surface-area-to-volume ratio and sample thickness distribution and channel size distribution standard deviations of designed and chemically prepared bijel template architectures.

Architecture	Internal Surface-Area-to-Volume Ratio for a unit of volume (μm^{-1})	Sample Thickness Distribution Standard Deviation (μm)	Channel Size Distribution Standard Deviation (μm)
Gyroid	0.14	0.65	2.24
Diamond	0.16	1.50	5.43
Cubic	0.22	4.42	6.75
Bijel	0.11	7.95	13.64

Considering an ideal preform formation and reinforcement infiltration, the sample thickness distribution and channel size distribution of the template architectures become the sample thickness distribution of the reinforcement and ceramic matrix, respectively. A lower standard deviation (increased uniformity) increases the probability of crack interception at local reinforcement with average thickness. Both are likely to increase the stress transfer efficiency. The designed architectures decrease the standard deviation of the expected reinforcement, compared to the bijel, with the gyroid architecture having the lowest value (*Table 5.1*).

Higher surface-area-to-volume ratios, for architectures with equivalent volume, increase the number of local reinforcements likely intercepted by a crack, as described in the previous chapter (**Chapter 4 Section 4.5.2**). The solid volume fractions are equivalent for designed template architectures, unlike the bijel, and therefore the cubic architecture was confirmed as having the higher ratio (*Table 5.1*).

Assigning dimensions readies the designed architectures for further template preparation. The size modification of each architectural unit, demonstrated in *Figure 5.6*, can normalise either the average sample thickness (sample thickness distribution) or

the average channel size (channel size distribution) between architectures. This work first normalised the average channel size for all designed architectures to ensure adequate ceramic preform formation. Considering an ideal preform formation and reinforcement infiltration, the average channel size of the template becomes the average sample thickness of the ceramic matrix. Future work would require normalised average sample thickness of the template for a true experimental comparison of reinforcement microstructures with equal average sample thickness. However, the average channel size is normalised at this stage to develop a reliable preform formation procedure, as discussed in **Chapter 6**. *Table 5.2* reports the assigned dimensions, average sample thickness and average channel size (approximately normalised) of the designed architectural units (*Figure 5.7*) and the chemically prepared bijel template reported in the previous chapter (**Chapter 4 Section 4.5.2**).

Table 5.2 Dimensions, average sample thickness and average channel size of designed and chemically prepared bijel architectures.

Architecture	Dimensions (x=y=z) (µm)	Average Sample Thickness (µm)	Average Channel Size (µm)
Gyroid	105.6	20.6	67.0
Diamond	121.9	20.1	66.9
Cubic	80.0	15.7	67.0
Bijel	400.0	24.0	29.6

The assigned architectural dimensions are in the micrometer range for both the chemically prepared bijel and the designed architectures. The scale of microstructural features in relation to initial crack opening (grain size ~1 µm) also influences reinforcement and crack bridging. For an initial investigation, this scale range is

appropriate for template fabrication techniques, discussed in **Section 5.5.1.4**, and a reasonable average sample thickness and channel size for later impregnation of ceramic and reinforcement infiltration. However, future work involving thin-layered composites will require a smaller scale range and possibly more advanced instruments and techniques.

The average channel size of the designed architectures (*Table 5.2*) is much larger than the bijel, reducing any possible bottlenecks to ceramic preform formation. Designing architectures and normalising microstructural parameters in this way has reduced the solid volume fraction and increased the surface-area-to-volume ratio, standard deviation and average channel size compared to the chemically prepared bijel. The designed models represent the low solid volume fraction template architectures with 3D-interconnectivity required for high solid volume fraction ceramic preforms via sacrificial templating. The tunable designs demonstrate the adaptability of the templates to a sacrificial templating procedure modified for their impregnation. This innovation, along with other experimental challenges discussed in later chapters, has led designed architectures to be the primary focus of investigation for the fabrication of fibre-reinforced ceramic matrix composites. The next section reports another feature of architectural CAD generation that utilises the bijel architecture.

5.5.1.3. Computational 3D-Modification

Despite the limitations of the chemically prepared bijel template, reported in the previous chapter (**Chapter 4 Section 4.5.1**), the architecture is still of interest due to the highly tortuous, randomly-oriented microstructure. The bijel architecture may benefit composites by crack deflection, a less important mode of reinforcement. The

propagating crack may deflect due to features in the microstructure.[4] Regular repeating microstructures, such as those reported in the previous section (**Section 5.5.1.2**), are likely not to deflect a propagating crack as well as the tortuous bijel. However, in its current state, the chemically prepared bijel is not as desirable a template candidate as designed architectures. As such, employment of the bijel architecture requires a procedure for modifying its microstructural features.

Modifying the volume fraction of binary liquids that form a bijel can manipulate the solid volume fraction of templates, as discussed in the previous chapter (**Chapter 4 Section 4.5.3**). However, the range of volume fractions is limited for spinodal decomposition and therefore the solid volume fraction of the template is limited.[5] Varying the size of the interfacially jammed colloidal particles can also modify the mean and Gaussian curvature distributions of the bijel. However, the required parameters for successful spinodal decomposition and therefore chemical bijel preparation limit the extent of template modification; employing CAD overcomes this issue.

The 3D-rendered model of a bijel template analysed by μCT, reported in the previous chapter (**Chapter 4 Section 4.5.1**), can be computationally modified. The sample thickness distribution indicates local regions of the bijel with small diametral thickness compared to the average thickness of the architecture. Applying a standard uniform re-sizing or 'shrinkage' operation to the architecture will result in a loss of thinner regions, compromising the integrity of the architecture and maintaining the wide distribution of sample thickness, demonstrated by *Figure 5.8*. The red circle (*Figure 5.8*) highlights a region where sample thickness tapering has resulted in two disconnected solid pieces that were previously connected.

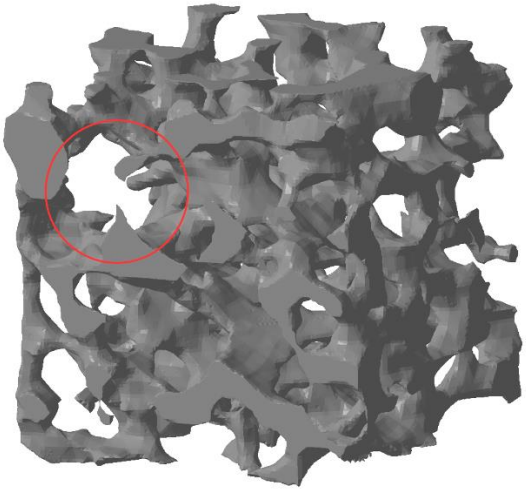

Figure 5.8 Computational image of compromised bijel template architecture on uniform shrinkage.

Applying shrinkage operations to the architecture without loss of integrity requires a more advanced technique. *Figure 5.9* shows the medial axis of a portion of the original bijel 3D-model generated in analysis software, as described in the experimental methods section (**Section 5.3.2**).

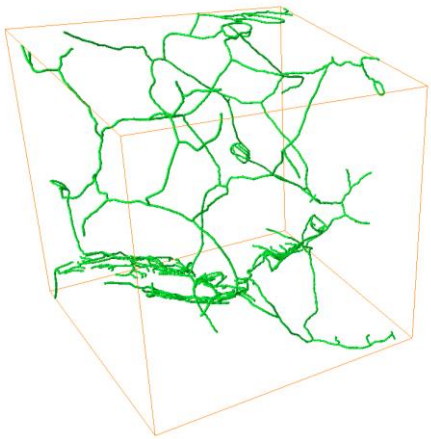

Figure 5.9 Computational image of the medial axis of a bijel 3D-model architecture.

The computational addition of uniform volume to the medial axis is a process described in the experimental methods section (**Section 5.3.2**). *Figure 5.10* shows the

capability of defining the volume fraction, whilst maintaining the integrity of the bijel medial axis. *Figure 5.11* reports the bijel architecture with a solid volume fraction of 15 %, similarly to the previously designed gyroid, diamond and cubic architectures (**Section 5.5.1.1**).

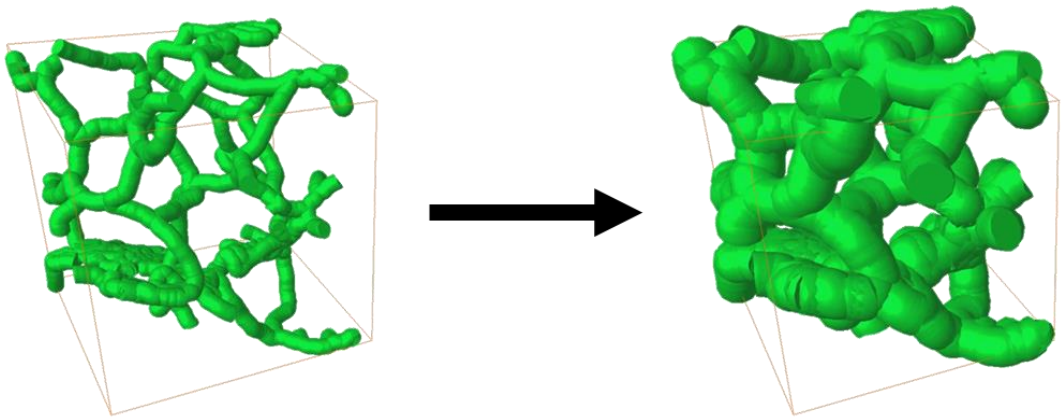

Figure 5.10 Computational images showing uniform volume growth around the medial axis of bijel template architecture.

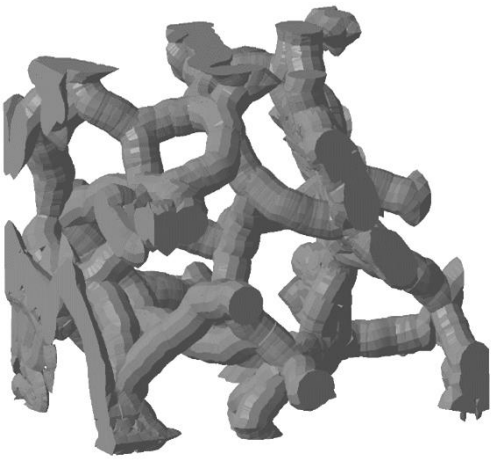

Figure 5.11 Computational image of a bijel template 3D-model architecture with modified solid volume fraction.

Table 5.3 reports the full list of microstructural parameters for architectures including the modified bijel architecture (*Figure 5.11*). The modified bijel has improved on a number of microstructural parameters compared to the chemically prepared bijel.

Firstly, the solid volume fraction is significantly less, in line with the other designed architectures, at approximately 15 %. This is a major advantage over the chemically prepared bijel considering the required solid volume fraction of ceramic preform after formation. Secondly, the average channel size is significantly larger, corresponding to the shrinkage operation and in line with the other designed architectures, at approximately 70 μm. This is beneficial for filling of the templates compared to the much smaller average channel size of the chemically prepared bijel (29.6 μm). However, the initial non-uniform shrinkage operation to generate the medial axis for the modified bijel has significantly increased the standard deviation of the channel size distribution. This may create bottlenecks in the ceramic preform, but the large increase of the average channel size likely prevents this from becoming an issue. Thirdly, the average sample thickness is approximately the same, but the standard deviation of the sample thickness distribution decreases. The uniform volume growth around the medial axis accounts for the smaller standard deviation, likely improving later infiltration and local area crack interceptions of the reinforcement. Maintaining the integrity of the sample architecture (*Figure 5.8* vs. *Figure 5.11*) also accounts for the similar average sample thickness. Finally, the surface-area-to-volume ratio of the modified bijel template architecture has increased against the chemical bijel, despite a large decrease in solid volume fraction. This indicates the modified bijel architecture would have significantly improved theoretical number of local reinforcements intercepted by a crack, compared to the chemical bijel architecture. Improving the bijel architecture in this way makes it a suitable candidate for further investigation.

Table 5.3 Microstructural parameters of designed and chemically prepared bijel template architectures.

Architecture	Dimensions (x=y=z) (μm)	Solid Volume Fraction (%)	Internal Surface-Area-to-Volume Ratio for a unit of volume (μm^{-1})
Gyroid	105.6	15.6	0.14
Diamond	121.9	15.4	0.16
Cubic	80.0	15.6	0.22
Chemical Bijel	400.0	39.9	0.11
Modified Bijel	240.0	15.6	0.14

Architecture	Sample Thickness Distribution Standard Deviation (μm)	Channel Size Distribution Standard Deviation (μm)	Average Sample Thickness (μm)	Average Channel Size (μm)
Gyroid	0.65	2.24	20.6	67.0
Diamond	1.50	5.43	20.1	66.9
Cubic	4.42	6.75	15.7	67.0
Chemical Bijel	7.95	13.64	24.0	29.6
Modified Bijel	4.20	23.07	23.4	69.9

As discussed and predicted in the previous chapter (**Chapter 4 Section 4.5.3**), the gyroid architecture's regularity and zero mean curvature give it the lowest standard deviation (most uniform) for sample thickness distribution and channel size distribution. With the normalisation of solid volume fraction and average channel size, the gyroid is the primary candidate for template architecture. However, the surface-area-to-volume ratio is lower than the diamond and cubic architectures also making them candidates for further investigation. Having improved on the chemically prepared architecture, the

modified bijel is also of interest for further study as a means of investigating the increased effect of tortuosity on stress transfer efficiency. Having prepared different architectures and assessed microstructural parameters, the fabrication of such designs as templates is reported.

5.5.1.4. 2-Photon Stereolithography Synthesis

Rapid prototyping is a group of techniques tasked at fabricating physical parts of scale models. They utilise CAD to create computational 3D-models, such as the design work reported in this chapter, to define physical parts. The typical processes for prototyping are additive manufacturing or '3D printing' that includes extrusion deposition, granular material binding, laminating, powder fed directed energy deposition, metal wire processes, continuous liquid interface production and photo-polymerisation, as discussed in **Chapter 1 Section 1.10**. Of these, photo-polymerisation, the process of polymerising photosensitive monomer to polymer with light, has the highest resolution of any rapid prototyping technique. Stereolithography is the technology that utilises photo-polymerisation and prints on a layer-by-layer fashion. The experimental methods section (**Section 5.3.3**) describes the 2-photon stereolithography technique used in this work that achieves the required resolution.

This chapter uses 2-photon stereolithography to fabricate physical parts with the architectures reported in previous sections. The technique is highly suited to sacrificial templating and replication procedures due to the precise definition and fabrication of templates. Variations of ceramic feature sizes and any future investigation into thin layered reinforced composites will require the high resolution of 2-photon stereolithography. Highly cross-linked polymers compose the printed parts and become

templates for ceramic electrolyte preform formation. The optical image shown in *Figure 5.12* shows the laser polymerisation of UV-initiated monomer to polymer under optical microscopy.

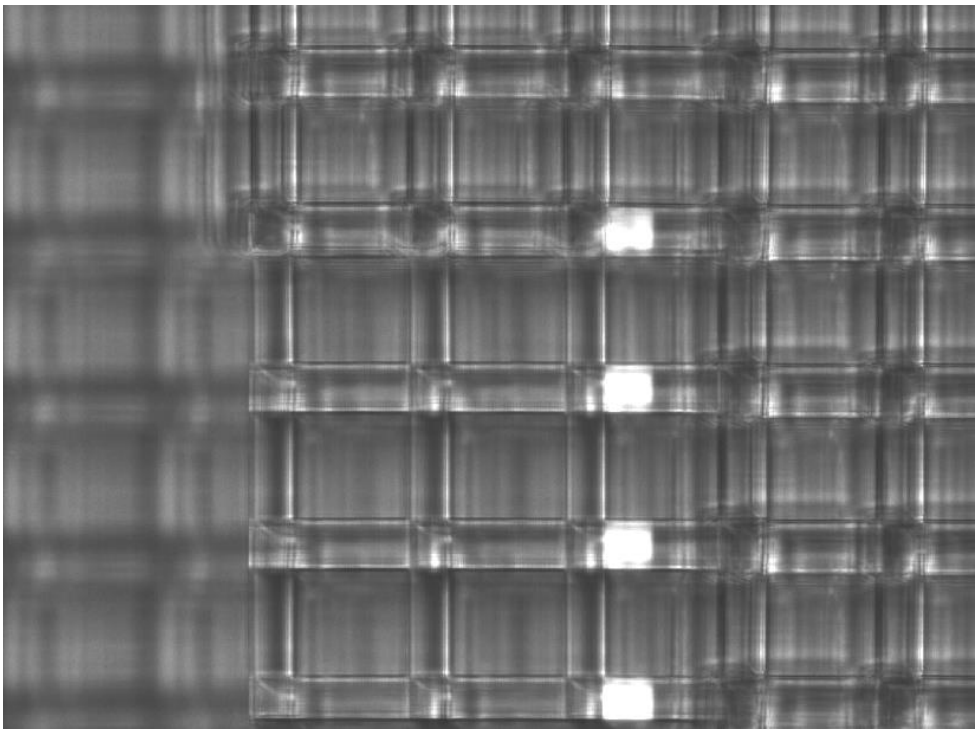

Figure 5.12 Optical image of the stereolithography laser printing in resin.

The designed template architectures (*Table 5.3*) require preparation for printing as usable template parts. Repeat template units of the gyroid, diamond and cubic architectures create 'print blocks' that maximise the available print field of the instrument, as described below. The modified bijel architecture, reported in *Figure 5.11*, is a portion of the original chemically prepared bijel template 3D-model, reported in the previous chapter (**Chapter 4 Section 4.5.1**). The portion selected for modification maximises the print block dimensions and has normalised average channel size along with the other designed architectures (*Table 5.3*).

Repeating and connecting print blocks by the instrument creates a macroscopic sized part with microscopic features. *Table 5.4* details the size of units, the number of units per print block and the number of print blocks per part for the different templates. *Figure 5.13* demonstrates the unit, print block and full part of the gyroid architecture and *Figure 5.14* shows each computed print block, as outlined in *Table 5.4*. Finally, *Figure 5.15* reports a series of SEM images showing the features of the final printed templates with different architectures.

Table 5.4 Print specifications of the designed template architectures.

Architecture	Unit Dimension (x=y=z) (µm)	Units Per Print Block (x, y, z)
Gyroid	105.6	2 x 2 x 2
Diamond	121.9	2 x 2 x 2
Cubic	80.0	3 x 3 x 3
Modified Bijel	240.0	1 x 1 x 1

Architecture	Print Block Dimension (x=y=z) (µm)	Print Blocks Per Part (x, y, z)	Part Dimension (x, y, z) (µm)
Gyroid	211.1	12 x 6 x 6	2534 x 1267 x 1267
Diamond	243.8	10 x 5 x 5	2458 x 1239 x 1239
Cubic	240	10 x 5 x 5	2400 x 1200 x 1200
Modified Bijel	240	10 x 5 x 5	2400 x 1200 x 1200

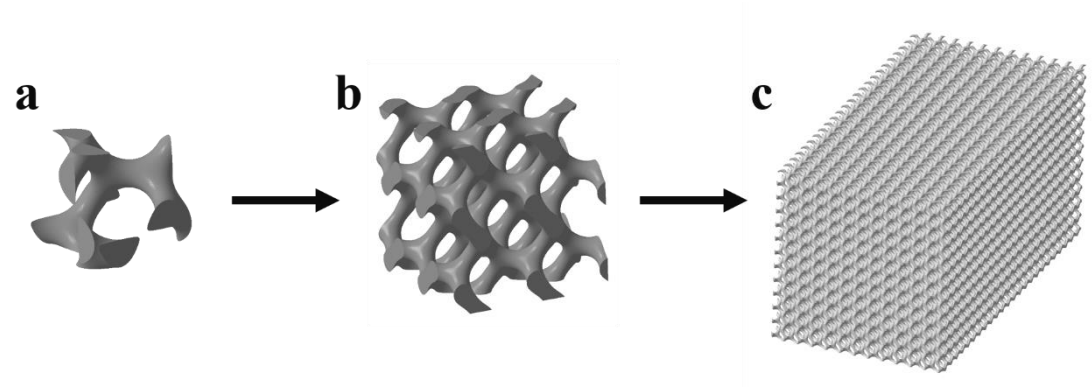

Figure 5.13 Computational images showing the development of the (a) gyroid unit into (b) a print block and (c) the final printed part.

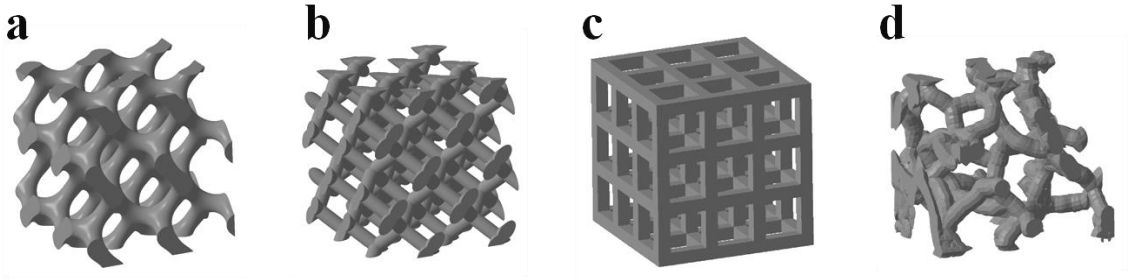

Figure 5.14 Computational images of the print blocks of the designed (a) gyroid, (b) diamond, (c) cubic and (d) modified bijel template architectures.

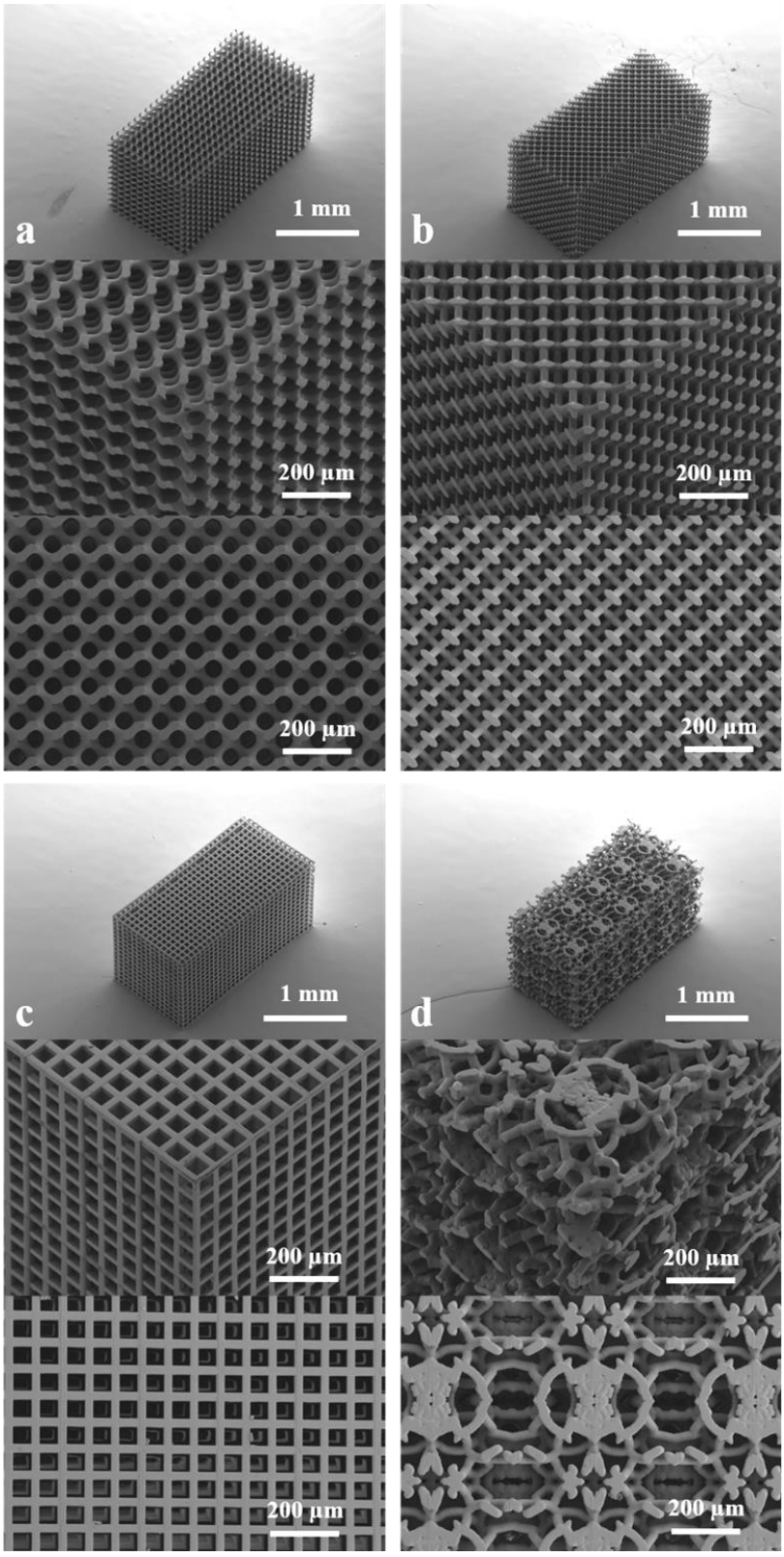

Figure 5.15 SEM images showing the printed template architectures of the (a) gyroid, (b) diamond, (c) cubic and (d) modified bijel viewed with magnification from (top to bottom) corner x25, corner x100 and top x100.

The templates reported here are composed of highly cross-linked polymer formed from photosensitive monomer after photopolymerisation. The monomer mixture or 'resin', as described in the experimental methods section (**Section 5.3.3**), is a commercial product called IP-S (Nanoscribe GmbH) containing 4-hydroxybutanoic acid lactone and 4,4'-bis(diethylamino)benzophenone, the latter being a photoinitiator. Another resin is IP-Dip (Nanoscribe GmbH), an alternative commercial monomer to IP-S. The printing process operates in the same way with both resins, where IP-S is best suited to larger 3D-parts like the templates reported. On the other hand, IP-Dip is best suited for high-resolution parts, but can be used for templates of this size also. IP-Dip contains the acrylic monomer pentaerythritol thiacrylate and 7-diethylamino-3-thenoylcoumarin. *Figure 5.16* reports the TGA data analysing the thermal stability of the printed template polymers of IP-S and IP-Dip.

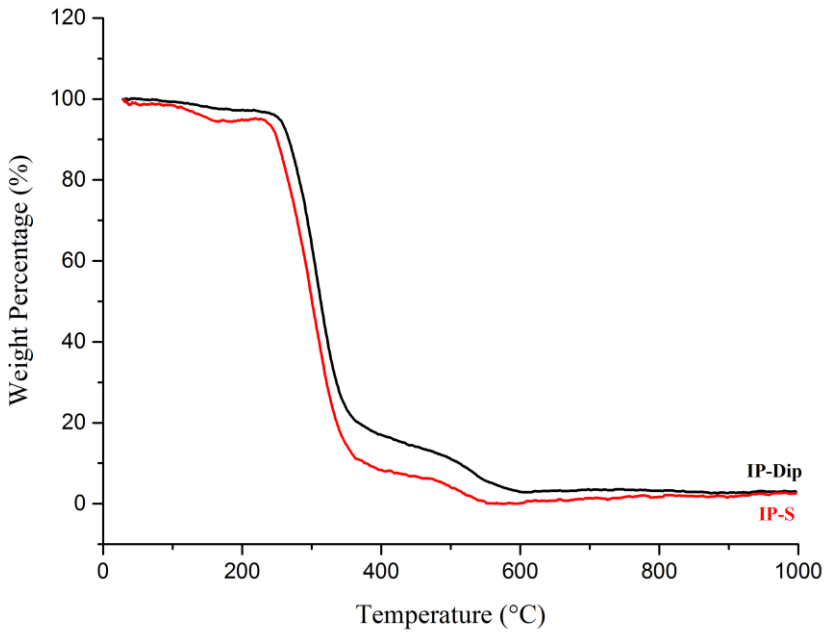

Figure 5.16 TGA curve of polymerised IP-S and IP-Dip resins in air.

The TGA data (*Figure 5.16*) suggests both resins are suitable as polymer templates. The materials remain stable at lower temperatures up to 250 °C and combust completely at 550 °C in air. This should allow the formation of a ceramic phase and template removal on sintering in air. Therefore, the printed templates are suitable for further processing in an adapted 3D-interconnected sacrificial templating procedure, as discussed in the following chapter. The following section investigates the fabrication of templates for an adapted replication procedure.

5.5.2. Hierarchical Template Microstructure for Replication

The second type of template is that designed for replication, described in **Chapter 1 Section 1.9**. This section reports printed templates similar to those reported in the previous section, but with modified internal template microstructure. The two major challenges with replication are fabricating high solid volume fraction ceramic preforms and maintaining the architectural integrity of the preform from the template. The typical replication procedure fabricates ceramic preforms from thin-film precursor coatings on the template surface. To ensure architectural integrity without preform collapse, the templates typically have low average sample thickness. This can result in a ceramic preform with low solid volume fraction that leads to ceramic weakening. Therefore, this work develops a novel type of template to address these challenges.

Sol-gel synthesis methods, typically used in replication procedures, operate by heating or drying a metal alkoxide solution to form a gel-like diphasic system of liquid and solid. The Pechini sol-gel synthesis for oxide ceramic electrolyte lithium aluminium germanium phosphate, reported in **Chapter 3 Section 3.3.1**, is an example of this system. The gelation of the precursor solution forms a film that can deposit onto a

substrate, shown in *Figure 5.17*. A dried gel layer forms a xerogel film that densifies on the surface of the substrate by heating. The xerogel synthetic route is of particular interest to replication with the potential formation of dense films on template surfaces. Other routes utilise wet gels to form a dense ceramic monolith or aerogel or sol to form uniform particles or ceramic fibres. These synthetic routes are incompatible with 3D-porous template replication and are therefore not considered.

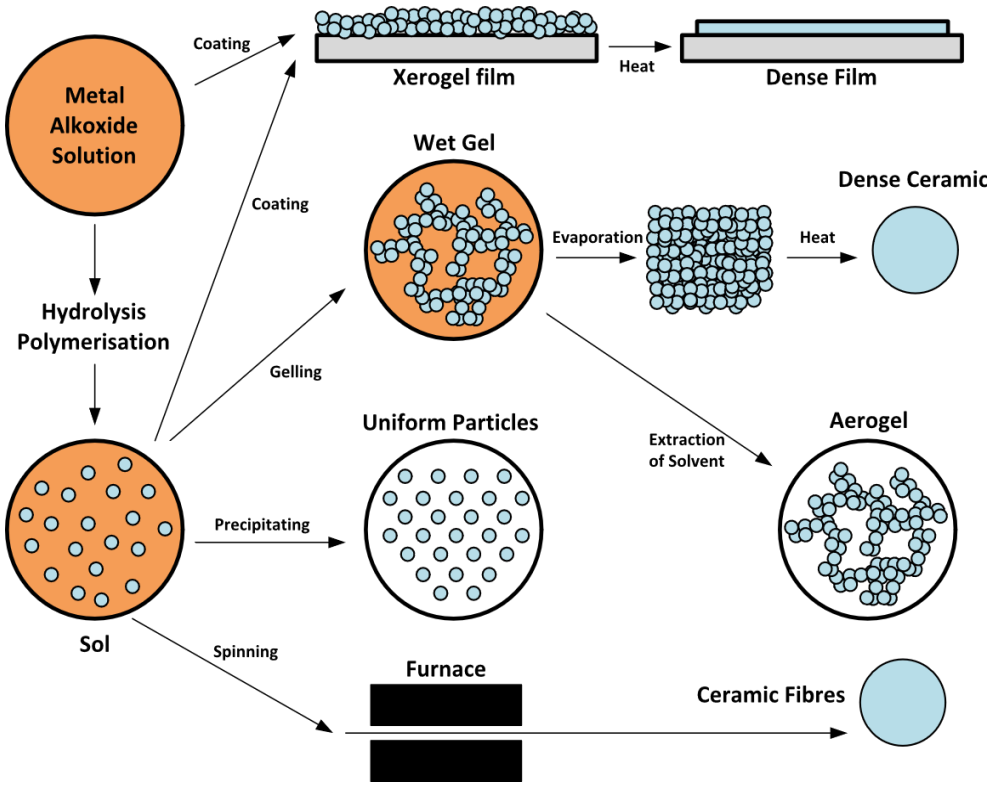

Figure 5.17 Schematic representation of the different process routes for sol-gel syntheses.[6]

Figure 5.18 illustrates the formation of xerogel films on a 3D-template surface, such as those reported in the previous section (**Section 5.5.1.4**), during the replication procedure. Fabrication of a ceramic electrolyte preform replica requires xerogel densification by heating and template removal by combustion, before sintering for grain connectivity.

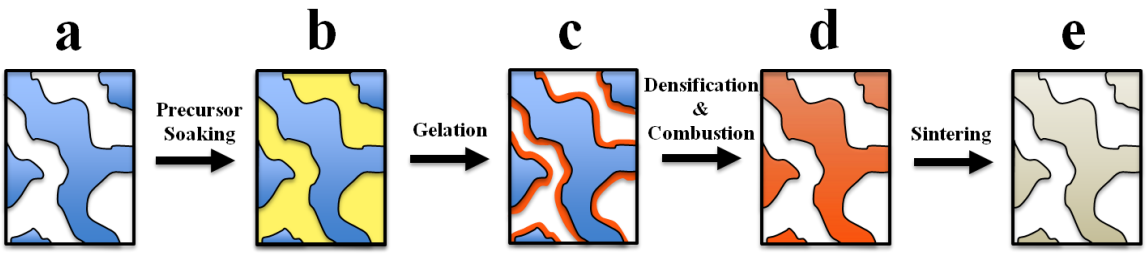

Figure 5.18 Schematic representation of the replication of a 3D-template to ceramic with stages: (a) template (blue), (b) template precursor (yellow) soaking, (c) template precursor gel coating (orange), (d) ceramic preform and (e) sintered ceramic preform (cream).

A template with small average sample thickness allows for accurate consolidation of the original template microstructure by the densifying xerogel coating, illustrated by *Figure 5.18 (c)* and *(d)*. This process relies on sufficient xerogel deposition and appropriate template sample thickness. However, the high solid volume fraction requirements of a reinforced ceramic matrix require an improved replication procedure.

By exploiting the fabrication principles of printing, described in the following section (**Section 5.5.3**), the specific surface area of a template can be maximised in order to fabricate a preform replica of high solid volume fraction. The distance between and orientation of polymeric lines that compose a printed part can be modified in a way to create open internal surfaces. *Figure 5.19* demonstrates the concept of hierarchical surfaces for xerogel film deposition in the confines of a template outer surface. Here, the internal surfaces allow for increased xerogel film deposition that in theory can increase the solid volume fraction and ensure architectural integrity of the final sintered preform.

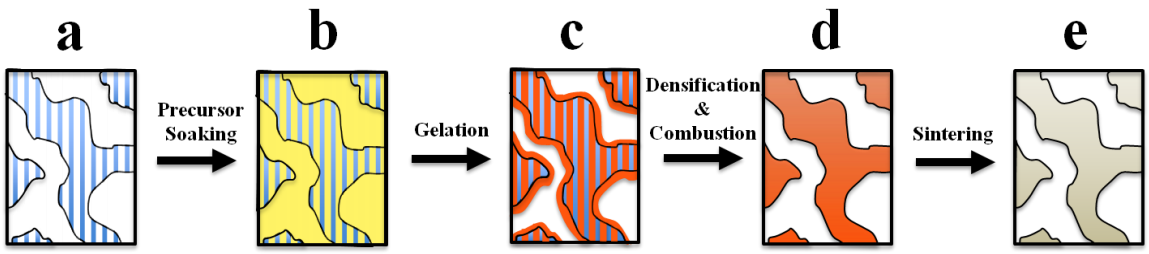

Figure 5.19 Schematic representation of the replication of a hierarchical template to ceramic with stages: (a) hierarchical template (blue), (b) template precursor (yellow) soaking, (c) template precursor gel coating (orange), (d) ceramic preform and (e) sintered ceramic preform (cream).

The distance between consecutive print lines is known as hatching distance and their orientation is known as hatching offset angle. These parameters are modifiable and can create different hatching patterns, shown in the computational images of *Figure 5.20* with the original gyroid template.

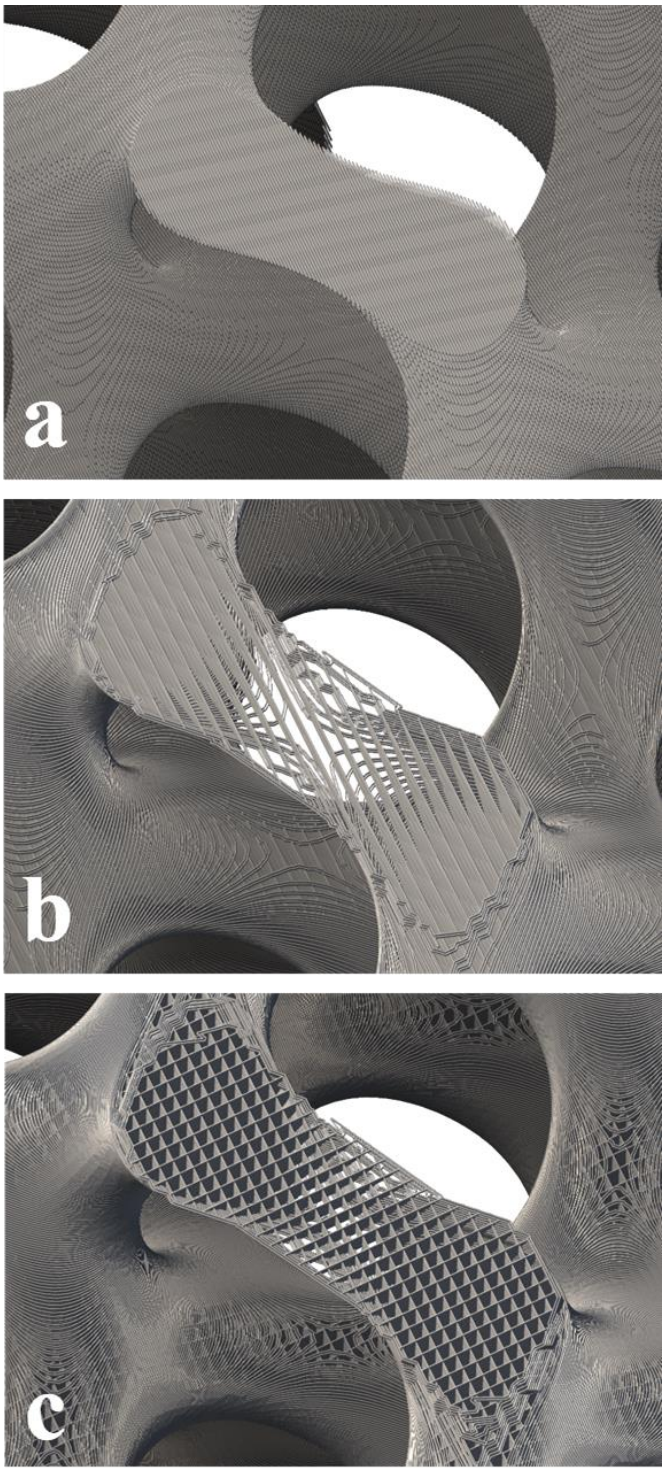

Figure 5.20 Computational images of programmed print lines of gyroid architecture with (a) conventional template, (b) straight hatched hierarchical template and (c) cross hatched hierarchical template microstructures.

The gyroid architecture, shown in *Figure 5.2*, best applies the hierarchical architecture due to the curved outer surfaces of the template. The curvature of the

gyroid reduces compartmentalisation of internal surfaces, thus allowing access to internal volume for precursor solution, shown by the surfaces of *Figure 5.20 (b)* and *(c)*. Therefore, the gyroid architecture is used solely for hierarchical templates. *Figure 5.21* reports the computational print block model of hierarchical templates with straight hatching and cross hatching.

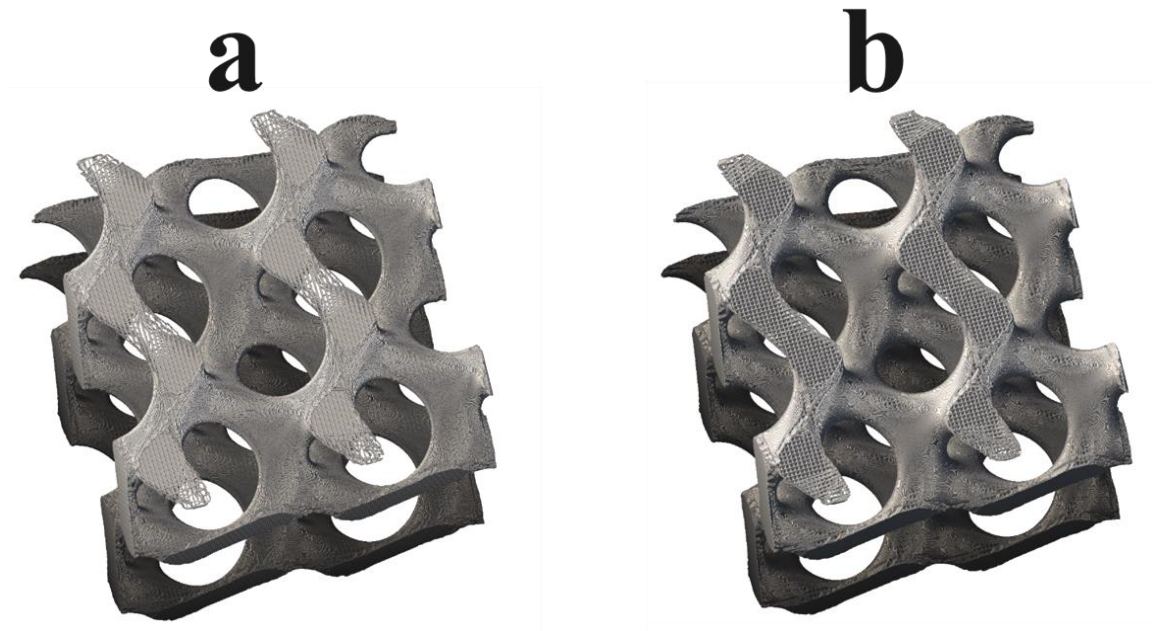

Figure 5.21 Computational images of (a) straight hatched and (b) cross hatched hierarchical template print blocks.

Preparation for printing of the hierarchical template architecture is equivalent to those reported in **Section 5.5.1.4**. *Figure 5.22* shows SEM images of printed template print blocks that compare the *(a)* straight hatching and *(b)* cross hatching modes processed from the computational images shown in *Figure 5.21*.

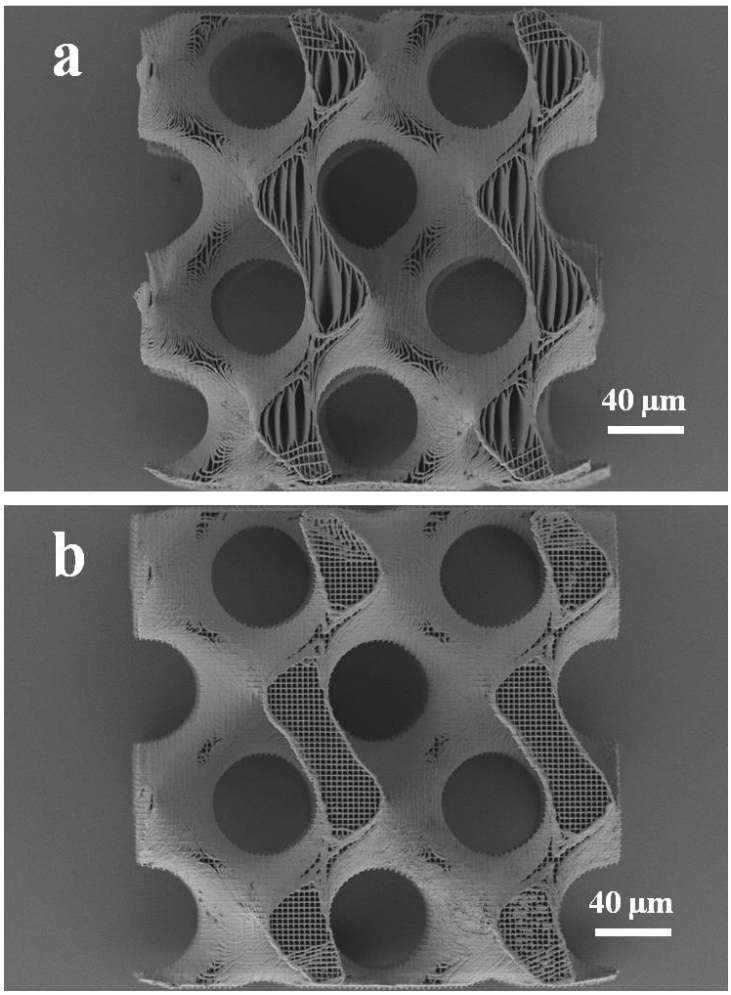

Figure 5.22 SEM images of the printed (a) straight hatched and (b) cross hatched hierarchical template print blocks.

It is clear from *Figure 5.22 (a)* that the integrity of the printing has lapsed at the internal surfaces, likely due to very thin unsupported print lines. The same defect is not seen for the cross hatched hierarchical template (*Figure 5.22 (b)*), suggesting the perpendicular print lines support one another. The collapse of internal microstructure may impede later impregnation and sintering steps for ceramic precursor gel replication. This would suggest cross hatched hierarchical templates would be better for replication. The following chapter investigates the replication of ceramic electrolyte preforms with

templates of different hierarchical parameter. The next section discusses an important approach for increasing the throughput of printed parts.

5.5.3. Print Optimisation

2-photon stereolithography systems have been developed by industry and excel primarily in micro-fabrication of 2D surface patterning. The fabrication of macroscopic templates with microscopic features requires this precise system, but also presents a number of challenges. The main challenge is time and throughput of printing. Though stereolithography is a much faster process than other types of additive manufacturing at this scale, a usefully sized sample may take several days to print, limiting the scope of investigation.

The speed of stereolithography systems can be improved by multiple light sources, stage mechanisms, responsive resins or the 'galvo-mirrors' of the Nanoscribe system described in the experimental section (**Section 5.3.3**). The time it takes to print a part depends on its size and complexity and the system used. The complex microscopic features and required size of templates reported in previous sections consume a large amount of printing time. The template fabrication procedure requires optimisation to maximise throughput whilst maintaining feature size.

A computational workflow converted architecture 3D-models to print-ready template files. The print files contain co-ordinates to determine the length and position of individual printed lines and layers and commands to define various printing parameters. Stabilisation functions are automatically applied to the print-ready file in order to prevent disturbances and vibrations from fast moving instrument components. This maintains the precision of the printing at junctions in the printing process, as

demonstrated by *Figure 5.23*. *Figure 5.24* shows a generalised sample of the conventional print code with stages referring to those labeled in *Figure 5.23*.

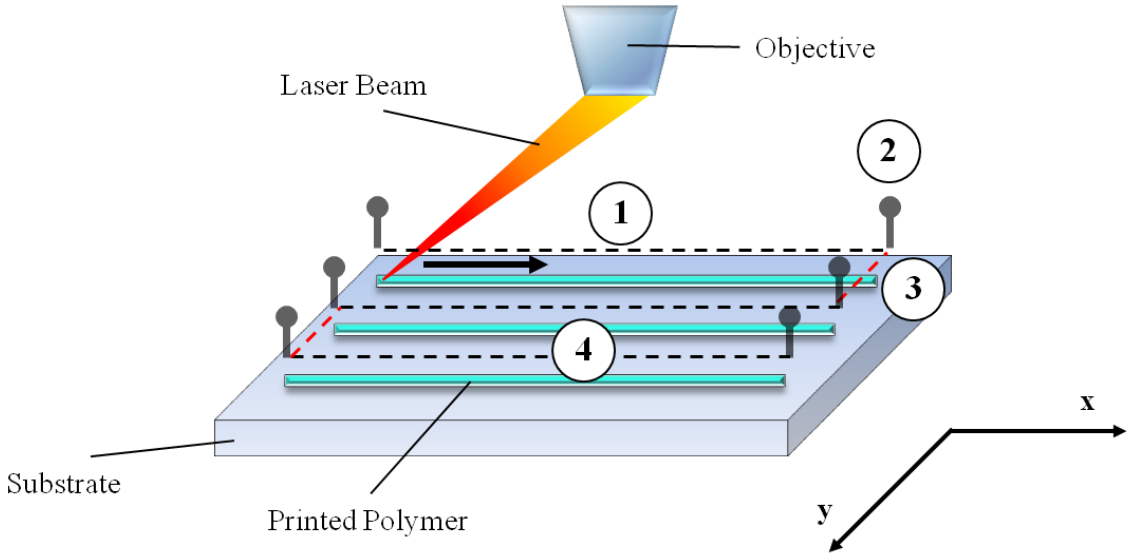

Figure 5.23 Schematic representation of the conventional printing process with printed lines (light blue), defined printed positions (black dashed line) and laser beam position movements (red dashed line). Annotations represent different stages of printing (circled numbers), direction of laser beam (black arrow) and coordinate orientation (axis).

Stage	Coordinate (x)	Coordinate (y)	Coordinate (z)
	0	0	0
1	0 + x	0	0
2	Write		
3	0 + x	0 + y	0
4	0	0 + y	0
	Write		

Figure 5.24 Sample print code for the conventional printing process with reference to different stages.

In *Figure 5.23* and *Figure 5.24*, Stage 1 corresponds to the polymerisation of a line by the laser beam moving through the monomer from the start coordinates to the coordinates defining the end of the line. In Stage 2 the laser beam moves to the end of the line, implements the 'write' command, stops and turns off. The 'write' command stabilises the laser beam and prevents unwanted polymer artifacts to the line. Once the laser is off and the system stabilised, the laser beam position moves to the coordinates of the new line designated by the print code, shown in Stage 3. Before printing at the new location, the system stabilises again to prevent disturbances from the galvo-mirror movements directing the laser beam. Finally, the next line is printed in Stage 4 as in Stage 1.

The stabilisation functions, demonstrated by Stages 2 (*Figure 5.23* and *Figure 5.24*), are the most time consuming operations in the printing process. Optimising print times removes the stabilisation functions from the code by removing the 'write' commands. However, laser power and movement between print lines requires a new mode of operation. The optimised print code utilises a laser power command to define the sections along the path of the moving laser beam position to be printed. The generalised print code is shown in *Figure 5.25*, which references the stages in *Figure 5.26* that demonstrates the resultant optimised print process.

Stage	Coordinate (x)	Coordinate (y)	Coordinate (z)	Laser Power
	0	0	0	On
1	0 + x	0	0	On
2	0 + x	0	0	Off
3	0 + x	0 + y	0	Off
	0 + x	0 + y	0	On
4	0	0 + y	0	On
	0	0 + y	0	Off

Figure 5.25 Sample print code for the optimised printing process with reference to different stages.

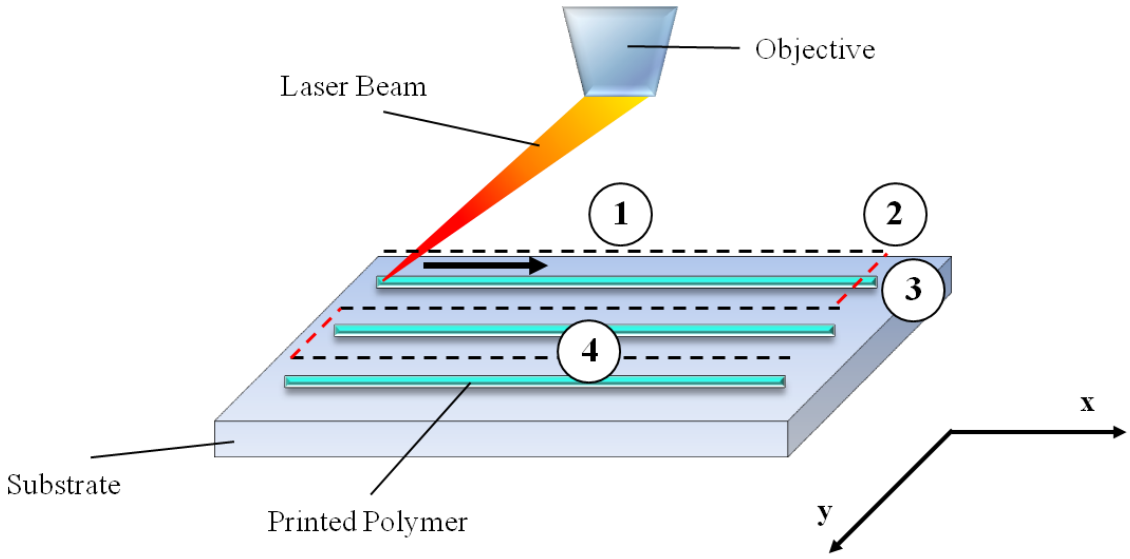

Figure 5.26 Schematic representation of the optimised printing process with printed lines (light blue), defined printed positions (black dashed line) and laser beam position movements (red dashed line). Annotations represent different stages of printing (circled numbers), direction of laser beam (black arrow) and coordinate orientation (axis).

In *Figure 5.25* and *Figure 5.26*, Stage 1 corresponds to the polymerisation of a line by the laser beam moving through the monomer from the start coordinates to the coordinates defining the end of the line. In Stage 2 the laser power is switched off.

Instantaneously and without 'write' commands, the laser beam position moves to the coordinates of the new line designated by the print code, shown in Stage 3. Once the position reaches the designated coordinates, the laser beam switches on and starts printing the new line immediately, shown in Stage 4. The effect of the optimised process is having the laser move at constant speed with the laser power switching on and off to define the printed part. *Table 5.5* reports the print times of each template print block and template part of the different architectures. The cubic architecture demonstrates the optimised and unoptimised print-ready files. The time decrease is significant with the final cubic template part printed over two times faster, allowing for a much higher throughput of templates.

Table 5.5 Print times optimised and unoptimised print blocks and template parts for different designed architectures.

Architecture	Code	Scan Speed ($\mu m\ s^{-1}$)	Time per Print Block (mins)	Time per Part (mins)
Gyroid	Optimised	150000	1.9	822
Diamond	Optimised	150000	3.0	750
Bijel	Optimised	150000	1.8	450
Cubic	Optimised	150000	2.8	700
Cubic	Unoptimised	150000	5.8	1450
Cubic	Unoptimised	100000	5.8	1450
Cubic	Unoptimised	50000	7.1	1775

The removal of stabilisation functions during the printing process results in a loss of stability in printing. *Figure 5.27* reports SEM images of the loss of resolution at the surface of the part.

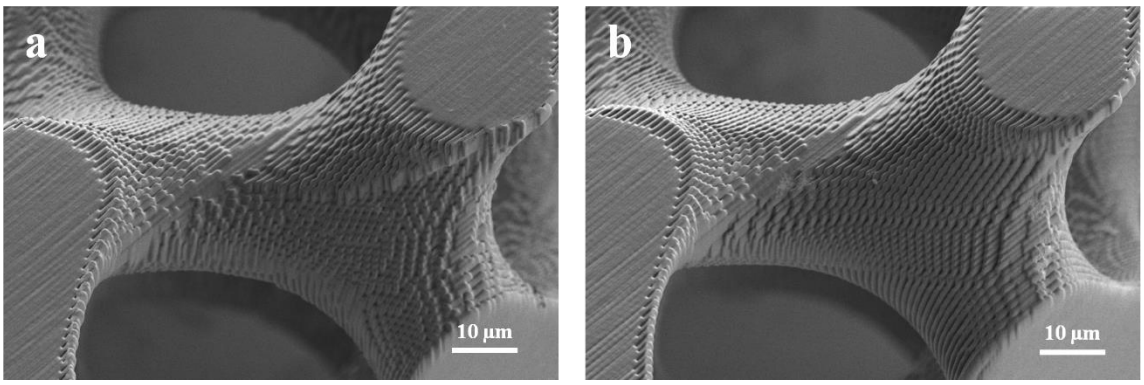

Figure 5.27 SEM images of the surface microstructure of an (a) optimised and (b) unoptimised printed template.

The loss of surface resolution for the optimised printed templates is minimal considering the scale of the template microstructure. The formation of ceramic preforms should not require a high surface resolution and therefore the printed templates are acceptable. The SEM images of printed templates reported in **Section 5.5.1.4** include the optimised printing process.

Another key consideration in print optimisation is the binding of adjoining print blocks. The print blocks of a part need to overlap in order to form a strong bond that does not break. *Figure 5.28* demonstrates the process of placing print blocks in relation to one another to ready them for printing. *Figure 5.28 (b)* shows the ideal continuation of the gyroid architecture across adjacent print blocks. However, the surfaces of the print blocks only touch in this placement, but printing blocks that remain physically connected require overlap. *Figure 5.28 (c)* shows overlapping of print blocks in their current state that prevents ideal continuation of gyroid architecture and creates changes

to the microstructural parameters of the part. Adding adjacent slices or print-extensions to each side of a print block for overlap, as shown in *Figure 5.29*, maintains the original defined parameters and repeat architectural continuity. 10 μm print extensions are enough to bind the print blocks with a 20 μm overlap maintaining the repeating architecture. The procedure, as described in the experimental methods section (**Section 5.3.4**), also maintains the defined microstructural parameters regardless of part dimension.

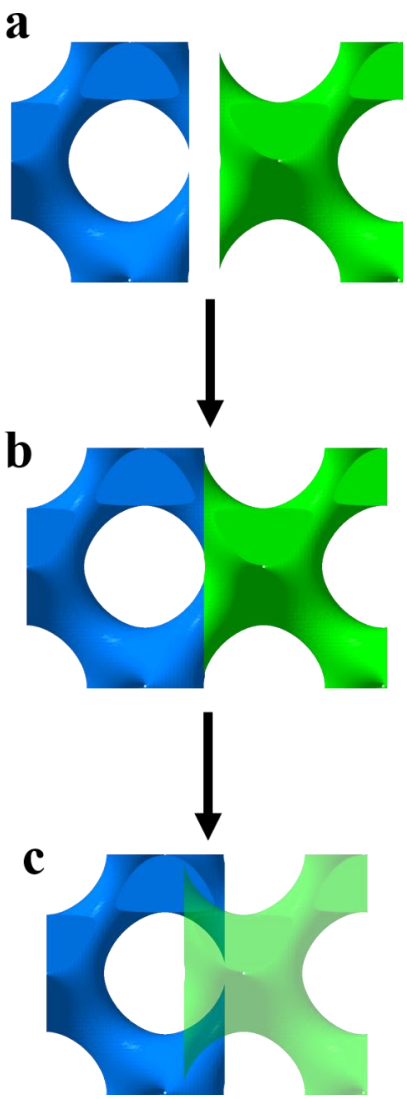

Figure 5.28 Computational images showing the (a) separation, (b) touching and (c) overlapping of two adjacent print blocks (blue and green).

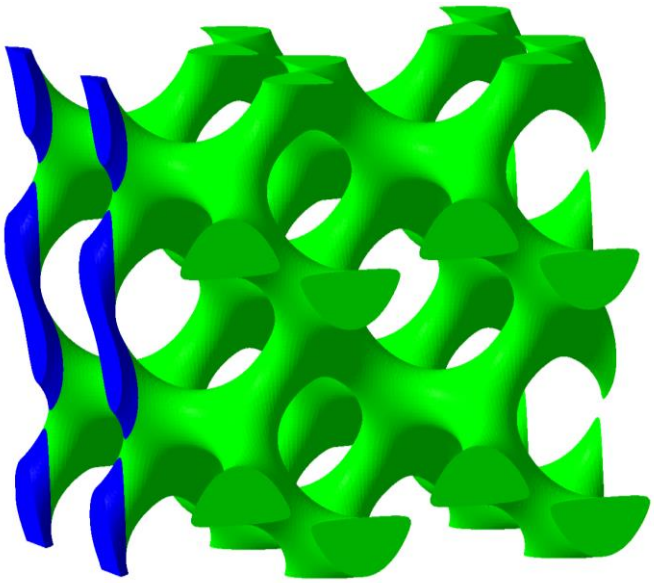

Figure 5.29 Computational image showing the adjacent print extensions (blue) of the gyroid print block (green).

The SEM images of printed templates and images of computational print blocks and parts reported in **Section 5.5.1.4** include the print extensions discussed here.

5.6. Conclusion

This work has shown that templates can be fabricated, analysed and modified for use in replication and sacrificial templating procedures. The reported fabrication procedure by stereolithography and computer-aided design is an alternative route to the chemically prepared bijel template, reported in the previous chapter (**Chapter 4**). A computational workflow of computer-aided design has been developed to fabricate 3D-model architectures. 3D-interconnected polymer templates with low solid volume fraction were successfully designed and printed for sacrificial templating. Further design work has looked to enhance the template architecture for replication by introducing hierarchical surfaces for improved sol-gel deposition. TGA analysis of the

printed parts has confirmed their suitability as combustible templates for replication and sacrificial templating.

The reported techniques present a reliable and versatile procedure for employing stereolithography in template formation. However, the templates do not guarantee formation of suitable oxide ceramic electrolyte preforms. Microstructural parameter analysis has identified key properties of template architectures. In conjunction with this analysis, computer-aided design can modify microstructural parameters for the optimisation of fabrication processes and stress transfer efficiency. On this basis, a fibre-reinforced ceramic matrix composite may have optimised toughness and tensile strength by a designed interpenetrating composite microstructure.

Print code optimisation and print extensions have enabled more extensive and versatile investigation with the printing process. Replication and sacrificial templating with the presented templates is discussed in **Chapter 6**.

5.7. References

[1] Schwarz, H. A. in *Gesammelte Mathematische Abhandlungen* (Springer, Berlin, 1933).

[2] Neovius, E. R. in *Bestimmung zweier spezieller periodischer Minimal achen* (Akad. Abhandlungen, Helsinki, 1883).

[3] "Diamond Lattice Model" by pmoews is licensed under CC BY 3.0 and changes were made. at http://www.thingiverse.com/thing:13601

[4] Travitzky, N. Processing of ceramic–metal composites. *Advances in Applied Ceramics* **111**, 286-300 (2012).

[5] Reeves, M., Stratford, K. & Thijssen, J. H. J. Quantitative morphological characterization of bicontinuous pickering emulsions via interfacial curvatures. *Soft Matter* **12**, 4082-4092 (2016).

[6] "Schematic representation of the different stages and routes of the sol-gel technology" by Claudionico is licensed under CC BY-SA 4.0 and no changes were made. at https://en.wikipedia.org/wiki/Sol-gel#/media/File:Sol-Gel_Scheme.svg

Chapter 6: 3D-Porous Oxide Ceramic Electrolyte Preform Formation

6.1. Aim

The design, control and fabrication of templates with specific microstructure by computer-aided design and stereolithography have been demonstrated, but a procedure for the reproduction of the microstructure in oxide ceramic electrolyte is still required. The main aim of this chapter is to fabricate ceramic preforms with desirable properties. Sacrificial templating and replication procedures have been selected, along with the printed templates reported in the last chapter, to achieve this. The preform formation procedures will require adaptation to the novel templates to ensure the best reproduction of microstructure and desirable electrolyte properties. Forming ceramic preforms with the desired microstructure would be an excellent step in fabricating a fibre-reinforced (FR) ceramic matrix composite (CMC) with oxide ceramic electrolyte.

6.2. Introduction

The previous chapter outlines the fabrication and modification of printed templates. Being able to define the microstructural parameters of the templates should assist in subsequent fabrication steps and optimisation of the final composite material. To fabricate a FR-CMC of oxide ceramic electrolyte with an interpenetrating composite (IPC) microstructure requires an adequate preform formation procedure. Sacrificial templating and replication are known preform formation procedures and have been

identified as potential routes for introducing 3D-porosity to ceramic electrolytes (**Chapter 1 Section 1.9**).

Preform formation should aim to fabricate ceramic electrolytes that are adequate lithium-ion conductors, maintain high density for inherent compressive strength and have 3D-interconnected porosity for subsequent infiltration of reinforcement. The typical preform formation procedures will require adaptation in order to maintain inherent electrolyte properties whilst allowing for reinforcement infiltration. Replication and sacrificial templating are excellent methods for introducing and modifying porosity.[1]

Studart *et al*. reviewed the synthetic routes for ceramic preform fabrication known in literature.[1] *Figure 6.1* reports the average pore size and porosity of known procedures and demonstrates the challenge of this work. Sacrificial templating achieves the lowest values for porosity and average pore size, making it the obvious candidate for preform formation. On the other hand, replication from polymer and wood templates forming 'polymer replicas' and 'wood replicas', give much higher porosities and average pore sizes. However, the direct reproduction of 3D-interconnected template microstructure makes it an attractive route. Direct foaming by gas incorporation achieves far higher porosity than the other procedures and lacks adequate control over microstructure and 3D-interconnectivity of pores.

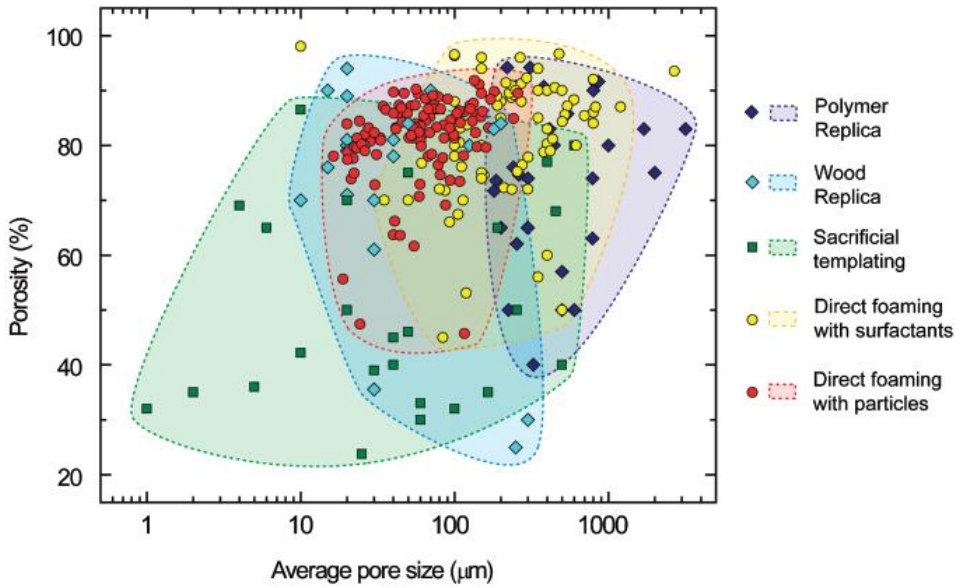

Figure 6.1 Graph of ceramic preform porosity and average pore size for different preform formation techniques.[1]

Figure 6.2 demonstrates typical sacrificial templating by suspension drying. Here, a solvent allows a homogeneous suspension of both ceramic and sacrificial particles to form (*Figure 6.2 (a)* and *(b)*). The continuous ceramic phase consolidates on drying (*Figure 6.2 (c)*) before removal of sacrificial material to leave porosity (*Figure 6.2 (d)*). For colloidal particle suspensions, setting agents and binders may be employed.[1] However, for non-colloidal suspensions, particles settle or sediment during drying.

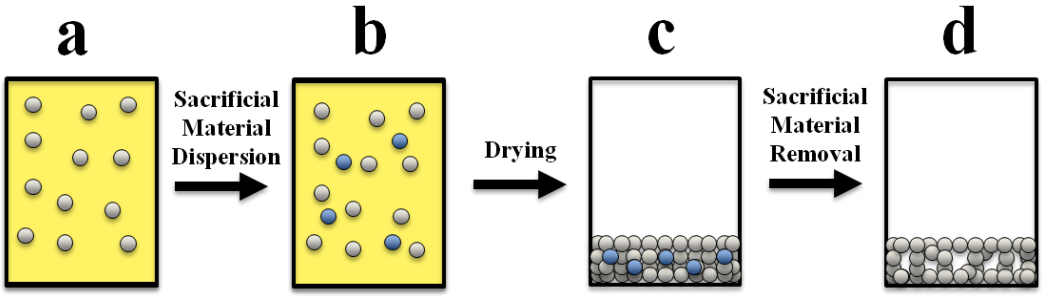

Figure 6.2 Schematic representation of a sacrificial templating procedure via particle suspension drying showing solvent (yellow), ceramic particles (white spheres) and sacrificial particles (blue spheres).

Figure 6.3 describes the formation of xerogel films on a 3D-template surface during a typical replication procedure with sol-gel synthesis. Here, a 3D-template is soaked with sol-gel precursor solution and coated with an xerogel film on gelation (*Figure 6.3 (a)*, *(b)* and *(c)*). The ceramic replica begins to form as the xerogel film undergoes pyrolysis and densification by heating and the template is removed by combustion (*Figure 6.3 (c)* and *(d)*). The ceramic replica is formed on sintering to ensure grain connectivity (*Figure 6.3 (d)* and *(e)*).

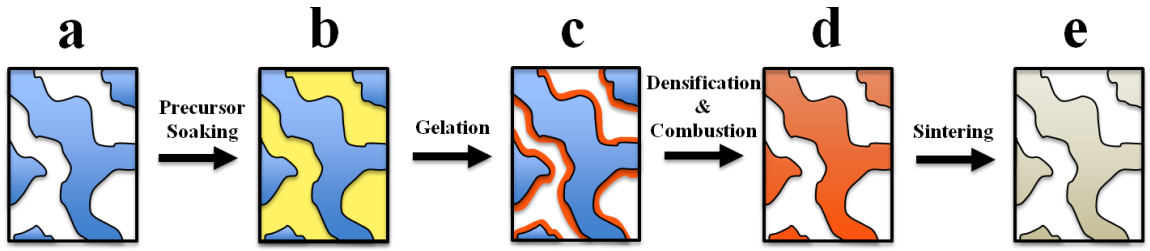

Figure 6.3 Schematic representation of a replication procedure with a 3D-template to give ceramic preform replica showing template (blue), precursor (yellow), gel (orange) and sintered ceramic (cream).

Figure 6.4 reports the relative density and relative compressive strength of ceramic preforms to their dense (pelletised) counterparts, fabricated via different synthesis routes known in literature.[1] There is a strong positive correlation between relative density and relative strength, which highlights the importance of fabricating preforms with high relative density (high solid volume fraction). Sacrificial templating achieves the highest density and compressive strength of all the routes. This is due to preforms with little porosity being easily prepared by simply adding less sacrificial material. On the other hand, replication procedures achieve significantly lower relative density, due to the inability to create low porosity preforms.[1]

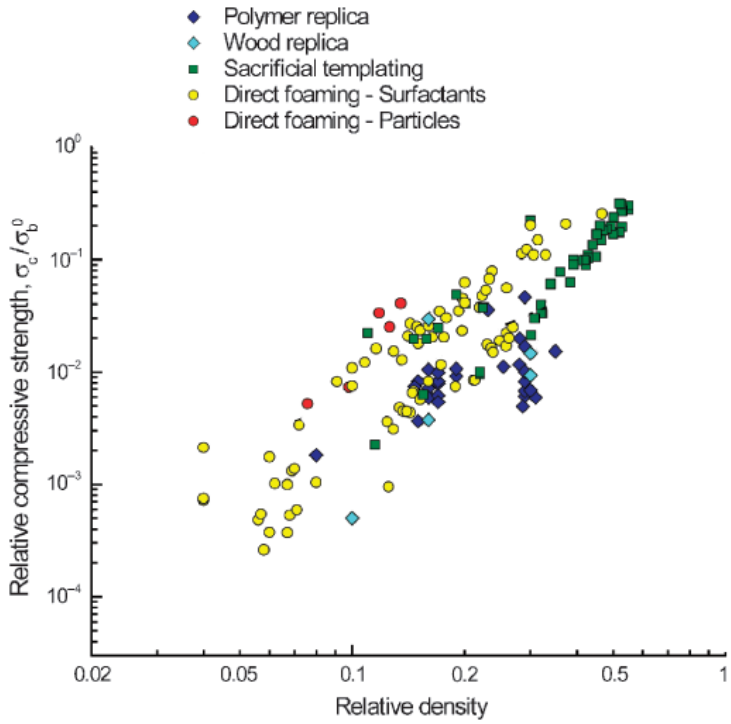

Figure 6.4 Graph showing relative compressive strength and relative density for different preform formation procedures.[1]

In addition to maintaining high compressive strength, the material density (excluding introduced porosity) is also important for interconnectivity of grains to maintain a reasonable ionic conductivity for ceramic electrolytes. Loose ceramic powders are typically pressed to ensure a highly dense material that produces highly interconnected grains on sintering. In one sacrificial templating procedure ceramic powder with dispersed sacrificial particles are pressed to introduce porosity. However, for procedures using 3D-interconnected templates to produce 3D-interconnected porosity, such pressing would destroyed the microstructure. Therefore, a preform formation procedure has to ensure high material density of ceramic without pressing. This chapter aims to improve known replication and sacrificial templating procedures, utilising the templates prepared in **Chapter 5**, to form ceramic preforms with high density (solid volume fraction), low average pore size and high compressive strength,

whilst maintaining reasonable ionic conductivity (high material density) and introducing 3D-interconnected porosity. Such a preform would be adequate for further processing in the fabrication of FR-CMC electrolyte layers.

6.3. Experimental Methods

6.3.1. $Li_{1.6}Al_{0.6}Ge_{1.4}(PO_4)_3$ (LAGP) Adapted Replication Procedure

LAGP was prepared by a Pechini sol-gel synthesis according to literature.[2] Synthetic grade starting materials were purchased from Sigma-Aldrich. 275.8 mg of lithium nitrate (99.99 %), 562.7 mg of aluminium nitrate nonahydrate (99.997 %), 885.5 mg of germanium ethoxide (≥99.95 %) and 880.3 mg of ammonium dihydrogen phosphate (99.999 %) were dissolved in a 0.2 M aqueous solution of 3.8 g of citric acid monohydrate (≥99.0 %) and 90 mL of distilled water. 1.1 g of ethylene glycol (99.8 %) was added and the solution stirred and heated at 80 ˚C for 1 h to form a homogeneous solution. A printed polymer template from IP-Dip resin was immersed in cyclohexane (≥99.8 %) before LAGP precursor solution was added to form a 50:50 volume ratio mixture. The mixture was vortex mixed at 2000 rpm for 5 minutes. The aqueous-organic mixture was left open to air and unperturbed overnight to evaporate cyclohexane. The solution was heated to 130 ˚C for 5 h to initiate gelation. The temperature was then increased to 170 ˚C for 24 h for drying. The gel was heated to 900 ˚C for 5 h at a slow ramp rate of 2 ˚C min^{-1} in air using a platinum crucible to obtain the final product.

6.3.2. LAGP Adapted Sacrificial Templating

LAGP was prepared by a Pechini sol-gel synthesis according to literature.[2] Synthetic grade starting materials were purchased from Sigma-Aldrich, unless otherwise stated. 275.8 mg of lithium nitrate (99.99 %), 562.7 mg of aluminium nitrate nonahydrate (99.997 %), 885.5 mg of germanium ethoxide (≥99.95 %) and 880.3 mg of ammonium dihydrogen phosphate (99.999 %) were dissolved in a 0.2 M aqueous solution of 3.8 g of citric acid monohydrate (≥99.0 %) and 90 mL of distilled water. 1.1 g of ethylene glycol (99.8 %) was added and the solution stirred and heated at 80 ˚C for 1 h to form a homogeneous solution. The temperature was increased to 170 ˚C for 24 h to initiate gelation. The gel was heated to 400 ˚C for 4 h in air using a platinum crucible. The obtained product was ground in an agate mortar and pestle before being heated again in air using a platinum crucible at 800 ˚C for 5 h to produce the powder LAGP product that was again ground in an agate mortar and pestle. 0.5 g of LAGP powder in 0.5 mL of ethanol (≥99.8 %) were then ball milled in a Retsch EMAX high energy ball mill with zirconia-lined milling vessel and 21.5 g of zirconia 5 mm balls at 600 rpm for 10 minutes. The resultant LAGP powder was recovered and dried at 80 ˚C overnight. 100 mg of LAGP ball milled power was then mixed in 0.7 mL of methanol (99.99 %, Fisher Scientific) before immersing a printing polymer template from IP-S resin. The mixture was twice sonicated for 5 minutes and centrifuged at 2000 rpm for 2 minutes giving sediment of the LAGP powder. The supernatant methanol was removed and the sediment was left to dry at room temperature for 2 minutes. The template was recovered from the sediment with excess LAGP rubbed from the surface. The impregnated template was heated to 900 ˚C for 5 h at a rate of 2 ˚C min^{-1} to yield the LAGP preform.

6.3.3. Polypropylene Impregnation of LAGP Preform

An excess of polypropylene (isostatic, average Mw ~12000 Da, Sigma-Aldrich) was melted at 180 ˚C. LAGP preforms were added to the melt and polymer allowed to percolate the porosity under dynamic vacuum for 2 h. The composites were removed from the melt and left to cool to ambient temperature. Excess polymer was removed by placing the polypropylene-filled preforms on aluminium foil covering a hot plate at 100 ˚C.

6.4. Characterisation

The morphology of materials was investigated using a Carl Zeiss Merlin field emission scanning electron microscope (SEM) with a Gemini II column and a Carl Zeiss EVO MA10 SEM. Samples were mounted on adhesive copper tape applied to a stub and holder. For replicated preforms the crucible was mounted on tape and stub to avoid fracture. Measurements were taken at a voltage range of 3-10 kV with a current range between 100-190 pA. Cross-sections were prepared using a scalpel.

The 3D-interconnectivity of computational 3D-models was investigated in Netfabb Professional (7.4.0). An inverse phase model was generated using a Boolean operation before both the original model and inverse phase were analysed for number of individual (non-connecting) shells.

The microstructural parameters of different architectural models were analysed using a variety of software packages. The solid volume fraction was calculated as an automatic function in Netfabb Professional (7.4.0). The internal surface-area-to-volume ratio used the repair function of Netfabb Professional (7.4.0) to remove external faces of each model to give only the internal surfaces, before automatic calculations of surface

area were given. The sample thickness distribution (STD) and channel size distribution (CSD) were analysed using the auto-skeletonisation and distance mapping tools of Avizo (9.1.1).

Powder X-ray diffraction (PXRD) data from synthesised LAGP powder were collected using a 3 kW Rigaku SmartLab X-ray diffractometer with Cu $K_{\alpha 1}$ radiation. The diffraction patterns were collected at room temperature in the 2θ range of 10-50 ˚ at 0.01 ˚ increments.

Alternating current electrochemical impedance spectroscopy (AC EIS) was used to investigate the electrical behaviour of a composite of LAGP and polypropylene. The sample surface was polished using 3M Tri-M-ite Fre-Cut abrasive sheet (P1200) before drying at 70 °C for 20 minutes, sonicating in cyclohexane for 10 minutes and drying again at 70 °C for 20 minutes. Gold blocking electrodes approximately 30 nm thick were sputtered onto opposite sides of the preform. Conductivity measurements were made using a Solartron Analytical Modulab over 0.1 Hz – 1 MHz frequency range and voltage amplitude of 10 mV. Impedance data were fitted against an equivalent circuit to calculate the total ionic conductivity. All temperature variable measurements were carried out on a Julabo F32-MA cryostat. Low temperature measurements used liquid nitrogen to reach -30 ˚C. Temperature dependent measurements were carried out in the range of -30 to 75 ˚C in 5 ˚C steps. The data were analysed using ZView (3.4c) and an equivalent circuit generated to the best fit.

6.5. Results & Discussion

6.5.1. Replication

6.5.1.1. Sol-Gel Synthesis

The preform formation procedures, sacrificial templating and replication, present respective challenges when utilised for ceramic electrolyte reinforcement. The replication procedure, discussed in **Chapter 1 Section 1.9** and the previous chapter (**Chapter 5 Section 5.5.2**), typically uses a 3D-interconnected template with low solid volume fraction in order to maintain architectural integrity. However, maintaining the inherent compressive strength of a ceramic part requires a high solid volume fraction, as discussed in the introduction section (**Section 6.2**). Achieving a ceramic preform with high solid volume fraction and architectural integrity from the template is a considerable challenge. CAD and stereolithography have demonstrated the ability to create hierarchical template microstructures, in the previous chapter (**Chapter 5 Section 5.5.2**), which aim to increase the deposition of precursor gel for high solid volume fraction preforms by replication.

Colombo reported the chemical vapour deposition (CVD) of alumina on polyurethane sponge templates.[3] *Figure 6.5* shows *(a)* the template, *(b)* the resultant ceramic preform and *(c)* the cross-section of the hollow strut running through the ceramic. The low solid volume fraction of the template allows fabrication of the part by CVD. The presence of hollow struts in the ceramic preform (*Figure 6.5 (c)*) decreases the average sample thickness and relative density and increases the likelihood of stress concentrators, which both decrease the effectiveness of reinforcement (**Chapter 1 Section 1.8**). Therefore, an alternative synthetic route is considered.

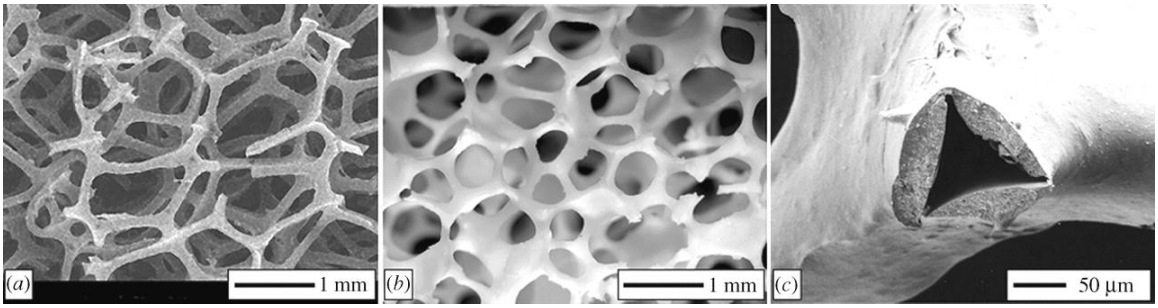

Figure 6.5 (a) SEM image of polyurethane foam template, (b) optical microscope image of alumina foam replica and (c) SEM image of a hollow ceramic strut.[3]

Replication procedures predominately utilise sol-gel or suspension syntheses to impregnate porous templates, deposit precursor layers and form ceramic. Sol-gel syntheses are known for oxide ceramic electrolytes, as the efficient mixing of precursor atoms in the solution lowers the fabrication sintering temperatures compared to dry powder mixing.[2] **Chapter 3** reports a Pechini sol-gel synthesis used to fabricate LAGP used in a structural FR-CMC of oxide ceramic electrolyte. For comparison and relative ease of preparation the NASICON-type LAGP was also prepared for 3D-preform fabrication. **Chapter 3 Section 3.5.1** reports the composition and microstructure of Pechini sol-gel synthesised LAGP.

Utilising the LAGP Pechini sol-gel method in a replication procedure requires an understanding of the reaction's thermal behavior in relation to a template. In the remaining sections on replication, the reported experiments consider sol-gel LAGP and stereolithographically printed templates (**Chapter 5**). Above 100 °C polycondensation between citric acid and ethylene glycol occurs to form a polymer citrate gel (xerogel). Citric acid establishes complexes with precursor ions that distribute throughout the gel. *Figure 6.6* reports TGA data analysing the thermal behavior of the formed LAGP precursor gel dried at 80 °C for 24 h and the IP-Dip and IP-S polymer templates in air.

The low temperature weight loss at 0-200 °C is due to loss of moisture from the LAGP gel and templates.

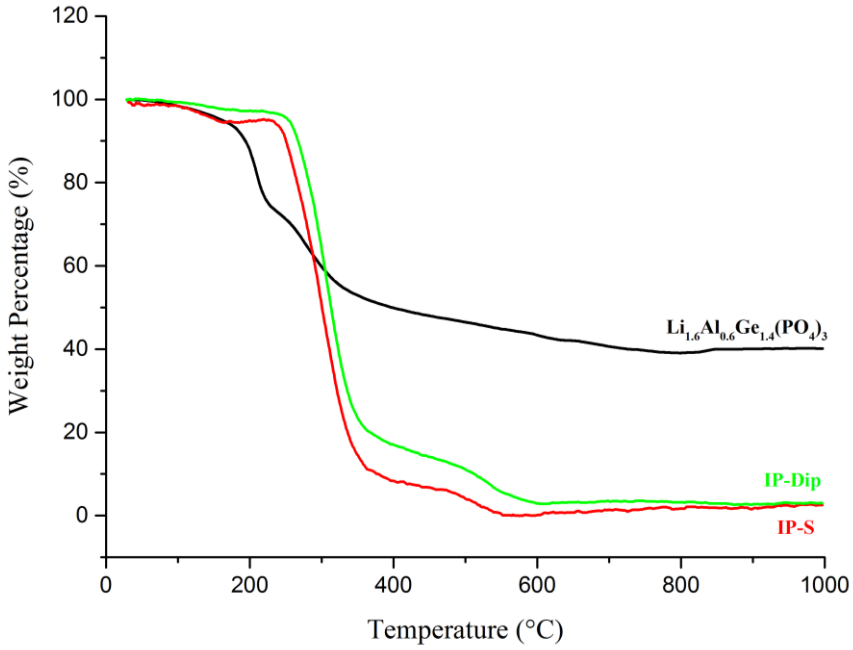

Figure 6.6 TGA curves of LAGP precursor gel and IP-Dip and IP-S polymer templates in air.

Further weight loss at 200-300 °C corresponds to the oxidation of some organic material. It is at this stage that the majority of the IP-Dip and IP-S template polymer materials are also combusted. However, 21 wt% of the LAGP precursor gel is lost at 300-800 °C, due to the further oxidation, pyrolysis and carbon combustion of the polymer gel leaving a final weight of 39 wt%. Such weight loss above 300 °C, where only 50 wt% of the template polymers remain, is likely to affect the replication of the ceramic preform, as the template acts as a support for the precursor as it forms the final ceramic. Loss of structural integrity of the template at low temperatures before final mass changes of the LAGP precursor could result in collapse of the structure. The final weight loss of the template polymers occurs at 400-550 °C, due to combustion of

pyrolysed material. Above 550 °C the templates are completely combusted and the LAGP replication must maintain integrity in absence of the supporting template until after annealing and sintering at 800 and 900 °C, respectively. Sintering involves the densification of grains, which may also contribute to a loss of integrity in microstructural features. Therefore, the TGA data predicts that the structural integrity of the ceramic preforms formed via replication using printed polymer templates may suffer on template removal and sintering (*Figure 6.3 (c), (d)* and *(e)*). However, the IP-Dip polymer is marginally more stable than IP-S and is hence selected as the template material for all following experiments involving replication.

6.5.1.2. Printed Template Replication

A printed template was investigated with a replication procedure via sol-gel route based on that described in the introduction section (**Section 6.2**). The gyroid template used had a pore size of approximately 40 μm, being much lower than the ceramic replicas fabricated via other syntheses (*Figure 6.3*). The smaller pore sizes are desirable for composites due to the relative size of micro-cracks requiring reinforcement. The experimental methods section (**Section 6.3.1**) describes the replication procedure via an LAGP Pechini sol-gel synthesis used for all templates reported in this chapter. *Figure 6.7* reports the *(a)* computational image of the designed template microstructure, *(b) SEM* images of the printed template microstructure, *(c)* the overall ceramic replica, *(d)* the side of the replica, *(e)* the replica microstructure and *(f)* a ceramic hollow strut. Though the solid volume fraction required is much higher, templates with 20 % were initially used to demonstrate the procedure. The templates are printed with specifications, described in the previous chapter (**Chapter 5 Section 5.5.2**),

with short hatching distance of 0.5 µm, indicating the consolidated solid polymer phase seen below (*Figure 6.7 (a)* and *(b)*).

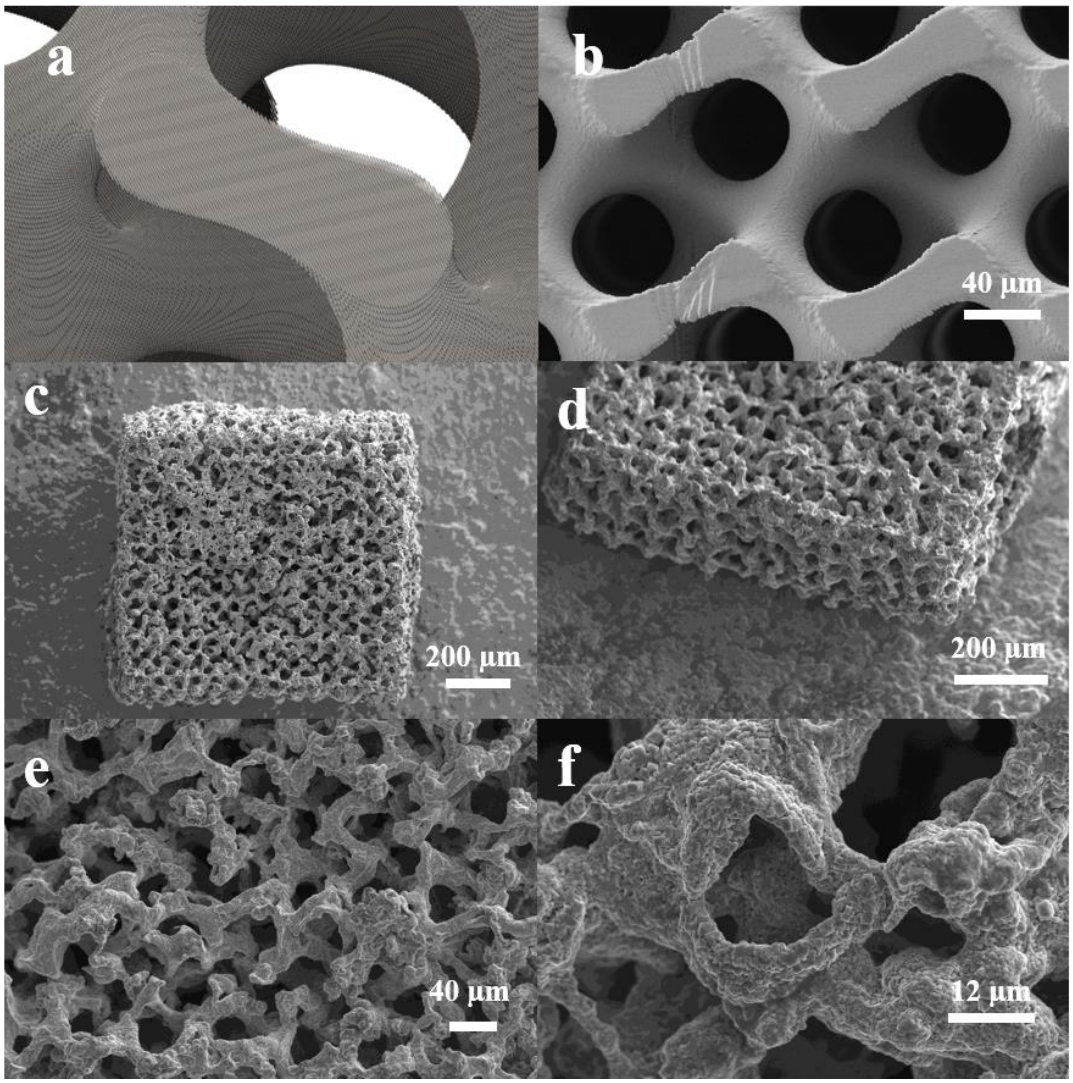

Figure 6.7 Computational image of (a) the gyroid template microstructure, SEM images of (b) the resultant printed template microstructure viewed from the top at magnification x400, (c) the resultant LAGP replica viewed from the top at magnification x70, (d) corner x100, (e) top x250 and (f) top x1500.

Figure 6.7 (f) shows the LAGP grain microstructure that confirms the replication of ceramic. The 3D-microstructure introduced to the ceramic has gyroidal character. However, the integrity of the replica architecture is poor compared to that of the template, with segments of the ceramic being collapsed. On the other hand, the pore

size has been significantly lowered compared to previously reported polymer replicas (*Figure 6.3*). This suggests that printed templates of this kind can replicate ceramic preforms in a desirable scale range. Although, this is due in part to the large decrease in overall dimension from the template (1742 x 1742 x 507 µm) to the ceramic replica (846 x 780 x 189 µm). The ceramic replica preform is approximately 8 vol% (total dimensions) of the original template.

The shrinkage and loss of architectural integrity (*Figure 6.7 (c)*) is likely due to the high solid volume fraction (thickness) of the template relative to that of the ceramic precursor coating. When the template burns off at 550 °C, the ceramic precursor undergoes further combustion and sintering at 900 °C for 5 h (*Figure 6.6*). The thickness of the precursor coating dramatically decreases on sintering to the final ceramic, during which the template is not present as support and therefore increases the likelihood of buckling during densification. This has the effect of architectural integrity loss, evident in *Figure 6.7 (f)* where the hollow strut has morphed by the densifying ceramic compared to *Figure 6.5 (c)*. The mechanical weakness of the ceramic replica, which crumbles with handling, highlights the negative effect of the hollow struts and thin ceramic layer thickness.

Eradicating hollow struts and increasing the relative density of the ceramic replica may be achieved by an adapted sol-gel replication procedure. Removing hollow struts and increasing the relative density should also result in increased architectural integrity and mechanical robustness of the ceramic replica. The following section discusses a route to improve these issues by increasing the deposition of precursor to the template with hierarchical microstructure.

6.5.1.3. Hierarchical Template Replication

For the sol-gel replication method previously discussed in the introduction (**Section 6.2**) and previous section (**Section 6.5.1.2**), it is essential for good quality replicas that the precursor soaking of the template is complete and the deposited xerogel coating is thick (*Figure 6.3 (b)* and *(c)*). The replication method is repeated for all the following ceramic preforms in this section. The viscosity of the infiltrating precursor solution is typically the defining synthesis parameter, where low viscosity assists soaking of the template and high viscosity assists thickness of deposited gel coating. The implementation of hierarchical surfaces (open internal porosity of the template) attempt to increase the deposited xerogel while maintaining complete soaking of the template, eradicating hollow struts and poor architectural integrity reported in the previous section.

Figure 6.8 demonstrates the concept of hierarchical surfaces for xerogel film deposition in the confines of a template outer surface. Here, the internal surfaces allow for increased xerogel film deposition that in theory increases solid volume fraction and ensures architectural integrity of the final sintered preform without hollow struts.

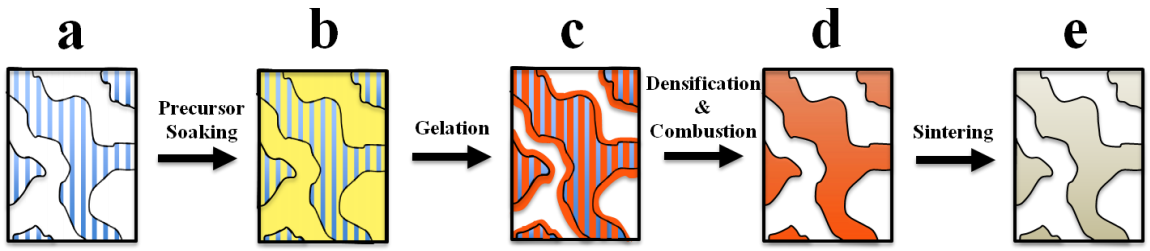

Figure 6.8 Schematic representation of the replication of a hierarchical template to ceramic with stages: (a) hierarchical template (blue), (b) template precursor soaking (yellow), (c) template precursor gel coating (orange), (d) ceramic preform and (e) sintered ceramic preform (cream).

This method utilises the gyroid template architecture, due to the accessibility of the internal hierarchical microstructure surfaces. However, the hierarchical microstructure presents an additional volume of the template that requires complete soaking by the solution and deposition by gel. The gyroid template architecture used was the same as in the previous section, but with hierarchical microstructure that lowers the solid volume fraction of the polymer by adding porosity. Though the hierarchical templates are lower in solid volume fraction, the outer surfaces confining the template are equal (20 %). The resultant ceramic replicas should increase in solid volume fraction due to the increased volume of precursor solution and xerogel deposition in the hierarchical template.

The experimental procedure can be found in the experimental methods section (**Section 6.3.1**). The first experiment used printed templates with open straight hatching, referring to the orientation of the print lines and presence of hierarchical microstructure, with a 3 μm hatching distance. *Figure 6.9* reports *(a)* a computational image of the designed hierarchical template microstructure with 3 μm open straight hatching, *(b)* SEM images of the printed template print block and *(c)* the resultant ceramic replica.

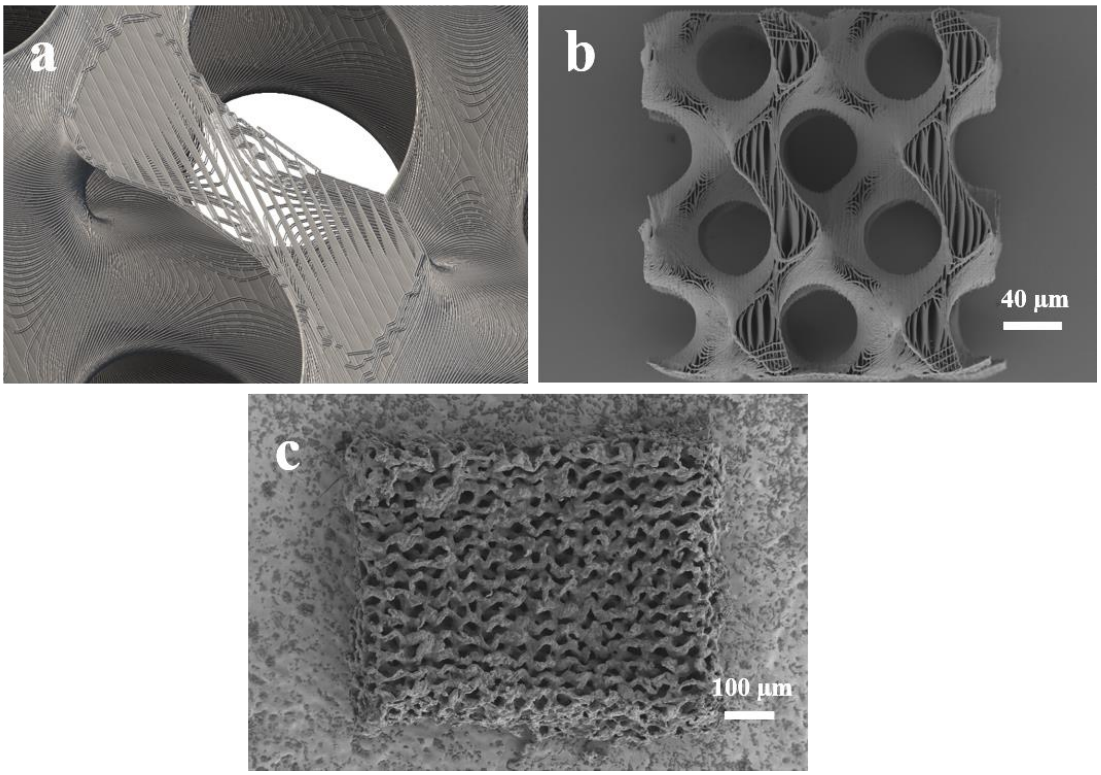

Figure 6.9 Computational image of (a) the designed hierarchical template microstructure with 3µm open straight hatching, (b) SEM images of the resultant printed template print block and (c) the resultant LAGP replica.

The replica (*Figure 6.9 (c)*) shows slightly improved gyroidal character (*Figure 6.9 (b)*) with no visible hollow struts compared to the original template replica in the previous section (*Figure 6.7*), but remains poor. The bowing of the hierarchical surfaces seen for straight hatched template (*Figure 6.9 (b)*) may prevent adequate infiltration of the internal surfaces by precursor. Additionally, the overall preform shrunk considerably to 7 vol% of the original template, below that of the original template preform (8 vol%). In an attempt to improve the architectural integrity of the replica, cross hatched hierarchical templates (**Chapter 5 Section 5.5.2**) were utilised. Not only do they increase the internal surface area for deposition compared to the open hatched templates, but the cross-hatching supports the surfaces better and prevents bowing (*Figure 6.10 (b)*). Open cross hatched templates with a 3 µm hatching distance were

initially used. *Figure 6.10* reports *(a)* a computational image of the designed hierarchical template microstructure with 3 µm open cross hatching, *(b)* SEM images of the printed template print block and *(c)* the resultant ceramic replica.

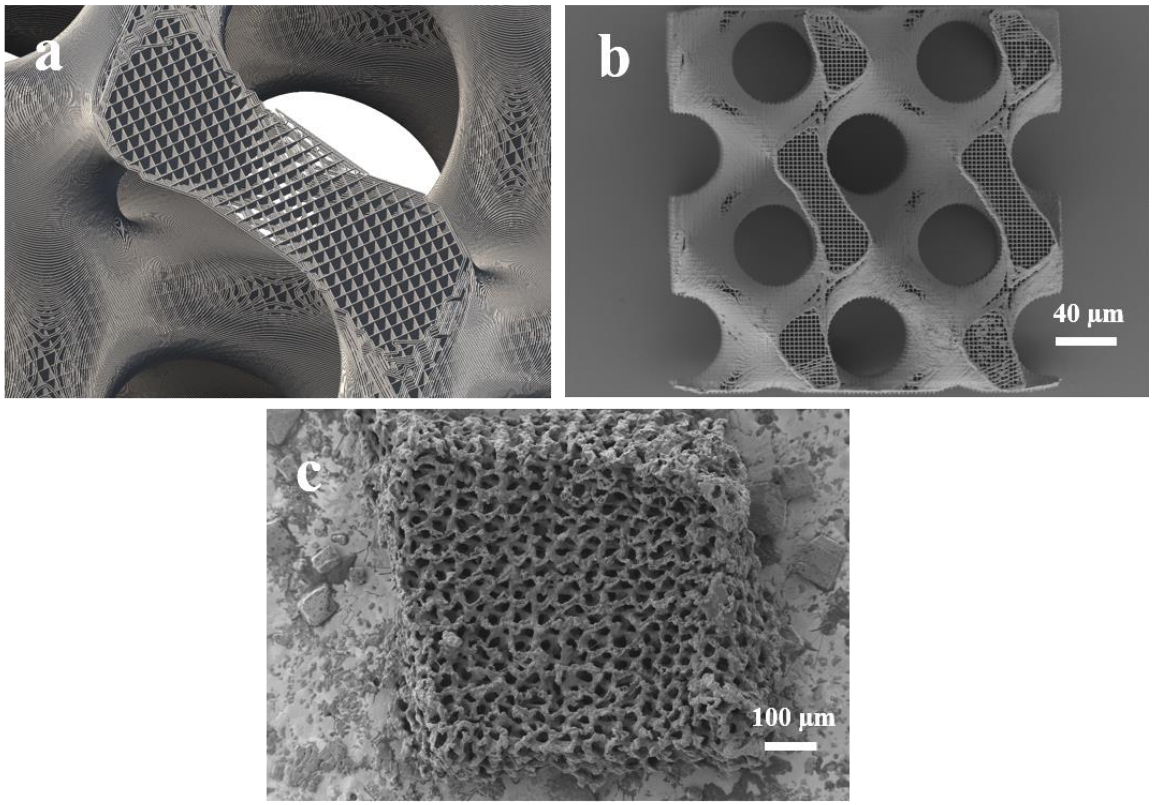

Figure 6.10 Computational image of (a) the designed hierarchical template microstructure with 3µm open cross hatching, (b) SEM images of the resultant printed template print block and (c) the resultant LAGP replica.

Unfortunately, the cross hatching of the hierarchical template microstructure appears to degrade the quality of the ceramic replica. The total replica part collapsed on the right side, with the ceramic microstructure being less gyroidal in character and showing signs of hollow struts (*Figure 6.10 (c)*). The collapse of microstructure is the result of large shrinkage with the preform being 4 vol% of the original template. The decreased hierarchical pore size of the cross hatched template likely impedes the soaking of solution or infiltration of gel, hence decreasing deposition. A ceramic replica

with less ceramic material on replication would be more susceptible to collapse. This could account for the larger shrinkage and collapse of replica microstructure (*Figure 6.10 (c)*).

The hatching distance between cross hatched lines was increased to 6 μm to promote solution soaking and gel infiltration to the internal surfaces. *Figure 6.11* reports *(a)* a computational image of the designed hierarchical template microstructure with 6 μm open cross hatching, SEM images of *(b)* the resultant printed template print block, *(c)* the resultant ceramic replica, *(d)* corner view x100, *(e)* top view x200 and *(f)* top view x750.

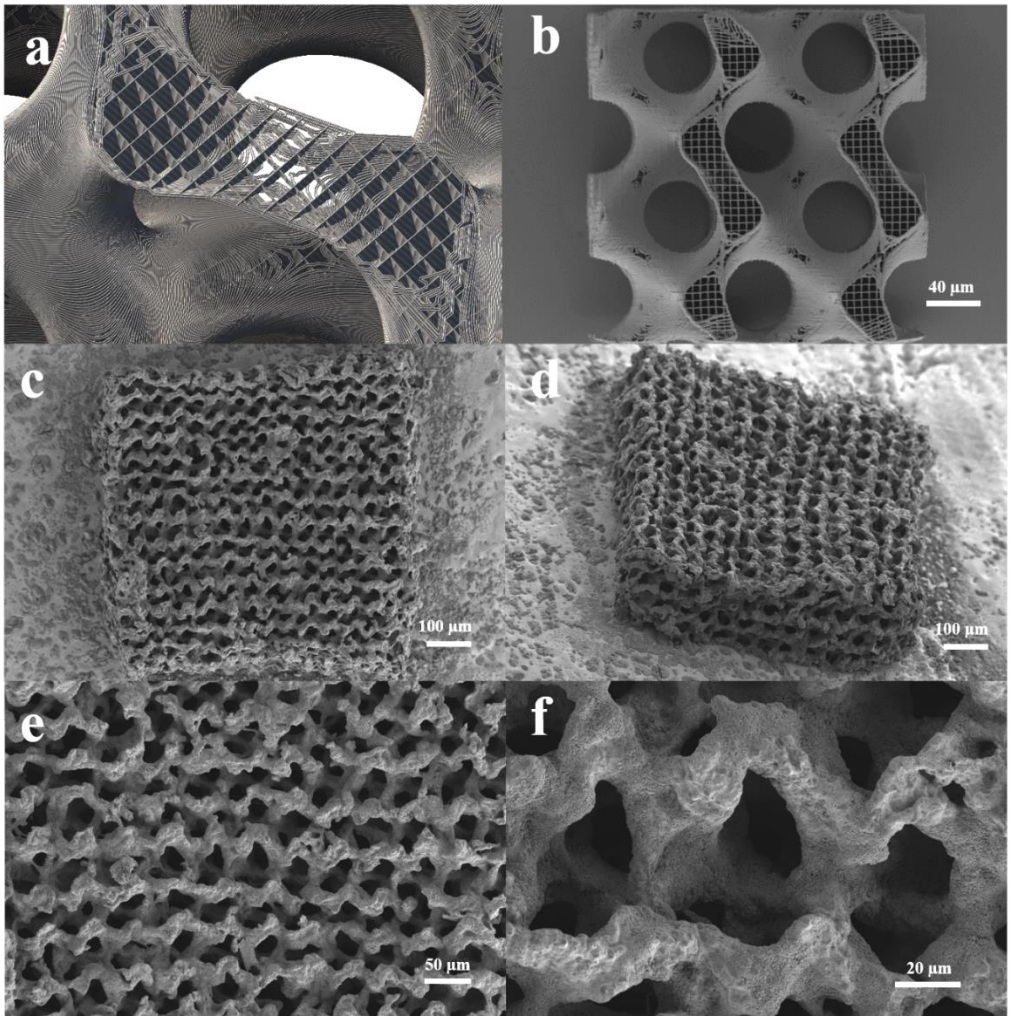

Figure 6.11 Computational image of (a) the designed hierarchical template microstructure with 6µm open cross hatching, SEM images of (b) the resultant printed template print block viewed from the top at magnification x300, (c) the resultant LAGP replica viewed from the top at magnification x100, (d) corner x100, (e) top x200 and (f) top x750.

The increased hatching distance improves the architectural integrity and gyroidal character of the ceramic replica from the template. This confirms that cross hatching is beneficial compared to straight hatching for replication in this way. It also highlights the susceptibility of the replication process to internal template microstructure, with an increased hatching distance making a considerable difference. Compared to the 3 µm cross hatched template, the replica reported in *Figure 6.11* maintains good overall

structure with fewer signs of hollow struts. The final replica was 6 vol% of the original template and therefore still underwent considerable shrinkage.

The shrinkage of replicas is such that any usable sample size would require large templates. Replication of ceramic preforms in this way would not be feasible due to time-consuming print processes. However, one advantage of shrinkage is the increased solid volume fraction of the final preform. As the overall dimensions shrink, the ceramic solid volume fraction increases, increasing the density and compressive strength. Using μCT data a computational 3D rendered model was created of the replica shown in *Figure 6.11*. *Figure 6.12* shows an image of a computational 3D model taken as a 150 x 150 x 30 μm portion of the total μCT data.

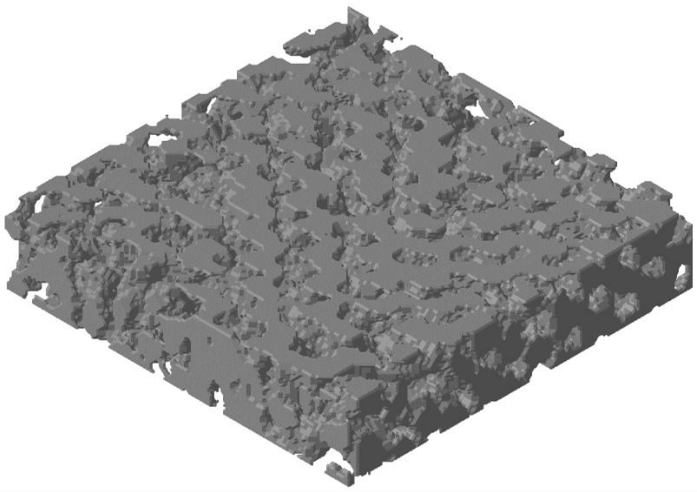

Figure 6.12 Computational image of a 150 x 150 x 30 μm 3D model of LAGP replica microstructure. [2]

Computational volume analysis of the model, described in the experimental methods section (**Section 6.4**), enabled calculation of the solid volume fraction of the 3D model as 55 %. This is significantly larger than the expected 20 % solid volume

[2] μCT data acquired and provided by Dr Job Thijssen at the School of Physics and Astronomy, The University of Edinburgh

fraction of the ceramic preform considering a perfect replication from and occupation of the original template phase. The increase is likely due to the large shrinkage of the replica reported above, but cannot be relied upon as a means of achieving high solid volume fractions due to loss of architectural integrity. However, replication with printed templates achieves lower pore size (approximately 20 μm), observed in *Figure 6.11 (f)*, compared to those known in literature (*Figure 6.3*).

Despite improvements, the reported LAGP replica preforms were mechanically unstable during handling making further testing or processing difficult. The poor mechanical stability suggested poor interconnectivity of grains, thin sample thickness and closed porosity acting as stress concentrators. Therefore, the replicas likely have low ionic conductivity. This was due in part to the large shrinkage of the replicas from the template and possible presence of hollow struts, which remained an issue. However, the preforms where recovered and crushed for PXRD characterisation of the crystal structure of the replicated LAGP. *Figure 6.13* reports the diffraction patterns of a replicated preform, prepared according to the characterisation section (**Section 6.4**), compared to a reference pattern, pelletised LAGP and aluminium phosphate impurity.

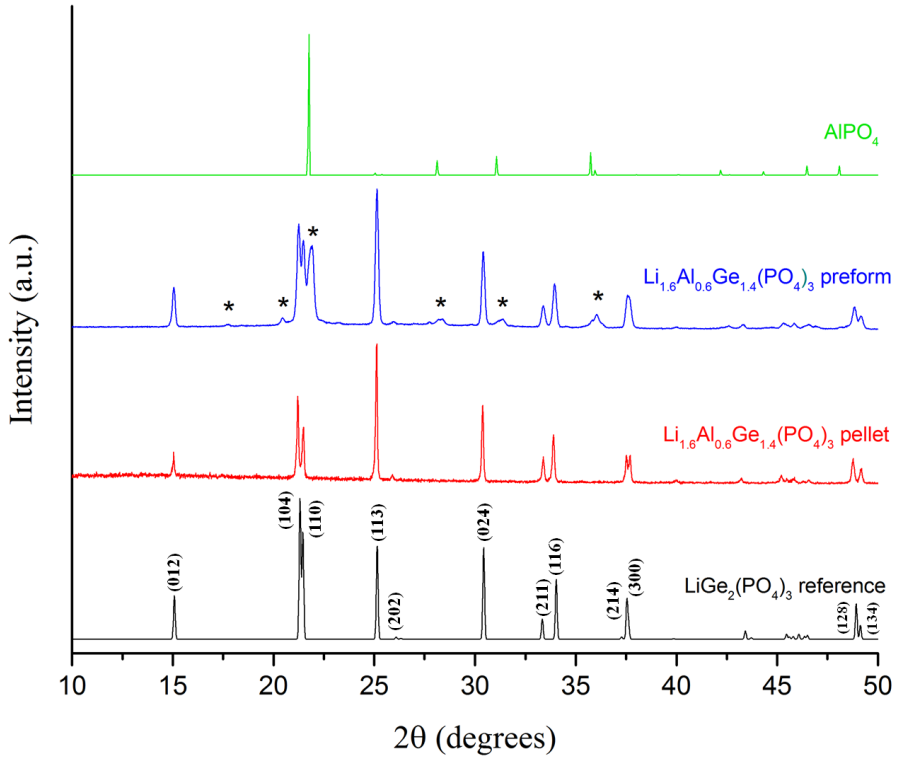

Figure 6.13 Calculated PXRD diffraction pattern of $LiGe_2(PO_4)_3$ and $AlPO_4$, experimental diffraction patterns for an LAGP pellet and LAGP preform via replication and (*) impurity.

The diffraction patterns confirm the formation of LAGP and are similar for all samples prepared by this replication synthesis. There is a large increase in impurity (aluminium phosphate) compared to the LAGP pellet (*Figure 6.13* (*) peaks), likely due to the increased lithium loss during sintering of the thin layered 3D-ceramic preform with high surface-area-to-volume.[4] The other two impurity peaks at 17 ° and 21 ° are reported to be germanium oxide.[2] Other potential causes of impurity include inadequate mixing of ceramic ions in the pre-ceramic polymer during replication, lack of ceramic compression and contact with polymer/carbonaceous material from the template during sintering. A series of experiments utilising ball milling, uniaxial pressing and added polymer material could be carried out to ascertain the exact cause of

impurity, but the replication procedure still prevents any adaptation in this way. *Figure 6.14* shows a SEM image of the surface of the ceramic preform (*Figure 6.11*) that shows the impurity phases as darker and lighter regions between LAGP grains. The ionic conductivity will decrease with large quantities of non-conductive impurity.

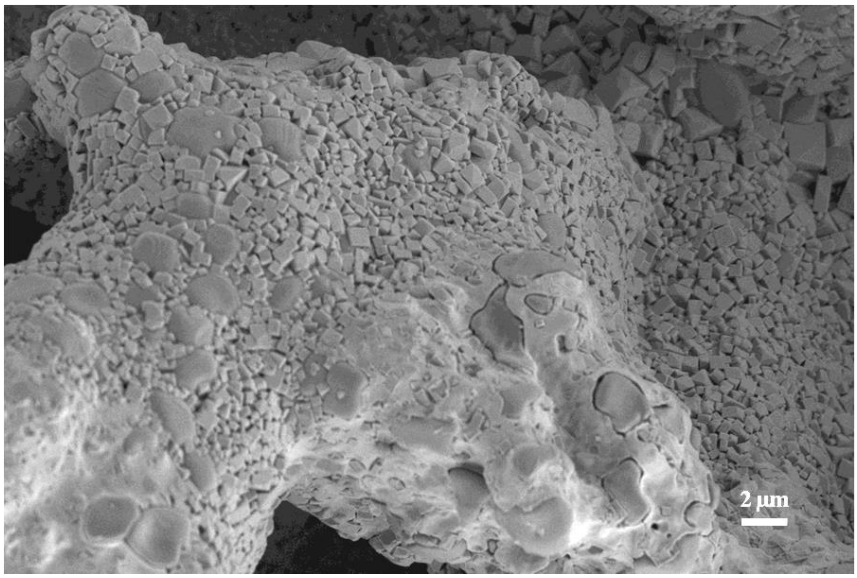

Figure 6.14 SEM image of the LAGP replica surface showing the different morphologies of impurity and grains.

Another approach to increasing the solid volume fraction of replicas is modifying the viscosity of the precursor. Richardson *et al*. showed that increasing the viscosity of infiltrating sol-gel precursor would result in complete filling of the template porosity rather than coating the template surface.[5] The result is a ceramic preform that is more similar to sacrificial templating than replication. However, sacrificial templating is superior for filling the template pore phase, as ceramic particles undergo minimal mass change during synthesis. Nevertheless, varying the viscosity of sol-gel precursor may lead to thicker coatings for replicas, as discussed above, reducing the amount of

shrinkage for hierarchical templates. This investigation is not within the scope of this work, though is a potentially valuable synthesis route for future work.

The replicas reported in this section do not meet the requirements of an oxide ceramic electrolyte preform for further investigation as a composite reinforcement. Nevertheless, the investigated technique demonstrates lower pore size than previously reported replication procedures (*Figure 6.3*). The following section reports the investigation of sacrificial templating for ceramic preform formation.

6.5.2. Sacrificial Templating

6.5.2.1. Sacrificial Particles

The sacrificial templating procedure, discussed in **Chapter 1 Section 1.9** and the previous chapter (**Chapter 5 Section 5.5.1**), typically uses dispersed particles of sacrificial material as templates. The sacrificial particle number, size and distribution define the solid volume fraction (relative density) and the presence of 3D-interconnectivity of the ceramic preform porosity. However, these properties are mutually exclusive, as increasing the solid volume fraction of the preform by reducing particle number results in non-guaranteed 3D-interconnected porosity. Achieving a ceramic preform with high solid volume fraction and 3D-interconnected porosity from the template will maintain inherent ceramic compressive strength and enable complete infiltration of reinforcement, but is a considerable challenge. CAD and stereolithography have demonstrated, in the previous chapter (**Chapter 5 Section 5.5.1**), the ability to create 3D-interconnected low solid volume fraction templates, which aim to fabricate the desired preforms by sacrificial templating.

Kokal *et al*. showed the fabrication of 3D-porous interconnected $Li_5La_3Ta_2O_{12}$ (LLTO) via a colloidal crystal sacrificial templating procedure, but with low solid volume fraction (*Figure 6.15*).[6]

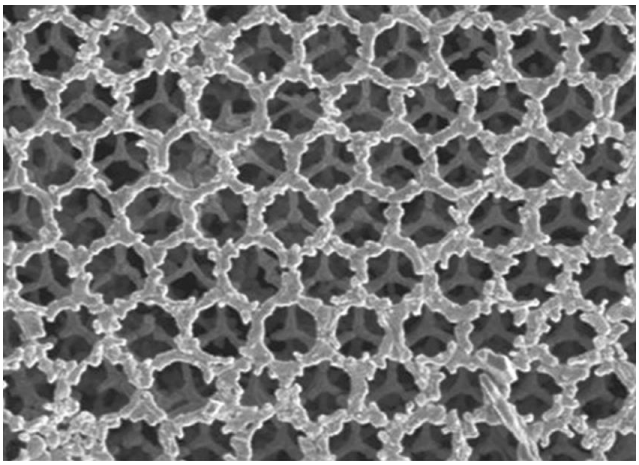

Figure 6.15 SEM image of LLTO preform fabricated from 5 μm mono-dispersed polystyrene sacrificial templates.[6]

6.5.2.2. Printed Templates with Sacrificial Templating Sedimentation

This section first investigates the use of printed templates, fabricated in the previous chapter (**Chapter 5 Section 5.5.1.4**), with a typical sacrificial templating procedure involving ceramic particle suspension sedimented during drying. The solid volume fraction of the printed template is 15 %, with the potential to introduce 15% porosity into the ceramic, being lower than other reported syntheses (*Figure 6.3*). An initial synthesis was used, similar to the experimental methods section (**Section 6.3.2**), to demonstrate the typical sacrificial templating with sedimentation via drying in ambient conditions. *Figure 6.16* shows SEM images of a ceramic preform fabricated via sacrificial templating of a gyroid template with ceramic particle sedimentation and drying.

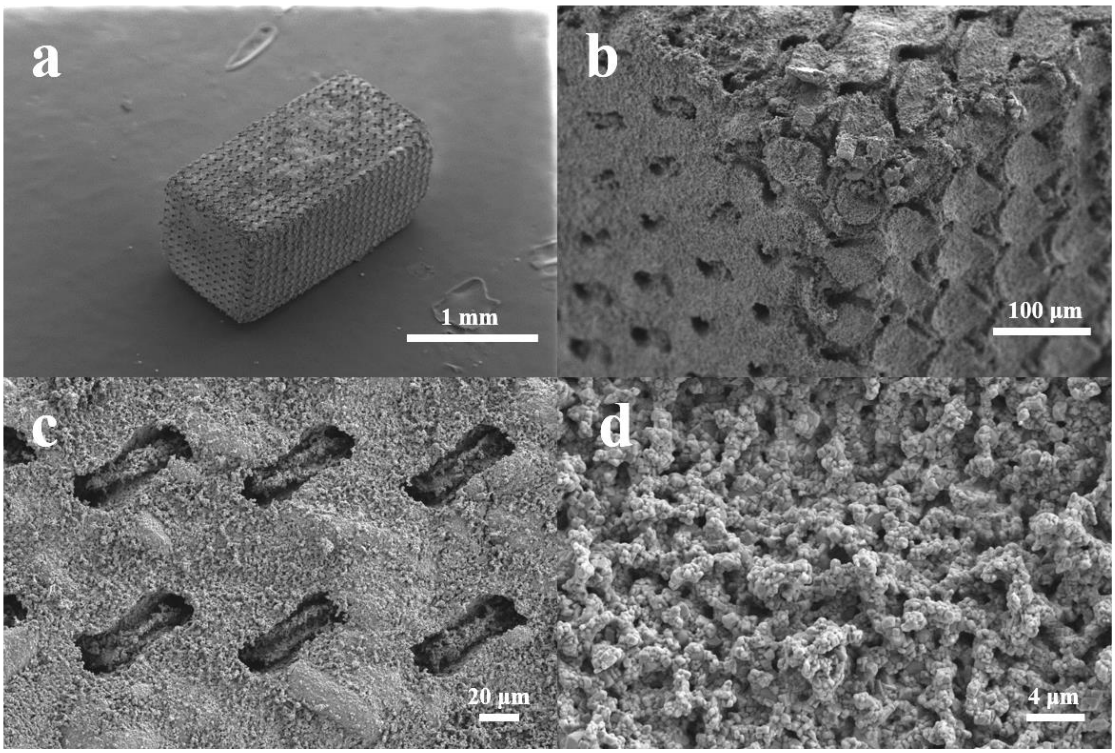

Figure 6.16 SEM images of an LAGP preform fabricated via sacrificial templating of a gyroid template with sedimentation and drying of an LAGP suspension.

The microstructure of the ceramic preform is visible and the porosity well resembles that of the gyroid template (*Figure 6.16*). However, the reproduction from the template is poor with the microstructure being compromised by a secondary ceramic phase (*Figure 6.16 (b)* and *(c)*). The LAGP surface also shows significant micro-porosity (*Figure 6.16 (d)*), indicating poor compaction of the ceramic during sedimentation that may cause issues with the reproduction of microstructure. In order to improve the compaction of LAGP and therefore reproduction of template microstructure, an adapted procedure was developed.

6.5.2.3. Adapted Sacrificial Templating Procedure

The first challenge of a sacrificial templating procedure with a 3D-interconnected template is impregnation. Unlike typical procedures, the printed

templates cannot be mixed or suspended into a ceramic particle suspension or precursor. Instead, a ceramic particle suspension or precursor must be impregnated into the template. The previous section demonstrated the inadequate impregnation by sedimentation, where compaction of the ceramic particles into the template was insufficient. Improving the compaction is important for fabricating the ceramic preform with high density. This is likely to assist in sintering and give the ceramic preform adequate ionic conductivity.

The adapted procedure for sacrificial templating of oxide ceramic electrolyte with 3D-interconnected templates utilises centrifugation as a means of efficient consolidation and compaction of the continuous ceramic matrix phase, as described in the experimental methods section (**Section 6.3.2**). The procedure utilises the templates reported in the previous chapter (**Chapter 5 Section 5.5.1.4**) to ensure fabrication of ceramic preforms applicable to FR-CMC with IPC microstructure. *Figure 6.17* illustrates the novel sacrificial templating procedure. Here, a uniform suspension of ceramic is formed (*Figure 6.17 (a)*) and then a 3D-interconnected sacrificial template is infiltrated with said suspension by soaking (*Figure 6.17 (b)*). The continuous ceramic phase consolidates within the template on centrifugation and drying (*Figure 6.17 (c)*) before removal of sacrificial material to leave 3D-interconnected porosity (*Figure 6.17 (d)*).

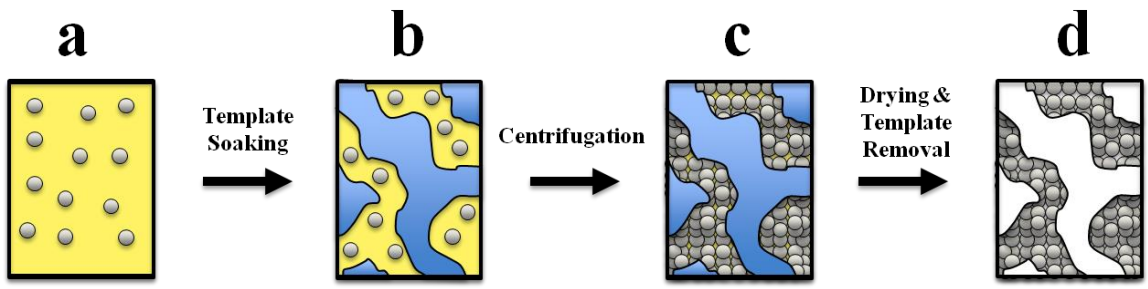

Figure 6.17 Schematic representation of the adapted sacrificial templating procedure with stages: (a) ceramic particles (grey) suspended in solvent (yellow), (b) template (blue) soaking, (c) centrifugation and (d) template removal and ceramic sintering.

Figure 6.18 reports SEM images of the *(a)* gyroid, *(b)* diamond, *(c)* cubic and *(d)* bijel architectures of *(i)* templates, *(ii)* templates impregnated with LAGP after drying at 80 °C for 24 h (*Figure 6.17 (c)*) and *(iii)* the sintered preforms (*Figure 6.17 (d)*). The sintered LAGP preforms were fabricated according to the procedure described in the experimental methods section (**Section 6.3.2**). The close contact between ceramic and polymer phases suggests successful impregnation and consolidation of the continuous ceramic matrix inside the templates (*Figure 6.18(ii)*). The bright white seen in some of the images indicates electron charging of the polymer templates. Removing the sacrificial templates on sintering determines the success of the impregnation, consolidation and compaction of the ceramic.

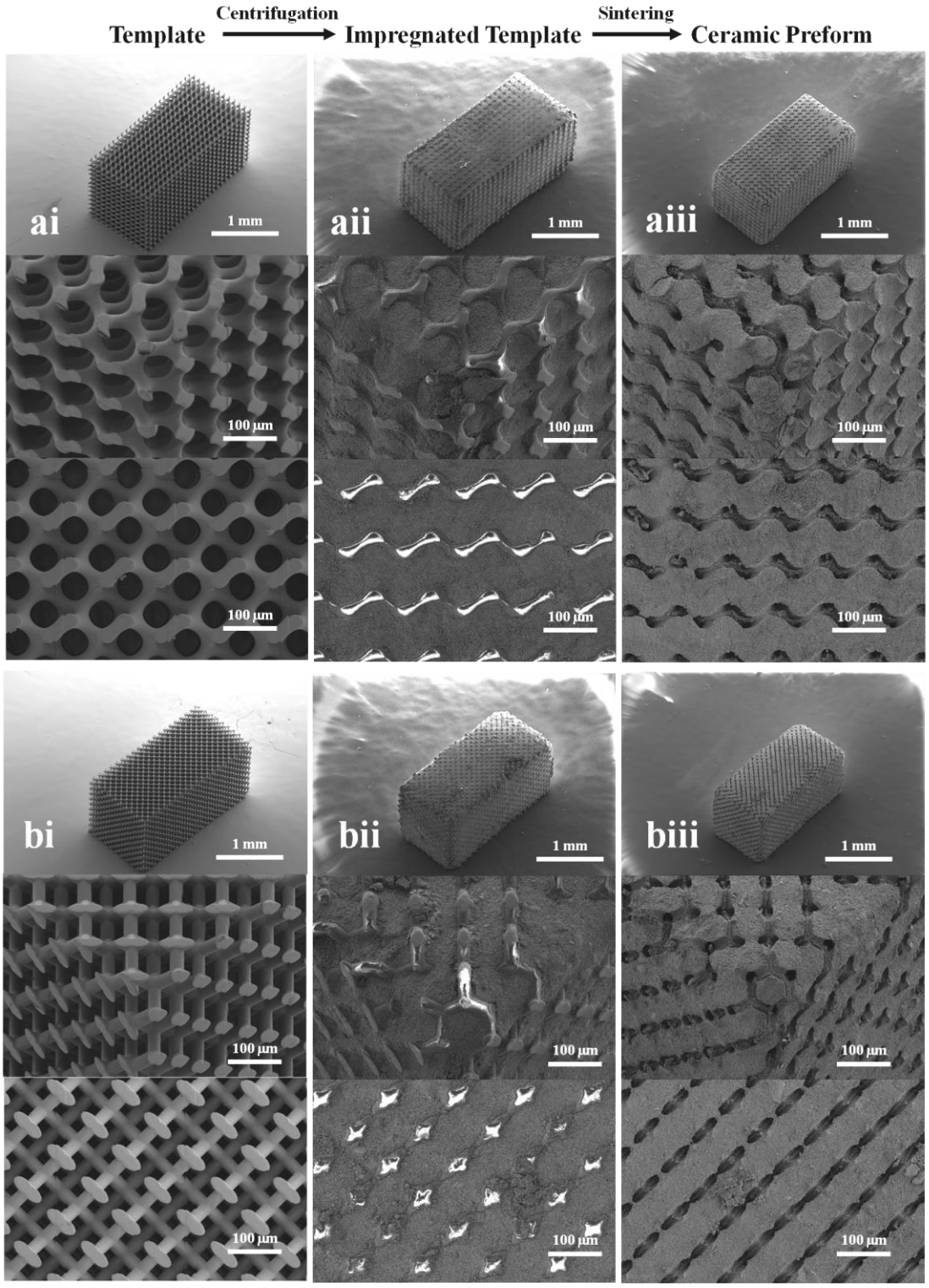
Template
Centrifugation
Impregnated Template
Sintering
Ceramic Preform
ai
aii
aiii
bi
bii
biii
1 mm
100 µm

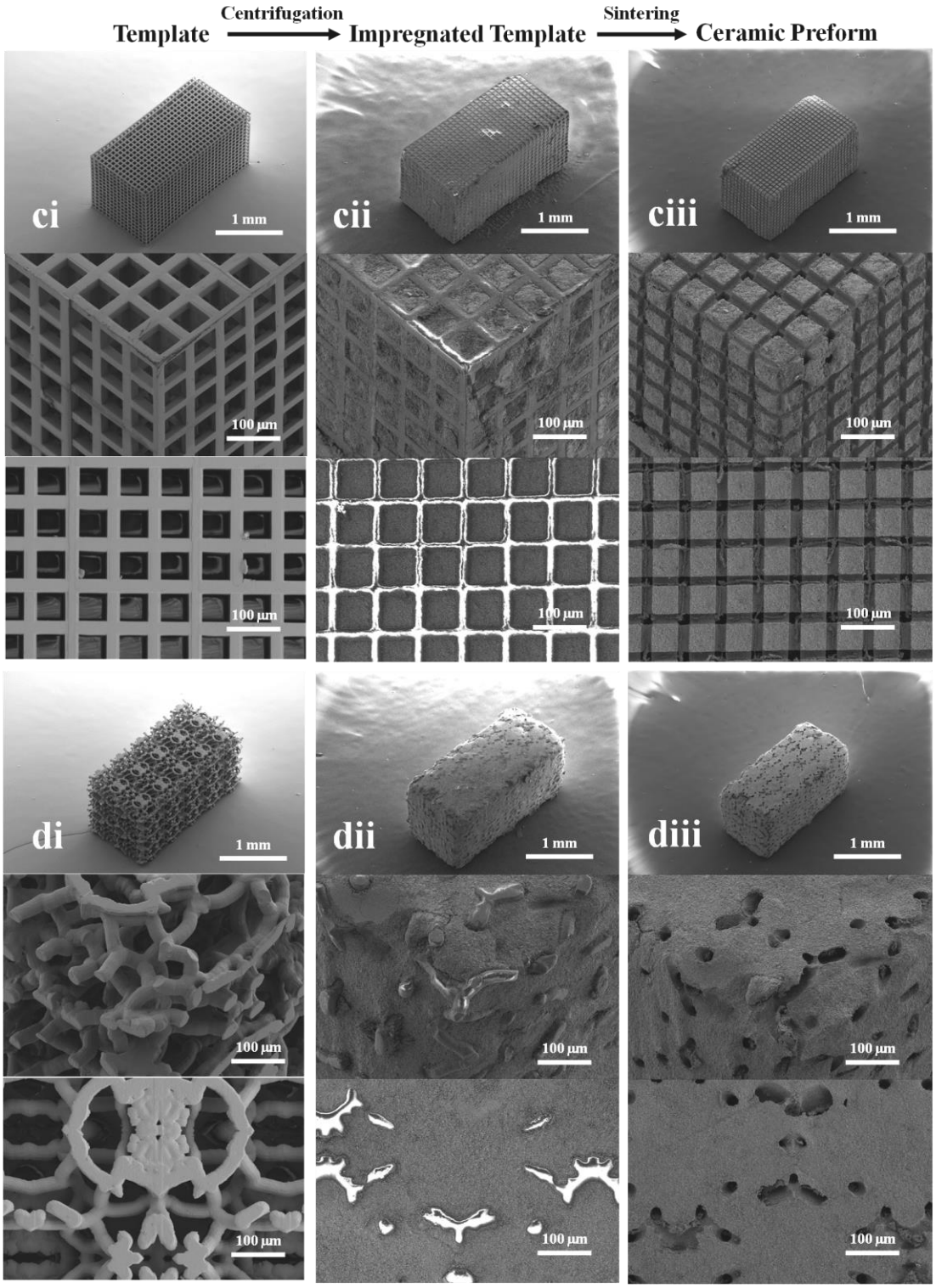

Figure 6.18 SEM images of the (a) gyroid, (b) diamond, (c) cubic and (d) bijel architectures of (i) the template, (ii) the impregnated template with LAGP and (iii) the sintered LAGP via centrifugation with magnification (top to bottom) corner view x25, corner view x200, top view x200.

For all the freestanding ceramic preforms it appears that successful sacrificial templating has occurred. The pore architecture of the preforms appears to coincide with that of the sacrificial templates, indicating successful and intended templating. The reproduced template microstructure in the prepared preforms (*Figure 6.18 (iii)*) is superior to that previously reported for sedimentation drying (*Figure 6.16*). This suggests compaction by centrifugation improves reproduction. It is clear that sacrificial templating achieves a preform with much higher solid volume fraction than replication; therefore, one expects an increased mechanical stability and strength. Indeed, the preforms are mechanically stable by touch and can be handled. *Figure 6.18 (iii)* also shows secondary LAGP deposits in the channels of the final sintered preforms, but much less than previously reported (*Figure 6.16*). The secondary LAGP deposits are likely the result of degradation of the ceramic surface, caused by loose ceramic particles being pulled from the surface by the receding template on combustion removal.

Higher magnification SEM analysis, reported in *Figure 6.19*, shows the microstructure of the LAGP grains. The grains appear well sintered with good interconnectivity and low porosity, suggesting good ionic conductivity. This further highlights the benefit of the centrifugation compared to sedimentation on drying (*Figure 6.16 (d)*) The theoretical density of LAGP is 3.42 g cm^{-1}.[7] The pellet density of LAGP, reported in **Chapter 3 Section 3.5.1**, was 3.02 g cm^{-1}, which has a relative density (fraction of theoretical density) of 0.88. The reported preforms prepared by sacrificial templating (*Figure 6.18 (iii)*) had an LAGP density (excluding the introduced porosity) of 2.67 g cm^{-1}, which is a relative density of 0.78. This suggests increased porosity in the solid LAGP preforms than the pressed pellet of LAGP which may lower the comparable conductivity. However, the relative preform density becomes 0.66 when

including the introduced porosity into the calculation. Compared to the literature values reported in *Figure 6.4*, this value is at the upper range of relative densities possible for sacrificial templating and preform formation in general. This suggests high relative compressive strength being adequate for FR-CMC. Therefore, the following section and chapter reports further investigation with these preforms.

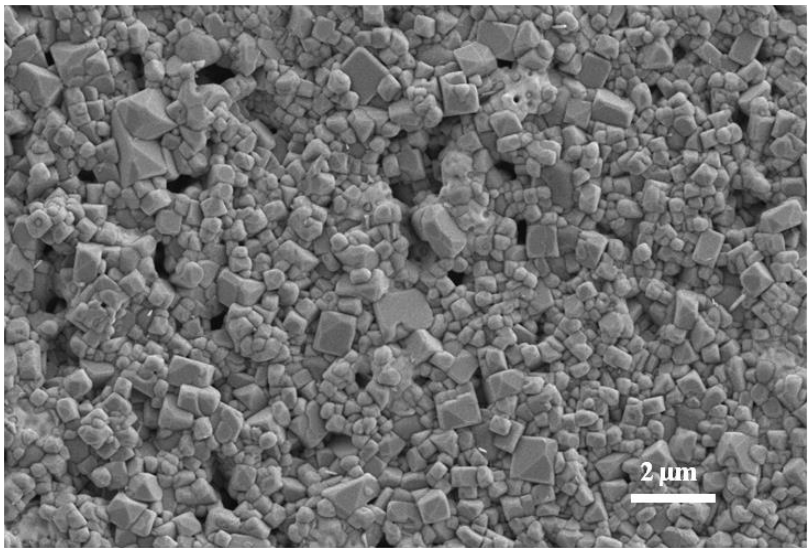

Figure 6.19 SEM image of the LAGP preform surface microstructure via adapted sacrificial templating with centrifugation.

6.5.2.4. Ceramic Preform Analysis

PXRD characterises the crystal structure of the LAGP formed during the sacrificial templating procedure. *Figure 6.20* reports the diffraction patterns of crushed samples prepared according to the characterisation section (**Section 6.4**).

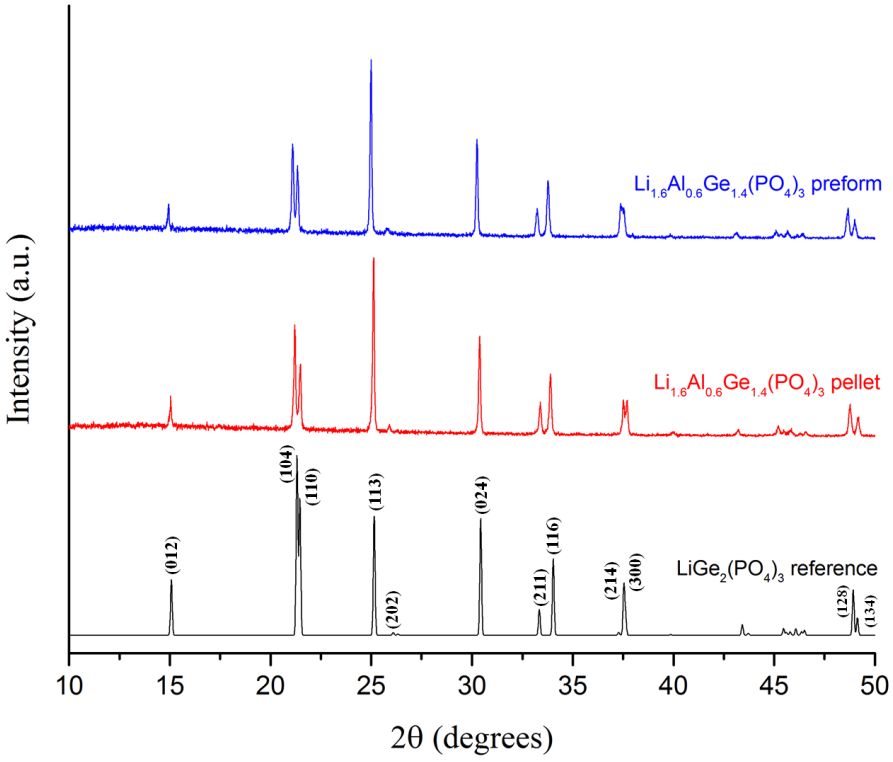

Figure 6.20 Calculated PXRD diffraction pattern of $LiGe_2(PO_4)_3$ and experimental diffraction patterns for an LAGP pellet and LAGP preform via sacrificial templating.

The diffraction patterns confirm the presence of LAGP formed via sacrificial templating and are comparable to the pellet pattern and calculated reference. There is no discernible increase of impurity for LAGP prepared in this way. This is a substantial improvement compared to the PXRD of replicated LAGP preforms that showed large amounts of impurity (*Figure 6.13)*. This is likely due to the higher solid volume fraction and lower surface-area-to-volume of the ceramic formed by sacrificial templating, discussed below.

Figure 6.21 shows images of computational 3D models taken as 500 x 500 x 500 µm portions of total µCT data. Linkage analysis, described in the characterisation section (**Section 6.4**), evaluates the 3D models for 3D-interconnectivity in both sample and channel phases. The analysis confirms that each model had a 3D-interpenetrating

microstructure required for FR-CMC fabrication (enabling complete infiltration of reinforcement).

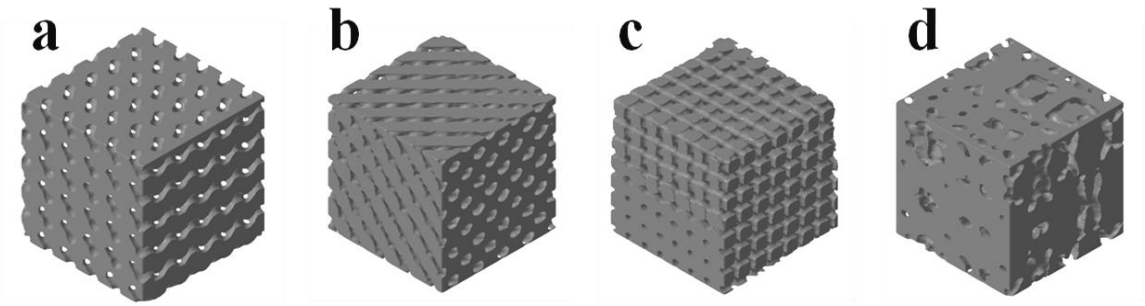

Figure 6.21 3D-rendered computational 500 x 500 x 500 µm models from µCT data of the (a) gyroid, (b) diamond, (c) cubic and (d) bijel LAGP preforms via sacrificial templating.[3]

The 3D models allow for microstructural parameter analysis, according to the characterisation section (**Section 6.4**). Comparing the microstructural parameters of LAGP ceramic preforms (*Figure 6.18 (iii)*) against the templates used to introduce porosity, indicates the quality of microstructural reproduction via the adapted sacrificial templating procedure with 3D-interconnected templates. *Table 6.1* reports the solid volume fraction (SVF) and internal surface-area-to-volume ratio (SAVR) of 3D models for the LAGP preforms formed via sacrificial templating (*Figure 6.21*) and the designed template architectures, reported in the previous chapter (**Chapter 5 Section 5.5.1.3**).

[3] µCT data acquired and provided by Dr Job Thijssen at the School of Physics and Astronomy, The University of Edinburgh

Table 6.1 Solid volume fraction and internal surface-area-to-volume ratio of different templates and LAGP preforms via sacrificial templating.

Architecture	Template SVF (%)	Preform SVF (%)	Template Internal SAVR for a unit of volume (μm^{-1})	Preform Internal SAVR for a unit of volume (μm^{-1})
Gyroid	15.6	72.6	0.14	0.04
Diamond	15.4	72.5	0.16	0.05
Cubic	15.6	71.4	0.22	0.04
Bijel	15.6	78.2	0.14	0.03

The solid volume fraction for LAGP preforms (*Table 6.1*) fabricated via the adapted sacrificial templating procedure (*Figure 6.21*) are significantly greater than those, previously reported in **Section 6.5.1.3,** fabricated via replication (55%). This suggests that preforms formed via sacrificial templating will achieve better compressive strength than via replication, also confirmed by the high relative density and stability in handling reported in the previous section.

Ceramic preforms formed via sacrificial templating occupy the pore phase of the original template (*Figure 6.17*). An ideal sacrificial templating procedure would result from the exact reproduction of the template microstructure to the introduced porosity of the ceramic preform. In this case, the solid volume fraction of both template and preform would equal 100 %. The solid volume fraction of the ceramic preforms (*Table 6.1*) was lower than expected for an ideal formation from templates. For instance, the ideal solid volume fraction of the gyroid preform would be 84.4 % instead of 72.6 %. Here, the bijel ceramic preform is closest to the ideal solid volume fraction at 78.2 %. This indicates a non-ideal reproduction of template microstructure to the introduced

porosity of the ceramic preform via the adapted sacrificial templating procedure with 3D-interconnected templates.

Shrinkage may account for the lower than expected solid volume fraction observed for LAGP preforms (*Table 6.1*). The first shrinkage from the computational 3D model template designs is after printing. Printed samples are known to shrink after being prepared for use by washing and drying due to the removal of remaining un-polymerised monomer resin. However, the major shrinkage is observed after sintering to form the final ceramic preforms as the material densifies (*Figure 6.18 (ii) and (iii)*).

The surface-area-to-volume ratio is an indicator to the number of local reinforcements intercepted by a crack in the final FR-CMC (**Chapter 4 Section 4.5.2**). A larger surface-area-to-volume ratio of materials with the same solid volume fraction would indicate more iterations of an architectural geometry and therefore more iterations of interceptable local reinforcements that increase stress transfer efficiency. From the computationally designed internal surface-area-to-volume ratio of the templates (*Table 6.1*), the cubic architecture has the highest ratio (0.22 μm^{-1}). However, the non-ideal sacrificial templating procedure results in a non-uniform increase in solid volume fraction of the preforms from the designed template architectures. This has the effect of changing the relative values of internal surface-area-to-volume ratio so that the cubic architecture no longer has the highest ratio. After formation, the diamond architecture preform has the highest internal surface-area-to-volume ratio of 0.05 μm^{-1} making it the best for stress transfer efficiency of subsequent FR-CMC.

The sample thickness and channel size are 3D-structure thickness analyses of the solid and empty volumes of 3D-porous material, respectively. With an ideal sacrificial templating procedure, the sample thickness parameters of a template equal the channel

size parameters of a preform and vice versa. The sample thickness distribution and channel size distribution standard deviations are a measure of how the distributions differ from the mean value. The sample thickness distribution and channel size distribution standard deviations indicate the degree of uniformity in either solid or pore (empty) phase of the template and preform and therefore the creation of bottlenecks affecting ionic conductivity, mechanical properties and isotropic nature of reinforcement (**Chapter 4 Section 4.5.2**).

Table 6.2 reports the sample thickness distribution (STD) and channel size distribution (CSD) standard deviations of 3D models formed from µCT data for the LAGP preforms formed via sacrificial templating (*Figure 6.21*) and the designed template architecture, reported in the previous chapter (**Chapter 5 Section 5.5.1.3**). The preform channel size distribution standard deviation increases compared to the template sample thickness distribution standard deviation and vice versa for all architectures apart from the diamond sample thickness distribution. This is possibly due to uneven shrinkage of the solid vs. empty volume (*Table 6.1*). The increasing standard deviations indicate the worsening of the microstructural integrity upon preform formation. After formation, the gyroid architecture preform has the lowest sample thickness distribution and channel size distribution standard deviations (2.65 µm and 2.22 µm, respectively), making it the most evenly distributed of volumes in both phases. This should result in fewer bottlenecks in the subsequent FR-CMC.

Table 6.2 Sample thickness distribution (STD) and channel size distribution (CSD) standard deviations of different templates and LAGP preforms via sacrificial templating.

Architecture	Template STD Standard Deviation (µm)	Preform CSD Standard Deviation (µm)	Template CSD Standard Deviation (µm)	Preform STD Standard Deviation (µm)
Gyroid	0.65	2.22	2.24	2.65
Diamond	1.50	3.22	5.43	4.31
Cubic	4.42	4.68	6.75	7.98
Bijel	4.20	5.67	23.07	25.69

The average sample thickness and average channel size define the magnitude of the sample thickness distribution and channel size distribution, respectively. With an ideal sacrificial templating procedure, the average sample thickness of the template equals the average channel size of the preform and vice versa. The average sample thickness and channel size of a preform has an effect on the mechanical properties of the final FR-CMC, indicating the area of ceramic and reinforcement, respectively, intercepted by a crack (**Chapter 4 Section 4.5.2**).

Table 6.3 reports the average sample thickness and average channel size of the 3D models formed from µCT data for the LAGP preforms formed via sacrificial templating (*Figure 6.21*) and the designed template architecture (**Chapter 5 Section 5.5.1.3**). The average sample thickness of the preforms decreases compared to the average channel size of the templates. For the gyroid, the channel size decreases from 67.0 µm for the template to 45.0 µm average sample thickness of the preform. Such a decrease suggests shrinkage and surface degradation of the preform previously reported above. However, the average channel size of the preforms remains similar to the average sample thickness of the templates, except for the cubic architecture. This

suggests shrinkage and surface degradation of preforms on sintering has more of an effect than the shrinkage of the templates, because the average channel size of the preform changes less than the average sample thickness. This confirms the previous observation made from SEM (*Figure 6.18*) and solid volume fraction calculations (*Table 6.1*) about the shrinkage of preforms on sintering. On the other hand, the average channel size of the cubic preform (21.3 μm) increases from the average sample thickness of the cubic template architecture (15.7 μm), unlike the other architectures. This suggests a mode of microstructure degradation specific to the cubic architecture that either hinders sacrificial templating or promotes shrinkage or surface degradation. The right angles of the cubic architecture are one possible cause, indicating templates with harsh angles (instead of curvature like the gyroid) impede the preform formation procedure.

Table 6.3 Average sample thickness and channel size of different templates and LAGP preforms via sacrificial templating.

Architecture	**Template Average Sample Thickness (μm)**	**Preform Average Channel Size (μm)**	**Template Average Channel Size (μm)**	**Preform Average Sample Thickness (μm)**
Gyroid	20.6	21.8	67.0	45.0
Diamond	20.1	19.3	66.9	43.0
Cubic	15.7	21.3	67.0	45.2
Bijel	23.4	23.2	69.9	60.5

The average sample thickness of the bijel preform (60.5 μm) (*Table 6.3*) is significantly higher than the other architectures (~45 μm) and much closer to the

template average channel size (69.9 µm). The better reproduction of preform thickness is also seen in the higher solid volume fraction of the bijel preform (*Table 6.1*), suggesting the bijel architecture promotes successful sacrificial templating. The significantly higher template channel size distribution standard deviation (*Table 6.2*) of the bijel architecture (23.07 µm), though the origin of smaller channels and potential bottlenecks within the preform, suggests larger channels are also present to assist in the impregnation of ceramic particles during sacrificial templating.

The microstructural parameter analysis presented above indicates the most suitable preform architecture for further investigation with FR-CMC fabrication. Though the bijel architecture appears to reproduce the original template microstructure better than the other architectures, the likelihood of bottleneck effects on the FR-CMC properties is high. On the other hand, the gyroid architecture preform has similar solid volume fraction, surface-area-to-volume ratio, average channel size and sample thickness to the cubic and diamond architectures, but has the lowest sample thickness distribution and channel size distribution standard deviations. This indicates the architectures uniformity and hence reduces the likelihood of bottleneck effects in the final FR-CMC. Therefore, microstructural parameter analysis suggests the gyroid architecture is best suited for FR-CMC.

6.5.2.5. Ionic Conductivity of Preform via Sacrificial Templating

The prepared gyroid LAGP preform of the previous section was immersed and impregnated with polypropylene melt**.** On cooling and polishing, the preliminary ceramic-polymer composite was prepared for further analysis, as described in the

experimental methods section (**Section 6.3.4**). The complete infiltration of the preform with polypropylene prevents major stress concentrators of the pore architecture from mechanically failing the preform. This gives the ability to polish and sputter the surface for AC EIS. The low viscosity of the melted thermoplastic polymer, polypropylene, makes it ideal for infiltration into the preforms. Other thermoplastic and thermoset polymers are viable in this application, but the increased evacuation time on melting rather than setting, respectively, ensures complete infiltration. *Figure 6.22* shows SEM images of the gyroid preform impregnated with polypropylene and polished surface. The lighter regions of the SEM images are that of LAGP and the darker regions that show some charging (bright white) are polypropylene.

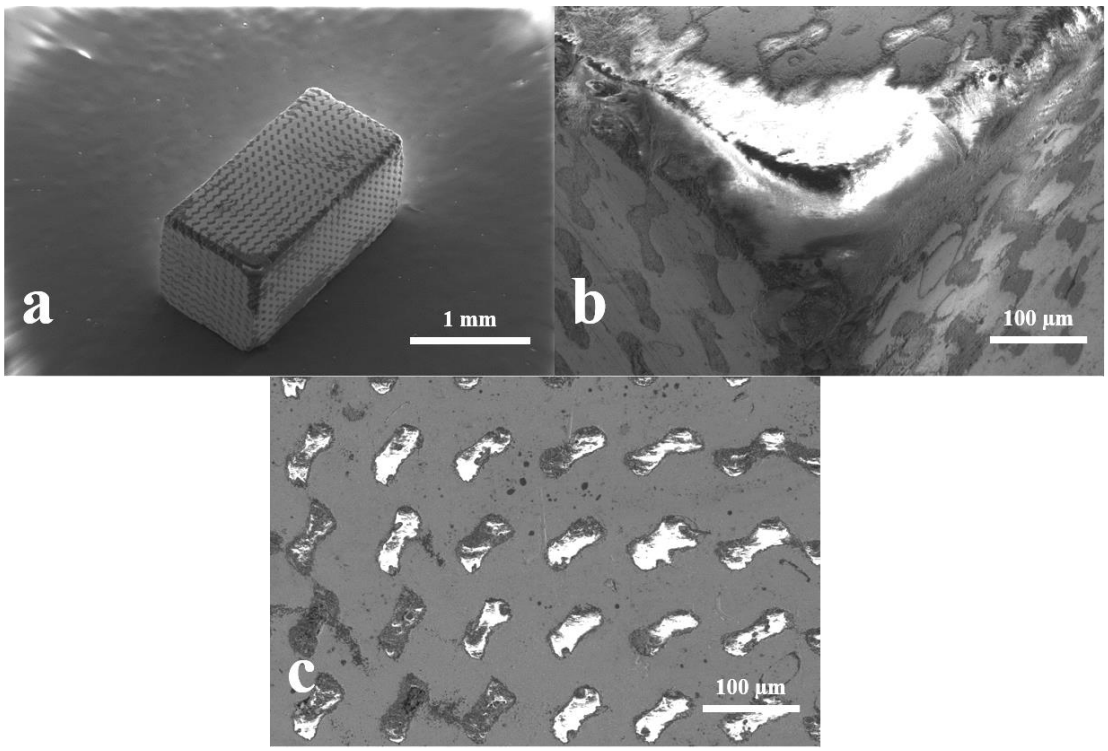

Figure 6.22 SEM images of the gyroid LAGP preform via sacrificial templating filled with polypropylene and polished with magnification (a) corner view x25, (b) corner view x200 and (c) top view x200.

Figure 6.23 shows a Nyquist plot of an LAGP pellet and the LAGP preform composite (*Figure 6.22*) derived from AC EIS, using a gold blocking electrode symmetric cell setup, prepared according to the characterisation section (**Section 6.4**). The full electrical behaviour of the preform composite, like the pellet (*Figure 3.4*), is not observed within the frequency window of the experiment at room temperature (*Figure 6.23*). Therefore, an equivalent circuit containing only a single set of parallel components, accounting for the observed experimental data, is used and only the total ionic conductivity reported (*Figure 3.4*). The full component values are reported in **Appendix 5**. The total ionic conductivity of the preform composite LAGP at room temperature is 1.69 x 10^{-4} S cm^{-1}, which is slightly lower than the LAGP pellet at 2.84 x 10^{-4} S cm^{-1}. This was expected due to the lower density observed for the sacrificial templating procedure.

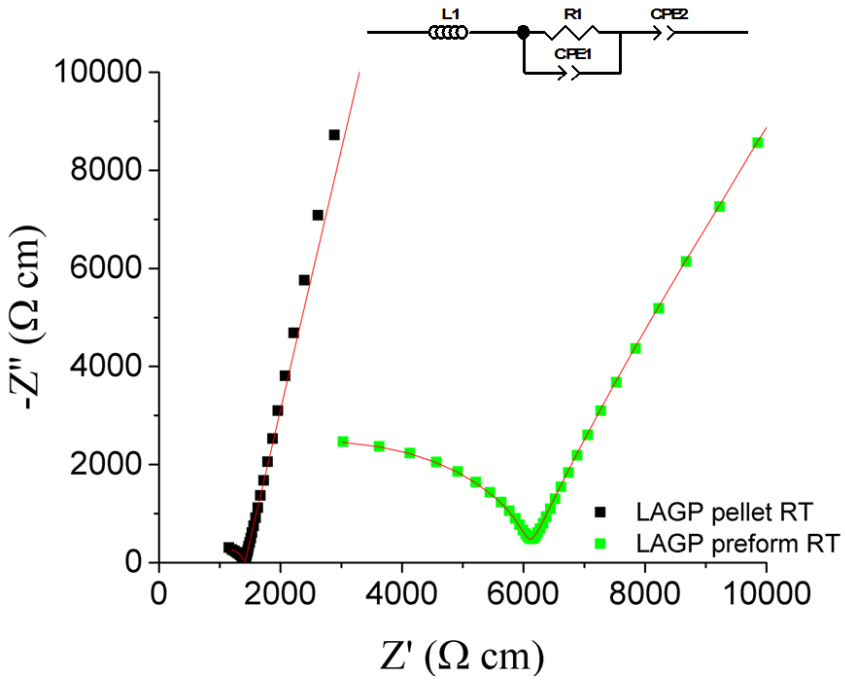

Figure 6.23 Impedance plot of an LAGP pellet and LAGP preform via sacrificial templating measured at room temperature.

Figure 6.24 shows the low-temperature measurement (-30 °C) of the LAGP pellet and LAGP preform composite with the equivalent circuits (red lines) fitting the data, with full component values reported in **Appendix 6**. The LAGP preform plot shows a depressed broad semicircle (*Figure 6.24*), which is characteristic of both bulk and grain boundary time constants merging. Like in *Figure 4.17*, this occurs when the time constants become similar and overlap at certain frequencies. A typical equivalent circuit with two sets of parallel components (**Chapter 2 Section 2.3**) is used for the preform composite (*Figure 6.24*), with an inductor and constant phase elements (CPE), according to **Chapter 3 Section 3.5.1**. Further experimental work with a four, as opposed to a two, electrode cell could be carried out to investigate the different time constants. The total ionic conductivity of the preform composite LAGP at -30 °C is 7.17 x 10^{-6} S cm^{-1}, which is also slightly lower than that of the LAGP pellet at 8.87 x 10^{-6} S cm^{-1}.

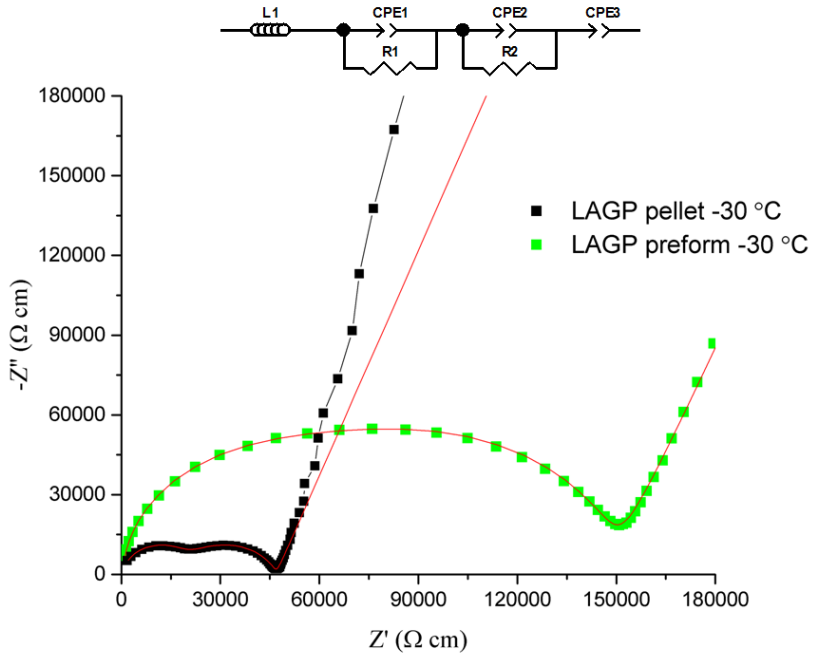

Figure 6.24 Impedance plot of an LAGP pellet and LAGP preform via sacrificial templating measured at -30 ˚C.

Figure 6.25 reports the temperature dependent total ionic conductivity of the LAGP pellet and the LAGP preform composite. The activation energy for the LAGP preform composite is 0.35 eV compared to the LAGP pellet of 0.36 eV. The activation energy and total ionic conductivity (1.69 x 10^{-4} S cm^{-1}) are well within the acceptable ionic conductivity range of LAGP.[2, 8]

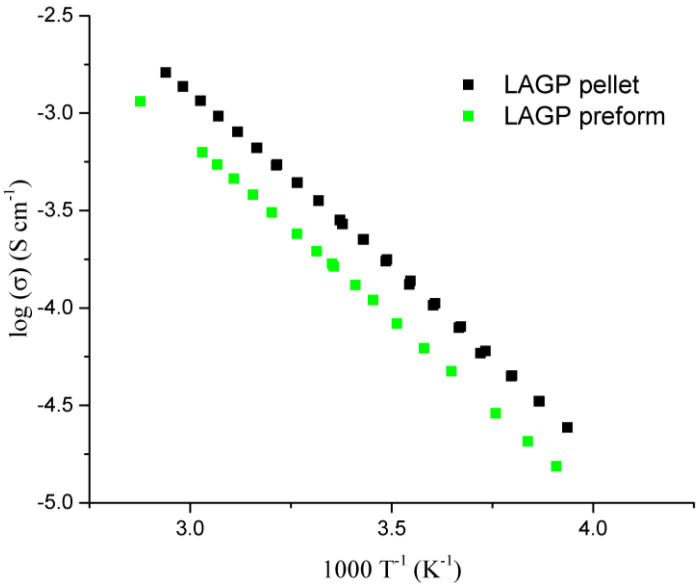

Figure 6.25 Arrhenius plot of total conductivity on heating and cooling for an LAGP pellet and LAGP preform via sacrificial templating.

The successful fabrication of an oxide ceramic electrolyte preform with adequate retention of its ionic conductivity is a great achievement. The preforms prepared via sacrificial templating have excellent relative density, good retention of ionic conductivity and 3D-interconnected porosity for reinforcement infiltration. For this reason, sacrificial templating has demonstrated far greater potential than replication to produce preforms for further investigation. Therefore, the fabrication of a FR-CMC in the following chapter utilises the prepared gyroid preforms reported in this chapter by adapted sacrificial templating with printed templates.

6.6. Conclusion

The templates presented in **Chapter 5** have been used to investigate two different preform formation procedures: replication and sacrificial templating. For replication, stereolithographically printed templates have achieved much lower replica pore sizes than those previously reported. Hierarchical microstructures have been used in an attempt to remove hollow struts and increase solid volume fraction of ceramic replicas compared to previously reported procedures. The replication procedure has been modified to improve the architectural integrity of the replica by adjusting the hierarchical microstructure. However, the solid volume fraction remains too low for retention of mechanical strength and shrinkage too high for retention of gyroid architectural integrity and sizes comparable to the original template. The final replicas also showed solid impurity, identified via PXRD and SEM, which would have a detrimental effect on ionic conductivity.

Sacrificial templating has been investigated with 3D-interconnected templates to improve the solid volume fraction, architectural integrity and shrinkage limitations of replication. The 3D-interconnected templates guarantee the 3D-porous interconnectivity of the ceramic preforms with high solid volume fraction. An adapted sacrificial templating procedure has been developed to produce ceramic electrolyte preforms with good reproduction of the original template microstructure and adequate ionic conductivity. Furthermore, microstructural parameter analysis has concluded that the gyroid architecture is best suited in FR-CMC. These presented preforms are suitable for further investigation in fabricating fibre-reinforced ceramic matrix composites. Therefore, the following chapter investigates fibre-reinforced ceramic matrix

composites with LAGP preforms fabricated via sacrificial templating with printed templates.

6.7. References

[1] Studart, A. R., Gonzenbach, U. T., Tervoort, E. & Gauckler, L. J. Processing routes to macroporous ceramics: a review. *J. Am. Ceram. Soc.* **89**, 1771-1789 (2006).

[2] Zhang, M. *et al*. Preparation and electrochemical properties of Li1+xAlxGe2-x(PO4)3 synthesized by a sol-gel method. *J. Electrochem. Soc.* **159**, A1114-A1119 (2012).

[3] Colombo, P. Conventional and novel processing methods for cellular ceramics. *Philos. Transact. A Math. Phys. Eng. Sci.* **364**, 109-124 (2006).

[4] Francisco, B. E., Stoldt, C. R. & M'Peko, J. Lithium-ion trapping from local structural distortions in sodium super ionic conductor (NASICON) electrolytes. *Chem. Mater.* **26**, 4741-4749 (2014).

[5] Richardson, J. T., Peng, Y. & Remue, D. Properties of ceramic foam catalyst supports: pressure drop. *Appl. Catal., A* **204**, 19-32 (2000).

[6] Kokal, I., van den Ham, E. J., Delsing, A. C. A., Notten, P. H. L. & Hintzen, H. T. Preparation and characterization of three dimensionally ordered macroporous Li5La3Ta2O12 by colloidal crystal templating for all-solid-state lithium-ion batteries. *Ceram. Int.* **41**, 737-741 (2015).

[7] Yang, J., Huang, Z., Huang, B., Zhou, J. & Xu, X. Influence of phosphorus sources on lithium ion conducting performance in the system of Li2O–Al2O3–GeO2–P2O5 glass–ceramics. *Solid State Ionics* **270**, 61-65 (2015).

[8] Thokchom, J. S., Gupta, N. & Kumar, B. Superionic conductivity in a lithium aluminum germanium phosphate glass–ceramic. *J. Electrochem. Soc.***155**, A915-A920 (2008).

Chapter 7: Fibre-Reinforced Ceramic Matrix Composite Fabrication

7.1 Aim

The fabrication of oxide ceramic electrolyte preforms with desired microstructure and maintained ionic conductivity have been demonstrated, but a procedure for the infiltration of reinforcement to form the fibre-reinforced (FR) ceramic matrix composite (CMC) is still required. The main aim of this chapter is to fabricate a FR-CMC of oxide ceramic electrolyte and fibre-reinforced polymer (FRP). FRP of aramid fibres and epoxy have been selected to reinforce the ceramic matrix. The FR-CMC fabrication procedure will require complete infiltration of the ceramic preform to ensure optimal mechanical reinforcement and an analytical means of determining the enhanced mechanical properties. Fabricating a FR-CMC with enhanced mechanical properties due to reinforcement would be a substantial step in demonstrating the potential of this material in an all-solid-state battery.

7.2. Introduction

The previous chapter outlines the formation of oxide ceramic electrolyte preforms via sacrificial templating and replication. The preform structure defines the interpenetrating microstructure optimised for reinforcement. To fabricate a FR-CMC from the previously reported preforms requires an adequate reinforcement infiltration procedure. Fibre-reinforced polymer (FRP) is the most suited reinforcement for the oxide ceramic electrolyte preforms.

This chapter considers the infiltration of LAGP preforms, fabricated via sacrificial templating from stereolithography printed polymer templates, with FRP. The reinforcement aims to increase the tensile strength of the ceramic preform. The previous chapter demonstrated the introduction of IPC microstructure to the ceramic preform whilst maintaining ionic conductivity and high relative density (compressive strength). Maintaining the existing properties of the preform whilst enhancing the tensile strength requires an appropriate infiltration procedure.

The high tensile strength of fibres in the FRP aims to achieve an increased tensile strength for the FR-CMC. Long aligned fibres have anisotropic tensile strength along the fibre axis, but pose a fabrication challenge to infiltrate the 3D-porous preforms. Nevertheless, randomly arranged fibres enhance tensile strength isotropically and are theoretically more resilient to tensile forces in all directions as may be experienced by an FR-CMC with IPC microstructure in an electrochemical cell. Therefore, this chapter investigates short randomly distributed aramid fibres in an epoxy polymer matrix as a means of increasing tensile strength of the solid electrolyte.

7.3. Experimental Techniques

7.3.1. Preparation of Aramid Dispersion

An aramid dispersion was prepared according to literature.[1] 50 mL of dimethyl sulfoxide (DMSO) (99.9 %, Sigma-Aldrich), was added to a large plastic container with stir bar. 0.15 g of potassium hydroxide (>85%, Fisher Scientific) was dissolved in 0.25 mL of distilled water and added to DMSO. 0.1 g of KEV60 short chain aramid fibres (Goonvean Fibres Ltd) with maximum fibre length of 250 μm and average fibre thickness of 15 μm were added to the solution. The mixture was stirred at 400 rpm for

24 h to yield a uniform aramid dispersion. The amount of DMSO in the dispersion was reduced by rotary evaporation using a Buchi Rotavapor R-3 at 95 ˚C. The dispersion was recovered just prior to gelation to yield a concentrated viscous liquid.

7.3.2. Infiltration of Ceramic Preform with Aramid

Prepared ceramic preforms were immersed in an excess of aramid dispersion reported in the previous section (**Section 7.3.1**). The mixture was left for 12 h under dynamic vacuum before being heated to 220 ˚C for 15 minutes to remove DMSO. The sample was weighed before repeating the previous steps twice more. The final coated preform was then immersed in distilled water for 12 h and rinsed before drying at 100 ˚C for 1 h.

7.3.3. Epoxy Infiltration of Aramid-LAGP Preform

An epoxy-hardener mixture was prepared by first adding 0.4 mL of Epofix hardener (Struers ApS) to 3 mL of Epofix epoxy resin (Struers ApS) and mixing. The prepared aramid-ceramic preforms reported in the previous section (**Section 7.3.2**) were immersed in the epoxy mixture and placed under vacuum for 2 h. The preform was recovered and excess epoxy removed from the surface. The preform was left for 3 h in ambient conditions before heating at 100 ˚C for 12 h.

7.4. Characterisation

The morphology of materials was investigated using a Carl Zeiss Merlin field emission scanning electron microscope (SEM) with a Gemini II column. Samples were mounted on adhesive copper tape applied to a stub and holder. Measurements were

taken at a voltage of 1 kV with a current of 72 pA. Cross-sections were prepared using a scalpel.

The flexural strength of material beams was analysed using an Instron 3366 Dual Universal Testing System with a four-point bending adaptor. Beams were rested on the lower supports before a pre-loading sequence brought the upper beams into contact with the specimen. Force-displacement measurements were made at a rate of 5 μm min^{-1}.

7.5. Results & Discussion

7.5.1. Aramid Preparation

This work uses aramid fibres with epoxy to fabricate FRP for oxide ceramic electrolyte reinforcement, similarly to **Chapter 3**. Aramid is the highest tensile yield strength polymeric material, which makes it ideal for FRP in a solid oxide ceramic electrolyte FR-CMC. The interpenetrating microstructure of the $Li_{1.6}Al_{0.6}Ge_{1.4}(PO_4)_3$ (LAGP) ceramic preforms fabricated in the previous chapter (**Chapter 6 Section 6.5.2**) should optimise the tensile strength increase by reinforcement and maintain ceramic compressive strength and ionic conduction through the layer. Formation of FRP inside the 3D-porous LAGP preforms requires complete infiltration of the channels. The pore sizes of LAGP preforms reported in the previous chapter (**Chapter 6 Section 6.5.2.4**) present a challenge for aramid and epoxy infiltration, due to the relative size of aramid fibres.

The use of short chain aramid fibres may allow infiltration into the small pores of the LAGP preforms. *Figure 7.1* reports a SEM image of ball-milled aramid fibres known as 'KEV60' (Goonvean Fibres Ltd). The fibres are approximately 250 μm long

and 15 μm thick, in agreement with the product specifications described in the experimental section (**Section 7.3.1**).

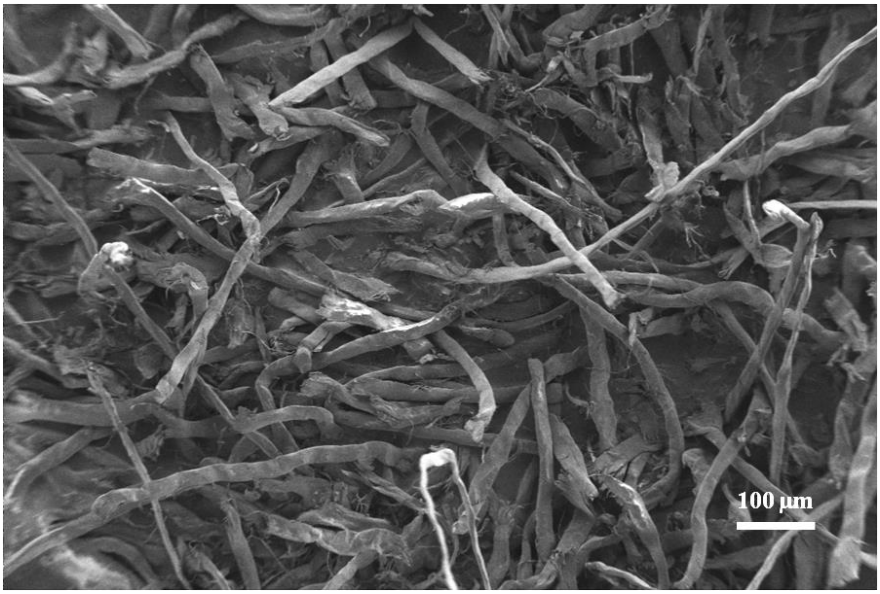

Figure 7.1 SEM image of KEV-60 ball-milled aramid fibres.

The average channel size of LAGP preforms fabricated via sacrificial templating from printed templates reported in the previous chapter (**Chapter 6 Section 6.5.2.4**) are 21.8 μm, 19.3 μm, 21.3 μm and 23.2 μm for the gyroid, diamond, cubic and bijel architectures, respectively. The aramid fibres are too large to enter the channels effectively, clogging the pores and preventing complete infiltration of the pristine fibres when mixed directly with the epoxy resin mixture. An approach to solving this issue is reducing the size of the fibres.

Yang *et al*. reported the fabrication of nanofibres by dispersing and stirring aramid in DMSO.[1] Here, the synthesis was adapted by decreasing the stirring time, as described in the experiment methods section (**Section 7.3.1**), to 24 h with KEV-60 (*Figure 7.1*). *Figure 7.2* shows a SEM image of the resulting aramid fibers being

approximately 1 μm long and 10 nm thick. The white spherical regions (*Figure 7.2*) are remaining potassium hydroxide from the synthesis, as described in the experimental methods section (**Section 7.3.1**).

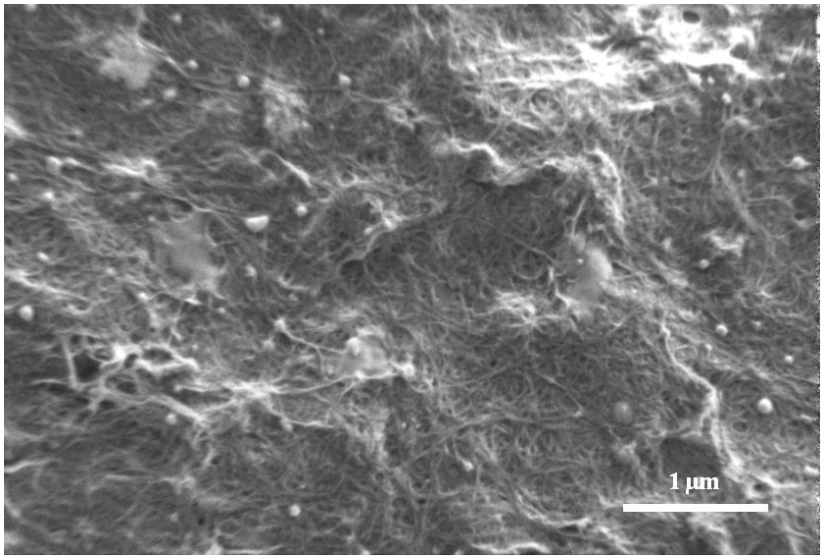

Figure 7.2 SEM image of shortened aramid fibres via DMSO dispersion.

The decrease in aramid fibre length makes the fibers more appropriate for infiltration of the LAGP preforms. Dried fibres could not be re-dispersed in epoxy resin after recovery from DMSO, due to the formation of an entangled solid (*Figure 7.2*). Martí *et al*. reported an epoxy coating synthesis from epoxy dispersed in DMSO, which represents a promising route for direct FRP fabrication and infiltration from the aramid dispersion.[2] The prepared aramid-DMSO dispersion, reported above, can be used instead of pure DMSO. However, the aramid concentration of the prepared aramid-DMSO dispersion, reported in this section as described in the experiment methods section (**Section 7.3.1**), was 8 mg mL^{-1}. Therefore, for a 1 wt% aramid mixture, 1.64 mL of aramid dispersion was required to mix with epoxy resin and hardener.

Unfortunately, the amount of DMSO added to the epoxy mixture is well above the stated amount in literature (0.33 mL), which resulted in a large amount of shrinkage.

The infiltration of ceramic preforms with this mixture was not complete due to the observed shrinkage. When 0.33 mL of aramid-DMSO dispersion was used, minimal shrinkage of the FRP was observed. However, the aramid concentration of the resultant FRP is only 0.02 wt%, which is far too low a concentration to yield optimal reinforcement in the FR-CMC.[3] Therefore, the concentration of the original aramid dispersion and low amount of DMSO required to avoid shrinkage limits the concentration of aramid in the prepared FRP. Furthermore, the concentration of the original aramid dispersion cannot be increased without gelation, limiting the aramid concentration for shrinkage free FRP.

7.5.2. LAGP Preform Infiltration and Deposition with Aramid

A two-step reinforcement infiltration procedure was considered to avoid shrinkage of the epoxy-aramid dispersion FRP, reported in the previous section (**Section 7.5.1**). An initial deposition of aramid fibres into the LAGP preforms, reported in the previous chapter (**Chapter 6 Section 6.5.2**), was made using the aramid-DMSO dispersion reported in the previous section. The experimental methods section (**Section 7.3.2**) describes the repeat infiltration of aramid dispersion and drying of the LAGP preform. *Table 7.1* reports the gravimetric analysis of a gyroid LAGP preform after repeat infiltration and drying steps showing a final deposition of 0.7 mg of aramid fibre. *Figure 7.3* shows cross-section SEM images of the final washed aramid-coated preform.

Table 7.1 Gravimetric analysis of LAGP preform infiltration with aramid dispersion and drying.

Deposition Step	Weight (mg)
0	40.38
1	40.76
2	41.14
3	41.77
Washed	41.08

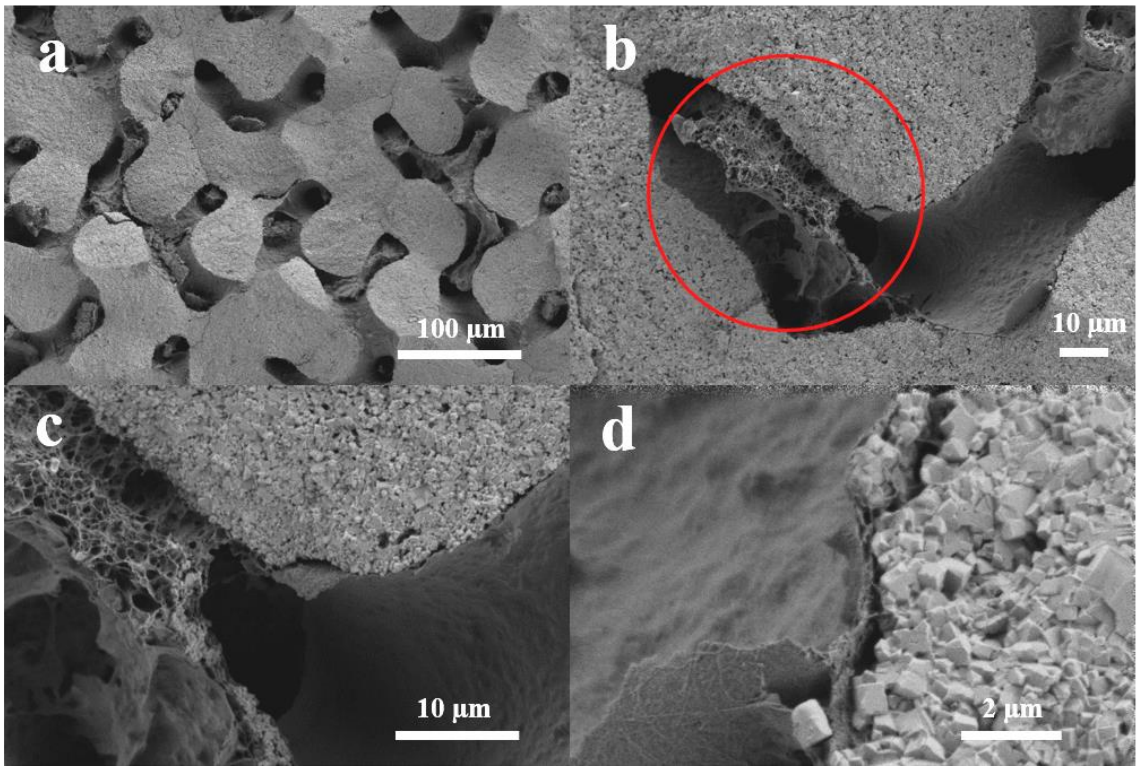

Figure 7.3 SEM cross-section images of washed aramid fibre coating on the surface of a gyroid LAGP preform.

The internal LAGP preform surface is coated in aramid fibres that are observed as darker fibrous regions against the lighter grain regions of the ceramic (*Figure 7.3*). The LAGP strands observed as artifacts in the empty pore microstructure, reported in

the previous chapter (**Chapter 6 Section 6.5.2**), are also coated with aramid fibre (*Figure 7.3 (red circle)*). The aramid-coated LAGP preform is the first step to forming the FR-CMC with epoxy infiltration being the final step.

7.5.3. FR-CMC Preparation by Epoxy Infiltration of Aramid-LAGP Preform

Fabricating the final FR-CMC requires formation of the FRP by infiltrating the aramid-coated LAGP preform reported in the previous section with epoxy. The experimental methods section (**Section 7.3.3**) describes the synthesis of the epoxy mixture infiltration of the preform. The weight of infiltrated epoxy was 4.85 mg, meaning the resultant FRP was 12.6 wt% of aramid. This is substantially higher than the aramid-epoxy dispersion reported in the previous section (**Section 7.5.1**) (0.02 wt%). *Figure 7.4* shows cross-section SEM images of the final FR-CMC with FRP after epoxy infiltration.

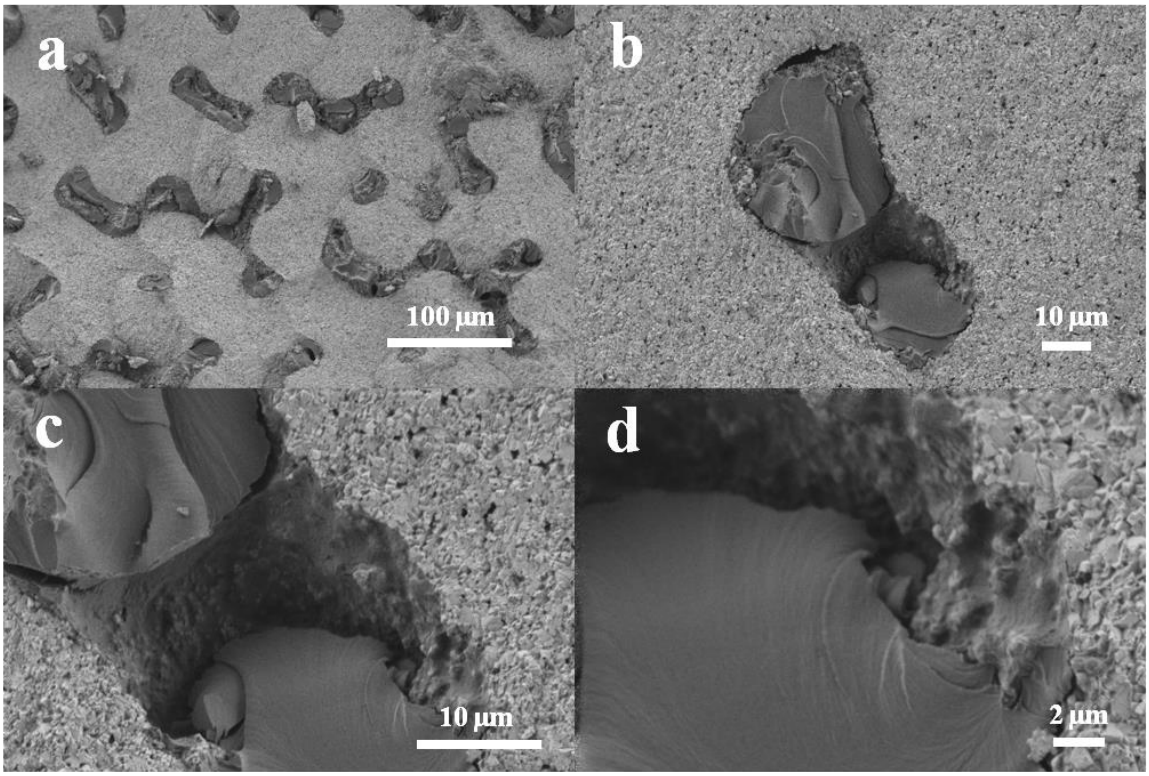

Figure 7.4 SEM cross-section images of the FR-CMC formed from the aramid-coated LAGP gyroid preform with epoxy infiltration.

The epoxy has completely filled the preform (*Figure 7.4 (a)*). The aramid and epoxy are also shown to form a bilayer with aramid at the surface of the LAGP preform (*Figure 7.4 (d)*). The epoxy does not appear to encase the aramid fibres in the bilayer as the aramid fibre coating of the LAGP surface is still seen (*Figure 7.4 (d)*) similarly to the coated preform without epoxy (*Figure 7.3 (d)*). This is not ideal as stress transfer to the fibres will not be as efficient and the full tensile strength of the aramid will not be gained by the composite. Nevertheless, the composite in this state represents the final FR-CMC fabricated via sacrificial templating of printed templates and infiltration of aramid and epoxy in this preliminary investigation. The following section reports investigation of the mechanical properties of the FR-CMC.

7.5.4. FR-CMC Mechanical Analysis

In the previous chapter (**Chapter 6 Section 6.5.2.5**) the electrochemical performance of the ceramic preform was investigated. This showed that adequate ionic conductivity, density and microstructural parameters of the LAGP ceramic matrix were viable as a solid electrolyte. This section reports the complementary mechanical analysis of the FR-CMC to demonstrate the benefit of reinforcement and IPC microstructure to the mechanical properties of the ceramic electrolyte. Standard tensile testing typically requires a bone-shaped specimen to grip shoulders and apply tensile loading to the gage length, demonstrated by *Figure 7.5*. Complex bone-shaped specimens with relatively large gage lengths are required for micro-tensile testing. Due to the size limitations of the printing process, it would be impractical to produce such a sample.

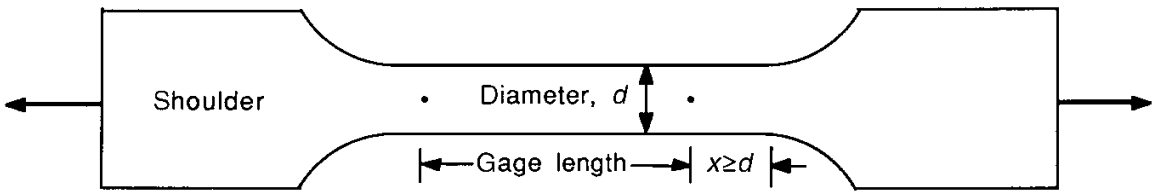

Figure 7.5 Schematic representation of a typical bone shaped tensile testing specimen part.[4]

An alternative to standard tensile testing is four-point bending, which requires much simpler specimen types. Four-point bending, discussed in **Chapter 2 Section 2.7**, analyses the flexural strength of straight beams. Unlike three-point bending, the beam experiences zero shear force and constant bending moment between symmetrically placed loads.[5] Though the tensile strength is not directly measured, it contributes to the flexural strength of the beam that can fail by tensile failure of outer surfaces. *Figure 7.6* illustrates the failure modes of fibre-composite beams by three- and four-point

bending.[5] Brittle materials, such as oxide ceramic electrolytes, have significantly lower tensile strength than compressive strength and therefore expect to fail by tensile fracture modes. Other fracture modes are possible with fracture by interlaminar shear being a disadvantage of the bending analysis. However, short chain aramid with high tensile strength and low weight percentage of the total FR-CMC makes fibre 'pull-out', discussed in **Chapter 3 Section 3.5.3**, and tensile fracture, respectively, more likely than tensile fracture of fibres. Therefore, tensile fracture of the outer surface is the expected fracture mode and relates flexural strength to the tensile strength of the material.

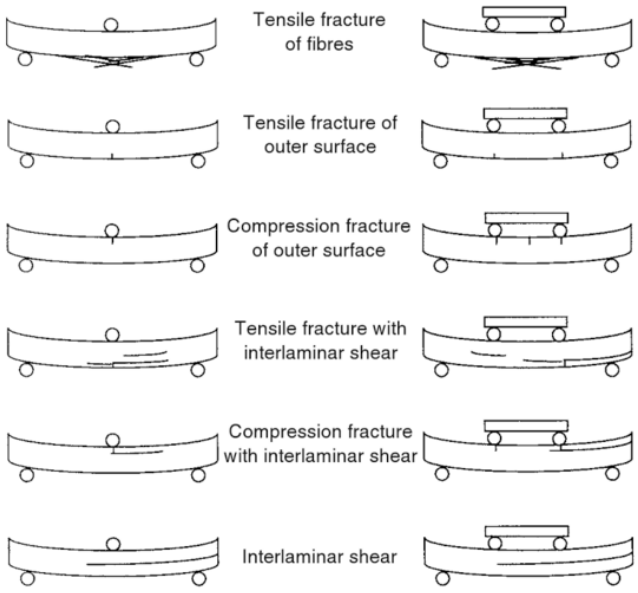

Figure 7.6 Schematic representation of the different fracture modes observed in three- and four-point bending.[5]

The beams were prepared according to the previous chapter, but with longer and thinner templates to fit the four-point bending adaptor. *Figure 7.7* shows images of *(a)* the prepared FR-CMC beam loaded into the four-point bending adaptor and *(b)* the beam after fracture. The fracture at two-thirds the length of the beam and forming on the

underside (connected by reinforcement at the top), indicates the beam failed due to tensile fracture of the outer surface (*Figure 7.6*).

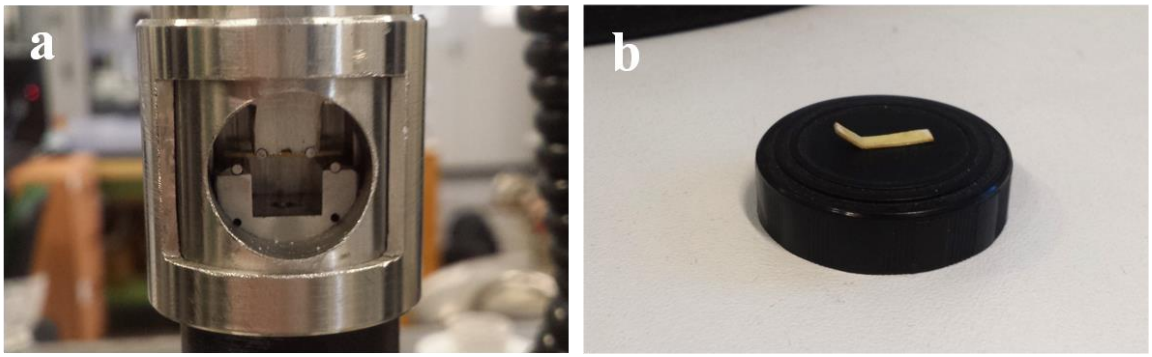

Figure 7.7 Images of the FR-CMC beam (a) placed in the four-point bending adaptor and (b) after tensile fracture.

The beams for four-point bending analysis include the benefit of implemented print extensions, discussed in **Chapter 5 Section 5.5.3**, that maintain the defined microstructural parameters regardless of the overall preform size. Therefore, the microstructural parameters of the LAGP preform (**Chapter 6 Section 6.5.2**) define the microstructural parameters of the ceramic matrix and therefore those of the total FR-CMC for mechanical testing (*Figure 7.7*). The characterisation section (**Section 7.3**) describes the analysis of LAGP beams for four-point bending. The maximum load before fracture can be used to deduce the maximum stress (flexural strength) at the outer surface of the beam. The following equation calculates the flexural strength, σ_f, for load span of 5 mm and support span of 10 mm (**Chapter 2 Section 2.7**):

$$\sigma_f = \frac{3PS}{4bh^2} \tag{7.1}$$

Where P, S, b and h are the applied load at fracture, support span length, specimen width and specimen thickness, respectively. *Figure 7.8* reports the four-point bending analysis stress-strain curve of the FR-CMC (*Figure 7.7*), a reference sample of an LAGP only beam (without microstructure) and an LAGP-epoxy composite without aramid fibres.

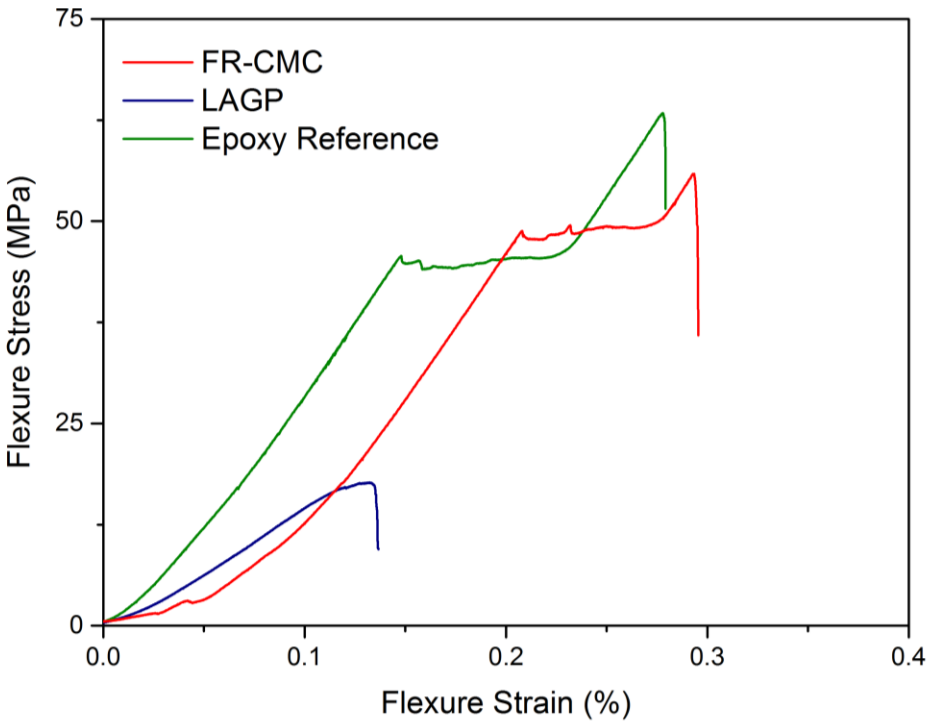

Figure 7.8 Stress-strain curve from beams of FR-CMC with aramid-epoxy-LAGP, epoxy reference with epoxy-LAGP without aramid fibre and LAGP without aramid, epoxy or microstructure.

The force at the point of fracture for the FR-CMC, epoxy reference composite and LAGP only specimens were 4.91 N, 6.03 N and 2.28 N, respectively. Therefore, the flexural strengths (*Equation 7.1*) of the FR-CMC, reference composite and LAGP only specimens were 55.85 MPa, 63.36 MPa and 17.71 MPa, respectively. The sharp drop observed in all plots corresponds to the complete fracture of the beam. The plateau regions of the FR-CMC and epoxy reference samples demonstrate plastic deformation

of the reinforcement after crack initiation has occurred in the beam. Both composites experience greater flexure stress and flexure strain before fracture. The addition of aramid fibres has decreased the flexural strength of the composite, which is explained in detail below. However, the epoxy-LAGP composite reference sample has increased the flexural strength compared to LAGP by 45.65 MPa. This is significantly larger than the 1.64 MPa increase in tensile strength observed with an aramid and epoxy-LAGP structural composite, reported in **Chapter 3 Section 3.5.4**. The interpenetrating composite microstructure has clearly enhanced the ceramic, with flexural strength values between that of the LAGP (17.71 MPa) and epoxy (approximately 100-130 MPa). The epoxy reinforces the ceramic in a similar way to what was intended with the aramid fibres. The stress at the tip of the propagating crack in the ceramic transfers to the ductile epoxy making it plastically deform. This demonstrates the effectiveness of increased internal crack bridging even without fibre reinforcement. With an optimised fibre-reinforced polymer with a high weight percentage of uniformly dispersed aramid fibres encased in epoxy, the increase in flexural strength and therefore toughness of the composite is expected to increase even further.

Figure 7.9 shows SEM images of the fracture cross-section of the FR-CMC after four-point bending analysis (*Figure 7.8*).

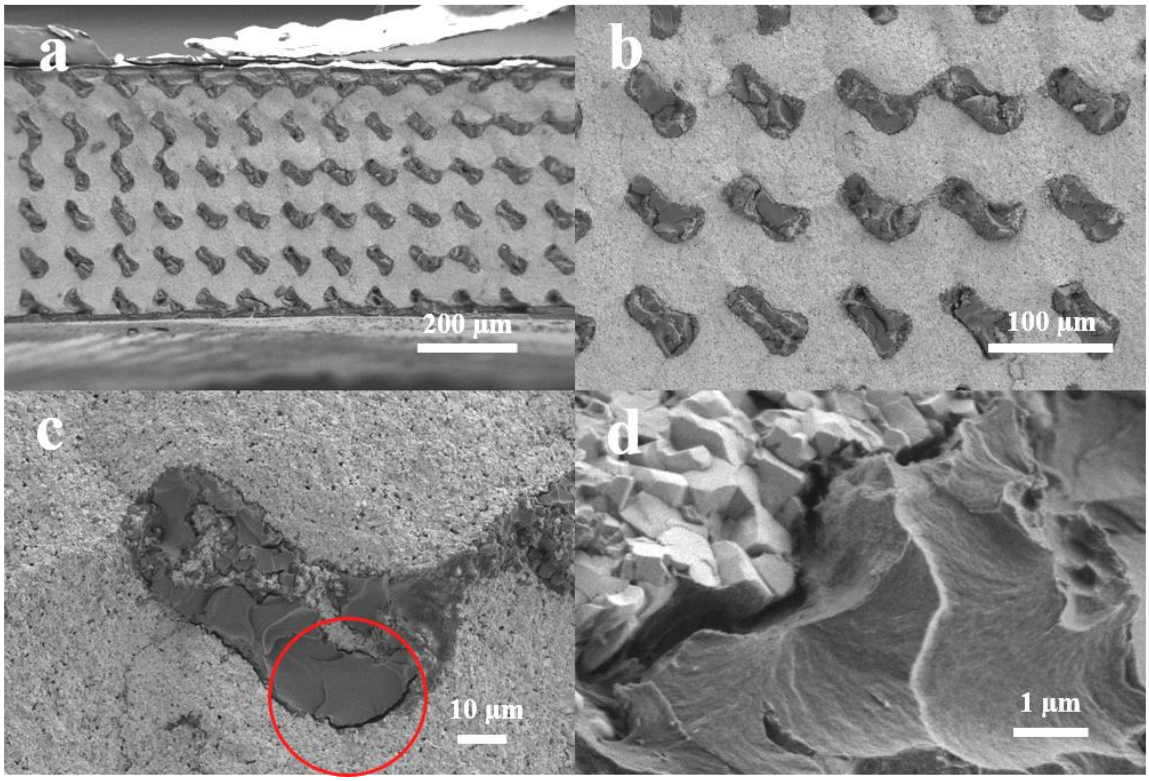

Figure 7.9 SEM cross-section images of the FR-CMC fractured surface by four-point bending showing delamination (red circle).

The fractured cross-section (*Figure 7.9*) looks similar to the prepared cross-section previously reported (*Figure 7.4*). The darker regions of the SEM images show epoxy that has plastically deformed in the fractured cross-section (*Figure 7.9 (d)*). However, there are no signs of fibre pull-out, which is a typical failure mode of FRP.[6, 7] The size of the fibres is too small to observe such phenomena and the previously observed bilayer, where fibre without encasement was suspected, would prevent this from happening (*Figure 7.4 (d)*). On closer inspection of *Figure 7.9 (c)* and *(d)*, a portion of what looks like delamination (red circle) has occurred at the interface of the previously reported bilayer, which is another common failure mode.[7] Without encasement of aramid fibres in epoxy, the two layers appear to come apart under loading promoting delamination. This could account for the lower flexural strength of

the aramid-epoxy-LAGP FR-CMC compared to the epoxy-LAGP composite without aramid fibres, as the stress transfer from the ceramic to the reinforcement is impeded.

Unfortunately, the FR-CMC in its current state does not successfully reinforce oxide ceramic electrolyte beyond that of epoxy. However, the epoxy-only composite has demonstrated increased flexural strength compared to an LAGP-only beam. This confirms the ability of an oxide ceramic electrolyte with interpenetrating composite microstructure to benefit from the mechanical properties of reinforcement. An improved synthesis of FRP that allows for a uniform dispersion of aramid fibre in the epoxy, should improve the mechanical reinforcement even further.

Increasing the weight ratio of aramid to epoxy is known to increase the tensile strength of the resultant FRP. *Figure 7.10* shows literature values for the tensile mode of fracture toughness (K_{IC}) of FRP short chain aramid-epoxy specimens with increasing fibre concentration.[3] Maximising the tensile or flexural strength of the FR-CMC requires further investigations in this area.

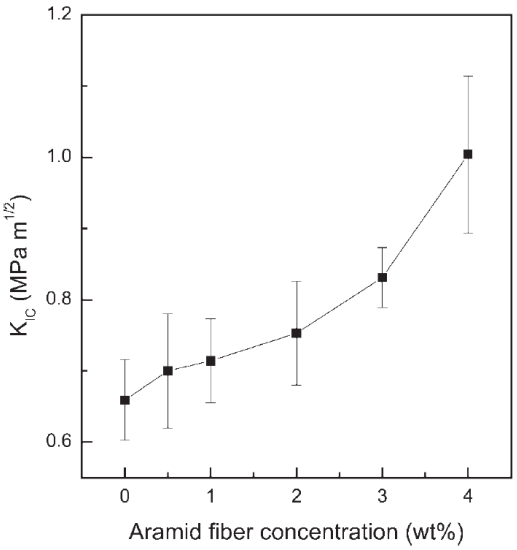

Figure 7.10 Graph showing the increase in fracture toughness with increased aramid fibre concentration in polymer.[3]

7.6. Conclusion

This work has shown that oxide ceramic electrolyte preforms can be infiltrated with fibre-reinforced polymer to form a fibre-reinforced ceramic matrix composite. Aramid fibres and epoxy compose the fibre-reinforced polymer infiltrated via a two-step infiltration procedure. Four-point bending analysed the flexural properties of the FR-CMC against a reference and an LAGP only specimen. The analysis represents a preliminary investigation into the FR-CMC in its current state and confirms the enhancement of flexural strength by polymeric-reinforcement.

The reported methodology of an initial reinforcement infiltration procedure was not shown to impart the tensile strength of the aramid fibres. An epoxy-LAGP composite without aramid fibre was shown to have higher flexural strength than the FR-CMC with fibre reinforcement, due to delamination in the latter composite. An alternative procedure for direct infiltration of FRP, of uniformly dispersed aramid fibres in epoxy, from a DMSO dispersion of aramid and epoxy has been outlined. However, the synthesis required a higher concentration of aramid that resulted in greater shrinkage to the FRP, due to more DMSO. Future work could increase the number of repeated infiltrations to counteract the added shrinkage.

The previously reported microstructural parameters of the LAGP preform became those of the final FR-CMC. Such analysis allows the modification of different FR-CMC parameters to investigate and optimise the stress transfer efficiency and therefore the mechanical properties of the composite. The presented work on template fabrication, preform formation and reinforcement infiltration represents a solid foundation to achieve this.

7.7 References

[1] Yang, M. *et al*. Dispersions of aramid nanofibers: a new nanoscale building block. *ACS Nano* **5**, 6945-6954 (2011).

[2] Martí, M., Molina, L., Alemán, C. & Armelin, E. Novel epoxy coating based on DMSO as a green solvent, reducing drastically the volatile organic compound content and using conducting polymers as a nontoxic anticorrosive pigment. *ACS Sustainable Chem. Eng.* **1**, 1609-1618 (2013).

[3] Wang, L., Tjiu, W. C., Teh, S. F., He, C. & Liu, T. Fracture and toughening behavior of aramid fiber/epoxy composites. *Polym. Compos.* **26**, 333-342 (2005).

[4] Davis, J. in *Tensile Testing*. (ASM International, 2004).

[5] Hodgkinson, J. M. in *Mechanical Testing of Advanced Fibre Composites* (ed Hodgkinson, J. M.) (CRC Press, 2000).

[6] Travitzky, N. Processing of ceramic–metal composites. *Advances in Applied Ceramics* **111**, 286-300 (2012).

[7] Yan, L. & Chouw, N. Dynamic and static properties of flax fibre reinforced polymer tube confined coir fibre reinforced concrete. *Journal of Composite Materials* **48**, 1595-1610 (2014).

Chapter 8: Conclusion & Outlook

The main aim of this work was to fabricate a FR-CMC of oxide ceramic electrolyte and fibre-reinforced polymer with IPC microstructure. The reinforced composite fabrication procedure required development of suitable templates for microstructure reproduction to 3D-porous ceramic. Suitable ceramic preform fabrication procedures were then required for optimal reproduction from the templates and a final reinforcement infiltration procedure to the FR-CMC.

In **Chapter 3** it was proven that the tensile strength of oxide ceramic electrolyte pellets can be increased by fibre-reinforced polymer structural composites. A structural composite has been formed by fibre alignment and epoxy lamination to the surface of the ceramic pellet. The structural composite, though not appropriate as an electrolyte layer due to covering of the ceramic surface, exhibited an increase in tensile strength against an epoxy coated reference sample without fibre. This demonstrated the successful reinforcement of the ceramic matrix by polymeric-fibre and supports further investigation of this approach. However, the increase in tensile strength was moderate compared to the theoretical tensile strength of the aramid fibres and therefore an IPC microstructure was considered to improve stress transfer efficiency and tensile strength of the composite.

Data presented in **Chapter 4** have shown that a 3D-interpenetrating solidified bijel can be fabricated as a template and can be further processed to a ceramic preform via sacrificial templating and then to a polymer-ceramic composite. The ceramic preform microstructure took on bijel character, but the filling of the bijel template by

ceramic particles during sacrificial templating was suspected to be poor. μCT and microstructural parameter analysis were used to characterise the template and preform. The microstructural parameters of the preform showed large deviation and shrinkage from the original template. Both indicated the presence of bottlenecks in the template that likely impeded sacrificial templating and worsened the quality of the preform. The poor ionic conductivity of the ceramic preform, compared to a pressed pellet, confirmed the presence of microstructure bottlenecks that may have impeded the ceramic preform formation procedure. Therefore, advanced template fabrication procedures were investigated.

The results of **Chapter 5** have shown that templates can be designed and fabricated with interpenetrating microstructures with the intention of introducing 3D-porosity to ceramic electrolyte. Computer-aided design and stereolithography demonstrated the capacity to obtain polymer templates with desired and engineered microstructures. Designed architectures of cubic, gyroid, diamond and bijel were printed as low solid volume fraction 3D-interconnected polymer templates. These templates provided a route for sacrificial templating, allowing the theoretical formation of high solid volume fraction preforms, which provide high ceramic compressive strength and interconnected porosity for complete reinforcement infiltration. Modification of print specifications enabled the fabrication of hierarchical microstructures. Templates with hierarchical microstructure provided a route for replication, with the potential to avoid detrimental hollow struts and low solid volume fraction preforms. The template design and fabrication workflow has enabled the ability to adjust and define microstructures for further processing and reinforcement of the final FR-CMC. Therefore, both preform formation procedures were investigated.

Further work in **Chapter 6** demonstrated the formation of a ceramic preform via sacrificial templating with a printed template, suitable as the ceramic matrix of a FR-CMC. An adapted sacrificial templating procedure using centrifugation produced ceramic preforms with excellent reproduction of the template microstructure, high solid volume fraction and 3D-interconnected porosity. Further analysis by PXRD confirmed the formation of LAGP material with no observed impurity. The gyroid architecture preform presented the most suitable microstructural parameters for further FR-CMC investigation having the most uniform channel size and sample thickness. A preliminary composite of the gyroid preform with polypropylene demonstrated comparable ionic conductivity to a prepared pellet of the same material, confirming the capability of the ceramic matrix to function as an electrolyte layer.

Chapter 7 has shown the final FR-CMC with IPC microstructure of oxide ceramic electrolyte and FRP having beneficial mechanical properties compared to pure ceramic. Fabrication of the final FR-CMC with aramid-epoxy FRP and LAGP ceramic matrix formed via sacrificial templating with a printed gyroid template. An adapted literature synthesis was used to prepare an aramid dispersion. The dispersion was used to coat the LAGP preform before epoxy infiltration formed a bilayer with the fibre coating. The prepared material formed the final FR-CMC. Four-point bending analysis showed an increase in flexural strength of the FR-CMC against a ceramic only reference sample. However, the aramid fibres were found to worsen the mechanical reinforcement compared to a ceramic-epoxy composite without fibre. It was concluded that another synthesis was required for FRP fabrication into the ceramic preform.

The prepared FR-CMC and epoxy-ceramic composite has demonstrated a mechanical advantage over pure ceramic and reinforced ceramic without

interpenetrating microstructure. The composites with interpenetrating microstructure validated the novel route of mechanical reinforcement justifying further work in this area. The introduced pore microstructure could also be investigated to compare different parameters and architectures. This work, with highly controlled template microstructure, presents a solid foundation for the further development and implementation of this novel composite electrolyte.

This work has investigated the development of the FR-CMC system with LAGP oxide ceramic electrolyte. However, developing the synthesis to form practical electrolyte layers for use in commercial batteries requires further investigation. The compatibility of the prepared composite requires cycling performance analysis within an electrochemical cell with different materials. Furthermore, fabricating the FR-CMC as a thin-layer for an electrochemical cell and analysing its properties is key to implementing this work. Current 2-photon stereolithography technology has the ability to print structures with approximate feature sizes of 200-600 nm. However, complex template architectures and FR-CMC fabrication becomes more challenging at this length scale. The specific mechanical forces that a solid electrolyte experiences in an electrochemical cell may also vary with cell type, environment and cycling performance. This area has yet to be studied extensively, but is pertinent to this work on mechanical reinforcing thin-layer electrolytes.

The current FR-CMC has only been fabricated with LAGP, which is not suitable for use with metallic lithium. However, other solid oxide ceramic electrolytes are known for their stability against metallic lithium and could be investigated for fabrication in a FR-CMC and all-solid-state lithium metal cell. The reported work presents an initial processing route for investigation with other materials. The

reinforcement of ceramic would allow surface microstructure modifications of the FR-CMC previously reported to prevent lithium dendrite growth in oxide ceramic electrolytes. The surface modification causes microstructural features that have a detrimental mechanical effect on an oxide ceramic electrolyte thin-layer. However, reinforcement could counteract this effect.

Should a thin-layered fibre-reinforced ceramic matrix composite afford beneficial mechanical properties and dendrite resistance, while maintaining and enhancing the conductance and therefore performance of an all-solid-state metallic lithium cell, then it is likely to replace conventional lithium-ion batteries containing liquid electrolyte.

Appendices

Appendix 1

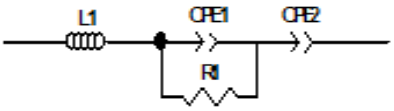

Element	Freedom	Value	Error	Error %
L1	Free(+)	2.1783E-05	8.4116E-06	38.615
CPE1-T	Free(+)	4.159E-10	2.2231E-10	53.463
CPE1-P	Free(+)	0.86207	0.039949	4.6341
R1	Free(+)	1412	4.0915	0.28977
CPE2-T	Free(+)	2.3925E-06	9.6682E-09	0.4041
CPE2-P	Free(+)	0.88131	0.0010509	0.11924

Chi-Squared:	0.0015556
Weighted Sum of Squares:	0.2846

Component	Ionic Conductivity, σ (S cm^{-1})
Total	2.84 x 10^{-4}

Appendix 2

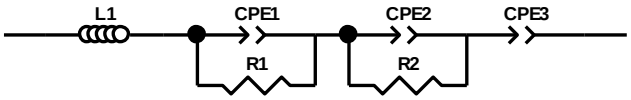

Element	Freedom	Value	Error	Error %
L1	Free(+)	0.00016088	6.6135E-06	4.1108
CPE1-T	Free(+)	2.6348E-11	1.9383E-13	0.73565
CPE1-P	Fixed(X)	1	N/A	N/A
R1	Free(+)	18476	155.25	0.84028
CPE2-T	Free(+)	4.338E-09	3.0475E-10	7.0251
CPE2-P	Free(+)	0.79701	0.0068965	0.8653
R2	Free(+)	28426	236.19	0.83089
CPE3-T	Free(+)	3.4715E-06	2.563E-07	7.383
CPE3-P	Free(+)	0.78361	0.016452	2.0995

Chi-Squared:	0.0003539
Weighted Sum of Squares:	0.033267

Component	Ionic Conductivity, σ (S cm^{-1})	Capacitance, C (F cm^{-1})
Bulk	2.25×10^{-5}	1.10×10^{-11}
Grain Boundary	8.87×10^{-6}	1.82×10^{-10}
Total	8.87×10^{-6}	-

Appendix 3

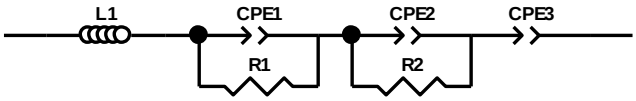

Element	Freedom	Value	Error	Error %
L1	Free(+)	5.6697E-05	6.7492E-06	11.904
CPE1-T	Free(+)	4.5743E-13	4.0613E-13	88.785
CPE1-P	Free(+)	1.39	0.081649	5.874
R1	Free(+)	795.5	264.06	33.194
CPE2-T	Free(+)	1.1938E-09	8.1119E-11	6.795
CPE2-P	Free(+)	0.78801	0.0080536	1.022
R2	Free(+)	11673	279.56	2.3949
CPE3-T	Free(+)	2.8009E-06	5.9971E-08	2.1411
CPE3-P	Free(+)	0.66795	0.0037966	0.5684

Chi-Squared:	0.00014902
Weighted Sum of Squares:	0.012368

Component	**Ionic Conductivity, σ (S cm^{-1})**	**Capacitance, C (F cm^{-1})**
Bulk	2.45×10^{-4}	3.97×10^{-11}
Grain Boundary	1.56×10^{-5}	1.15×10^{-11}
Total	1.56×10^{-5}	-

Appendix 4

```
a=2*pi;

s=2*pi/60;

[x,y,z]=meshgrid(-a:s:a,-a:s:a,-a:s:a);

cx = cos(2*x);

cy = cos(2*y);

cz = cos(2*z);

u = 50.0*(cos(x).*sin(y)+cos(y).*sin(z)+cos(z).*sin(x))-0.5*(cx.*cy+cy.*cz+cz.*cx)-52;

[f,v]=isosurface(u,0);

vertface2obj(v,f,'thinfig%.obj')
```

Appendix 5

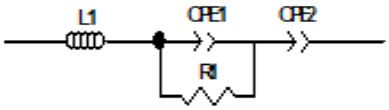

Element	Freedom	Value	Error	Error %
L1	Free(+)	5.3673E-05	1.7736E-05	33.045
CPE1-T	Free(+)	6.1795E-11	1.871E-11	30.278
CPE1-P	Free(+)	0.94592	0.020376	2.1541
R1	Free(+)	5892	34.112	0.57895
CPE2-T	Free(+)	5.0341E-07	3.2243E-09	0.64049
CPE2-P	Free(+)	0.70797	0.0013896	0.19628

Chi-Squared:	0.0019346
Weighted Sum of Squares:	0.26311

Component	**Ionic Conductivity, σ (S cm^{-1})**
Total	1.69 x 10^{-4}

Appendix 6

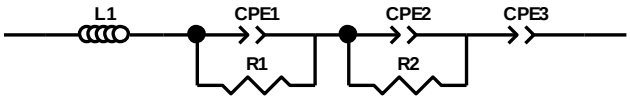

Element	Freedom	Value	Error	Error %
L1	Free(+)	0.00030595	4.9778E-06	1.627
CPE1-T	Free(+)	2.5243E-11	2.0809E-13	0.82435
CPE1-P	Fixed(X)	1	N/A	N/A
R1	Free(+)	58093	607.27	1.0453
CPE2-T	Free(+)	1.9003E-10	7.3463E-12	3.8659
CPE2-P	Free(+)	0.92849	0.0033727	0.36325
R2	Free(+)	90039	665.34	0.73895
CPE3-T	Free(+)	7.7136E-08	2.8849E-09	3.74
CPE3-P	Free(+)	0.77027	0.0054838	0.71193

Chi-Squared:	7.0134E-05
Weighted Sum of Squares:	0.0050496

Component	**Ionic Conductivity, σ (S cm^{-1})**	**Capacitance, C (F cm^{-1})**
Bulk	1.83×10^{-5}	2.68×10^{-11}
Grain Boundary	7.17×10^{-6}	8.67×10^{-10}
Total	7.17×10^{-6}	-